به نام خدا

# مرکز دانلود رایگان
# مهندسی متالورژی و مواد

## www.Iran-mavad.com

# Cubic Zirconia
# and
# Skull Melting
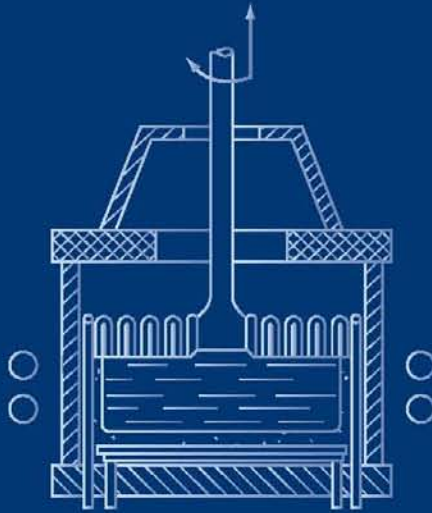
Yu. S. Kuz'minov,
E. E. Lomonova
and
V. V. Osiko

# Cubic Zirconia and Skull Melting

# CUBIC ZIRCONIA
# AND
# SKULL MELTING

Yu.S. Kuz'minov, E.E. Lomonova
and V.V. Osiko

www.iran–mavad.com

مرجع دانشجویان و مهندسین مواد

# CONTENTS

# Preface*

Many branches of science, technology and industry require refractory oxide single crystals, glasses with the melting point higher than 2000°C, and fused ceramic materials. There is also a large number of important national economy and scientific–technical problems whose solution is delayed because of the absence of materials stable at high temperatures and in corrosive media. For example, at the moment, there are no electrical heating furnaces capable of working at temperatures higher than 2000°C in an oxidation atmosphere, because the conventional heaters made of silicon carbide or molybdenum disulphide cannot reach of these temperatures. At the same time, high-temperature heating systems, working in air or in the oxygen atmosphere, are urgently required for various technological processes: annealing of crystals, synthesis of luminofors, sintering of ceramic components, production of sitalls, etc. The development of materials with simultaneously high electrical conductivity and resistance to the effect of the oxidation atmosphere at temperatures of approximately 2000°C is a very important technological task. This also includes tasks of the development of highly homogeneous and corrosion-resisting refractory materials for the intensification of pyrometallurgical processes and increasing the quality of melted alloyed steels and alloys, solid electrolytes for chemical current sources, artificial jewellery stones, and many other areas.

The absence of these materials or their low quality are caused mainly by technological difficulties. The point is that the currently use methods of producing polycrystalline ceramic high-temperature materials have considerable shortcomings, reflected in the quality of components produced from them. For example, the main shortcoming of the method of sintering a powder charge at temperatures below the melting point is that the synthesis of compounds in the solid phase does not take place to the end and, consequently, the reaction product contains impurities of the phases of unreacted components. This greatly reduces heat resistance and other properties of ceramic materials. In the production of fused materials in arc furnaces the materials are contaminated with the products of combustion of the electrodes; heat fields are highly heterogeneous resulting in fractionation of the melt. Many substances as, for example, calcium oxides or compounds

---

*This preface was written by Nobel Prize Laureate A.M. Prokhorov for the book Fianites, published by Nauka, Moscow, in 2000.*

www.iran–mavad.com

مرجع دانشجویان و مهندسین مواد

based on them, cannot be generally produced in a relatively pure condition by arc melting. Finally, to grow single crystals of high-temperature compounds from the melt, it is necessary to develop crucibles from materials capable of withstanding high temperatures and not reacting chemically with the melt. The range of these materials is extremely small, with the most suitable being metallic iridium which is in short supply. This material oxidises at elevated temperatures in air and, in addition to this, cannot be used at temperatures higher than 2500–2150°C. Other metals are characterised either by low (in comparison with iridium) melting point or chemically interact with the melt and contaminate it.

The difficulties can be overcome by the technology of fused ceramic materials and oxide high-temperature single crystals produced by direct high-frequency melting in a cold container. The method was developed at the P.N. Lebedev Institute of Physics of the Russian Academy of Sciences. Industrial equipment has been constructed, technologies of melting and directional solidification of a large number of oxide materials of simple and complicated compositions have been proposed, and the properties of new materials and components based on them investigated.

This book, written by V.V. Osiko and Yu.S. Kuz'minov, the well-known experts in the area of growth and investigation of crystals, generalises a large amount of experimental and theoretical material for the technology of melting in solidification of high-temperature dielectrics, produced both at the Scientific Centre of Laser Materials and Technologies of the General Physics Institute of the Russian Academy of sciences, and throughout the world. Undoubtedly, the book will be useful to chemical technologies, students of appropriate specialisations, and will help advances in the area of development of new materials and technologies.

*Academician A.M. Prokhorov*
Nobel Prize Laureate

# Introduction

Single crystals, glasses and molten ceramic materials, based on nonmetallic high temperature compounds, are used widely in technology and industry. Components of optical devices, working elements of lasers and mazers, refractory components of metallurgical and glass furnaces, components of electrical engineering systems, electrodes and insulating elements of magnetohydrodynamic current generators – this list does not exhaust the entire range of applications of high-temperature nonmetallic materials.

In this book, the high-temperature materials refer not only to materials working at high temperatures (more than 1500°C), but also materials produced at high temperatures, irrespective of the application temperature. This type of material includes single crystals, glasses, polycrystalline ceramics based on oxides, fluorides, nitrides, and also borides.

The technology of high-temperature materials is an independent branch with its methods, equipment and, of course, unsolved problems. These problems include:

– the production of new single crystals, glasses and fused ceramics produced at temperatures higher than 2000°C. These temperatures require the development of completely new technological processes;

– the production of single crystals with a faultless homogeneous crystal structure. To satisfy this condition, it is necessary to develop technological processes with highly stable parameters over a long period of time;

– the production of single crystals, glasses and fused ceramics with high chemical purity. For example, the majority of laser crystals and glasses must not contain impurities of iron, copper, rare earth elements and other impurities with the concentration greater than $10^{-4}$%, with the exception of intentionally added admixtures, and glasses for optical fibre communication should not contain some optically active impurities in the amount greater than $10^{-6}$%. These conditions require special 'pure' technological processes in which the initial reagents are not contaminated;

– the production of materials in special oxidation–reduction gas media;

– the production of the required materials in large volumes with

a minimum consumption of natural resources, *i.e.*, energy, water, etc. and also with minimum waste.

The combination of these problems is the main difficulty for technologies. For example, high temperatures can be easily produced in industrial processes by arc melting. However, in this melting method it is quite difficult to maintain the chemical purity of the material and create the required oxidation–reduction conditions, and also ensure a stable crystallisation process. On the other hand, melting using radiation furnaces results in the required high purity of the material and the required oxidation–reduction medium, but it is not possible to produce large quantities of materials. Considerable difficulties are also found in other technological processes of producing high-temperature materials. As an example, the process of growth of high-temperature single crystals from the melt by the Czochralski method will be considered [1]. A melt of a crystallising substance is produced in a metallic crucible, heated with a resistance furnace or HF current. The crucible plays not only the role of a container for the melt but also of a heating body from which the heat is transferred to the melt. This method is used in the production of the majority of synthetic crystals for science and technology. The possibilities of the method are restricted by crucibles which are produced using only a small number of materials: for the oxidation atmosphere (air, oxygen) these are the expensive materials of the platinum group; in the neutral and reduction atmosphere – metals tungsten and molybdenum or graphite. The crucible material should have a higher melting point than the melt placed in it, and should not interact with the melt and the surrounding atmosphere. Unfortunately, none of the materials mentioned previously is characterised by the entire set of the required properties and this creates considerable difficulties in the development of a technology of high-temperature crystals. Similar problems are also found in the technology of glasses and fused ceramic materials.

We believe that the technology described in this book may prove to be more efficient in solving the problem of production of high-temperature materials from the melt. It is based on the method of direct high-frequency melting in a cold container. The process consists of three main stages: 1) initiation of the process using a special procedure – starting melting, 2) interaction melting of the substance by high-frequency current, 3) maintaining the melt in a solid shell (in a skull) with the composition completely identical with the composition of the melt.

These main elements of the method were proposed earlier by different authors. For example, in 1905 it was proposed to melt metals in a

solid shell produced from the same material [2]. This concept was so efficient that it became a basis for the extensive application of skull melting methods in pyrometallurgy. The energy sources in melting metals included mostly the plasma jet, the electric arc and also the electron beam [3]. The induction melting of a metal in a cold crucible was proposed at a considerably later time [4, 5]. However, the method was not used widely because of the special features of the method described below. It was also attempted to use high-frequency melting in a skull for the synthesis of semiconductors [6, 7]. In 1961, Monforte [8] used the method of high-frequency heating in a solid shell for melting ferrites. In Russia, work continued on the growth of iron garnet crystals [9].

Starting in the middle of the 60s, the work in Russia on the technology of high-temperature materials by the method of direct high-frequency melting, the construction of appropriate equipment and the production of crystalline materials was conducted at the Lebedev Institute of Physics of the Russian Academy of Sciences (FIAN) [10,11] where the first technological systems for melting high-temperature dielectrics were also constructed and the main relationships governing the process were described. This period indicates the start of a systematic investigation of the conditions of melting in solidification of different chemical compounds: fluorides, halides, simple oxides, complex oxide compounds. The synthesis conditions of single crystals, glasses, and fused ceramic materials, including polyphase compositions, were investigated. Ruby and leucosapphire crystals were grown for the first time by the Czochralski method at the FIAN. Large single crystals of stabilised cubic zirconia and hafnia were produced for the first time, in addition to single crystals of oxides of rare earth elements, scandium, yttrium, gadolinium and erbium. Many fused high-temperature compounds have better properties than identical materials produced previously by solid phase synthesis. They include the compounds such as mullite, beta-sodium-alumina, chromires of yttrium, lanthanum and rare earth elements, titanates, zirconates and hafnates of elements of the second and third group of the periodic table of elements, high-temperature glasses and other materials. The experience accumulated in these investigations shows that the new technology has a number of principal advantages in comparison with the conventional technologies. The main are:

    – the temperature in the process may reach 3000°C without any principle restrictions;

    – the absence of contact of the melt with chemically foreign substances guarantees the high 'purity' of the process. The synthesised

materials contain impurities of secondary elements with the content at least not higher than the purity of the initial component. In many cases, the purity proved to be even slightly higher because high-temperature impurities, such as oxides of alkali elements, chlorides, nitrates, sulphates and many others are removed from the melt;

– the process can be realised in various gas atmospheres: in air, oxygen, neutral gases, and also in vacuum, so that it is possible to produce different oxidation–reduction conditions and carry out melting in oxidation, reduction or neutral atmospheres;

– the process is highly suitable for carrying out chemical reactions in the melt at high temperatures, for example, the synthesis of complex oxide compounds. Almost any type of chemical reaction can be carried out in a cold container in the melt, both in the single-phase and heterophase systems. Thus, the cold container is used successfully as a chemical reactor:

– the process of melting and crystallisation can be not only periodic but also continuous so that the process can be automated.

The previously mentioned advantages indicate that it may be possible to develop a new universal industrial process of producing high-temperature single crystals, glasses and fused ceramic materials.

Reports which appeared in recent years indicate that the new technology of melting high-temperature materials is used widely both in Russia and abroad. Intensive research is being carried out in the USA, North Korea, South Korea, Japan, and some other countries [12, 13].

In the book, special attention is given to the technology of zirconia crystals with a stabilised cubic structure. The method of directional solidification of this compound is used as a basis of the technologies for many other crystals. Zirconia crystals themselves are of considerable scientific and practical interest. Zirconia is characterised by several phase transformations, the last of which (monoclinic) results in complete fracture of the crystals. Therefore, the stabilisation of the cubic structure by yttrium, calcium, rare-earth elements and transition metals is an important scientific and technical task. The crystal lattice of zirconia has a relatively porous structure and permits the implantation of a large amount of secondary elements. Because of this, it is possible to produce a wide range of crystalline substances with interesting physical and mechanical properties, with jewelry stones being the most important products. Pure zirconia, stabilised by yttrium or calcium, can be used for imitating diamond crystals whose optical, mechanical (hardness) and other characteristics become closer and closer to the natural diamond. It may have diamond faceting, so that it is very

difficult to distinguish them from real diamonds. The methods of identification of diamonds and of their imitators are also described in this book. Doping of zirconia crystals with rare earth elements and transition metals enables the production of an entire range of natural precious stones, including izumrud.

Large cubic zirconia crystals were synthesised and produced for the first time at the Lebedev Institute of Physics (FIAN) and referred to as **fianites** in honour of the Institute. In the world, they are referred to as cubic zirconia (CZ).

Investigation of the phase transformations in zirconia in stabilisation of the cubic structure by different elements, taken in different proportions, has shown three independent directions. The first direction are fianites in cases in which zirconia is fully stabilised and the crystals should have a stable cubic structure up to a melting point of approximately 2800°C. They are referred to as fully stabilised zirconia (FSZ).

Partially stabilised crystals are also interesting. In this case, we obtain crystals or, more accurately, intergrown polycrystals in which the different phases (cubic, tetragonal and monoclinic) are represented in different ratios, which depend on the nature of the stabilising element, the process kinetics and prior thermal history of the specimen. These materials are referred to as partially stabilised zirconia (PSZ). In the book, we examine in detail phase transformations, domain structure and mechanical properties of PSZ. A characteristic feature of these materials is their high mechanical strength and hardness so that they are regarded as promising materials for the fabrication of components of mechanisms in which these properties are of considerable importance.

The third direction are the crystals in which the amount of the stabilising element or of several elements is considerably greater than that required for the complete stabilisation of the cubic lattice (from 20 to 40 mol.% $R_2O_3$, where R – Y, Gd–Lu). The substances retain the cubic structure but because of the high density of the stabilising oxides with a large ionic radius, the optical properties of these substances differ from fianites. The investigated crystals are referred to as cubic oxides, C–OX). In the book, the physicochemical and mechanical properties of these substances are described and practical applications indicated. In addition, we examine the technology of oxide compounds produced for the first time in the single crystal state, and also of the well-known crystals, ceramics and glasses, synthesised by the cold container method. In most cases, the physicochemical properties of these compounds are considerably higher than those of the crystals produced by the traditional methods.

# References

1.  J. Czochralski, *Z. Phys. Chem.*, 92, 219, 1917.
2.  W.V. Bolton, *Elektrochemie*, 11, 45, 1905.
3.  A.A. Neustruev and G.L. Khodorovskii, Vacuum Skull Furnaces, Metallurgiya, Moscow, 1967.
4.  A.A. Fogel, *Izv. AN SSSR, Metallurgiya Toplivo*, 24, 2, 1959.
5.  G.H. Schipereit, *British Journal of Metals,* 13, 2, 140, 1961.
6.  H.F. Sterling and R.W. Warren, *ibid*, 67, 404, 1963.
7.  L.L. Kochergin, et al., *Byull. Izobret.*, 11, 52, 1961.
8.  F.K.Y. Monforte, *Appl. Phys.*, 32, 959, 1961.
9.  Yu.B. Petrov and E.I. Bezrukova, *Izv. AN SSSR, Neorg. Mater.*, 4, 1162, 1968.
10. V.B. Aleksandrov, et al., in: Current Topics in Materials Science, vol. 1, North Holland Publ., 1978.
11. V.I. Aleksandrov, et al., *Vest. AN SSSR*, 12, 29, 1973.
12. Yu.A. Polonskii, et al., *Ogneupory*, 7, 26, 1973.
13. J.F. Wenkus, Study, Design and Fabrication of a Cold Crucible System, Sci. Rep., Boston, No. 1, 1974.

# Physical fundamentals of melting in a cold crucible

## 1.1. INDUCTION HEATING OF MATERIALS. DEVELOPMENT OF THEORY

The theory of induction heating, which has been studied in a large number of investigations [1–5], has been developed in detail and concerns mostly metals. However, the main conclusions of the theory are also fully applicable to the case of heating nonmetallic materials.

The method of induction heating is based on the interaction of an alternating electromagnetic field with a heated object without electrical contact. The variation of the electromagnetic flux with time $t$ in the material, placed in the induction circuit, results in the formation of an electromotive force (EMF) which is determined by the Faraday electromagnetic induction law:

$$e = -kd\psi / dt \qquad (1.1)$$

where $e$ is the instantaneous value of the EMF, V; $\psi = \omega\Phi$ is the total flux linkage number of the circuit, consisting of $\omega$ turns and penetrated by magnetic flux $\Phi$, Wb; $k$ is the proportionality coefficient, in the Gauss unit system $k = 1/s$, in the SI system $k = 1$. The minus sign determines the direction of the induction flux in accordance with the Lentz rule. The induction EMF is equal to the work carried out in displacement of an unit charge along a closed circuit, carried out by the forces of a vortex electromagnetic field.

If the dependence of flux $\Phi$ on time is close to sinusoidal $\Phi_M = \sin 2\pi f t$, the actual value of the EMF in the material is.

$$E = 4.44 f\omega \Phi_m, \text{ V} \tag{1.2}$$

where $\Phi_m$ is the amplitude of the magnetic flux in the material, Wb, $f$ is the frequency of oscillations of the field, Hz. Consequently, according to the Joule–Lentz rule, the thermal power, generated in the material, will be

$$p = E \cdot I \cos\varphi = 4.44 f\omega I \cdot \Phi_m \cos\varphi, \text{ W} \tag{1.3}$$

Here $I$ is the current passing in the material, A.

Equation (1.3) shows that power $P$ is proportional to frequency, with other conditions being equal. Increasing frequency increases the energy generated in the same volume, *i.e.* the power related to the unit volume increases.

In addition to frequency, the nature of absorption of the energy of the alternating electromagnetic field is determined by the electrical and magnetic properties of the material. The relationship of these properties of substances with the electromagnetic field is determined by the Maxwell equations. If the incidence of an electromagnetic wave onto a flat semi-bounded solid is examined, the transformation of the Maxwell equations and the transition to the coordinate system make it possible to obtain a relationship between the amplitude of the strength of the magnetic and electrical field:

$$H_m = H_{me} \exp(-x/\Delta), \tag{1.4}$$

$$E_m = H_{me}\left(\sqrt{2}/\gamma\Delta\right)\exp{-x/\Delta}, \tag{1.5}$$

where $H_{me}$ is the amplitude of the strength of the magnetic field on the surface of the solid, $x$ is the distance from the surface of the solid (depth), $\gamma$ is the specific conductivity of the solid; $\Delta$ is the depth of penetration of current into the material.

The expression for the depth of penetration has the following form:

$$\Delta = 503\left(\rho/\mu f\right)^{1/2}, \text{ m} \tag{1.6}$$

where ρ is the specific electrical resistance of the material, Ohm·m, μ is the relative magnetic permittivity.

At $x = \Delta$ are: $J_m/J_{me} = E_m/E_{me} = H_m/H_{me} = 1/e = 0.368$, where $J_m$ and $J_{me} = E_{me}/\Delta = H_{me}\sqrt{2}/\Delta$ are the density of alternating current at depth $x$ and on the surface of the conductor, respectively. Thus, the value of $\Delta$ characterises a decrease in amplitudes $E$, $H$ and $J$ with the depth of penetration of the electromagnetic field. In addition to this, the active power in a layer with thickness $x$ also depends on in the following manner [1]:

$$P_{0-x} = Sp_0\left[1 - \exp(-2x/\Delta)\right] \tag{1.7}$$

where $S$ is the surface area of the material through which irradiation passes; $p_0 = 0.25(J_{me})^2\rho\Delta$ is the specific power on the surface; at $x = \Delta$, expression (1.7) is transformed to the following form:

$$P_{0-x} = Sp_0\left(1 - e^{-2}\right) = 0856 Sp_0. \tag{1.8}$$

Consequently, in approximate calculations it may be assumed that the entire thermal energy is generated in the layer with thickness $\Delta$.

For a solid infinite cylinder, situated in a homogeneous alternating electromagnetic field, the Maxwell equations are usually written in cylindrical coordinates. In this case, the distribution of H, $E$ and $P$ along the radius of the cylinder at constant frequency $f$ is determined by the ratio $r_z\sqrt{2}/\Delta = d_z/\Delta\sqrt{2} = m$, where $r_z$, $d_z$ is the radius and diameter of the cylinder, respectively. This relationship is referred to as the relative diameter of the cylinder and characterises the degree of transmittance of the cylinder for electromagnetic radiation. As the value of $m$ decreases, the transmittance of material of the cylinder increases. In [1] it was shown that for a cylinder with height $a_z$, which is a part of the infinite cylinder (*i.e.* disregarding the edge effects), the equation of the power, generated in the cylinder, has the following form:

$$P_z = 0.5\pi\rho\left(m^2\right)A\left(H_{me}\right)^2 a_z, \text{ W} \tag{1.9}$$
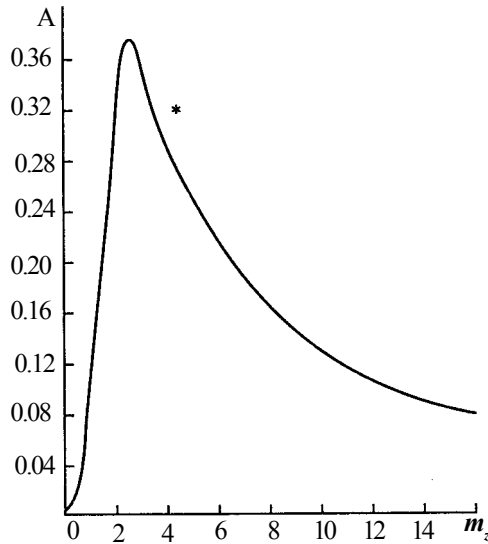
**Figure 1.1**. Graph of function $A$, calculated from equation (1.9).

where $A=(2/m)[\text{ber } m\cdot\text{ber}'m+\text{bei } m\cdot\text{bei}'m]/(\text{ber}^2m+\text{bei}^2m)$, where ber and bei are the Bessel cylindrical functions. The functional dependence of $A$ is shown in Fig. 1.1.

We examine the distribution of current density and power in the cross-section of the cylinder for different frequencies of the electromagnetic field. At $m < 1$, the distribution of current density and the strength of the magnetic field depend only slightly on frequency and with a further decrease of frequency they change almost linearly, depending on the radius of the cylinder [1]. Consequently, the distribution of power in the cross-section of the cylinder also becomes independent of frequency. It is evident that the depth of penetration of current into the heated cylinder may be disregarded in these conditions. In this case, it is necessary to introduce the thickness of the active layer $\xi$ and by analogy with the depth of penetration of current specify this depth in such a manner that 86.5% of the total amount of energy, supplied to the cylinder, is generated in the layer. Consequently, in the presence of a strong surface effect $\xi = \Delta$, and at low frequencies inequality $\xi<\Delta$ applies, and the depth of penetration of radiation $\Delta$ may exceed the radius or diameter of the cylinder. It was shown in [1] that at $m < 1$, the depth of the active layer is $\xi \approx 0.2\ d_z$, and the calculations carried out in [6] show that the approximate equality is already fulfilled at $m < 3.5$. In this case, with a decrease in
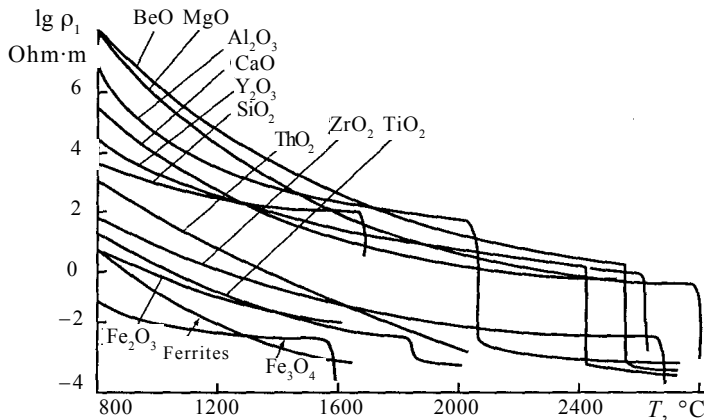
**Figure 1.2.** Temperature dependence of specific electrical resistivity of some oxides [9].
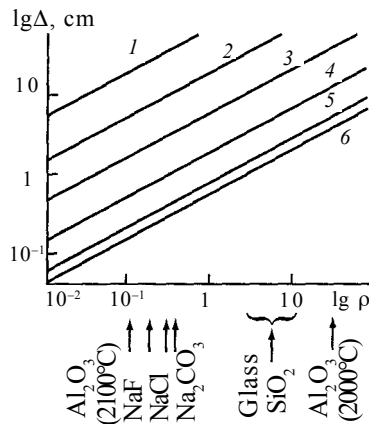


**Figure 1.3.** Frequency dependences lg $\Delta = f(\rho)$ for different substances [16]. 1,2) kHz; 3–6) MHz; $\rho$, ohm · cm.

current frequency or cylinder diameter, the depth of the active layer $\xi$ remains constant, but $\Delta$ increases and generated power $P_z$ decreases in accordance with equation (1.9). At $m > 6$, the depth of penetration depends only slightly on radius $r$, the intensity of surface absorption in these conditions rapidly increases and the dependences $H(r)$, $E(r)$, J($r$) and P($r$) have the same form as in the case of a semi-bounded medium with a flat surface. In this case, it may be approximately assumed that the entire energy of the electromagnetic field is generated in a hollow or cylinder with wall thickness $\Delta$.

In [7, 8], a mathematical model was used for analysis of the

electrical parameters of induction furnaces with a cold crucible. For the energy characteristics of the process of melting of oxides in a coldcrucible, it has been proposed to use the power coefficient of the induction coil:

$$\cos\varphi = P_m / (\eta_i S_i) \qquad (1.10)$$

where $P_m$ is the power generated in the melt; $S_i$ is the total power supplied to the induction coil. At a constant level of $S_i \cos\varphi \sim P_m$ because in this case the value of $\eta_i$ becomes constant and equal to 0.90–0.95 because of a very large difference in the specific electrical resistance values of copper, the material of the induction coil $\rho_i$ and the heated material $\rho$ [7]. It was established that the optimum conditions of generation of energy in the melt are fulfilled when the height of the induction coil is similar to the height of the melt in the crucible and at $m = 2\div7$ [4, 7]. In [8], the range of variation of $m$ was expanded to 2–7 where heating is most efficient. However, as reported in [9], the increase of $m$ is not a critical condition for the melting process and the temperature of the melt or diameter of the crucible can be increased 2–3 times in comparison with the optimum size, if the power of the generator allows this.

The graph of function $A$ (Fig. 1.1) and equation (1.9) shows that with increasing frequency and increasing value of $m$, the efficiency of induction heating becomes the highest at $m \geq 2.5$ then the condition $d_z > 3.5\Delta$ is fulfilled. Taking into count equation (1.6), it is possible to determine the minimum frequency required for heating the body of the cylinder [9]:

$$f \geq 3\cdot10^6 \rho / (d_z)^2, \text{ Hz} \qquad (1.11)$$

It is well-known [10–12] that at room temperature, the oxides are efficient dielectrics (Fig. 1.2). In order to ensure the generation of energy of the alternating field in the dielectrics, it is necessary to use very high frequencies. For example, for heating a cylinder with a diameter of $d_z = 0.1$ m from a material with $\rho = 10^5$ Ohm·m, in accordance with equation (1.11) it is necessary to use a frequency of $4.5\cdot10^7$ MHz, which corresponds to the infrared region of the spectrum. However, the frequencies used in practice of induction heating rarely exceed 10 MHz because of difficulties in the

**Table 1.1.** Electrical conductivity of several solid and molten nonmetallic materials [16]

| Compound | State | Temperature, °C | Specific electrical resistivity, Ohm · cm |
|----------|-------|-----------------|-------------------------------------------|
| LiF | Molten | 900 | $1.2 \cdot 10^{-1}$ |
| NaF | " | 1020 | $1.9 \cdot 10^{-1}$ |
| KF | " | 900 | $2.6 \cdot 10^{-1}$ |
| NaCl | " | 800 | $3.3 \cdot 10^{-1}$ |
| MgO | Solid | 2000 | $5 \cdot 10^{2}$ |
| $SiO_2$ | " | 1700 | $9 \cdot 10^{3}$ |
| $ZrO_2$ | " | 2000 | 1 |
| $Y_2O_3$ | Molten | 2430 | $5 \cdot 10^{-2}$ |
| $Y_2O_3$ | Solid | 1500 | $3 \cdot 10^{1}$ |
| $Al_2O_3$ | " | 1875 | $2.2 \cdot 10^{4}$ |
| $Al_2O_3$ | Molten | 2200 | $1 \cdot 10^{-1}$ |

generation and transfer of high power at these frequencies [9].

As already mentioned, in order to evaluate the possibility of melting oxide high-temperature materials, it is necessary to know the electrical properties in the solid state and in the melt. Table 1.1 shows the values of electrical conductivity of several oxides [13]. The dependence of lg $\Delta$ on lg $\rho$ makes it possible to determine substances which can be melted by the induction method. The specific resistance of a melt of the substances should not exceed 10 Ohm·cm (Fig. 1.3), otherwise the optimum frequency is outside the technically rational ranges [13].

Since at room temperature the majority of oxide materials are dielectrics, heating of these substances to the melting point directly with a high frequency field is not possible. Therefore, it is necessary to carry out of the so-called starting melting, i.e. application of additional heating sources in order to obtain temperatures at which the material itself starts to absorb the energy of the high frequency field. There are a large number of methods of starting heating [8]. However, the main method used in

this case is the method based on the application of an auxiliary electrically conducting (at room temperature) material, *i.e.* heating body. From the viewpoint of technology, it is most efficient to use small quantities of a metal of the appropriate oxide, included in the composition of the molten material. The metal is heated with a high frequency field and oxidised with atmospheric oxygen, and the generated heat case the surrounding material to the melting point. During heating, the charge are gradually melt, with the exception of the layer in the immediate vicinity of the watercooled walls of the container. The volume of the melt can be increased by adding new portions of the charge.

In order to determine scientifically substantiated methods of development of equipment for induction melting of oxide components, ensure the maximum productivity of this equipment with minimum energy losses, and also ensure the automatic control of the process of crystal growth in these systems, it is necessary to analyse thermal and electrodynamic processes taking place in the heated solid. In the literature concerned with induction melting of oxides, special attention is given to applied problems and the number of theoretical studies, concerned with examination of special features of the process, which greatly differs from the induction melting of metals, is extremely small. In particular, this is associated with a need to examine the electromagnetic field together with thermal processes in the melt. In this case, the thickness of the layer of the melt in which the energy of the high frequency (HF) field depends strongly on the main characteristics of the melt. In turn, the thermal and energy characteristics of the melt greatly change at high temperatures because of different types of processes taking place in the melt. The thermal and electrical characteristics of melt of oxides and oxide compounds and their temperature dependences in the temperature range 2000–3000 K are examined in only a small number of studies of guidance type. The absence of these data does not make it possible to calculate with sufficient accuracy the parameters of the actual system in heating dielectrics with a high frequency field. In addition, 'forced' assumptions, made in mathematical modelling of the system, cause that the resultant calculations are of qualitative nature and provide only approximate recommendations for the realisation of the actual process. However, these theoretical models make it possible to under stand more efficiently the relationships governing physical–chemical processes associated with direct high-frequency heating of oxide materials and

use them for controlling the crystal growth process.

The process of melting and crystallisation in a cold crucible differs from the process of melting in a heated crucible. In commercial melting in a 'hot' crucible, layers of the charge adjacent to the walls of the crucible are the first to melt. The intensity of the heat flow to the interface depends on the rate of propagation of heat in the melt. In direct high-frequency heating in a cold crucible, the heat from the volume of the melt, adjacent to the interface, is transferred directly to the solid phase resulting in its melting. In turn, the melted areas themselves become sources of thermal energy. This schema of the process was used [14, 15] in examination of the process of starting melting – for determining the melting time and the speed of movement of the interface to the crucible walls, the energy losses in this stage of the process in relation to the frequency of the generator and the initial volume of the melt. The experimental results show that in cases in which is considerably smaller than the diameter of the region of starting melting, the melting time increases with frequency as a function of $f^{1/2}$, and the energy, required for melting decreases as a function of $f^{-1}$. The energy losses are almost completely independent of the initial diameter of the region of starting melting because the main part of energy is used in the final stage of melting when the melt reaches the walls of the crucible.

The authors of [7, 9, 19] investigated processes, associated with the energetic of the process of melting in a cold crucible, in particular, the conditions in which the energy of the HF field is efficiently absorbed by the oxide melt. This is important for economic aspects of the process of melting different materials by this method. The authors of the above studies showed that the maximum power, generated in the melt, is determined mainly by the power factor of the induction coil $\cos\varphi$ Figure 1.4a shows the dependence of $\cos\varphi$ on parameter $m = \sqrt{2r}/\Delta$, where $r$ is the radius of the crucible with the melt. The presence of a distinctive maximum indicates that the heating conditions are optimum. Figure 1.4b shows the dependence of $\cos\varphi$ on the ratio of the height of the melt to the height of the induction coil. The dependence of $\cos\varphi$ on the position of the induction coil in relation to the level of the melt is identical. These experimental results show that it is possible to determine the optimum conditions of heating the melt: optimum frequency of the generator, position of the melt in relation to the induction coil and the ratio of the height of the melt and the
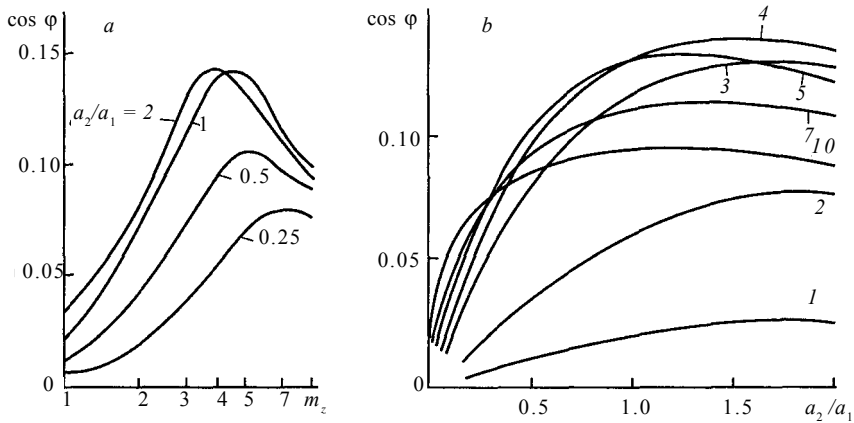
**Figure 1.4.** Dependence of cos φ on the radius of a crucible with a melt (in relative units) $m^2 = D(2)/\Delta\sqrt{2}$ (a) and on the ratio of the height of the melt to the height of the induction coil $a_1/a_2$ [9].

induction coil for specific materials.

In melting using HF heating of high-temperature nonmetallic materials, the spatial instability of the phase boundary is very important. This was mentioned for the first time in [17–20]. This problem is very important for controlling the process of crystallisation of the melt, especially in single crystal growth.

The formation of spatial instability is associated with specific features of direct HF heating and is determined by a rapid increase of the electrical conductivity of the material with increasing temperature and also with a large increase in the extent of heat transfer during melting. In induction melting of metals it was reported [4] that if the volume of molten metal has at least one variable parameter, for example, depth or diameter, which changes with the change in the level of supplied power, two types of heat balance appear: stable and unstable. The conditions of stability of the stationary thermal state are as follows:

1. The power balance $P_2 = P_1$, where $P_2$ is the power generated in the melt; $P_1$ is the power of heat losses [9, 15, 19–21];

2. $dp_1/da_2 > dp_2/da_2$, where $a_2$ is the height of the melt or, which is the same, $dp_1/dT_m > dp_2/dT_m, T_m$, where $T_m$ is the temperature of the melt. The dependences $P_2 = f(a_2)$, $P_1 = f(a_2)$ are shown in Fig. 1.5. Point 3 and 4 characterise the conditions in which the balance of the powers (condition 1) is fulfilled. It should be mentioned that point 3 characterises the unstable state in which small deviations of the system from the equilibrium condition result
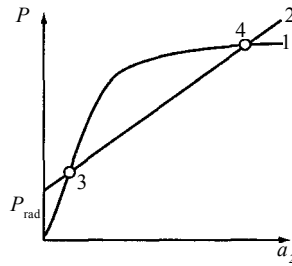
**Figure 1.5.** Dependences of generated power $P_2$ (1) and the power of thermal losses $P_1$ (2) on the depth of the melt $a_2$ [9]; (points 3 and 4 characterize the conditions in which the power balance is established).

either in crystallisation of the melt as a result of inequality $P_1 > P_2$ or in transition of the regime to point 4 in which the regime of stable balance is fulfilled, because both conditions are fulfilled and any deviation of $T_m$ or $a_2$ returns the system to the initial condition.

The existence of an instability of induction heating has been reported in the process of growth of crystals by internal melting [22, 23] which may be regarded as one of the modifications of direct HF melting. In this method, a pressed bar is melted inside the volume by means of direct heating in a high-frequency field. The resultant molten zone is situated inside the bar which is cooled on the external side as a result of radiant removal of heat. The molten zone moves along the axis of the bar and the resultant melt solidifies. In the above investigations, the authors presented a quantitative theory of the instability phenomenon formed in the process of induction heating of ceramic specimens. For this purpose, they solved a system of nonlinear differential equations determining the strength of the electromagnetic field and temperature in HF heating of dielectric materials whose. electrical conductivity depends exponentially on temperature: $\sigma = \sigma_0 \exp [-T_A / T]$. An example of a solution by the iteration method is presented in Fig. 1.6, which shows the dependence of the reduced temperature of the specimen on dimensionless parameter $A$ of the power supplied to the crucible.

The heat transfer from the specimen takes place as a result of radiation, which is especially intense at high temperatures, or by other transfer mechanisms. This dependence has the form of a double S-shaped curve whose upper part corresponds to the melting process. The variation of the shape of the curve in the upper part is due to a rapid increase of the electrical conductivity of the resultant melt. This is typical of oxide and many other dielectric
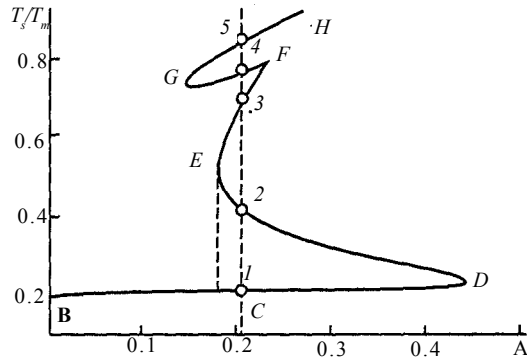
**Figure 1.6**. Surface temperature of the specimen $T_s$ normalized to the melting point $T_m$, as a function of parameter A characterizing the power of the HF field supplied to the melt [25,37].

**Table 1.2.** Calculated parameters of systems for cylindrical specimens with a diameter of 3 cm [25]

| Material | Frequency, MHz | Current, A | Power, kW | Material | Frequency, MHz | Current, A | Power, kW |
|---|---|---|---|---|---|---|---|
| BeO | 45000 | 1 | 6 | $ZrO_2$ | 5 | 16 | 7 |
| MgO | 450 | 2 | 13 | $HfO_2$ | 5 | 22 | 14 |
| $Al_2O_3$ | 90000 | 1 | 2 | $CeO_2$ | 450 | 69 | 13 |
| $SiO_2$ | 45000 | 1 | 1 | $ThO_2$ | 45 | 240 | 16 |
| $TiO_2$ | 230 | 1 | 1 | $UO_2$ | 5 | 15 | 7 |

materials. At a power level corresponding to $A = 0.2$, there are five stationary states of which only state 2 is unstable, and the remaining states are metastable. The states 4 and 5 correspond to the minimum and maximum volumes of the liquid core of the heated bar.

To control the solidification process, it is necessary to investigate the behaviour of material in the temperature range close of the melting point. The authors of [22] investigated the stability of the processes of HF heating and cooling of the material in relation to a large number of parameters of the system and evaluated the possibilities of controlling the process and its optimum parameters for specific substances, presented in Table 1.2. This approach can be extended to systems with a cold crucible, if the removal of heat from the volume of the heated material is taken into account. This may lead to specific recommendations for controlling the

crystallisation process. Using melting of a glass-forming material as an example, the parameters, characterising the real system, consisting of a generator, an induction coil and a melt, are presented below.

## 1.2. PARAMETERS OF DIRECT HF HEATING OF THE MELT

The method of mathematical modelling was used for analysis of the behaviour of the thermal and electrical parameters of a high-frequency furnace in relation to parameter $m = r_0\sqrt{2}/\Delta$. The authors established that the most critical parameter of induction melting in a cold crucible is the power factor of the induction coil $\cos\varphi = r_a/Zf$, where $r_a$ and $z_f$ is the active and total equivalent resistance of the induction coil, respectively [16]. The power factor of the induction coil characterises the active power generated in the melt at the maximum power of the induction coil *S*. Figure 1.4a shows the dependence $\cos\varphi = f(m)$ for different ratios of the dimensions of the induction coil and the volume of the melt. The extreme form of the curves indicates the existence of optimum conditions of generation of energy in the melt which are fulfilled at $r_0\sqrt{2}/\Delta = 5 \div 7$, where the height of the induction coil should be similar to the height of the melt. However, as shown in [9], in a real system the value of *m* should be higher than $m_{opt}$ because of the need to ensure the unstable state of the melt.

In order to determine the main parameters of direct high-frequency induction melting of the material, *i.e.* the size of the crucible and the working frequency of the generator, it is necessary to know the electrical characteristics of the melt. It is well-known [26] that at room temperature the oxide glasses are typical dielectrics with a specific electrical resistance of $10^{15}$–$10^{17}$ ohm·cm, so that they cannot be heated directly by the high-frequency field at frequencies of 1–10 MHz. This frequency range is examined because the application of higher fre-quencies in practice is associated with problems in the generation and transfer of high powers at these frequencies. Starting materi-als, usually used for boiling of glass ($SiO_2$, $Na_2CO_3$, $MgCO_3$, $CaCO_3$, *etc.*) are also dielectrics at room temperature. The specific electrical resistance of glasses of different grades (Fig. 1.7) decreases with increasing temperature and in the temperature range 1200–1400°C, used in most cases for boiling of glass, they are equal to 3–50 ohm/cm.
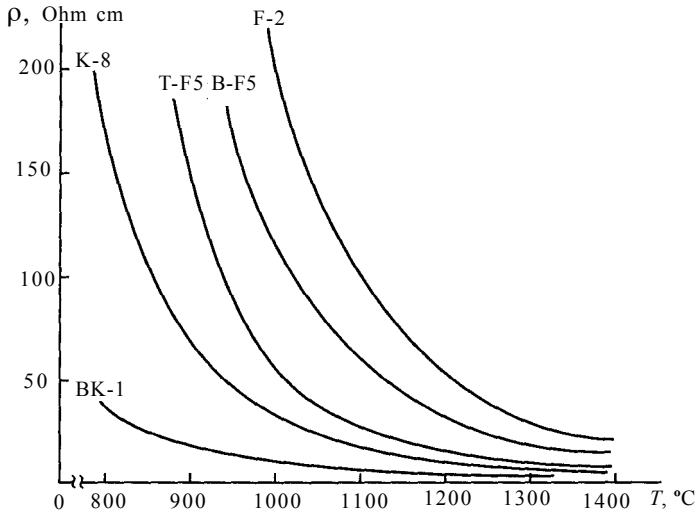
**Figure 1.7.** Temperature dependences of specific electrical resistivity of optical glasses [26].
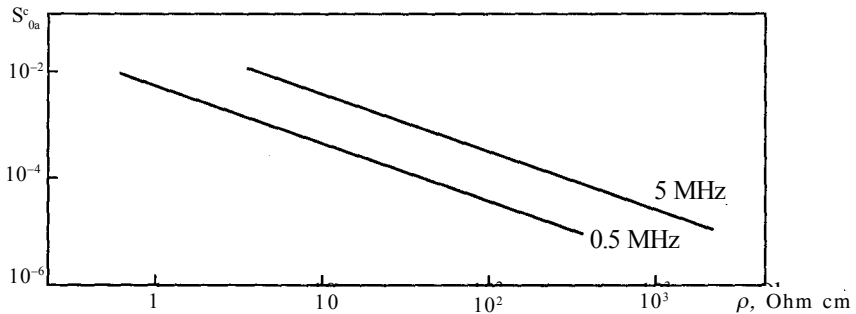


**Figure 1.8.** Power absorbed by the melt in relation to the electrical resistivity of the melt for frequencies of 0.5 and 5 MHz, crucible radius $r_o$ = 2.5 cm [27].

Therefore, in direct induction melting of glass it is necessary to carry out preliminary heating with an additional heat source at temperatures at which the melt becomes sufficiently electrically conducting for direct absorption of the energy of the high-frequency field.

The required size of the crucible will be evaluated on an example of glass of the BK-1 type, with the composition given in Chapter 6. Figure 1.7 shows that at a temperature of 1400°C, the specific electrical conductivity of the melt is ~3 ohm·cm [24]. At a field frequency of 5 MHz, $\Delta \cong 3.9 \, cm$; the minimum diameter of the crucible should be $d_{min} = 2\Delta = 7.8 \, cm$. The optimum diameter is
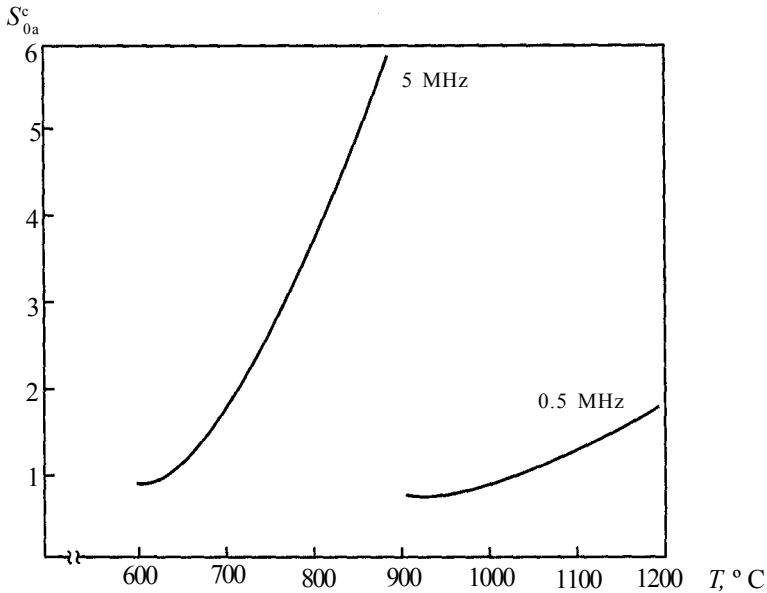
**Figure 1.9**. Power absorbed by the melt in relation to melt temperature. Chemical composition of the melt $20Na_2O \cdot 80SiO_2$, $r_0 = 2.5$ cm [27]

determined by the relationship $r_0\sqrt{2}/\Delta = 5 \div 7$ and $d_{opt} = (27.5 - 38.5)$ cm. Numerical calculations of the power, generated in the melt situated in a crucible with the radius $r(0) = 2.5$ cm at two frequencies $f_1 = 0.5$ MHz and $f_2 = 5$ MHz (Fig. 1.8) were carried out in [25]. The graph indicates that at the same electrical conductivity of the melt, the power, generated in the melt increases by an order of magnitude with the frequency increasing from 0.5 to 5 MHz.

Using the temperature dependence of the electrical conductivity of the melt, it is possible to determine the dependence of the power, generated. in the melt, on the melt temperature. For a glass with the composition $20Na_2O \cdot 80SiO_2$, this dependence is shown in Fig. 1.9 which shows that at a frequency of 0.5 MHz the glass must be treated to a temperature of 1000°C, and the preheat at a frequency of 5 MHz is 600°C.

Thus, an increase in frequency makes it possible to reduce greatly the temperature of starting heating of glass. However, it should be mentioned that at a frequency of 5 MHz, the power absorbed by the melt increases with increasing melt temperature more rapidly than at a frequency of 0.5 MHz and this complicates the regulation of the melt temperature.

## 1.3. THE MECHANISM OF MELTING OF DIELECTRICS BY THE HIGH-FREQUENCY FIELD

The heat generated during the passage of current through a material is calculated using the Joule–Lentz law. $Q$ is the heat generated in a conductor with resistance $R$ during time $t$ in the course of passage of current $I$ through the material and is given by the equation: $Q = aI_2Rt$, where $a$ is a coefficient which depends on the selection of measurement units. When measuring the current in amperes, resistance in ohms and time in seconds, the value of $Q$ is expressed in calories, $a = 0.239$, and in Joules $a = 1$.

Previous considerations show that the stages of starting melting and holding of the melt in the stationary condition, included in the process of melting of oxides, have been studied quite extensively from a theoretical viewpoint. However, in the cited investigations, almost no attention has been given to the mechanism of formation of the volume of the melt. Therefore, it is interesting to consider theoretical investigations of the induction melting of dielectrics carried out at the Institute of Chemical Physics of the Russian Academy of Sciences.

The process of melting in a cold crucible differs greatly from the process of melting in a heated crucible. In conventional melting in a 'hot' crucible, the melting process starts in layers of the charge adjacent to the wall of the crucible which is a heat source. The heat flow to the interface depends on the heat conductivity of the melt between the solid phase and the crucible wall. In induction heating, the heat generated in the conducting melt during the passage of electric current through the melt is transferred into the layers of the solid phase adjacent to the interface, heats them and causes them. to melt. In turn, the molten areas become new heat sources and melt subsequent layers. Thus, a melting wave propagates in the dielectric and the volume of the melt increases.

The authors of [26] assume that many processes, accompanied by heat generation, may take place in conditions identical with the combustion conditions. The combustion process is accompanied by the generation of heat during chemical transformations of matter, but the heat can generate not only as a result of the chemical reaction. The passage of electric current through the matter is also accompanied by the generation of heat (Joule heat). Another important property of the combustion wave is the strong nonlinear temperature dependence of the source of heat generation at the
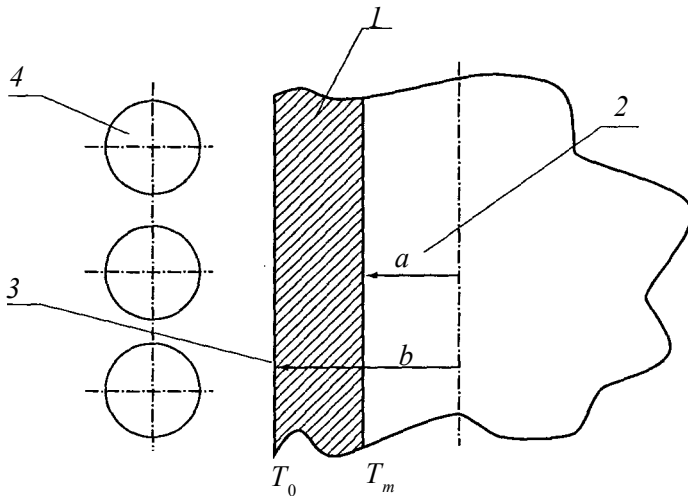
**Figure 1.10.** Schematic of an infinite two-phase cylinder in an infinite induction coil [18]. 1) solid phase, 2) melt, 3) crucible, 4) induction coil.

front of the wave. This is observed in induction melting of dielectrics as a result of the strong temperature dependence of electrical conductivity. Thus, the melting waves, propagating in the dielectric during heating of the melt due to Joule heat, are a sufficiently effective analogue of the combustion wave and can be described by mathematical facilities used widely in the theory of combustion and are regarded as an efficient means of examination of a wide range of thermal waves, similar to combustion waves [17, 20, 29].

Examination of the melting waves in induction heating was carried out on a model in which the region of the melt was in the form of an 'infinite' cylinder coaxial with the 'infinite' coil of the inductor, Fig. 1.10 [18]. The movement of the interface is accompanied only by a change of the radius of the region of the melt and its cylindrical shape remains unchanged. The propagation of the melting waves in the system requires a combined solution of a number of problems from the area of thermophysics and electrodynamics. However, the solution of the problem is simplified assuming that the conductivity of the solid phase is equal to zero and the conductivity of the melt remains constant and independent of temperature. In this condition, the mutually matched equations are separated and have independent solutions.

When solving an electrodynamic problem, an equation was obtained for the density of the thermal power at distance $r$ from the axis of the cylinder:

$$Q_r = Q_0 \left[ J_1 \left( \sqrt{2} ir / \delta \right) / J_1 \left( \sqrt{2} ia / \delta \right) \right]^2, \; r < a \qquad (1.18)$$

where $r$ is the cylindrical coordinate, $a$ is the radius of the melt; $\delta$ is the depth of penetration of the field into the melt; $J_1$ is the Bessell function; $Q_0$ is the specific power of heat generation on the surface of the melt, which depends on the conductivity and the radius of the melt and also on the dimensions of high-frequency equipment (frequency, voltage, the size of the induction coil, and other factors).

Equation (1.18) shows that the heat in the melt generates in a nonuniform manner. The main part of the heat is generated in the surface layer with thickness $\delta = c_0 / \sqrt{2 \pi \gamma \omega}$, where $C_0$ is the velocity of light; $\gamma$ is the conductivity of the melt; $\omega$ is circular frequency. In the limiting case of high frequencies, the source is a purely surface one, and at low frequencies the heat is generated in the volume of the melt. For a small thickness of the skin layer $(\delta / a \ll 1)$, the value of $Q(r)$ may be approximated by an exponential function $Q = Q_0 \exp \left[ 2(r-a)/\delta \right]$.

In a thermophysical problem of the propagation of a melting wave, the characteristic size is the width of the front of the wave $\xi / v$, where $\xi$ is thermal diffusivity, $v$ is the speed of the interface. In melting of oxides in cold crucibles, the radius of the volume, occupied by the melt, is large in comparison with the width of the melting wave, *i.e.* the inequality $\xi / v \ll a$ holds. Consequently, the curvature of the surface of the melt in the crucible may be ignored. In addition, this is accompanied by a disruption of the stationary nature of the process of melting: with increasing volume of the melt, the impedance of the melt increases and, correspondingly, the power of heat generation also increases and this in turn influences the time characteristics of the process. The last circumstance is indicated by the inequalities $\sim a/v \gg \xi / v^2$, where $\xi / v^2$ is the characteristic time during which the wave travels the distance equal to the width of the front of the melting wave. Consequently, at the given radius of the cylinder a, the instantaneous movement of the interphase boundary $da/dt$, is determined by power $Q$, generated in the melt. With the variation of the radius by the quantity $\sim \xi / v$, this power may be regarded as constant, *i.e.* the interface travels in the quasistationary regime. This assumption and also the ignorance of the curvature of the melt make it possible to calculate the mass speed of the melting wave:

$$u = (\lambda / c\delta)\left\{\left[1 + (Q_0 / \lambda)\delta^2 / (T_m - T_0 + L / c)\right]^{1/2} - 1\right\}, \qquad (1.19)$$

where $\lambda$ is the heat conductivity coefficient of the melt, $c$ is the specific heat capacity which is assumed to be identical for both phases; $L$ is the specific heat of melting; $T_0$ is the temperature of the medium, $T_m$ is the melting point. Mass speed $u$ is linked with the speed of movement of the interface $v$ by the relationship $u = \Omega v$, where $\Omega$ is the density of the dielectric. In a limiting case of a strong skin effect $(\delta \ll \xi / v)$:

$$u \approx (Q_0 \delta / 2c)\left[T_m - T_0 + (L / c)\right], \qquad (1.20)$$

The melting rate is independent of the heat conductivity of the melt. In this case, almost the entire generated heat is used for heating and melting the solid phase with a small superheating of the melt.

In the case of a weak skin effect $(\delta \ll \xi / v)$, equation (1.19) is transformed to the following form:

$$u \approx (1 / c)\left\{\sqrt{Q} \ \lambda / \left[T_m - T_0 + (L / c)\right]^{1/2} \right. . \qquad (1.21)$$

and for the speed of movement of the interface:

$$v \approx (1 / \Omega c)\left[(Q\lambda) / (T_m - T_0 + L / c)\right]^{1/2} . \qquad (1.22)$$

In the structure, equation (1.22) is identical with the equation of the speed of combustion with a wide heat generation zone [27]. Similar features of the examined processes result from the fact that in induction heating in a heat wave moving together with the interface, an 'electrical' heat source, similar to the exothermic reaction in the combustion wave operates and, consequently, the melting process is similar to the propagation of the combustion wave with a wide zone of the reaction. The speed of the wave is determined by the power of the source at the front edge of the zone of heat generation (in a layer with a width of $<\xi/v$) and is independent of the size of the zone $\delta$.

The authors of [15] estimated the speed of the thermal wave in melting of $Al_2O_3$: $v \sim 1$ mm/s, the width of the thermal wave $\xi/v \sim 10^{-1}$ cm, the depth of penetration of the field into the melt

δ ~ 1 cm. In [15] it was reported that the regime (1.21) is realised for the high-frequency range at a mean specific power.

Using numerical values of the melting rate and the power of heat generation, the authors of [15] carried out numerical calculations in the relative units of the duration of movement of the melting wave to the walls of the crucible and unavoidable energy losses were also determined.

However, when deriving equations (1.19)–(1.22) it was assumed that the heat is transferred from the melt as a result of heat conductivity in the direction of propagation of the melting wave. Later, in [28–30], the authors detected and investigated a strong effect of capillary spreading (saturation) on the propagation of a combustion wave of mixtures with melting components. The spreading of a component with a lower melting point (for example, titanium) in the voids of the non-melting component (for example, soot) in the heating zone resulted in the intensification of the chemical interaction of the reagents and in an increase of the combustion rate. On the basis of an analogy between the combustion wave and the melting wave, the authors of [15] reported that if the solid-phase is a porous medium (for example, a powder), a more efficient mechanism of propagation of the melting wave in the form of the capillary spreading of the melt through the voids of the solid phase may operate. The theoretical examination of the behaviour of the melting wave in a porous dielectric at a given power of heat generation in the melt heated by the high-frequency field has been carried out in detail in [31].

The capillary spreading of the melt is determined by the property of wetting of the natural solid phase by the liquid. In this case, the spreading of the melt through the voids corresponds to the transfer of heat sources.

The presence of non-conducting particles does not prevent the heating of the melt by induction currents because in any plane there is an infinite number of the methods of producing a closed contour between any two points of the liquid. It was also shown in [31] that the two-phase front is characterised by the solidification of the liquid phase and not by the melting of the solid substance. The leading edge of the spreading melt enters continuously into contact with new portions of the solid phase at a constant temperature $T_0$. The density of the heat flow into such a solid phase particle may be very high, and at the moment of contact the density may tend to infinity. Therefore, at any temperature of the melt at the leading

edge of the melting wave, the arrival of heat to the surface of the solid particles is not capable of compensating the losses for the heating of these particles and solidification of the melt takes place. With heating, the intensity of interfacial heat exchange. decreases and at a certain distance from the front edge, the generation of heat fully compensates the heat absorbed by the solid phase. The direction of the phase transition changes. Thus, the melting front propagates.

Since the energy of the high-frequency field is absorbed only by the melt, partial crystallisation results in weakening of the heat source. The stable propagation of the heat wave by means of the capillary spreading process is possible only at the generated power exceeding the threshold value, determined by the equation [33]:

$$Q_t = 4\lambda(1-\varepsilon)(T_m - T_0)^2 / d^2\varepsilon^2[T_m - T_0 + L/c], \qquad (1.23)$$

where $\lambda$ is the coefficient of heat conductivity of the melt; $\varepsilon$ is the initial porosity (prior to melting) of the solid substance; $d$ is the diameter of the voids or particles of the charge. Thus, if the density of power $Q$, generated in the melt, is higher than $Q_t$, the melting regime is stationary. If $Q < Q_t$, the spreading regime of the melt is disrupted as a result of the disruption of the interfacial heat balance, associated with a decrease of porosity resulting in weakening of the heat source below the threshold value $m >$ $(m/2)$ [31]. Consequently, the melt in the remaining voids solidifies and a layer of a continuous solid substance forms between the charge and the melt. This layer melts slowly as a result of heat conductivity. After melting of the layer, the melt enters into contact with the charge, spreads and solidifies, forming a new solidified area which then melts as a result of the heat conductivity of the melt. In this case, the mean rate of melting is determined by the slow conductivity stage and may be calculated from equation (1.19) [15]. The melting regime, characterised by the alternation of the stages of conductive melting and rapid spreading, is referred to as quasiperiodic. Equation (1.22) may be written in the following form:

$$v \simeq \sqrt{\xi} / \tau, \qquad (1.24)$$

where $\xi = \lambda\Omega c$ is the thermal diffusivity coefficient; $\tau = (T_m - T_0 + L/c)(\Omega c/Q)$ is the characteristic time required for melting of the

substance and the given power of the heater. The same authors [31] obtained an equation for the melting rate in the stationary regime which differs from the quasiperiodic equation (1.24) by the substitution of the coefficient of thermal diffusivity by the effective transfer coefficient:

$$K_{eff} = \alpha \cdot d / \eta, \qquad\qquad (1.25)$$

where $\alpha$ is the surface tension coefficient; $d$ is the diameter of voids or particles of the charge; $\eta$ is the viscosity of the melt. The dimension of $K_{eff}$ is that of thermal diffusivity.

As an example, attention will be given to the values of the coefficients of thermal diffusivity $\xi$, the effective transfer coefficient (1.25) and the threshold density of power $Q_t$ for aluminium oxide $Al_2O_3$ with the diameter of the voids of $d = 1\mu m$, porosity $\varepsilon = 0.5$ μm of the initial powder. The aluminium oxide was selected because the required information for this oxide is available in the liteature. The liquid aluminium oxide has the following properties [11,32]: $T_m = 2054°C$, $c = 138.16$ J/mol deg; $L = 113.04$ kJ/mol; $\lambda = 2.05\left(1 - 5.3 \cdot 10^{-4} \Delta T\right)$, W/m·deg, where $\Delta T$ is the super-heating of the melt above $T_m$; $\Omega = 3.03 \cdot 10^3 - 1.08 \Delta T$, kg/m³; $\alpha = 0.66 - 0.195 \cdot 10^{-3} \Delta T$, J/m²; $\eta = 0.06$ Pa·s at $T = T_m$; $\eta = 0.024$ Pa·s at 300°C. The values obtained in the calculations at $T_m$ are as follows: $\xi = 5 \cdot 10^{-7}$ m²/s, $\alpha \cdot d / \eta = 1.1 \cdot 10^{-5}$ m²/s, and the values resulting from calculations at $\Delta T = 300°C$, $\xi = 4.7 \cdot 10^{-7}$ m²/s, $\alpha \cdot d / \eta = 2.5 \cdot 10^{-5}$ m²/s.

The calculations show that the value of the effective transfer coefficient is tens of times higher than heat conductivity and this difference increases with increasing melt temperature. Thus, the melting of the solid particles by the melt spreading through the pores is considerably more efficient than heating of the solid phase as a result of heat conductivity.

The evaluation of the density of the threshold power gives: $Q_t = 2.4 \cdot 10^{13}$ kW/m³ $= 7.9 \cdot 10^9$ kW/kg. It should be mentioned that these equations are of the approximate nature and make it possible to calculate only the order of magnitude. An important circumstance is the formation of threshold values of power for the given melting conditions. However, the previously presented estimate of the value of $Q_t$ for the aluminium oxide cast doubts on the possibility of establishing the stationary conditions in melting of the porous absence in actual conditions.

Thus, the large number of various assumptions made in the

mathematical modelling of the melting waves and the limited literature data on the electrical and thermal properties of the melts of hightemperature oxide and also other refractory materials indicate that the theoretical investigations make it possible to obtain only the qualitative pattern of the process of melting of oxides. Nevertheless, these estimates are very important, in particular in the absence of experimental investigations, for the understanding of the processes taking place during induction melting of dielectrics. This understanding will support a successful solution of a number of problems of induction melting and growth of single crystals in a cold crucible [23] (see also Chapters 4 and 5).

## References

1.  Slukhotskii A.E., Ryskin S.E., Induction coils for induction heating of engineering components, Moscow and Leningrad, Energiya, 1974.
2.  Vainberg A.M., Induction melting furnaces, Moscow and Leningrad, Energiya, 1967.
3.  Gude Zh., Industrial electronics, Moscow and Leningrad, Energiya, 1960.
4.  Babat G.I., Induction heating of metals, Moscow and Leningrad, Energiya, 1965.
5.  Zagaevskii T., et al., Industrial electronics, Moscow, Energiya, 1976.
6.  Razorenov G.A. Izv. LETI im. B.I. Ul'yanova (Lenin),1940, 37-50.
7.  Petrov Yu.B., et al., *Elektrotekhnika*, 1982, No. 8, 16-19.
8.  Petrov Yu.B., Kanaev I.A., Induction furnaces for melting of oxides, Leningrad, Politekhnika, 1991.
9.  Petrov Yu.B., Induction melting of oxides, Leningrad, Energoatomizdat, 1983.
10. Krzhizhanovskii R.E., Shtern Z.Yu., Thermophysical properties of nonmetallic materials, Leningrad, Energiya, 1973.
11. Samsonov G.V. (editor), Physico-chemical properties of oxides, Metallurgiya, Moscow, 1978.
12. Bol'shakova N.V., Borisanova K.S., Burtsev V.I., Materials for electrothermal equipment, a handbook, Moscow, Energoatomizdat, 1987.
13. Borik M.A., Lomonova E.E., Osiko V.V., Prokhorov A.M., in: Problems of crystallography, Moscow, Nauka, 1987, 165–189.
14. Merzhanov A.G., et al., *Dokl. Akad. Nauk SSSR*, **221**, No. 5, 1114–1117.
15. Merzhanov A.G., et al., *Dokl. Akad. Nauk SSSR*, 1980 253, No. 2, 330–334.
16. Nezhentsev V.V., et al., *Izv. LETI*, 1981, No. 299, 14–20.
17. Aleksandrov V.I., et al., *PTE*, 1970, No. 5, 222–225.
18. Aleksandrov V.I., et al., *Vestn. AN SSSR*, 1973, No. 12, 29-39.
19. Aleksandrov V.I., et al., Current Topics in Material Sciences, Amsterdam, 1978, 421–480.
20. Aleksandrov V.I., et al., *Usp. Khimii*, 1978, **47**, No. 3, 385– 427.
21. Slukhotskii E.A. (editor), Using high-frequency currents in electrothermal applications, Leningrad, Mashinostroenie, 1973.
22. Hartzell R.A., Sekerka R.F., *J. Crystal Growth*, 1982, **57**, No. 1, 27–42.

23.  Sekerka R.F., Hartzell R.A., Farr B. J.,  *J. Crystal Growth*, 1980. Vol. 50. N 4. P. 783–800.
24.  Demkina L.I. (editor), Physico-chemical fundamentals of production of optical glass, Leningrad, Khimiya, 1976.
25.  Scott B., Rawson H., *Glass Technology*, 1973, **14**, No. 5. 115–124.
26.  Merzhanov A.G., Rumanov E.N., Combustion without fuel, Moscow, Znanie, 1978.
27.  Aldushin A.A., et al., *Fizika Goreniya i Vzryva*, 1972, **8**, No. 2, 202–212.
28.  Shkiro V.M., Brovinskaya I.P., *Fizika Goreniya i Vzryva,* 1976, **12**, No. 6, 945–948.
29.  Aldushin A.A., et al., *Fizika Goreniya i Vzryva,* 1976, **12**, No. 6, 819–827.
30.  Nekrasov E.A., et al., *Fizika Goreniya i Vzryva,* 1978, **14**, No. 5, 26–32.
31.  Rumanov E.N., Melting wave of porous matter, Preprint of the Institute of Chemical Physics, Russian Academy of Sciences, Chernogolovka, 1982.
32.  Murakh M.A., Mitin B.S., Liquid refractory oxides, Moscow, Metallurgiya, 1972.
33.  Shteiberg A.S., Raduchev V.A., *Dokl. Akad. Nauk SSSR*, 1991, **317**, No. 2. 370–373.

# Formation and treatment of the melt in the cold crucible

## 2.1. SPECIAL FEATURES OF HEATING MATTER IN THE COLD CRUCIBLE

Attention will now be given to several special features of the process of direct high-frequency heating of nonmetallic materials in a cold crucible, determined by the electrical properties of this type of material. Figure 2.1 shows the typical temperature dependences of the electrical resistance of a nonmetallic material (Fig. 2.1a) which is dielectric in the solid state, and of a metal (Fig. 2.1b).The figure indicates the principal difference between these two types of materials: in the first case, the electrical resistance of the melt is several orders of magnitude smaller than that of the solid phase, and in the second case, the melt is characterised by a resistance which is considerably higher than that of the solid metal. Figure 2.1c, d shows for the two cases schematically the nature of absorption of energy of the high frequency field by a two-layer cylinder, whose outer shell is represented by the solid phase, and the internal part is occupied by the melt of the same composition as that of the shell. This model accurately corresponds to the actual experimental conditions. Because in the case of metal the electrical resistance of the solid phase is lower than that of the melt, then in accordance with equations (1.1) and (1.2), presented in Chapter 1, the metal absorbs a larger part of the energy of the high-frequency field and screens the melt (Fig. 2.1d).

A different situation is observed in the case of a material with a 'drooping' temperature dependence of electrical resistance.In this
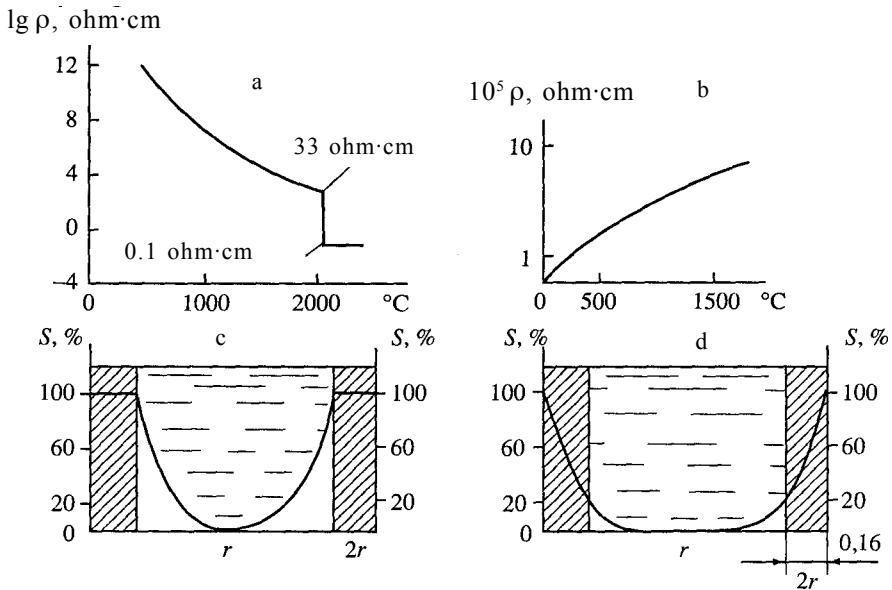
**Figure 2.1.** Temperature dependence of resistivity (a) and radial distribution of the energy of the high-frequency field (s) absorbed by a two-layer cylinder consisting of solid (outer cross-hatched layer) and liquid (inner part) phases with the same chemical composition [5]. a) aluminium oxide; b) steel; c) aluminium oxide cylinder; frequency of the electromagnetic field 5 MHz; d) a steel cylinder, frequency of the electromagnetic field 2500 Hz.

case, the solid shell is in principle 'pervious' to the electromagnetic field, does not prevent its penetration into the melt and is not heated by the field (Fig. 2.1c). Thus, direct induction heating in a cold crucible appears to be specially designed for materials characterised by the decreasing temperature dependence of electrical resistance and is not suitable for metals. In direct high frequency melting, the entire amount of the metal is melted and no solid shell forms between the melt and the walls of the cold crucible. This is the most significant advantage of this method in comparison with other methods: *i.e.* retention of the chemical purity of the initial material.The specific distribution of the power, generated in the melt, results in a situation in which the melt heated to a high temperature and the cooled crucible are always separated by a layer of the solid phase, not heated by the field, with the entire temperature gradient formed in this layer. It will be shown later that this factor results in a decrease of the energy losses in direct high frequency melting of nonmetallic materials in a cold crucible.

## 2.2 STARTING HEATING

The process of melting in a cold crucible consists of three stages. The first stage is the production of a 'seed' melt which, as already mentioned, may be produced only by using an additional heat source. The following methods are used for this purpose: 1. melting by supplying radiant energy, 2. using flames (gas or plasma torches), 3. electric arc, 4. melting by the introduction of a secondary electrically conducting material (heating body) into the material to be melted. The most suitable method for melting oxide and some other types of material is the method of starting melting based on the application of small amounts (usually several grams) of the metal included in the composition of the molten material. For example, it is aluminium in the case of aluminium oxide, yttrium in the case of yttrium oxide, and so on. Small pieces of metal, introduced into the charge, are heated by the energy of the high-frequency field and melt the surrounding charge. With melting, the metal is oxidised by atmospheric oxygen and the resultant oxide is included in the composition of the melt, without introducing secondary impurities into it. The physicochemical properties of the metals, used for starting heating, are presented in Table 2.1, [1].

Zirconium and yttrium are characterised by the highest heat of combustion. Zirconium can be easily ignited in air only in the re-fined condition (in the form of shavings or powder), compacted metallic zirconium is ignited in air only at a very high temperature [2].

After reaching the critical volume of the starting melt under the effect on the high-frequency field, the entire charge is gradually melted, with the exception of the layer which is in contact with the cooled walls of the crucible. The second, transition stage of the process is the addition into the crucible of new portions to the required volume of the melt. Complete melting of the charge is accompanied by the establishment of an equilibrium condition which may be maintained for a long period of time. This is the third stage of the melting process. When the generator is switched off, rapid mass crystallisation or formation of a glassy phase takes place, *i.e.* polycrystalline ingots or glasses are produced. In slow directional solidification of the melt by means of a gradual increase of the power of the generator or slow lowering of the crucible with the melt in relation to the induction coil it is possible to produce large single crystal blocks. Single crystals may also be produced by

**Table 2.1.** Physico-chemical properties of metals used for starting melting [5]

| Metal | Atomic mass, % | Melting point, °C | Heat of melting | $T_0$ – start of oxidation | Heat of formation of oxides, J/kg at 2000°C |
|-------|------|------|------|------|------|
| Y | 88.9 | 1585 | 113.2 | In air, burns at 470°C | 7430 |
| Zr | 91.22 | 2125 | 230.5 | Burns, refined at 500°C | 7880 |
| Gd | 157.3 | 1799 | 71.2 | Ignites at 400°C | 4400 |
| Yb | 173.04 | 1097 | 46.1 | As above | 4021 |

drawing of seed crystals. The processes of crystallisation and glass formation will be examined in greater detail in sections concerned with specific materials.

Thus, the process of high-frequency melting of refractory dielectrics' consists of heating the material from room temperature to the melting point and of holding of the material in the molten condition by supplying the energy of the high-frequency field.

Special attention will now be paid to the first stage of the process, the so-called process of starting melting (Fig. 2.2a). Initially, it is necessary to determine the amount of initial solid material which must be melted in order to ensure that the resultant melt is independently heated by the high-frequency field and its volume increases he condition of its 'viability' is determined by the inequality:

$$V \cdot P > K\left(T_m - T_0\right)\pi D^2,\tag{2.1}$$

where V is the volume of the starting melt; $P$ is the power, absorbed by the unit volume of the melt, $K$ is the coefficient of the transfer from the melt to the heat carrier (cooling water), $T_m$ is the temperature of the melt, $T_0$ is the temperature of the heat carrier, $D$ is the diameter of the droplet. In order to simplify the calculations, the heat of phase transition is not taken into account because, ideally, the melting process can be carried out at any suitable slow rate. When the droplet diameter $D$ is considerably smaller than the internal diameter of the crucible, it is assumed that specific
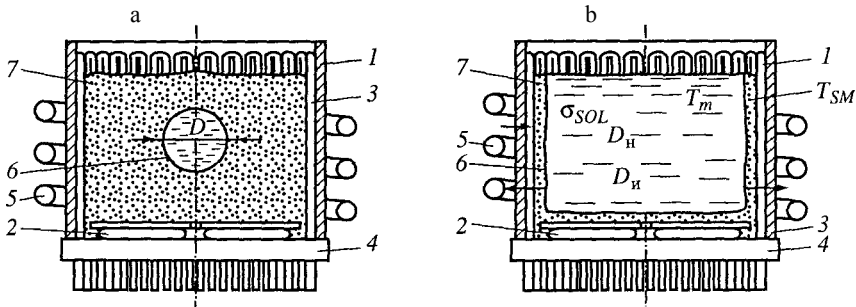
**Figure 2.2.** Scheme illustrating melting (a) and equilibrium state (b) of the melt–solid phase system (b) [6].

absorbed power $P$ is constant and equation (2.1) is simplified:

$$D > 6K / P\left(T_M - T_0\right). \tag{2.2}$$

The inequality shows that the critical size of the droplets of the startingmelt depends, at the given strength of the electromagnetic field and electrical conductivity of the melt which determine the value of P, on the heat-insulating properties of the solid phase.Thus, when condition (2.2) is fulfilled, a 'viable' droplet melt forms and, absorbing the energy of the high-frequency field, the droplet will grow as a result of melting of the surrounding solid-phase.

The authors of [3] propose to evaluate the amount of metal for the starting melt on the basis of different considerations. The starting zone of the melt is represented in the form of a disk with a diameter $d_{ST}$, height $h_{ST}$ and volume $V_{ST}$, positioned in the plane of the induction coil. According to [4], in heating in crucibles with an internal diameter of $d_K < 0.2$ m, the size of the zone should be: $d_{ST} = (0.7–1.0)\ d_K$, $h_{ST} = (0.5–0.1)\ d_K$, $V_{ST} = (0.4–0.08)d_K^3$. In crucibles with $d_K > 0.2 <$ volume $V_{ST}$ should be smaller than the recommended volume if the starting zone is produced in the form of a torus with the external diameter and the height corresponding to the previously presented relationships and with the radial width not smaller than the depth of the active layer $\xi$ (see Chapter 1). Induction heating is also possible in the case of smaller volumes of the starting melt, but this requires additional power of the generator which, however, can be used in the process of further melting and sustaining the melt in the stationary state [5].

According to [2], the amount of metal $G$, required for the reaction of oxidation with a calorific effect, sufficient for producing

**Table 2.2.** Specific ignition values of metals forming refractory oxides [1]

| Metal | $Z$, kg/m² | Metal | $Z$, kg/m² |
|-------|-----------|-------|-----------|
| Be | 420 | Nb | 1170 |
| Al | 480 | La | 1210 |
| Sc | 515 | Ce | 1460 |
| Ti | 550 | Sm | 1490 |
| Cr | 1220 | Hf | 2270 |
| Y | 985 | Th | 2570 |
| Zr | 1150 | U | 3375 |

the volume of the melt $V_{ST}$, can be determined from the equation

$$G = Z \cdot V_{ST}, \tag{2.3}$$

where $Z$ is the characteristic of starting heating, referred to as specific ignition, kg/m³. This characteristic represents the mass of combusted metal, required for heating and melting 1.0 M₃ of the oxide of this metal. Table 2.2 presents the values of the specific ignition for a number of metal forming refractory oxides. The oxides of Mg, Ca, Sr and Ba cannot be melted by combustion of their metals because the temperatures of ignition of their vapours are lower than the melting point of their oxides [6]. For starting heating of these oxides it is essential to use other methods of preheating.

## 2.3. MAINTAINING THE MELT IN THE STATIONARY STATE

To answer the question whether the process of melting will continue to complete melting of the entire solid phase or whether it will be interrupted in a certain stage, special attention will be given to the phase equilibrium condition, *i.e.* spatial stability of the interface between the melt and the solid phase (Fig. 2.2b). The phase equilibrium indicates that the temperature at any point of the phase boundary is equal to $T_{SM}$ and does not change with time. The amount of heat, transferred by the melt at the boundary of the solid phase under the condition of complete mixing of the melt, is determined by the expression: $Q_1 = \alpha_1 (T_M - T_{SM}) \cdot F \cdot \tau$, where $\alpha$ is the heat transfer coefficient, $T_{SM}$ is time, and the remaining

symbols are the same as previously. The amount of heat transferred to the heat carrier through the layer of the solid phase with thickness $\sigma_S$ and with heat conductivity $\gamma$ is: $Q_2 = \gamma/\sigma_S (T_{SM} - T_0)$ $\cdot F \cdot \tau$. For the ideal stationary regime $T_M = T_{SM}$, $Q_1 = Q_2$. Consequently, we obtain $\alpha_1 (T_M - T_{SM}) = (\gamma/\sigma_S) (T_{SM} - T_0)$, or:

$$(\lambda / \sigma_S)\alpha_1 = (T_M - T_{SM}) = (T_{SM} - T_0). \qquad (2.4)$$

Here $T_M - T_{SM} = \Delta T$ is the quantity, characterising the superheating of the melt. At $\Delta T \to 0$, $\sigma_S \to \infty$; This means that to sustain phase equilibrium, the melt should be superheated. It is assumed that $\gamma \alpha_1$ and $T_0$ independent of $\sigma_S$ and, consequently, we obtain:

$$\sigma_S \Delta T = \text{const}. \qquad (2.5)$$

Equations (2.4) and (2.5) show that when the temperature of the melt is increased or reduced, the system reacts by decreasing or increasing the thickness of the layer of the solid phase, respectively. On the other hand, complete melting of the solid phase requires infinitely large superheating. Any processes taking place in the solid shell, leading to a change of its heat conductivity (for example, sintering), disrupt the phase equilibrium and result in a change of either the temperature of the melt or the thickness of the solid layer (skull). The phase equilibrium condition is also affected by the intensity of mixing the melt which determines the value of the heat transfer coefficient. The requirement for superheating, determining the very existence of the melt in the investigated system, is the main feature by which the cold crucible differs from a heated crucible in which the substance can be heated to any temperature close to the melting point, and in some cases it is even possible to supercool the melt. Unavoidable superheating of the melt in the cold crucible result in important consequences in crystallisation of the melt, in particular, in single crystal growth (Chapter 4).

Attention will also be given to the reaction of the 'cold crucible–solid shell–melt' system to a reduction in absorbed power $\Delta P$ (caused, for example, by an uncontrolled reduction in the power of the high frequency generator). A decrease in the power results immediately in a decrease in melt temperature $T_M$ which disrupts the phase equilibrium: the thickness of the solid shell starts to increase, the ratio of the diameter of the load $(D_N)$ to the diameter
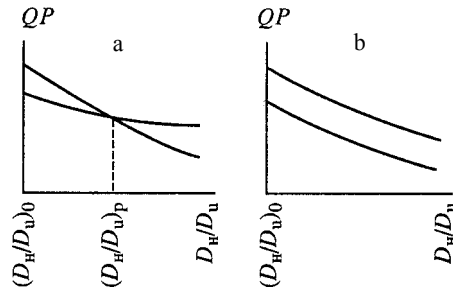
**Figure 2.3**. Reaction of the melt–solid phase system in a cold crucible to a decrease of the generator power [5]. a) stable system, b) unstable system. $D_H$ is the diameter of the crucible with the melt; $D_u$ is the diameter of the induction coil.

of the induction coil $(D_i)$ decreases. Two situations may occur in this case: 1.The establishment of a new equilibrium state with the value of $\sigma_S$ higher than previously; 2. uncontrollable cooling of the melt. The point is that an increase in $\sigma_S$ is also accompanied by a decrease in the diameter of the region of the melt representing the load of the induction coil of the high-frequency generator; the efficiency of con-nection with the induction coil decreases. On the other hand, with an increase in the thickness of the solid shell, thermal insulation increases and the heat flow from the melt to the cold crucible decreases. The rates of decrease in the power absorbed by the melt and in the heat losses differ. Figure 2.3a, b shows schematically two possible variants of the reaction of the system to a decrease in the generator power. The result of these competing processes is controlled by the heat conductivity of the solid phase: as the heat conductivity in-creases, the stability of the system decreases. The formation of the spatial instability of the phase boundary in high-frequency melting of refractory nonmetallic materials is a new factor not observed in the high-frequency heating of metals. The latter factor has a significant effect on the technical circumstances and technological regimes ofmelting and crystallisation of high-temperature materials.

After successful starting melting, the volume of the melt gradually increases as a result of melting of the adjacent solid phase represented by a charge or a mixture of a charge with crystal fragments from previous melts. This continues until the entire charge is melted, with the exception of the layer of the charge that is in contact with the walls of the crucible which together with the layer of the solidified melt forms the so called skull preventing direct contact of the melt with the crucible fittings cooled by water.

In addition to the skull, a layer of the melted charge in the form of a cupola forms above the melt. This layer greatly screens thermal radiation from the surface of the melt. To add new portions of the charge to the melt, a small hole is made in the cupola to ensure that the charge falls directly into the melt. After loading, the hole is covered with the charge. When the required volume of the melt is produced, the melt is held for some time at a constant level of the power supply to the melt to ensure that the entire system is transferred to the stationary condition.

## 2.4 DISTRIBUTION OF TEMPERATURE IN THE MELT VOLUME

The distribution of temperature in the cold crucible was examined on an example of glass-forming melts using a thermocouple. There are certain special features of the measurement of temperature in semi- transparent media. This problem has been examined in detail in [10] for the case of measurement of the temperature of glass mass in a glass-boiling furnace. If a thermocouple is immersed into the glass mass, the protective sheath of the thermocouple absorbs the radiation from the surrounding hotter sources. These sources may be represented by both the refractory lining of the furnace and by the regions of the glass mass with higher temperature. This absorption may result in errors in the measured temperature. To evaluate this error, investigations were carried out into the process of heat ex-change between a thermocouple and a glass mass, including radiant heat exchange and heat conductivity. The following assumption were made in the calculations: 1) the junction of the thermocouple has the form of an isothermal sphere with radius $r_0$; 2) convective heat transfer between the glass mass and the thermocouple is insignificant; 3) at a wavelength greater than 2.7 µm it is assumed that the glass mass is an absolutely black body and in the case of shorter wave-lengths it is a 'grey' body. Under these conditions, the following equation was obtained for the relative error in the determination of the melt temperature [8]:

$$\left(T_0 - T_f\right)/T_f = \left(r_0 \cdot \varepsilon n^2 \cdot \sigma \cdot T_f\right)/K_f \left\{1/2[(T_s/T_f)^4 + 1] - (T_0/T_f)^4\right\}, \qquad (2.6)$$

Here $T_0$ is the temperature of the thermocouple, $T_f$ is the actual temperature of the melt, $T_s$ is the temperature of the heating source, $K_f$ is the heat conductivity coefficient of the melt, $\varepsilon$ is the
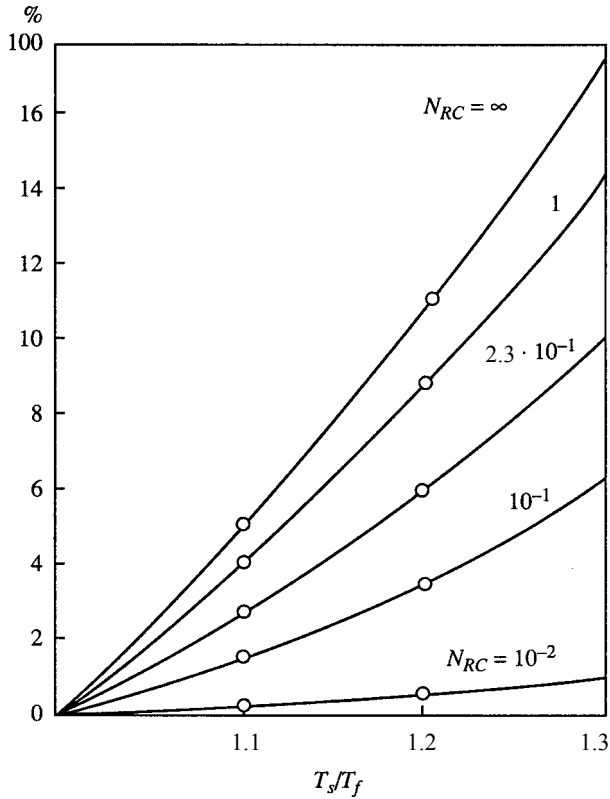
**Figure 2.4.** Relative errors in the measurement of melt temperature in relation to parameter $N_{RS}$ and the $T_s/T_f$ ratio of the temperature of the source to glass temperature [8].

emissivity of the material of the thermocouple in contact with the melt, $n$ is the refractive index of the melt (the glass mass in a specific case), sis the Stefan–Boltzmann constant: the multiplier in the right-hand part of the equation $N_{RC} = (r_0 \cdot \varepsilon \cdot n^2 \sigma \cdot T_f^3)/K_f$ is a dimensionless coefficient characterising the ratio of the heat transfer by radiation to the transfer by heat conductivity. The graphical solution of equation (2.6) is shown in Fig. 2.4 which shows that the error of measurement of temperature depends on two parameters: $N_{RC}$ and the $T_s/T_f$ ratio. In the case of low values of $N_{RC}$ the heat conductivity is controlling and the error of measurements decreases. The ratio $T_s/T_f$ is determined by the temperature gradients in the melt and the error of measurement also decreases with a decrease in temperature gradients. Here, the error of measurement is given for the following parameters of the melt [8,9]: $T_0 = 273\ K$ and $T_f = 1673\ K$, $T_s/T_f = 1.3$, $\varepsilon = 0.6$;
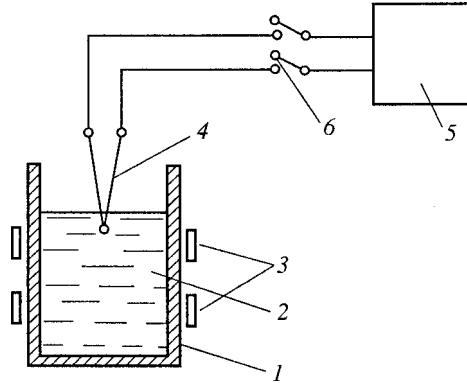
**Figure 2.5.** Measurement of melt temperature [16]. 1) water-cooled rucible; 2) melt; 3) induction coil; 4) thermocouple; 5) potentiometer; 6) thermocouple switch.

$n = 1.5$, $K_f = 1.7$ W/m K, and the error of measurement at $r = 1$ cm and $N_{RC} \approx 2.5 \cdot 10^{-2}$ is $\approx 2\%$.

   Thus, the application of a small thermocouple without protection greatly decreases the error of measurements. For this reason, the experiment described here were carried out using an unprotected thermocouple Pt/Rh-30–Pt/Rh-6 with $r = 0.025$ cm. It should be mentioned that the values of $T_S$ and $T_f$, selected for the evaluation of the error of measurement, correspond to the unfavourable measurement conditions.

   The main factors complicating the measurement of temperatures in the melt in the case of direct HF heating are: firstly, the presence of high-frequency interference resulting in induction heating of the thermocouple and, secondly, the fact that the melt is insulated from the body of the crucible by a dielectric layer (skull) and is under a voltage whose value may reach several kilovolts. The measurement of temperatures in the given conditions greatly complicates the measuring system as a result of the introduction of high-frequency filters and insulation of the recording device. Therefore, the melt temperature was measured immediately after switching the equipment off using the simplest circuits (Fig. 2.5). With the circuit open, the thermocouple was immersed in the melt with operating equipment.Simultaneously, when the high-frequency generator was switched off, the circuit of the thermocouple was closed and the potentiometer recorded the variation of the electromotive force of the thermocouple during the measurement period. The true temperature of the melt was determined by extrapolating the cooling curve of the thermocouple
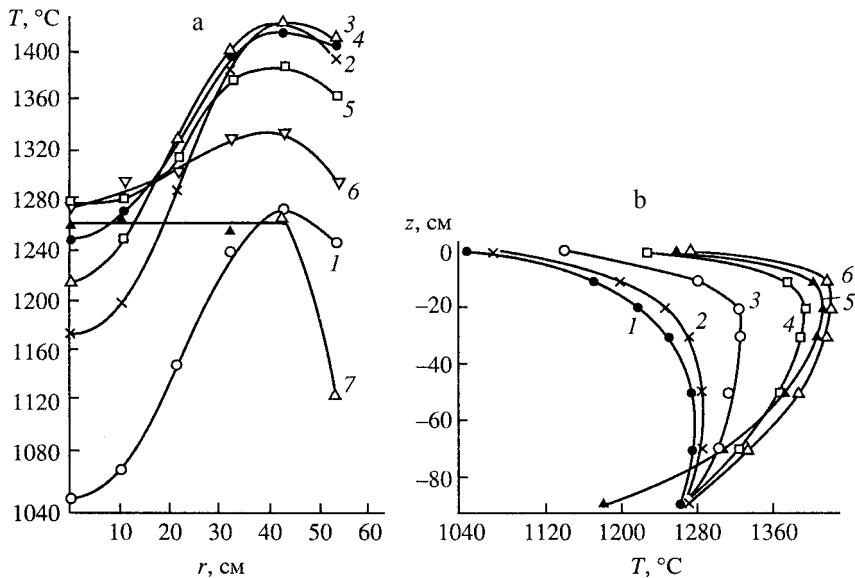
**Figure 2.6.** Variation of glass melt temperature along radius *t* [9]. a) at the depth of the melt of 0 (1), 10 (2), 20 (3), 30 (4), 50 (5), 70 (6), 90 (7) mm; b) at depth *z* and the distance from the axis of the crucible of 0 (1), 10 (2), 20 (3), 30 (4), 40 (5), 50 (6) mm (*r*, *z* along the axes, mm). The numbers are the numbers of the curves.

to the moment of switching off the equipment. In order to create reproducible conditions, after taking measurements at any single point and subsequent activation of equipment, the melt must be returned again to the initial condition. In order to maintain the melt in the stationary conditions, measurements were taken using a system for the stabilisation of the power of the high-frequency generator with respect to anodic current which transferred the melt to the initial condition. Multiple measurements of the temperature of the melt at any single point showed that the results are reproducible if the time between two measurements was at least 5 min. The accuracy of temperature measurements was determined by the error made in the recording thermal electromotive force on the diagram paper of the device and ±5°C. The temperature of the melt is also affected by the variation of the flow rate of water for cooling the crucible. However, special measurements of the melt temperature show that with the variation of the flow rate of water by a factor of 1.5, the temperature of the melt remains constant in the range ±5°C.

Figure 2.6 shows the results of the measurements of temperature along radius *r* and in the depth of the melt *z*. The radial distribution

of temperature to a depth of 70 mm is in qualitative agreement with the distribution of temperature on the surface of the aluminium oxide and with the theoretical calculation of the temperature distribution in a glass melt [10]. The radial distribution of temperature has a maximum whose position is constant up to a specific depth. The largest decrease of the melt temperature at $r > 40$ mm is determined by the effect of the water-cooled crucible walls and is characteristic of the melt in the cold crucible. It should be mentioned that the observed temperature maximum increases with increasing depth of the melt and at the depth greater than the critical value it completely disappears as a result of the rapid removal of heat through the bottom of the crucible and also due to a reduction of the intensity of heating in the lower part of the crucible.

A characteristic feature of the temperature distribution in the depth of the melt is the presence of temperature gradients in the surface layer of the melt at a depth of 10–15 mm, determined by the large heat losses from the open surface of the melt. The temperature distribution in the melt is shown in Fig. 2.7 a–d. Curves a–c correspond to different positions of the induction coil in relation to the surface of the melt at a constant volume of the melt and constant generated power. Analysis of the temperature distribution in the melt makes it possible to separated two regions of the melt: 1. The surface layer with a depth of 10–15 mm, 2. The remaining volume of the melt. With loading of the container, the axial gradient is greatly increased and the radial gradients of temperature in zone 1. The temperature distribution in region 2 becomes more uniform, but the range of the maximum temperature is displaced into the bulk of the melt and the size of this region decreases.

The observed changes may be explained using a model which takes into account the special features of direct high-frequency melting of materials in which the energy of the electromagnetic field is absorbed only by the layer of the melt whose thickness is determined by the working frequency of the generator and by the electrical conductivity of the melt. The remaining part of the melt is heated as a result of the heat transfer from this hot zone of the melt. As a model, induction heating may be regarded as heating from a heat source in the form of a hollow cylinder, immersed in the melt. The height of the cylinder is determined by the height of the induction coil, and the diameter of the cylinder by the thickness of the active zone of the melt. The lowering of the crucible is accompanied by the displacement of the heat source into the depth
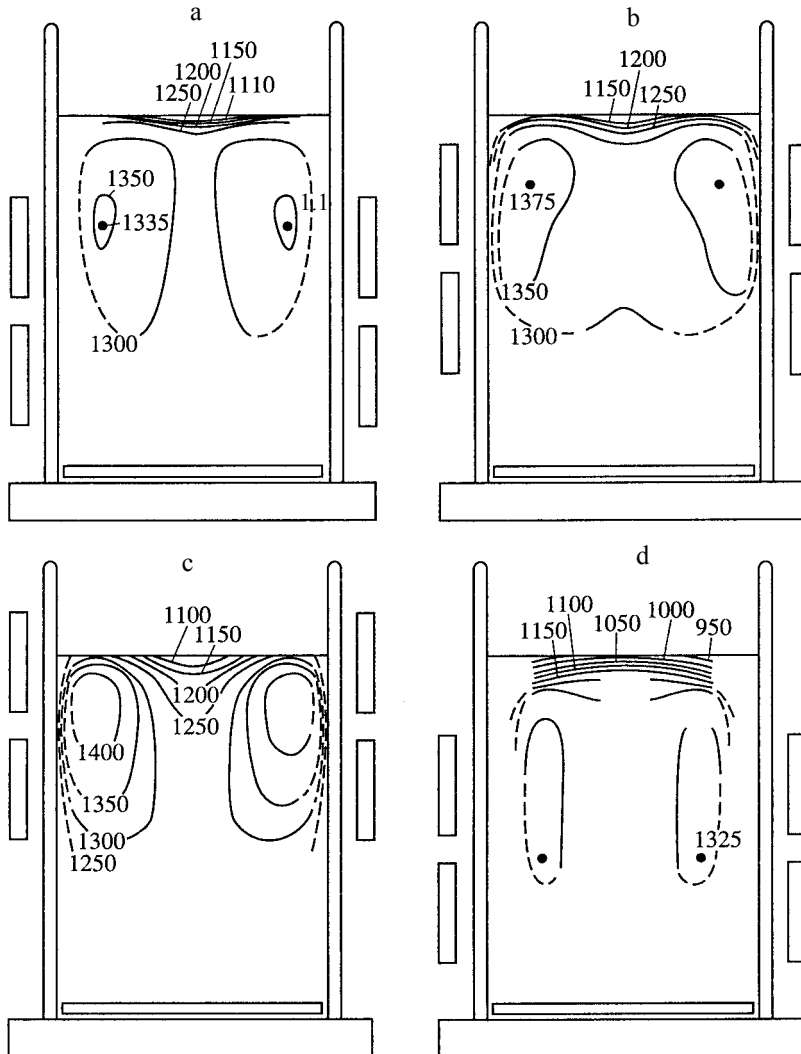
**Figure 2.7.** Distribution of temperature (°C) in a glass melt in relation to the position of the induction coil in relation to the melt surface and the power absorbed by the melt $Q_i$ [9]. a) $l = -35$ mm, $Q = 12.1$ kW; b) $l = -15$ mm, $Q = 12.1$ kW; c) $l = +20$ mm, $Q = 12.1$ kW; d) $l = 35$ mm, $Q = 9.9$ kW.

of the melt, the surface layers cool down, the viscosity of the melt increases and the intensity of convective heat transfer in the surface layers increases. The latter circumstance results in a rapid increase of the axial gradient in region 1. A decrease in the radial temperature gradient in this region is also caused by a decrease in the strength of the effect of the heat source with movement of the
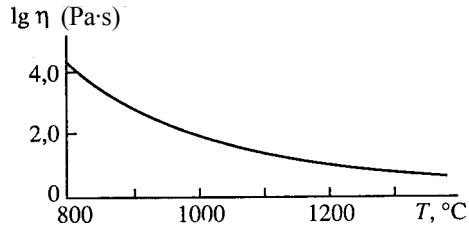
**Figure 2.8.** Temperature dependence of the viscosity of the melt of sodium-borosilicate glass [9].

source away from the surface. Figure 2.7 a,d also shows the temperature distribution in the melt with the variation of the power absorbed by the melt. A decrease in the power, absorbed by the melt, greatly changes the form of the temperature field in the melt: the melt temperature decreases, the region of maximum temperature is displaced into the depth of the melt, the axial gradient in region 1 becomes deeper, and the sign of the radial temperature gradient in the surface layer with a depth of 20 mm changes. To explain these phenomena, it is necessary to examine the temperature dependence of the viscosity of the melt, shown in Fig. 2.8. Since the heat source is relatively far away from the surface of the melt, a decrease in the intensity of the heat source increases the viscosity of the melt, especially in region 1. For example, when the melt temperature is reduced from 1300 to 1000°C, the viscosity of the melt increases by more than an order of magnitude. Therefore, the intensity of convective heat transfer from the depth of the melt decreases and the controlling factor in region 1 is now the removal of heat by the water-cooled walls of the crucible. This results in the inversion of the sign of the radial temperature gradient. In region 2, the temperature remains sufficiently high for the efficient mixing of the melt and equalisation of the temperature gradient.

Thus, the viscosity of the melt is an important factor determining the temperature distribution in the melt which must be taken into account in melting materials in a cold crucible.

## 2.5. EFFECT OF POROSITY OF THE INITIAL MATERIAL ON MELTING CONDITIONS

In the production of large, optically perfect crystals, a controlling role is played by the conditions in the stage of formation of the volume of the melt, for example, the shape of the solidification front, the structure and geometry of the heat-insulating layer (skull) at the

bottom and the wall of the cold crucible. In turn, the physical–
chemical characteristics of the skull depend on the initial
technological parameters of melting, with the porosity of the initial
charge being one of the most important parameters. On an example
of zirconia, the authors of [11] showed by means of experiments
that, in the actual conditions, there are two regimes of the melting
of dielectrics — stationary and quasiperiodic. For the same dielectric
with the same initial technological parameters, the type of the
melting conditions and the direction of propagation of the melt are
determined by the porosity of the initial charge. For this purpose,
the parameters of the generator determined in the melting process
were: the power, generated in the melt, heat losses in the cold
crucible, and also the mass and configuration of the melt.

The investigations were carried out in Kristal-401 Fianit
equipment, with an induction coil with a diameter of 250 mm and
a copper cold crucible, diameter 190 mm. Two types of charge,
differing in the shape and the grain size, which filled the specific
volume of the crucible, were used in the investigations. The porosity
of the charge was calculated from the equation:

$$\varepsilon = (V - V_0)/V,$$

Here $V$ is the total volume of the charge, $V_0$ is the volume occupied
by the particles of the charge whose porosity was $\varepsilon_1 = 0.78$ and
$\varepsilon_2 = 0.86$. Although melts were produced in the same, initial
conditions: the operating regime of the generator, the position of the
crucible and the starting metal in relation to the induction coil, the
size and mass of the tablets of the starting metal represented by
the pressed shavings of zirconia. During melting, the operating
parameters of the generator changed due to a change in the load
characteristics [7]. It was established that the increase of anodic
current to the maximum value corresponds to the increase of the
power, generated in the melt and, correspondingly, to an increase
of the mass of the melt. In the same experiments, the indicator of
the regime of the melting process was represented by the anodic
current of the generator lamp characterised by the high sensitivity
to changes of the load. Figure 2.9 a,b,c shows by points: the start
of increase of the constant component of anodic current $I_{ao}$,
determined by the formation of the melt (point 0), the start of rapid
linear increase (A, D), establishment of the maximum value (B and
E), and also the maximum frequency of the generator $f$ whose
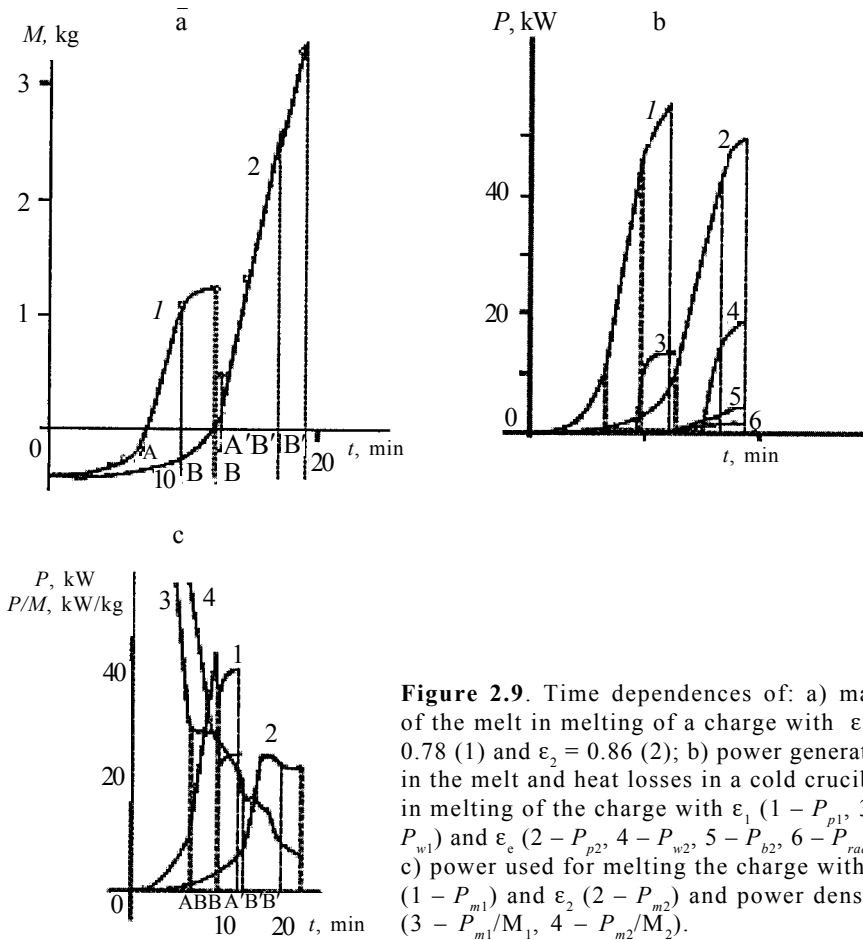
**Figure 2.9**. Time dependences of: a) mass of the melt in melting of a charge with $\varepsilon_1$ = 0.78 (1) and $\varepsilon_2$ = 0.86 (2); b) power generated in the melt and heat losses in a cold crucible in melting of the charge with $\varepsilon_1$ ($1 - P_{p1}$, $3 - P_{w1}$) and $\varepsilon_e$ ($2 - P_{p2}$, $4 - P_{w2}$, $5 - P_{b2}$, $6 - P_{rad2}$); c) power used for melting the charge with $\varepsilon_1$ ($1 - P_{m1}$) and $\varepsilon_2$ ($2 - P_{m2}$) and power density ($3 - P_{m1}/M_1$, $4 - P_{m2}/M_2$).

increase is also associated with an increase in the melt volume (C and F).

In order to determine the mass of the melt *M* melting was carried out to one of the characteristic moments of the procedure of loading and propagation of the melt in the crucible (Fig. 2.10 *a–g*); when these moments were reached, equipment was switched off, the solidified melt was separated from the charge and weighed. The amount of zirconia, formed from the starting metal, was deducted from the mass of the melt. Subsequently, the crucible was again filled with the investigated material and melting continued up to the next characteristic state, and so on. A similar procedure was used for producing a series of melt of the investigated material with different porosity. All working parameters of the generator and heat loses in the crucible were recorded during these experiments. The

heat losses in the crucible were determined by separate measurements, using differential thermocouples, of the temperature of the cooling water prior to and after passage through the wall ($P_w$) and the bottom ($P_b$) of the crucible at a constant flow rate. A radiation pyrometer was used for measurements of the losses of radiation power $P_{rad}$ through the open surface of the melt. The readings of the differential thermocouples and the pyrometer were continuously recorded in a potentiometer.

The following procedure was used for calculating the power generated in the melt. According to [12], for a lamp generator:

$$P(\sim) = P_o - P_a \tag{2.7}$$

where P($\sim$) is the power, generated in the oscillatory circuit of the generator, $P_a$ is the power used for heating the anode of the lamp, $P_o = (E_{ao} \cdot I_{ao})$ is the power supplied to the anode circuit of the lamp ($E_{ao}$ is anodic voltage, $I_{ao}$ is the constant component of anodic current). In turn, P($\sim$) is used for heating the melt, the oscillatory circuit of the induction coil, the grid of the lamp and the grid leak. Consequently, equation (2.7) may be used for deriving an equation for the power generated in the melt:

$$P_p = P_o - P_a - P_k - P_{ind} - P_c - P_g, \tag{2.8}$$

Here $P_k$, $P_{ind}$ and $P_c$ are the power of the thermal losses in the circuit, the induction coil, and the grid of the lamp; $P_g = I_{co}^2 R_g$, where $R_g$ is the power of the thermal losses in the grid leak, where $I_{co}$ is the constant component of grid current, $R_{gr}$ is the electrical resistance of the grid leak. The numerical value of $R_g$ is available, the values of $E_a$, $I_{ao}$, $I_{co}$ were continuously recorded in a potentiometer; $P_a$, $P_k$ and $P_{ind}$ were determined in the same manner as the power of the heat losses in the crucible, because the anode of the lamp, the circuit and the induction coil were cooled with water. In addition to this, the frequency meter was used for recording the frequency $f$ of the generator. The error of measurements of the absolute values of $P_w$, $P_b$ and $P_p$ did not exceed 5%, and that of $P_{ind}$ was not higher than 10%. In this case, the convective losses of the crucible may be ignored, and the losses as a result of the radiation of the layer of the charge above the melt (cupola) were calculated.

Figure 2.9a shows that the form of the curves 1 and 2 is identical, *i.e.* a small increase of the melting rate to the moments A and A', followed by a more rapid linear increase of the mass of the melt M; the curve 1 tends to saturation, and the curve 2 continues to increase at a lower rate; the mass of the melt M at the moments A′, B′, B′ is higher than in the corresponding moments A′, B′, B′. Consequently, Fig. 2.9b,c shows that power $P_{p1}$ (curve 1), generated in the first melt is higher than the power generated in the second melt $P_{p2}$ (curve 2); it may also be seen that the power $P_{w1}$ (curve 3) of heat removal from the crucible wall is smaller than the total sum of the powers of heat removal from the wall $P_{w2}$ (curve 4), the bottom of the crucible $P_{b2}$ (curve 5) and as a result of radiation $P_{rad2}$ (curve 3). Consequently, the power used directly for melting $P_m = P_p - P_w - P_b - P_{rad}$ is considerably higher in melting a charge with a lower porosity (Fig 2.9c).

In order to explain the experimental results, the authors used the theoretical model of induction melting of the dielectrics [13,14]. The rate of frontal melting depends on the heat flow to the inter-face. Because the heat is generated in the volume of the melt, the controlling parameter is power density $Q$, scattered in the melt. In [13] it was proposed that heating of the solid phase takes place as a result of heat conductivity. However, as shown in [14], the heating of the solid particles is far more efficient by the melt spreading through the pores which wets the solid phase. The stable propagation of the melting front by means of capillary spreading is possible only if the supplied power is higher than a specific threshold value. However, if the supplied power is lower than the threshold value, the regime of capillary spreading is unstable. The melt, penetrated into the pores, solidifies, forming a region of the continuous solid phase separating the porous charge from the melt. The rate of melting of this region is lower as a result of heat conductivity. When the melt enters again into contact with the charge rapid spreading takes place and a new solidifies region forms, and so on. Thus, a quasiperiodic melting process takes place. In the stationary regime above the threshold, the melt–charge boundary moves in a uniform manner. According to [14], the threshold power density is determined by the equation:

$$Q_1 = 4 \cdot \lambda (1 - \varepsilon)(T_m - T_o)^2 / r_n^2 \varepsilon^2 (T_m - T_o + L / C), \qquad (2.9)$$

Here λ, $T_m$, $T_0$ and ε is the heat conductivity, melting point, initial temperature and initial porosity (prior to melting) of the solid substance, respectively; $r_p$ is the diameter of the pores, $L$ is the heat of melting of the substance, $C$ is the heat capacity of the melt (for both types of charge, the values of $T_p$, $T_o$, $L$ and $C$ are identical). Because the charge is polydisperse, the determination of the radius of the pores $r$ is difficult, but the diameter of the pores may be related to porosity ε. Thus, in the present case, $Q_1$ is higher for the charge with $ε_1$ in comparison with that for the charge with $ε_2$. This is in agreement with the time dependences of the power density $P_m/M$ (Fig. 2.9c, curves 3, 4) used directly for the melting of the charge, and with the schema. of propagation of the melt shown in Fig. 2.10b–g, which correspond to the characteristic moments A–F.

As indicated by Fig. 2.7c and 2.8, the ratio $P_p(l)/M(l)$ in the time period O–B (charge with $ε_1$) initially rapidly decreases (to A) and subsequently decreases with a constantly decreasing rate, because the increase of $P_m(l)$ starts to catch up with the increase of M($l$). This takes place as a result of the high speed of propagation of the melt preferentially in the direction to the crucible wall resulting in a rapid change of the coefficient of filling of the window of the
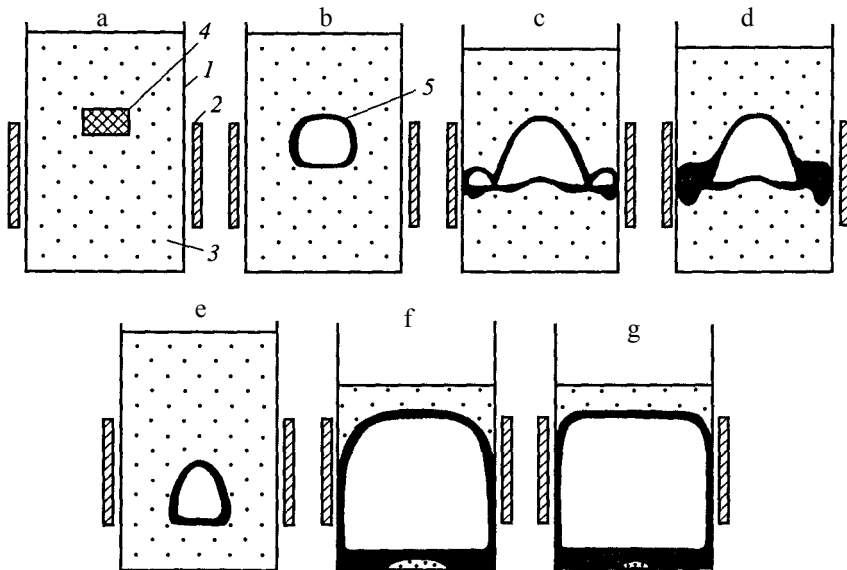


**Figure 2.10.** Schemes of initial loading of the cold crucible (a) and spreading of the melt in melting of the charge $ε_1$ (b–d) and $ε_2$ (e–g): (1 – crucible, 2 – induction coil, 3 – charge, 4 – starting metal, 5 – melt).

crucible by the melt $K_f$; a small increase of the coefficient results in a large increase of $P_p$ [3]. This explains the fact that $P_{p1} > P_{p2}$ and $P_{m1} > P_{m2}$ in all characteristic moments, with the exception of A and D, where the filling coefficients are close in values (Fig. 2.8 b,e) and consequently $P_{p1} \approx P_{p2}$ and $P_{m1} \approx P_{m2}$ (since $P_{w1}$, $P_{w2}$, $P_{b2}$, $P_{b2}$ are still absent).

At the moment of time B, the melt reaches the crucible wall and this results in a rapid increase of $P_w$ and a decrease of $P_{m1}/M_1$. Consequently, in the section B–C, an increase of the mass of the melt $M_1$ rapidly slows down. Evidently, at the moment of time B there is a transition from the stationary melting regime to quasiperiodic regime in which the heating of the solid phase takes place as a result of heat conductivity and the melting rate decreases. This indicates that the value of the threshold power density for the charge $\varepsilon_1$ is in the range 22–30 kW/kg. However, it must be remembered that this definition leads to a relatively a rough estimate, because the power density was calculated without taking the skin effect into account.

Additional experiments showed that the melting of the charge takes place mainly on the horizontal ring in the vicinity of the crucible wall. The layer of the solid phase, separating the melt from the charge, locally melts through, the melt again comes into contact with the charge and decreases to a new level. The melting process takes place up to reaching the bottom of the crucible and, subsequently, the central part of the charge melts in the quasiperiodic regime. Melting by this mechanism leads to an increase in the power generated by the generator during a long period of time in the vicinity of the crucible wall. This often results in damage of the skull layer and in irreversible changes in the conditions of the crystal growth process.

In melting of the charge with porosity $\varepsilon_2$, the superheating of the melt is less marked in comparison with the first case because the power density $P_{m2}/M_2$ (Fig. 2.9c, curve 4) and decreases uniformly. The melting process propagates mainly in the direction to the bottom of the crucible and the value of $K_f$ decreases. After passage through. point C, the melt drops below the edge of the induction coil and the extent of absorption of the energy of the high-frequency field in the volume of the melt de reases. However, the inequality $M_2 > M_1$ holds in all characteristic points. Melting in the stationary regime takes place up to complete melting of the main bulk of the load. Up to the moment of passage through point D, the vertical

direction of propagation of the melt is a consequence of a low threshold power and, consequently, the stable regime of capillary spreading is maintained in the vicinity of the centre of the crucible.

Thus, high-frequency heating in the cold crucible is characterized by two types of melting regime of the dielectrics – stationary and quasiperiodic. The realisation of a specific regime is determined by the ratio of the power density to the threshold density. The threshold power density depends strongly on the porosity of the initial charge and for a charge with $\varepsilon_1 = 0.78$ it is in the range 22–30 kW/kg.

## References

1.  Aleksandrov V.I., et al., *Usp. Khimii,* 1978, **47**, No. 3. 385-427.
2.  Borik M.A., et al., In: Problems of crystallography, Moscow, Nauka, 1987.
3.  Byndin V.M., et al., *Ogneupory*, 1983, No. 2, 41–45.
4.  Petrov Yu.B., Kanev I.A., Induction furnaces for melting of oxides, Leningrad, Politekhnika, 1991.
5.  Petrov Yu.B., Induction melting of oxides, Leningrad, Energoatomizdat, 1983.
6.  Khaneev N.P., Dissertation, General Physical Institute, Russian Academy of Sciences, Moscow, 1994.
7.  Cooper A.R., *J. Noncrystalline Solids*, 1977, **26**, No. 1–3, 27–37.
8.  Eryon N.D., Glicksman L.R., *J. Heat Transfer*, 1972, **94**, No. 2, 224–230.
9.  Aleksandrov V.I., et al., *Neorganicheskie Materialy*, 1983, **19**, No. 3, 443–447.
10. Aleksandrov V.I., et al., *Current Topics in Materials Science*, 1978, **1**, 421–480.
11. Aleksandrov V.I., et al., *Izv. AN SSSR, Neorgan. Mater*., 1991, **27**, 983–987.
12. Donskoi A.V., et al., High-frequency electrothermal equipment with valve generators, Leningrad, Energiya, 1974.
13. Merzhanov A.G., et al., *Dokl. Akad. Nauk SSSR*, 1980, **253**, No. 2. 330–334.
14. Rumanov E.N., Melting wave of porous matter, Preprint of the Institute of Chemical Physics, RAS, Chernogolovka, 1982.

# Main sections of equipment for direct radiofrequency melting in the cold crucible

## 3.1. RADIOFREQUENCY GENERATORS. COLD CRUCIBLE

At present, a series of radiofrequency (RF) equipment for induction melting of dielectric materials in the cold crucible of the Kristall-400 type has been developed and is manufactured by industry [1–4]. In these systems, equipment Kristall-401-Fianite, Kristall-403 and Kristall-405 differ in the power of the generator and the volume of the crucible and are designed for the melting of oxides and growing single crystals by directional solidification. All these systems have been constructed on the basis of the block principle using unified sections.

Equipment Kristall-401-Fianite is in fact the first industrial equipment for the growth of single crystals of oxides by directional solidification. The main technical characteristics of equipment, specially developed for the cold crucible method, are presented in Table 3.1, [5]. Equipment is powered from a three-phase AC mains with a voltage of 380 V, frequency 50 Hz. Equipment consists of the following units: a rectifier, a generator, a furnace, and a control unit. The rectifier unit, supplying power to the anode circuit of the generator, contains a thyristor regulator, a power transformer and a rectifier. The generator unit contains the anode (primary) circuit. The furnace includes a condenser bank of the loading (secondary) circuit with an electric drive for auto-setting of frequency, an induction coil and a crucible, placed inside a water-cooled chamber,

**Table 3.1.** Simple and complex compounds melted and synthesized in a cold crucible

| Compound (product) | $T_m$, °C, $T_{synth}$ | Comment | Compound (product) | $T_m$, °C, $T_{synth}$ | Comment |
|---|---|---|---|---|---|
| LiF | 842 | | $Tb_4O_7$ | 2330 | |
| NaF | 995 | | $Dy_2O_3$ | 2485 | |
| $CaF_2$ | 1403 | | $Ho_2O_3$ | 2395 | |
| NaCl | 800 | | $Er_2O_3$ | 2400 | a) |
| KCL | 770 | | $Tm_2O_3$ | 2390 | |
| MgO | 2880 | | $Yb_2O_3$ | 2420 | |
| CaO | 2585 | | $Lu_2O_3$ | 2470 | |
| SrO | 2430 | | $TiO_2$ | 1855 | a) |
| BaO | 1923 | | $ZrO_2$ | 2690 | |
| $Al_2O_3$ | 2046 | a) | $HfO_2$ | 2790 | |
| $Sc_2O_3$ | 2405 | a) | $V_2O_5$ | 670 | |
| $Y_2O_3$ | 2410 | a) | $Nb_2O_5$ | 1510 | |
| $La_2O_3$ | 2230 | | $Ta_2O_5$ | 1877 | |
| $CeO_2$ | - | | $Bi_2O_3$ | 817 | |
| $Pr_6O_{11}$ | 2040 | | $Cr_2O_3$ | 2300 | |
| $ND_2O_3$ | 2315 | | MnOx | 1700 | |
| $Sm_2O_3$ | 2320 | | $Na_2CO_3$ | 851 | |
| $Gd_2O_3$ | 2395 | a) | | | |

a) Single crystals were produced; b) Doped with 5% CaO, $Cr_2O_3$; c) Synthesis atmosphere: air and nitrogen, specific conductivity ($\Omega$ cm) 40 and $10^4$ respectively; d) As above; e) Optically transparent glass was produced

and a mechanism for moving the crucible. The generator and furnace units are screened in order to reduce emitted radio interference. The panel of the control block is used for controlling the entire equipment and also includes systems for stabilisation and automatic reduction of anodic voltage.

Since the parameters characterising the condition of the melt vary in a wide range, from the complete absence of the load (in starting heating) to the maximum load, the electrical parameters of the induction system also vary in a wide range. Therefore, the generator must have a wide range of regulation of the oscillatory

power and output voltage, with auto-setting of frequency and a wide range of variation of the feedback coefficient.

Kristall-401 equipment contains a two-circuit of the generator based on a GU-23A generator lamp with auto-transformer connection of the loading circuit to the anodic circuit and a capacitance feedback. Figure 3.1 shows the electrical diagram of the generator which is typical of all industrial systems designed for the induction melting of oxides in the cold crucible.

The anodic circuit consists of capacitance $C_1$ and circuits with inductance coefficients $L_1$, $L_2$, $L_3$. The voltage in the loading circuit is lower than in the anode of the generator lamp and is determined by the ratio of the inductance coefficients $L_2/(L_1 + L_2)$ which are variable parts of the inductance of the anodic circuit. The values of $L_1$ and $L_2$ depend on the spatial position of the controlling short-circuiting coil $L_3$. Varying the position of the coil, it is possible to change the value of the voltage transformation coefficient in the range 1.1–2.0. The excitation voltage in the grid of the generator lamp is generated using a feedback with a capacitance divider $C_3$, $C_4$. The bias voltage on the grid of the lamp is generated using a grid leak $R_g$, connected to the circuit through which the constant component of the grid current passes. The voltage in the grid is regulated by changing inductance $L_3$ by means of the short-circuited coil $L_4$ as a result of a change in the feedback coefficient. To set the working frequency of the generator, inductor $L_5$ and variable
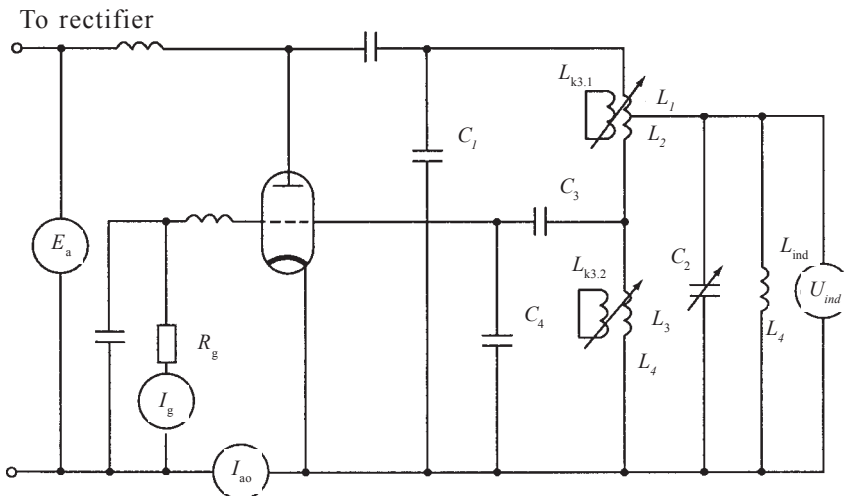


**Figure 3.1**. Functional electrical diagram of the RF generator of Kristall-401-Fianite equiment.

capacitance $C_2$ are included in the loading circuit.

The control panel contains regulators of anodic voltage, frequency setting, power (as a result of changes in the inter-circuit connection coefficient), the feedback coefficient and the speed of movement of the crucible. The operating regime of the generator is controlled by ammeters and voltmeters connected to the circuit (Fig. 3.1). The following parameters are controlled in the control panel: anodic voltage $E_a$, voltage in the inductor $U_{ind}$, the constant component of anodic current $I_{ao}$, the constant component of the grid current $I_g$. The circuit also includes a digital frequency meter for controlling the frequency of the generator.

The growth chamber is designed for protecting personnel against the effect of the high-frequency electromagnetic field and thermal radiation. The chamber is cylindrical with double walls made of stainless steel and is cooled with water. Easy access to the chamber is ensured by a door with a latch and a screw clamp, which is also cooled with water. The upper part of the chamber contains a hole for supplying the initial material, and also two holes for moving rods to which the crucible is secured. The mechanism for lowering the crucible is on the top part of the chamber.

The crucibles used for melting high-temperature materials consist of individual sections electrically insulated from each other and positioned parallel to the magnetic flux of the induction coil (Fig. 3.2). This design of the crucible ensures the highest permittivity for the RF field. The crucible and the inductor (consisting of one or many turns), cooled with water, are usually produced from a copper pipe with a diameter of 12–14 mm because of the high heat and electrical conductivity and also chemical resistance of copper.

Equipment Kristall-401 uses a single-turn inductor with a height of 100 mm, diameter 250 mm, and a copper crucible with a height of 350 mm and an internal diameter of 190 mm. A collector placed in the upper part of the chamber and connected with rubber hoses with the sections of the wall is used for supplying water into the sections forming the cylindrical wall of the crucible. The bottom of the crucible is cooled with water separately and may be separated from the side wall for easy unloading. The crucible is additionally fitted with a mechanism for unloading. If in the early types of equipment it was necessary to separate the crucible together with the solidifying ingot from the rod and subsequently move the ingot from the crucible, to extract the ingot in Kristall-401 equipment, the crucible is lifted upwards and the bottom together with the ingot
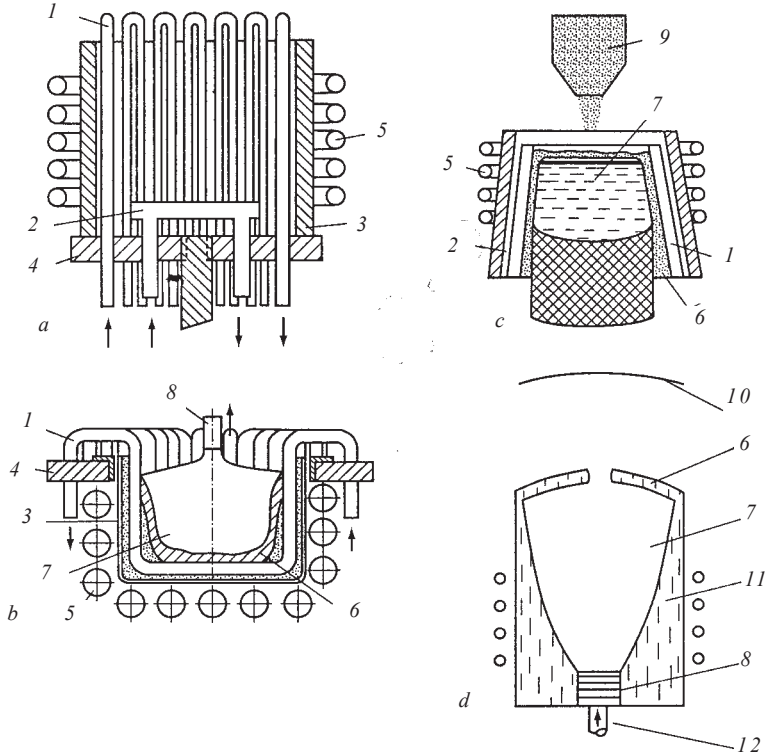
**Figure 3.2**. Design of cold crucibles for different applications. a) multielement cold crucible for periodic melting and solidification of inorganic materials; b) modification of cold crucibles for materials with heat conductivity in the solid state higher than 6 W/m·deg; c) cold crucible for continuous melting and solidification; d) cold crucible with an optical reflector: 1) tubular water–cooled element; 2) water-cooled bottom; 3) insulating quartz cylinder; 4) insulating gasket; 5) induction coil of the RF generator; 6) skull; 7) melt; 8) seed crystal; 9) hopper with a charge; 10) optical reflector; 11) unmelted charge; 12) cooling water [5,7].

remain stationary. Equipment contains a system for automatic loading the charge from a hopper. The external appearance of equipment is in Fig. 3.3.

Improved furnaces of the Fianite-1 type are used for the production of crystals by directional solidification of the melt (in particular, fianites), and also fused ceramic materials and glasses. The chamber is produced in the form of a right-angled box with opening doors ensuring free access to the crucible which is secured to a rod through a threaded joint. Water is supplied to the sections of the crucible and removed through the bar. This improvement makes it easier to replace the crucibles and load the molten
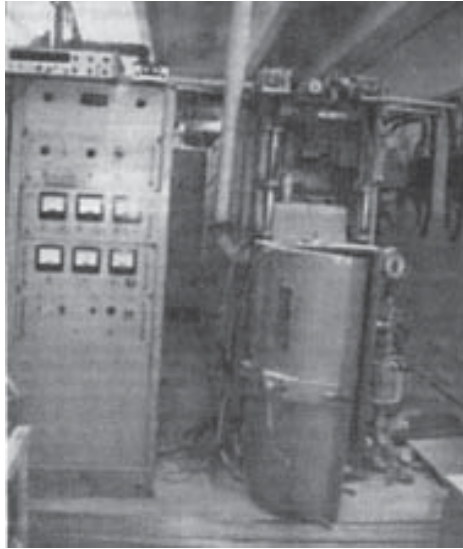
**Figure 3.3.** Industrial Kristall-401-Fianite equipment for growing crystals by the cold crucible method.

material and also makes it possible to reduce greatly the length of rubber hoses for connection with the collector for cooling water. This decreases the probability of fire when the melt leaks from the crucible and falls on the rubber hoses. In addition to this, the supply of water by means of the rod makes it possible to construct equipment with a rotating crucible.

The stabilisation of the pressure of cooling water with an error of ±0.05 atm is carried out using a system consisting of a electrical contact pressure gauge and a reversing drive, regulating the position of a valve on a water line.

Industrial variants of the equipment for RF melting of dielectrics include also equipment of the type Donets-4 and Kristall-402-Fianite. Donets-4 equipment is designed for growing crystals from a melt by both the method of directional solidification and by the Czochralski method. This equipment may also be used to produce fused materials and glasses. The power source in equipment is represented by a generator on non-controlled diodes. The rectified voltage is controlled using a thyristor regulator included in the primary winding of the transformer. A special programme is used for automatic setting of the given regime of variation of generator power. The upper part of the working chamber contains a withdrawal mechanism, the lower part the mechanism for lowering

**Table 3.2** Technical parameters of equipment for direct HF melting of dielectrics [5]

| Parameter | Parameters of equipment | | |
|---|---|---|---|
| | Kristall-401 | Kristall-403 | Kristal-405 |
| Rated power, kW | 100 | 200 | 280 |
| Oscillatory power, kW | 60 | 160 | 160 |
| Current frequency, MHz | 5.28 | 1.76 | 1.76 |
| Crucible diameter (inner), mm | 200 | 400 | 500 |
| Crucible height, mm | 300 | 700 | 1000 |
| Working temperature of the melt, K | 3000 | 2900 | 2900 |
| Productivity, kg/h: fianites, melted oxides | 0.15 | 3.0 | 3.0 |
| | | 25 | |
| Water consumption, m³/h | 6 | 10 | 8 |
| Working stroke speed, mm/min | 0.02–20.0 | 0.02–10.0 | 0.05–0.5 |
| Rated speed, mm/min | 100 | 200 | 200 |
| Weight of equipment, t | 3.1 | 5.5 | 8.4 |
| Area occupied by equipment, m² | 13 | 26 | 21 |

and lifting the crucible, the speed of displacement of both bars is regulated smoothly in the range 1–100 mm/h. The drives of the mechanisms for lifting and lowering the crucible are fitted on a special stand. The chamber can be sealed and crystals can be grown in any atmosphere and also in vacuum. This is achieved using a system for pumping and controlling the gas pressure in the chamber. There is also a system for stabilising the flow rate of cooling water with a pressure of up to 2 atm. The upper and lower rods are also cooled. The water for cooling the crucible is supplied to using rubber hoses connected to the collector. The technical parameters of equipment for direct RF melting are presented in Table 3.2.

The design of the crucible should be discussed quite extensively. The design of the cooled crucible has a number of specific requirements. Primarily, because the energy source is outside the crucible, the crucible must be 'pervious' to electromagnetic waves generated by the generator. This means that the crucible should be

made of a dielectric material or contain slits preventing the closure of the eddy currents. The crucibles are produced from materials with high heat and electrical conductivity. The crucibles shown in Fig. 3.2 are more suitable for melting and solidification of refractory nonmetallic materials. One of these crucibles, Fig. 3.2a, makes it possible to melt and solidify a large number of different materials. Some of these materials are summarised in Table 3.2. For solidification of materials whose conductivity in the solid state is higher than 6 W/m deg, it is recommended to use a different crucible (Fig. 3.2b) in which the electromagnetic energy is supplied not only from the side surface of the melt but also from the bottom of the crucible. The crucible shown in Fig. 3.2c is used for continuous melting and solidification of materials. The direct experimental determination of the efficiency of these systems shows that in the crucible with the melt up to 50–60% of electrical power supplied to the equipment is generated.

The technical–economic parameters of these systems are determined by both their technological schema and the nature of processed material. For equipment with periodic melting regime the productivity is up to 3 kg/h with a specific consumption of electric energy of 5–10 kW h/kg. In continuous melting, the productivity reaches 10–20 kg/h, and the specific consumption of electric energy is (1.5–7.0) kW h/kg.

The experience accumulated in the service of Kristall-403 equipment was utilised in its modernisation. A new variant of equipment is known as Kristall-405. The regulators of anodic voltage, frequency setting, power (the coefficient of inter-circuit connection), the feedback coefficient and the rate of lowering the crucible are installed on the control panel of equipment. The operating regime of the generator is controlled on the basis of readings of devices included in the circuit and displayed on the control panel. The following parameters are controlled: 1. Anodic voltage $E_a$, voltage in the inductor $U_{ind}$, the constant component of cathodic current $I_{ao}$, the constant component of grid current of the generator lamp $I_{ao}$. In addition to this, a digital frequency meter is used and the readings are utilised in the control of generator frequency $f$. The block diagram of Kristall-405 equipment is shown in Fig. 3.4. The distribution of the units is more compact and they occupy a smaller area.

The volume of the cold crucible is approximately three times larger, the speed of displacement is lower and the stability of
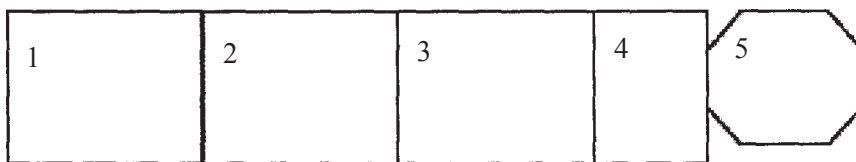
**Figure 3.4.** Flow chart of Kristall-405 equipment: 1) rectifier; 2) filter unit; 3)

displacement is improved. Equipment includes a system for automatic control of the lamp generator. The system makes it possible to carry out automatic operation of equipment in accordance with the given programme from the activation of the incandescent lamp to the unloading of the crystal block from the cold crucible. Table 3.1 gives the technical characteristics of the main types of industrial equipment.

## 3.2. METHODS AND DEVICES FOR CONTROLLING AND REGULATING THE TEMPERATURE OF THE MELT

As already mentioned, in the melting of dielectric materials the energy of the RF field is generated mainly in the melt and, consequently, the parameters of operation of the generator are determined by the composition and volume of the melt. Some of these parameters may be controlled using measuring devices included in the circuit of the generator (see section 2.1). Previously, it was reported in [6] that the constant component of the anodic current and grid current of the generator lamp are parameters sensitive to the change of the volume of the melt in the stage of formation of the melt. However, the authors of [2,4] reported that $I_{ao}$ may be used as an indicator of the condition of the melt only if the degree of superheating of the melt is not large and the depth of the melt may change. In the case of large superheating of the melt and a constant volume of the melt, the temperature of the melt is determined by the generated power. In this case, the condition is indicated by the voltage in the inductor $U_{ind}$. However, in the above studies, the authors did not describe the criteria for application of a specific parameter as the controlling parameter. For example, the degree of superheating at which $I_{ao}$ or $U_{ind}$ can be used as an indicator was not determined. The superheating of the melt may be evaluated (with a large error) on the basis of the electrical parameters of the generator. The authors of [16] controlled the process of growth of single crystals on the basis of
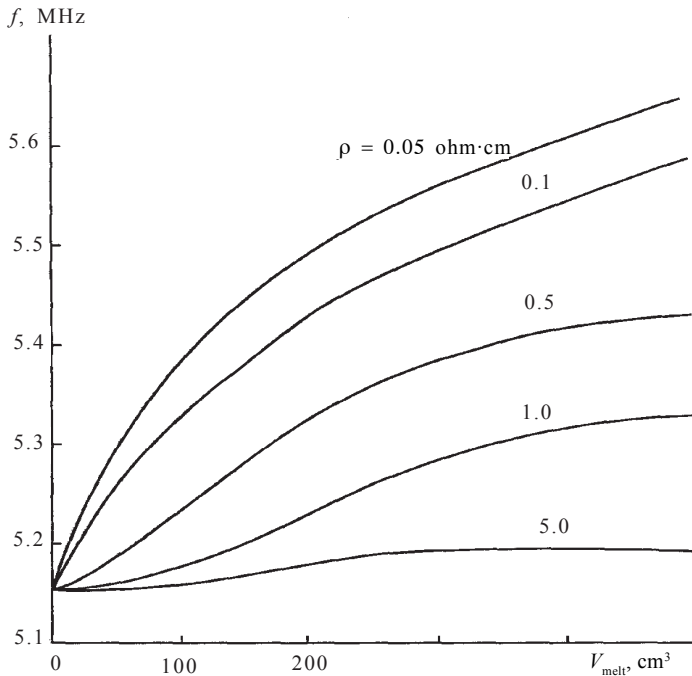
**Figure 3.5.** Dependence of the frequency of the HF generator on the volume and electrical resistance of the melt in a cold crucible [7]

the results of measurements of the power generated in the anodic circuit of the generator lamp ($E_a I_{ao}$). Because of the complicated nature and nonlinearity of the energy processes taking place in the generator and in the load, the power required by the generator lamp does not characterise unambiguously the stability of heating the melt in the cold crucible. In the melting and solidification stages, all electrical and thermal parameters of the generator–load the system are characterised by large changes.

In service of the initial prototypes of equipment for melting oxides it was noted that the frequency characteristic of the generator depends on the volume of the melt. In subsequent stages, this was confirmed in [7] in which the frequency dependences of the secondary circuit of the RF generator on the volume of the melt in the crucible for different specific electrical resistance of the melt were determined. Figure 3.5 shows the frequency characteristics of the RF generator in relation to the electrical resistance and the volume of the melt. The graph indicates that the increase of the frequency is proportional to the increase of the volume of the melt in the crucible. However, in the course of melting it is not possible

to determine the volume of the melt on the basis of the frequency of the generator $f$ because of the following reasons: 1. The temperature dependence of the specific electrical resistance of the melt remains unknown; 2. In the melting process, the operating regime of the generator is regulated by means of the transformation coefficient, feedback and the value of the variable capacitance in the secondary circuit. Each of these parameters affects the frequency of generation. Nevertheless, as reported in [2], the generator frequency is the most sensitive function of the variation of the volume of the melt. An increase of frequency $f$ indicates an increase of the volume of the melt and a decrease of frequency indicates that the solidification process prevails over the melting process. Thus, the generation frequency $f$ may be a sensitive indicator of the state of the melt and of the start of solidification.

In induction heating of the dielectrics in the cold crucible the energy of the electromagnetic field is generated in the melt. The state of the melt is determined greatly by the power absorbed in the melt $P_p$. The control and examination of the processes of melting and solidification can be carried out efficiently by measurement of the value of $P_p$. This can be carried out using an additional contactless method based on the measurement of the power factor of the inductor $\cos\varphi$, which has no restrictions with respect to temperature. This dimensionless coefficient changes in accordance with the variation of $P_p$ at a constant level of the total power supplied to the inductor. Therefore, the proposed method of control may be used only for the stationary or quasistationary condition of the melt [7]. In this case, in the determination of the appropriate value of $P_p$ using the available values of $\cos\varphi$, it is necessary to consider the parameters of the generator–load system which are often not available. In addition to this, the measurement of $\cos\varphi$ at frequencies higher than 1.0 MHz and at low absolute values of the measured quantity are associated with large difficulties. Industry does not produce standard devices for measuring $\cos\varphi$ and consequently, it was necessary to develop a laboratory prototype of a device which was described in [8] where the authors reported a large error in the measurement of this parameter. The dependence of $\cos\varphi$ on the parameters of the system is presented in Fig. 1.4, and the notations used in the figure are given in Chapter 1.

The power $P_p$ can be determined in a simple manner and with sufficient accuracy by means of experiments with the measu rement

of the power taken by the cooling water from the crucible and the power losses as a result of radiation from the open surface of the melt [6, 9]. However, these investigations can be carried out only for the stationary condition of the melt. Therefore, it is not justified to assume that the value of $P_p$ is the same as the losses of power removed by cooling water and radiation, as proposed in [10].

Thus, the previously mentioned electrical parameters of the generator (the control of these parameters is taken into account in the design of industrial equipment for the production of single crystals and fused materials by direct RF heating in the cold crucible) does not make it possible to characterise unambiguously the condition of the molten material and are only an indicator of the state. The other previously examined methods of controlling the state of the melt have a number of restrictions and shortcomings preventing experimental examination and control of not only the non-stationary (in melting and crystallisation) but also the stationary state of the melt. In addition to this, these methods do not make it possible to determine the dependence of the condition of the melt on the operating regime of the generator.

On the current level of technology, the regulation of the operating regime of the generator is carried out manually in the process of formation of the volume of the melt. In the stage of the process of directional solidification, it is necessary to maintain a constant value of $E_a$ by means of the system for stabilising the anodic voltage. In this case, the stationary nature of the working parameters of the generator in the process of melting and the quality of grown crystals are controlled by the operating experience of the operator of equipment, i.e. control of the process is unfortunately subjective.

Modernised equipment of the type Kristall-405 uses a system for the automatic control of the lamp generator on the basis of a microprocessor controller which enables automatic operation of equipment in accordance with a programme, starting from the point of heating of the generator lamp to the working displacement of the crucible [2]. Automation is based on the application of the criteria of the optimality of functioning of the subsystem consisting of a generator with a load which is a multi-parameter system. However, even this approach does not take into account completely the entire variety of the processes taking place in the load. These processes may have a significant effect on the operating regime of the generator.

As an example, we shall examine the time dependences $P_p$, $P_w$,
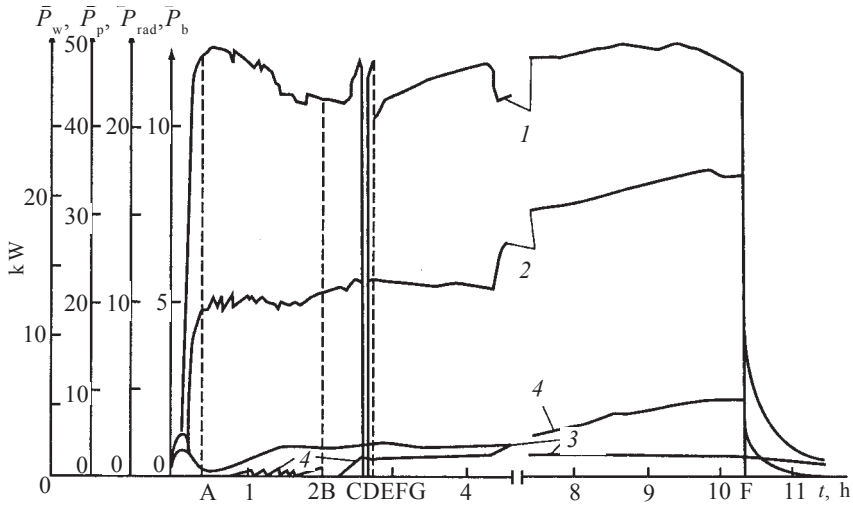
**Figure 3.6.** Time dependences of the power generated in the melt $P_p$ (1) and the power of heat losses: through the wall $P_w$ (2), the bottom of the cold crucible $P_b$ (3) and by radiation $P_{rad}$ (4) [11].

$P_b$, $P_{rad}$ shown in Fig. 3.6 (curves 1, 2, 3, 4, respectively). These relationships were obtained in the process of melting and growth of single crystals of zirconia  stabilised by yttrium oxide. The values of $P_{rad}$ were measured in the experiments using a radiation pyrometer [11].

When the generator is switched on, $P_w$ and $P_b$ rapidly reach the level (curves 2 and 3) corresponding to the power of natural losses of the cold crucible, in the absence of the melt in the crucible. The energy is used basically for heating the crucible and starting metal.

After the formation of the melt, $P_p$ rapidly increases, and $P_w$ and $P_n$ decrease as a result of the greater (in comparison with copper) flux linkage of the RF field with the melt, due to a large difference in the values of the specific electrical resistance. This decrease takes place until the melting front approaches the bottom and the wall of the crucible and, subsequently, they are heated as a result of heat removal from the melt. The power of natural losses of the crucible after filling with the melt in accordance with [11] is 1–2% of $P_p$. For the crucible used in [11], this power was approximately 1% of $P_p$.

After forming the starting melt, new portions of the material for increasing the volume of the melt were loaded in the time period A–B. It is interesting to note that when a hole is made in the cupola of the charge above the melt, the value of $P_{st}$ rapidly

decreases (curve 2). This is caused by melting of the melt as a result of radiation through the resultant hole and by the energy losses for melting of the newly supplied material. Subsequently, $P_{st}$ smoothly increases to the next charge, and so on. The value by which $P_w$ decreases depends on the position and the size of the hole, the time during which the hole remains open, and also on the volume of the melt. For example, in the examination of curve 2 in the time period A−B, there is a tendency for a decrease of the extent of oscillations of $P_w$, associated with making the holes for loading. This takes place as a result of an increase in the volume of the melt, with other parameters of the generator being constant. During the time when the hole in the layer of the charge remains open, $P_{rad}$ (curve 4) increases in a jump and, subsequently, rapidly decreases after loading. These jumps are not indicated in the graph because they are very short. The oscillations of $P_{rad}$ in the time period A−B are caused by gradual heating and melting of the layer of the charge, forming a cupola above the melt, and also additions of the new layers of the charge. Making the hole in the cupola and the supply of new portions of the charge in the melt affect the value of $P_p$ (curve 1) because in direct RF heating of the melt, the energy of the electromagnetic field of the inductor is almost completely transformed to heat and, consequently, the state of the melt affects the working parameters of the generator.

The bottom of the crucible is quite far away from the surface of the melt and, consequently, making the hole in the layer of the charge and additions of new portions of the material does not have any significant effect on the value of $P_b$ (curve 3). The section of the curve A−B is characterised by a decrease of power $P_p$. Subsequently, as a result of uncontrollable circumstances, the power emitted by the generator is greatly increased. This results in local melting of the skull and at the moment of time C a certain amount of the melt is discharged through the gaps between the sections of the crucible. This is followed by emergency shutdown of equipment and, consequently, $P_w$ starts to rapidly decrease. After cooling the melt and formation of a skull, equipment is again switched on and the previous value of $P_p$ prior to shutdown (the moment of time D) is restored. In this case, $P_w$ reached the value close to the value detected prior to discharge of the melt.

At the moment of time E power $P_p$ was also reduced and at F the crucible with the melt was lowered at a rate of 15 mm/h. The graph indicates that during lowering of the crucible, power $P_b$

decreases because the bottom of the crucible travels away from the heating zone. In this stage of the process, the values of $P_p$, $P_w$, $P_{rad}$ gradually increase and their total stable decrease at the end of the process indicates that the entire amount of the melt almost completely solidified and the generator was switched off. The largest decrease of the power removed from the crucible takes place on its walls. The curves 2–4, shown in Fig. 3.6, indicate the cooling of the crystal ingot.

Thus, the dependences make it possible to evaluate the interaction between the component elements of the generator–crucible–melt–solid–phase system and also the reaction of the system to external effects. The analysis carried out previously can be used for a detailed determination of the characteristics of the melt for different operating regime of the generator.

The application of the method has shown its high sensitivity and information content which make it possible to control the process of melting of crystallisation of the material and exert efficient effects on these processes. For example, after making a hole in the cupola and adding the charge, it is possible to evaluate the degree of cooling of the melt and, if necessary, increase the power supply to the melt. In addition to this, the value of this power and also the power removed from the crucible may be used to estimate the volume of the melt and determine the moment of the start of crystal growth.

Detailed consideration and analysis of the heat removed from the crucible and of the power generated in the melt would enable researchers to investigate different processes taking place in the melt and the solid phase, independently of the melting point of the material.

## References

1.  Petrov Yu.B., et al., *Vysokochistye veshchestva,* 1989, No. 3, 136–140.
2.  Petrov Yu.B., Kanaev I.A., Induction furnaces for melting of oxides, Leningrad, Politekhnika, 1991.
3.  Byndin V.M., et al., Induction heating in production of special purity materials, Leningrad, Mashinostroenie, 1980.
4.  Byndin V.M., et al., *Ogneupory*, 1983, No. 2, 41–45.
5.  Borik M.A., et al., in: Problems of crystallography, Moscow, Nauka, 1987.
6.  Aleksandrov V.I., et al., *Neorganicheskie Materialy*, 1983, **19**, No. 3, 443–447.
7.  Aleksandrov V.I., et al., Synthesis of laser materials from the melt by direct

HF heating in a cold container, Report of FIAN, Moscow, 1968.

8.   Lomonova E.E., Production and examination of single crystals of solid solutions based on $ZrO_2$ and $HFO_2$, Dissertation, Moscow, 1980.
9.   Petrov Yu.B., et al., *Elektrotekhnika*, 1981, No. 5, 55–59.
10.  Petrov Yu.B., et al., Induction melting of oxides, Leningrad, Energoatomizdat, 1983.
11.  Borik B.A, Development of technology and examination of oxide glasses for electronics, Dissertation, Moscow, 1985.
12.  Aleksandrov V.I., et al., *PTE*, 1991, No. 3, 231–234.

# Synthesis and crystallisation of refractory materials in the cold crucible

## 4.1. THE COLD CRUCIBLE – EFFICIENT CHEMICAL REACTOR

The rapid development of new branches of technology, for example, electronics, requires the application of precision ceramics. Consequently, it was necessary to produce high purity oxide substances and materials with specific physical-chemical properties: amorphous, finely dispersed, crystalline, fused with a specific phase composition, granulated, etc.

The most important element of the technology of high-temperature materials is chemical synthesis because the majority of materials are complicated chemical compounds: complex oxides, oxygen-containing salt-forming substances, complex fluorides, mixed or simple compounds into which additions were added. In order to produce single crystals, glass or polycrystalline ceramics, the initial simple substances must be synthesised to produce the required compounds. In most cases, synthesis is carried out by the method of solid-phase reactions (the sintering method). For this purpose, the initial substances in the form of fine-dispersion powders are thoroughly mixed and subsequently heated to temperatures below the melting point of the interaction product. Usually, the temperature is $(0.5-0.7)$ $T_m$. The mechanisms of chemical reactions in the solid phase are complicated and vary greatly. However, regardless of the components, an unavoidable stage of the process is the diffusion of

one of the components (or atoms of all components) through the layer of the solid reaction products. The coefficients of diffusion in the solids are not high and usually equal $10^{-6}$ to $10^{-12}$ cm$^2$/s. Thus, the diffusion process is a 'bottleneck' of the solid-phase reaction, restricting the rate of the reaction.

The consequence of the lower rate of solid-phase reactions is the long duration of the process of synthesis and the problems in completing the process. Consequently, the reaction products usually contain impurities of unreacted components, i.e. the synthesis products are not homogeneous [1]. These shortcomings are not found in the synthesis of compounds in the melt. In the interaction of components in the melt, diffusion is no longer a bottleneck because, firstly, the rate of diffusion in the liquid is considerably higher than in solids and, secondly, the liquid can rapidly move under the effect of a force or by means of convection and, consequently, the rate of the reaction increases. The liquid products of the reaction can be solidified and, consequently, their chemical purity can be increased and structural perfection improves. Regardless of the obvious advantages, the synthesis of high-temperature compounds in the melt is used only on a limited scale. There is only a small amount of investigations in which attention was given to melt synthesis in a solar furnace [2], in a plasma furnace [3] or in arc furnaces [4]. The cold crucible is a universal high-temperature chemical reactor which does not contaminate the reaction products. In the cold crucible, the melt of the initial substances and the reaction products are heated with high-frequency currents. Using this method, it was possible to synthesise a large number of complex oxide compounds which together with the equations of the reactions are presented in Tables 4.1 and 4.2. The majority of the reactions given in the tables related to the reactions of the compound and take place in a homogeneous system. Some of the reactions are combined: in addition to the interaction of liquid components, a heterogeneous reaction with the participation of the gas phase also takes place. Suitable examples of these reactions are synthesised solid solutions of zirconium and hafnium dioxides, stabilised with the oxides of rare-earth and transition metals with a variable valency. Examples of these are in Table 4.1. The nature of the reaction and the composition of reaction products change in relation to the composition of the gas atmosphere. Another characteristic example of the combined reaction is the synthesis of solid solutions of chromites of yttrium, lanthanum and rare-earth

**Table 4.1.** Compounds synthesized in a cold crucible

| Compound | $T_m$, °C | $T_{synth}$, °C |
|---|---|---|
| $Na_2O \cdot 11Al_2O_3$ | 1923 | 1970 |
| $MgO+Al_2O_3 \rightarrow MgAl_2O_4$ | 2130 | 2300 |
| $CaO + Al_2O_3 \rightarrow CaAl_2O_4$ | 1600 | 2300 |
| $BaO + Al_2O_3 \rightarrow BaAl_2O_4$ | 2000 | 2300 |
| $3Y_2O_3 + 5Al_2O_3 \rightarrow 2Y_3Al_5O_{12}*$ | 1930 | 2100 |
| $La_2O_3 + 5Al_2O_3 \rightarrow 2LaAlO_3$ | 2100 | 2300 |
| $3Al_2O_3 + 2SiO_2 \rightarrow 3Al_2O_3 \cdot 2SiO_2$ | 1910 | 2100 |
| $2Al_2O_3 + SiO_2 \rightarrow 2Al_2O_3 \cdot SiO_2$ | 1850 | 2100 |
| $SrO + TiO_2 \rightarrow SrTiO_3$ | 2038 | 2200 |
| $R_2O_3 + 2TiO_2 \rightarrow R_2Ti_2O_7*$ | - | 2000–2300 |
| (R = Sc, Y, La, Nd, Sm, Eu, Gd, Dy, Ho, Er, Tm, Yb) $CaO + ZrO_2 \rightarrow CaZrO_3$ | 2345 | 2600 |
| $Sc_2O_3 + 2ZrO_2 \rightarrow Sc_2Zr_2O_7*$ | 2700 | 2900 |
| $SrO + ZrO_2 \rightarrow SrZrO_3$ | 2470 | 2600 |
| $La_2O_3 + 2ZrO_2 \rightarrow La_2Zr_2O_7$ | - | 2400 |
| $SrO + HfO_2 \rightarrow SrHfO_3$ | - | 3000 |
| $Y_2O_3 + Cr_2O_3 \rightarrow 2YCrO_3**$ | 2290 | 2500 |
| $MgO + Cr_2O_3 \rightarrow MgCr_2O_4$ | 2150 | 2300 |
| $CaO + HfO_2 \rightarrow CaHfO_3$ | 2700 | 2900 |
| $La_2O_3 + Cr_2O_3 \rightarrow 2LaCrO_3**$ | 2430 | 2600 |
| $CaO + MoO_3 \rightarrow CaMoO_4$ | 1449 | 1700 |
| $SrO + MoO_3 \rightarrow SrMoO_4$ | 1468 | 1800 |
| $CaO + WO_3 \rightarrow CaWO_4$ | 1580 | 1800 |
| $SrO + WO_3 \rightarrow SrWO_4$ | 1566 | 1800 |
| $ZrO_2 + (8\div50$ mol.%) $MgO, CaO, SrO, Sc_2O_3, Y_2O_3, La_2O_3, TR_2O_3*$ | - | 2700–2900 |
| $HfO_2 + (8\div50$ mol.%) $MgO, CaO, SrO, Sc_2O_3, Y_2O_3, La_2O_3, TR_2O_3$ | - | 2800–3000 |
| $R_2O_3$–$Al_2O_3$–$SiO_2$ (R = Sc, Y La, Nd, Sm, Eu, Gd, Tb, Er, Yb)*** | - | 1800–2400 |

\* Single crystals were produced
\*\* Admixture 5 wt.% $CaCr_2O_4$
\*\*\* Optically transparent glasses

**Table 4.2.** Physical and mechanical properties of refractory ceramics synthesized by solidification in a cold crucible

| Properties | $3Al_2O_3 \cdot 2SiO_2$ | $Sc_2O_3$ | $Y_2O_3$ | $Gd_2O_3$ | $Er_2O_3$ |
|---|---|---|---|---|---|
| Purity, % | 99.7 | 99.0 | 99.9 | 99.9 | 99.9 |
| $T_m$(°C) | 1910 | 2405 | 2410 | 2395 | 2400 |
| Calculated density, g/cm³ | 3.15 | 3.86 | 5.03 | 8.33 | 8.66 |
| Measured density, g/cm³ | 2.5-2.6 | 3.28 | 4.25 | 6.8 | 7.5 |
| Porosity, % | 17-18 | 15-19 | 14.8 | 18.4 | 15.5 |
| Limit of mechanical stability | 500 | 1400 | 190 | 300–350 | 300–350 |
| Pressure, kg/cm² | | | | | |
| 20 °C | 150 | | 120 | - | - |
| 1000 °C | - | | 100 | 100–200 | 100–200 |
| 1300 °C | | | 125 | (20-1400 °C) | (20-1400 °C) |
| Elasticity moduli E · 10⁶, kg/cm | 0.37 | - | 1.5 | - | - |
| Temperature of deformation under load of 2 kg/cm² | 1760-1810 | 1950 | 1960 | 1700–1800 | 1700–1800 |
| Deformation in vacuum, mm/mm·h | - | - | $T = 1650°C$ | - | - |
| | | | $\sigma = 14.79$ kg/cm₂ | | |
| | | | $9.8 \cdot 10^{-4}$ | | |
| Thermal expansion coefficient, Gr-1·10⁻⁶ (20-800 °C) | 4.4 (850°) | - | 7.3 | 8.4 | 7.3 |
| Resistivity, Ω · cm | | | | | |
| vacuum 1000°C | | | $2.5 \cdot 10^6$ | | |
| 1500°C | | | $3.0 \cdot 10^3$ | $10^4$-$10^5$ | |
| vacuum 1000°C | | | $1.0 \cdot 10^6$ | | |
| 1500 °C | | | $3.0 \cdot 10^3$ | | 0.75 |
| Heat conductivity, kcal/m·h·gr (1200 °C) | | | | | |
| Thermal stability | | | | | |
| 1300 °C water cycles | | | 12-14 | | |
| Rates of evaporation (vacuum), g/cm² · s | | | | | |
| 1700 °C | $0.5 \cdot 10^{-7}$ | | | | |
| 1800 °C | $1.0 \cdot 10^{-7}$ | | | | |
| 1900 °C | | | $1.6 \cdot 10^{-8}$ | $6.0 \cdot 10^{-5}$ | $1.2 \cdot 10^{-5}$ |
| 2000 °C | | | $1.5 \cdot 10^{-7}$ | $2.0 \cdot 10^{-5}$ | $1.9 \cdot 10^{-5}$ |

elements with additions of chromites of magnesium, calcium, strontium and barium. The electrical conductivity of these substances greatly changes in relation to the composition of the atmosphere.

Examination of the kinetics of reactions of the compounds in the melts shows that the chemical interaction of the initial components takes place at a rate equal to the rate of dissolution of solid particles of the substance in the melt, i.e. with the melting rate. In the typical cases, the melting rate is 0.1–1.0 kg/min, depending on
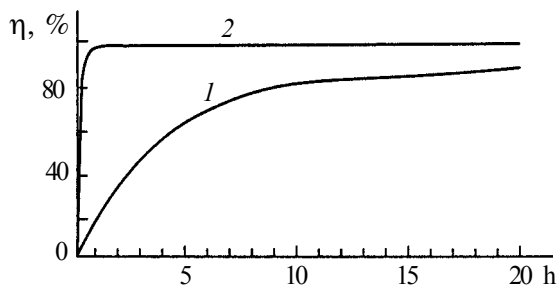
**Figure 4.1.** Kinetic curves (yield of the reaction product η in relation to time): 1) reactions in a mixture of solid phases $CaCO_3 + Fe_2O_3 \rightarrow CaFe_2O_4$; 2) reaction in themelt $CaO + ZrO_3 \rightarrow CaZrO_3$ [5].

the degree of superheating of the melt, viscosity and the heat of phase transition in melting initial substances. Thus, homogeneous chemical equilibrium in the melt is established during the time of several seconds to several minutes. Examination of the products of interaction by means of x-ray diffraction, microscopic and electron microscopy and spectral analysis methods shows clearly that for the strictly stoichiometric composition of the initial mixture of the components the content of the initial substances in the final product does not exceed 0.01–0.1 vol%. Figure 4.1 compares the kinetics of synthesis in the melt (2) with the appropriate dependence in solid-phase synthesis (1); comparison is in favour of synthesis in the melt.

The situation in the case of heterophase reactions is more complicated. In this case, the molten substance reacts with the gas atmosphere. Two limiting cases should be examined.

1. The acting component of the gas atmosphere does not dissolve in the melt. In this case, the contact surface is restricted by the open surface of the melt. The reaction rate is limited by the processes of diffusion of gas molecules through the phase boundary and by diffusion of the reaction products in the volume of the melt, if there is no mixing of the melt or if mixing can be ignored. Therefore, the viscosity of the melt plays a significant role. The dependence of the time of establishment of equilibrium on the viscosity of the melt can be clearly examined in comparing the rate of burnout of the starting metal and the products of reduction of the oxides of lanthanum, mullite ($3Al_2O_3 \cdot 2SiO_2$) and a glass with the composition $La_2O_3 \cdot Al_2O_3 \cdot 6SiO_2$ from the melt. The viscosity of the melt rapidly increases in transition from the lanthanum oxide to mullite and, in particular, to the glass. In full correspondence with this, the rates of burnout of metallic aluminium and the products of

reduction, dispersing the volume of the melt, greatly differ. From the $La_2O_3$ melt, aluminium burns out within 5–10 min, from the mullite melt in 15–20 min, and from the glass melt, aluminium does not burnout in 10 h at a  temperature of 2000°C.

2. The acting component of the gas atmosphere is soluble in the melt; in this case, the rate of the heterophase reaction is not restricted by the rate of diffusion of the reaction products. A suitable example of heterophase reactions with the dissolution of the gas component is the oxidation of metallic aluminium and the products of reduction in the melts of $Al_2O_3$, $YAlO_3$, $Y_3Al_5O_{12}$, $MgAl_2O_4$ and some other compounds. The experiments show that the melts of these substances absorb large quantities of gaseous oxygen [6]. Thus, the melt of aluminium oxide in contact with air dissolves more than 40 vol% of oxygen. In this case, heterophase equilibrium is established within 5 min in the volume of a 0.5 l melt. In rapid solidification of the melts, the dissolved oxygen is rapidly released, the melt 'boils up', and the solidified block is penetrated with a large number of large pores. It is important to note that as a result of combining 'the pure' method of heating and 'pure' method of melting in the skull, this method has no restrictions as regards the elemental composition of the synthesised compounds. Thus, in the melt synthesis of compounds in the cold crucible, it is possible to obtain high rates and 100% synthesis of the given chemical compound. This may be accompanied by additional purification of the product to remove impurities in comparison with the starting material.

The application of additional purification may be indicated on an example of the synthesis of an aluminium–magnesium spinel and solid solutions with the structure of the spinel in the $MgO–Al_2O_3$ system, being promising materials for the production of high-density ceramics. The initial materials were reagents of the oxides of the synthesised compounds included in the composition having 'analytical' and 'special purity' grades. The synthesised product solidified in the cold crucible, produced from copper pipes. The temperature of the melt was maintained in the range 2200–2250°C. The x-ray examination of the phase composition of the synthesised material showed only the presence of spinel. The impurity composition was determined on the basis of the content of the impurities of alkali and transition metals which were the main characteristics of the material and determined its suitability for practical application. The results of analysis presented in Table 4.2

show that the content of the impurities in the synthesised material is on the level of the content of these impurities in the initial reagents and has a tendency for a decrease in the content of iron, chromium and alkali metals.

Special attention should be paid the impurity of copper in the melt because of the induction coil and the crucible, used for melting, are produced from copper tubes. An increase of the copper content to $(10^{-4}–10^{-2})$% is typical of the examined process and shows that the skull, formed between the melt and the cold crucible, reliably protects the melt against contact with the crucible. According to the authors of [7], the main source of the increase of the copper content is the chemical interaction of the outgoing gases, containing 'inherited' impurities of the compounds of sulphur, chloride and other elements, with the surface of the crucible above the melt, and the adsorption of compounds of copper by the powders supplied into the crucible for melting. However, the impurities of copper in the melt, when the initial material 'inherits' nitrogen compounds, may be excluded using a crucible produced from aluminium or stainless steel. The application by coatings of chemically resistant metals is also an efficient method.

The qualitatively new characteristic of the materials, synthesised in induction heating in the cold crucible, is the production of these materials in the form of a crystalline block with a circular or other section, granules, dispersed powder, with the given phase composition, depending on application. Figure 4.2 shows the diagrams of different systems for the production of products of synthesis in the cold crucible. A crystalline oxide material in the form of a block should be used, for example, for loading into the crucible in the growth of single crystals from the melt by the Czochralski method. The blocks of aluminium oxide were used in the growth of optical leucosapphire by the Musatov method. The application of crystalline blanks makes it possible to simplify the preparatory stages of the technology of growth of single crystals and reduce the content of impurities. An important direction of the application of fused polycrystalline special purity materials are film-forming materials, compounds for spraying different optical coatings.

The induction melting of oxides in the cold crucible is a promising method for the production of polycrystalline refractory materials and cast refractory component [8]. This technology is used widely for remelting of powder oxides into a crystalline material. The
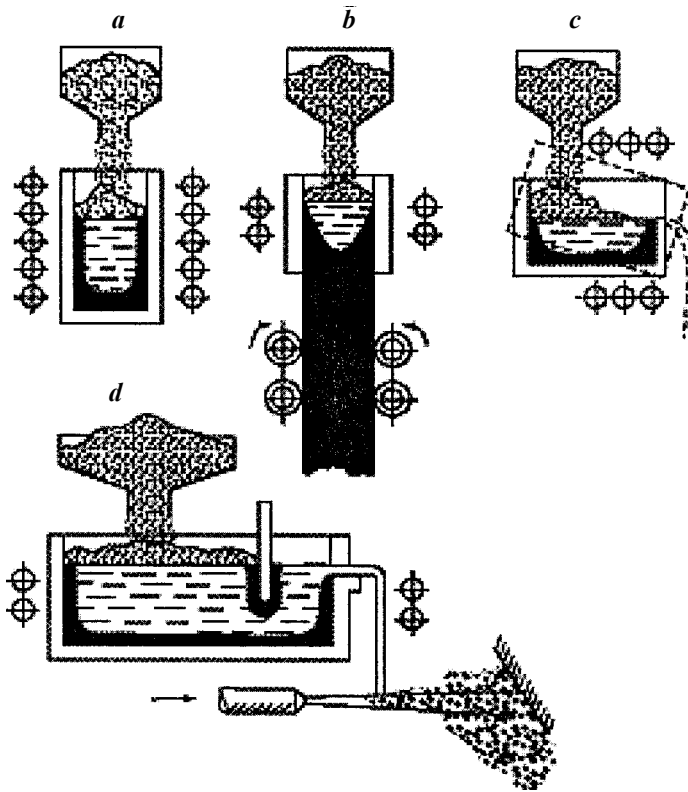
**Figure 4.2.** Design of cold crucibles for various applications [7]. a) production of a block of molten oxide in a cold crucible; b) continuous melting 'into a block'; c) periodic discharge of the melt from a horizontal cold crucible; d) continuous discharge of the melt from a crucible with a constant level and blowing of the jet of the melt stream for producing finely dispersed molten powder.

efficiency of remelting is determined by the high thermodynamic stability of the grains, produced in disintegration and milling of the crystalline materials, in comparison with the initial or sintered powder. The ceramics produced from the fused grains, is characterised by small shrinkage and deformation in sintering, constant properties in service, and sufficiently high heat resistance.

The application of the cold crucible for the remelting of oxides is justified by the high purity of final products which is maintained on the level of the purity of initial materials because the 'pure' induction method of heating and melting in the skull is used.

The moltem oxides are produced by the 'melting into a block' and 'melting for discharge' methods. The melting into a block method is realised by the crystallisation of the melt in the cold

crucible with the close bottom or by continuous melting of a block in a continuous cold crucible with a seed crystal in the lower part of the crucible. In continuous melting of the block, the productivity of the process is higher and the specific energy losses are lower. Equipment for continuous melting is designed in the form of a load-carrying frame whose internal part contains a moving frame with a seed crystal, travelling in the vertical direction, Fig. 4.2 [9]. In the process, it is necessary to match the heating conditions, the intensity of supply of the charge and the speed of travel of the seed crystal. The matching criterion is the constant position of the level of the melt in relation to the plane of the induction coil and, consequently, the parameters of equipment are regulated independently. In the design shown in Fig. 4.2, the height of the crucible is approximately equal to $(1.5–2.0)\ D_i$, where $D_i$ is the diameter of the induction coil; the bottom of the crucible is lowered below the induction coil to at least $D_i/2$. At this distance, the strength of the electromagnetic field is small and, consequently, the skull does not melt. Melting could result in discharge of the melt. The rate of flow of the water in the sections is in the range 1.0–1.5 m/s and is determined taking into account the need to prevent boiling in the jet cooling the wall of the section. The minimum flow speed of the water in the section is determined by the equation, $V_{min}$, m/s:

$$V_{min} \geq 5.5 \cdot 10^{-10} p^{-2/3} q_{max}^2, \tag{4.1}$$

here $p$ is the pressure of water in the cooling system, N/m²; $q_{max}$ is the maximum specific heat flow from the melt to water, W/m², which is determined by calculations on the level of the melt surface.

   In order to melt the centre of the ingot, the relative diameter of the crucible $m$ should be in the range:

$$1.0 \leq m \geq 7.0, \tag{4.2}$$

where $m$ is determined from the equation:

$$m = D_T / \Delta_P \sqrt{2}, \tag{4.3}$$

Here $D$ is the crucible diameter, m; $\Delta_p$ is the depth of penetration of current into the melt, m;

$$\Delta_P = 503\sqrt{\rho / f}, \tag{4.4}$$
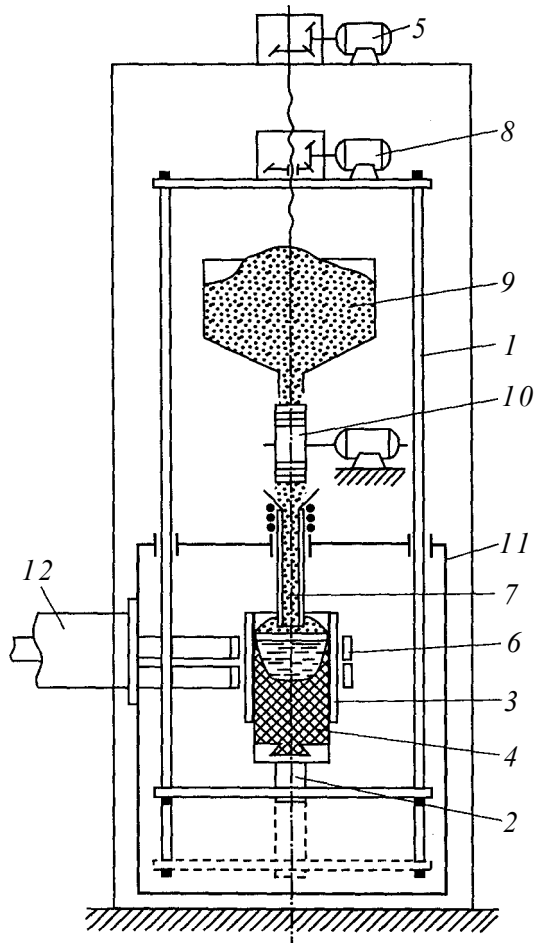
**Figure 4.3**. Diagram of equipment for induction melting in a cold crucible to produce blocks of molten oxides [9]. 1–7) notations in the text; 8) displacement mechanism of the seed crystals; 10) charge dosing device; 11) working chamber; 12) high-voltage cable; for the rest of the notations see the text.

where $\rho$ is the specific electrical resistance of the melt, ohm m; $f$ is the current frequency of the generator, Hz. If $m < 1$, the efficiency of the induction coil decreases and there is a risk of 'freezing' the melt. At $m > 7$ it is necessary to superheat the melt and this may have a detrimental effect on the thickness of the skull, with an increase of the probability of electrical breakdown between the crucible sections.

Table 4.1 shows the parameters of equipment for melting a number of oxides in cold crucibles of different diameters. To
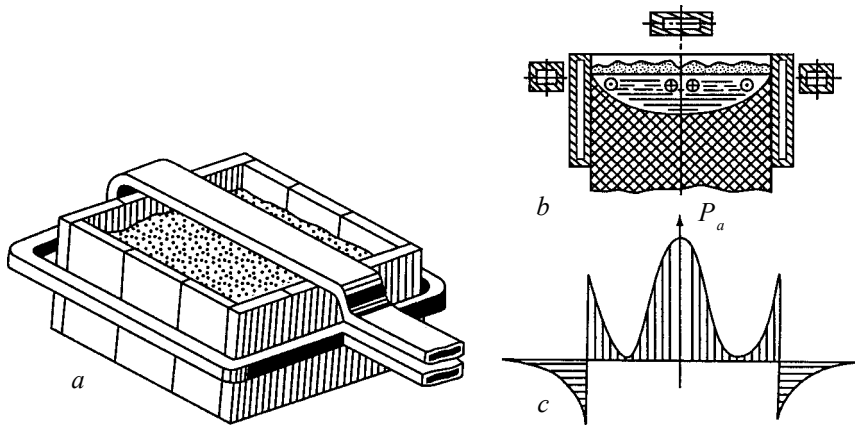
**Figure 4.4**. Inductor with a transverse busbar for producing a large block of molten oxide. a) crucible with an inductor; b) directions of circulation of currents in the melt; c) curve of specific power generated in the melt.

characterise the energy losses of the process, the Table gives the total specific losses of energy $\Delta W$, determined by experiments, and the specific energy of melting $\Delta W_T$, calculated from the equation:

$$\Delta W_T = (H_m - H_{293} + \Delta H)/3600M, \qquad (4.5)$$

Here $H_m$ is the enthalpy of the oxide at the melting point, kJ/mol; $\Delta H$ is the specific heat of melting, kJ/mol; $M$ is the molecular mass of the oxide, kJ/k·mol. The ratio $\Delta W_T/\Delta W$ corresponds to the total efficiency of equipment which depends on the nature of the oxide and the melting conditions. The Table shows that the total efficiency is minimum in the melting of oxides of rare-earth elements and is maximum for corundum. The total efficiency in melting in arc furnaces is higher in comparison with induction heating but the factors determining the quality of material make the latter method more attractive.

To increase the transverse dimensions of the ingot and melt the centre, it is recommended to use an induction coil with a transverse bus shown in Fig. 4.4. The presence of the induction lead (transverse bus) above the melt results in superheating of the melt in the centre of the crucible. This results in melting of the centre of the ingot and intensifies heat transfer from the melt to the charge, thus increasing the rate of the process. For the induction coil with the transverse bus, the ratio (4.2) is retained, and

expression (4.3) transforms to the following form:

$$m = B / 2\Delta_p \sqrt{2},$$                               (4.6)

where $B$ is the large transverse size of the cross-section of the crucible, m.

Thus, using induction melting of oxide materials in the cold crucible, it is possible to realise high productivity processes in order to produce fused materials for industrial and technical applications.

The method of the cold crucible is highly promising for methods (Fig. 4.4c, d) using different techniques of treatment of the jet of the melt which make it possible to produce granules, disperse powders, fibres from high purity oxide materials and also quench the metastable phases at a high cooling rate of the melt. The application of individual oxides and compounds in the form of related materials makes it possible to improve the efficiency of the processes of growth of crystals and casting of glasses, and the purity of the products increases.

The processes of production of high purity crystalline materials may be realised at present on the experimental or industrial scale. Information on equipment for these purposes is presented in Chapter 2.

## 4.2. PRODUCTION OF MOLTEN MULLITE

In this and subsequent sections, specific examples of the melt synthesis of materials in the cold crucible will be discussed. Because of the development of new metallurgical procedures, for example, vacuum treatment of steel, there has been special interest in high-alumina materials of the $Al_2O_3$–$SiO_2$ system, in particular, mullite, usually produced by electric melting [10]. The mullite, in accordance with the equilibrium diagram, forms phases with a variable composition [11]. In the synthesis of mullite by the Verneuil method, investigators produced single crystals with the composition $2Al_2O_3 \cdot SiO_3$, confirming the congruent nature of melting [12]. The mullite with the composition $3Al_2O_3 \cdot 2SiO_2$ melts without dissociation, but this compound could not be produced by melt synthesis in air [13, 14]. Equipment for melting mullite in air is shown in Fig. 4.5 [15]. The process is characterised by successive crystallisation of the block (*1*) in local melting of the powder charge (*2*) on its upper surface inside the crucible (*3*) situated inside the
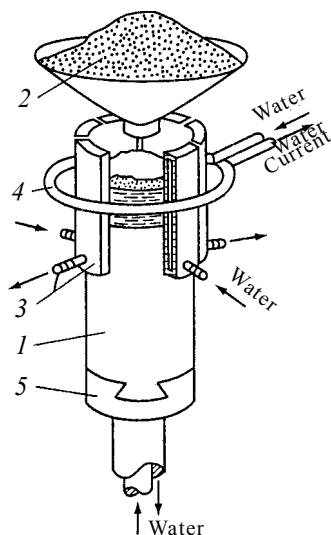
**Figure 4.5.** Schematic of the equipment for producing mullite by induction melting in a cold crucible [15].

high-frequency induction coil (*4*). When using a continuous crucible and a moving baseplate (*5*), it is possible to produce blocks whose length is determined by the design features of equipment.

In consecutive growth of the crystalline block it is possible to ensure the conditions in which the given ratio of the oxides and the degree of purity of the initial material is maintained. These conditions include a small volume of the melt (20–100 ml), short duration of holding material in the liquid phase (30–100 s), uniform heating of the melt and small superheating above the melting point (not more than by 50–100°C). The rate of cooling and crystallisation of the melt is 3–5°C/s and depends on the volume of the melt and the distance from the cold wall of the crucible. The speed of movement of the solidification front found is not greater than 5 mm/min and is similar to the quenching conditions. The results of microscopic analysis show that the main phase consists of mullite and only the samples with a high content of aluminium oxide contain corundum. The characteristic specimens of fused mullite are shown in Fig. 4.6. The specimens contained grains of efficiently solidified mullite, separated by thin glass layers. The amount of the glass phase is small and is determined by the ratio of the oxides of aluminium and silicon in the initial charge. The chemical composition of the synthesised mullite is presented in Table 4.3 which shows that the method of melting in the cold crucible makes it possible to
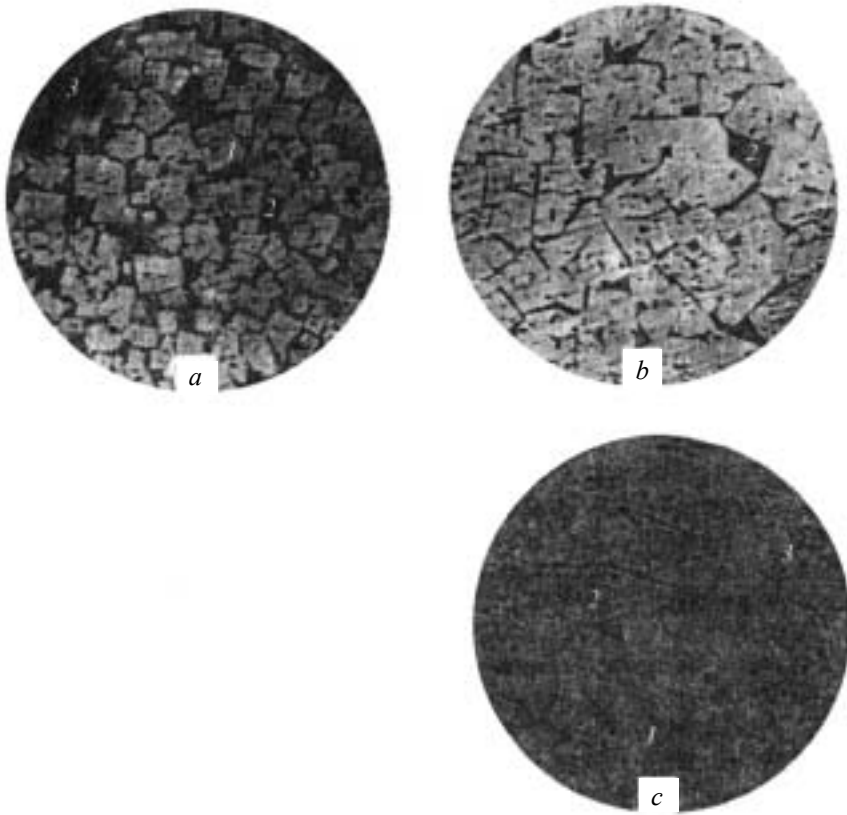
**Figure 4.6.** Photographs of sections of molten materials of the $Al_2O_3$–$SiO_2$ with the $Al_2O_3$ content of 60.5% (a), 64.9% (b), 70.4% (c): 1) mullite; 2) glass; 3) pores, ×110 [15].

produce compounds covering as regards composition a wide range of the solid solutions from mullite $3Al_2O_3 \cdot 2SiO_2$ to pragite $2Al_2O_3 \cdot SiO_2$. The comparatively high content of the glass phase indicates the nonequilibrium conditions of solidification of the melt and crystallisation of mullite. The parameters of the elementary cells of the crystal lattice of the solid solutions of mullites are presented in Table 4.4. The x-ray diffraction patterns of different zones of the fused mullite block are shown in Fig. 4.7.

It is also important to mention another important aspect of the method of successive crystallisation in the single ingot for the examination of the phase composition of the products of synthesis of complex oxide systems in the subliquidus region which is difficult to examine. As a result of melting charges of different composition

**Table 4.3.** Chemical composition of molten mullite

| Specimen No. | $Al_2O_3$ content in sample, % | Amount of insoluble residue, % | $Al_2O_3$ content in soluble residue, % | Composition of mullite κ*, according to the results of analysis | |
|---|---|---|---|---|---|
| | | | | chemical | X-ray** |
| 1 | not determined | 77.3 | 73.0 | 1.59 | 1.49(2) |
| 2 | 60.5 | 77.1 | 73.8 | 1.66 | 1.69(3) |
| 3 | 63.8 | 81.9 | 74.6 | 1.73 | 1.71(3) |
| 4 | 67.9 | 86.4 | 75.4 | 1.82 | 1.75(2) |
| 5 | 64.9 | 83.9 | 75.6 | 1.83 | 1.82(3) |
| 6 | 69.4 | 88.8 | 75.3 | 1.80 | 1.88(4) |
| 7 | 70.4 | 88.7 | 76.4 | 1.92 | 1.92(2) |
| 8 | 73.6 | 91.6 | 77.8 | 2.06 | 2.09(3)*** |
| 9 | 75.9 | 93.3 | 78.6 | not determined | 2.12(4)*** |
| 10 | not determined | 94.7 | not determined | | 2.04(4)*** |
| 11 | As above | 95.2 | As above | | not determined |

\*κ – $Al_2O_3$ : $SiO_2$ ratio in mullite, i.e. its basicity
\** Values in brackets are random errors corresponding to the fiducial probability of 0.9
\*** Samples contained corundum: sample No. 8 < 1%, No. 9 and 10 ≥ 5%

**Table 4.4.** Parameters of the crystal lattice of molten mullite

| Mullite composition, | Lattice parameters, Å | | | | | |
|---|---|---|---|---|---|---|
| | $a$ | Δ $a$ | $b$ | Δ $b$ | $c$ | Δ $c$ |
| 1.49 | 7.5705 | 0.0028 | 7.7038 | 0.0015 | 2.8899 | 0.0006 |
| 1.69 | 7.5648 | 0.0036 | 7.7014 | 0.0018 | 2.8913 | 0.0002 |
| 1.71 | 7.5645 | 0.0032 | 7.6975 | 0.0015 | 2.8897 | 0.0012 |
| 1.75 | 7.5596 | 0.0028 | 7.6975 | 0.0013 | 2.8927 | 0.0016 |
| 1.82 | 7.5541 | 0.0018 | 7.7032 | 0.0012 | 2.8927 | 0.0016 |
| 1.88 | 7.5540 | 0.0008 | 7.7016 | 0.0010 | 2.8906 | 0.0004 |
| 1.92 | 7.5634 | 0.0078 | 7.6958 | 0.0006 | 2.8886 | 0.0020 |
| 2.09 | 7.6038 | 0.0013 | 7.6927 | 0.0006 | 2.8929 | 0.0006 |
| 2.12 | 7.5997 | 0.0012 | 7.6926 | 0.0012 | 2.8925 | 0.0003 |
| 2.04 | 7.5987 | 0.0035 | 7.6957 | 0.0014 | 2.8942 | 0.0005 |
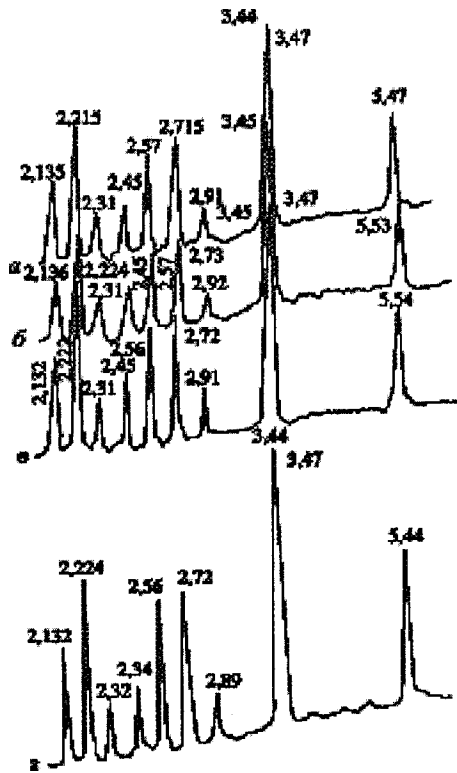
**Figure 4.7.** X-ray diffraction patterns of different zones of a molten mullite block [15]. a) upper, b) central, d) lower, d) peripheral zones.

in the same ingot, it is possible to ensure all theoretically possible ranges of concentration, including systems with volatile components, as shown on the example of the $Al_2O_3$–$SiO_2$ system. The proposed methods can be used efficiently for constructing equilibrium diagrams of the physical–chemical systems used partially in the synthesis of high-temperature glass (Chapter 6).

## 4.3. POLYCRYSTALLINE ELECTRICALLY CONDUCTING CHROMITES OF YTTRIUM AND LANTHANUM

An outstanding examp le of the efficient application of the cold crucible as a chemical reactor is a study carried out by a group of scientists at the Institute of General Physics and the Institute of High Temperatures of the Russian Academy of Sciences in the search for the optimum composition of electrically conducting

lanthanum chromite for the electrodes of powerful MHG generators and heaters of high-temperature furnaces. The cold crucible method makes it possible to synthesised quite rapidly tens or hundreds of chemical compounds and investigate their physical–chemical properties and, consequently, save resources in comparison with the application of traditional solid-phase synthesis.

The currently known refractory oxides of 17 elements of the periodic table of elements form 680 binary compounds which have been investigated sufficiently. Further increase in the complexity of the system as a result of increasing the number of components is evidently irrational because already in the four-component systems the melting point decreases in accordance with the equation

$$T_{max} \approx A - B \cdot n \text{ for } n \leq 5, \tag{4.7}$$

where A = 5100, B = 700.

The materials, produced by the new technology, are characterised by significant advantages in comparison with the materials used until recently for the fabrication of electrodes of MHG generators. Firstly, these materials are characterised by high chemical purity and, secondly, they are thermodynamically equilibrium at high temperatures because the processes of melt synthesis take place to a high degree at temperatures considerably higher than the working temperature in the channel of the MHG generator. Since the material was synthesised in air, it is in equilibrium with the oxidation atmosphere and retains the stability of its properties in the plasma flow characterised by the oxidation properties.

The most promising materials for the development of new electrodes of MHG generators are polyphase composite materials based on high-temperature oxides. Using these materials, it is possible to improve greatly the physical and physical–chemical properties of the electrodes. This method is promising and the following results were obtained using this method.

The new components for 'construction' of electrodes were represented by the following materials:

1. The single crystals of stabilised zirconia.

2. Lanthanum chromite with an additives of the oxides of alkali-earth metals in the concentrations from 2 to 15 mol%

3. Yttrium chromite, pure or with an addition of alkali-earth elements (2–15 mol%).
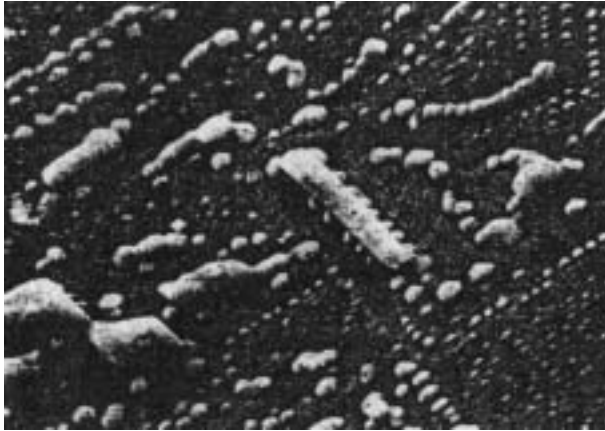
**Figure 4.8.** Electron micrograph of a LaCrO$_3$ ingot with an addition of 7 mol% of calcium chromite (for explanation see the text) [5].

4. Metallic chromium in the form of a powder.

The production and properties of single crystals of stabilised zirconia will be described in chapter 7. The synthesis conditions and a number of physical–chemical properties of the lanthanum chromites have been presented in [6]. Each of these substances has specific physical–chemical properties. For example, zirconia is characterised by the highest melting point (2750°C) and relatively high electrical conductivity at temperatures above 1200°C. The single crystals of cubic zirconia are characterised by high hardness (7.5–8.5 on the Moss scale) and strength which they retain at temperatures above 2000°C. The melted chromites of lanthanum and yttrium are characterised by high electrical conductivity already at room temperature and the ceramic materials produced from them have high thermal stability. In addition to this, the yttrium oxide which may be present in yttrium chromite after synthesis, does not interact with water and water vapours at high temperatures. Metallic chromium is also characterised by high electronic conductivity. The positive properties of this material include the relatively low capacity for oxidation as regards metals. The combination of these properties of the materials made it possible, using the cold crucible method, to develop electrodes for MHD generators and high-temperature furnaces. Figure 4.8 shows the electron micrograph of a cleavage of an ingot of lanthanum chromite  doped with of 7 mol% of calcium chromite. The photograph shows clearly the crystalline grains of the solid solution of lanthanum, calcium chromite and the droplet of the eutectic
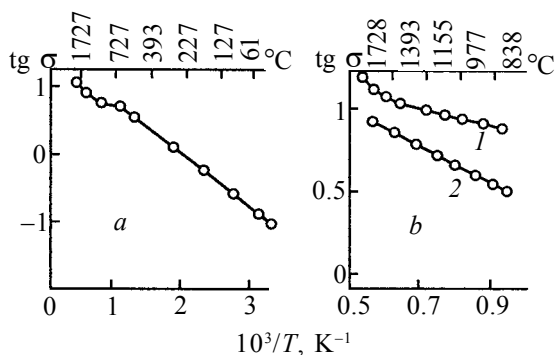
**Figure 4.9.** Temperature dependence of the electrical conductivity of lanthanum chromite with the addition to 7 mol% of calcium chromite [5].

composition, enriched with calcium oxide displaced to the boundaries between the crystals. The ingot of the chromites was refined and the produced powder was used for production of ceramic materials by ceramic technology methods. Figure 4.9 shows the temperature dependences of the specific electrical conductivity of these specimens. This material has high electrical conductivity already at room temperature. The special feature of the ceramics produced from lanthanum chromite is the strong dependence of electrical conductivity on the oxidation–reduction properties of the atmosphere. The high electrical conductivity in the temperature range from room temperature to 1000°C is obtained only after heating the specimen in the oxidation atmosphere. Heating in a redusing or neutral atmosphere, or in vacuum, greatly increases the specific resistance of ceramics in the low temperature range, as indicated by Fig. 4.9. Repeated heating in the oxidation atmosphere completely restores the initial electrical conductivity. X-ray diffraction examination of molten lanthanum chromite indicates that the metal subjected to reducing annealing contains a single phase $LaCrO_3$. After heating in the oxidation atmosphere, new lines, indicating the formation of the impurity of the new phase, appear. Thus, it may be concluded that electronic electrical conductivity below 1000°C is associated with the formation in the material of the impurities in which the valency of chromium is higher than 3. The fused chromites are efficiently combined with other metallic and nonmetallic phases, forming a new series of polyphase materials [14].

One of the main special features of the heaters produced from lanthanum chromite, modified with oxides of rare-earth elements,
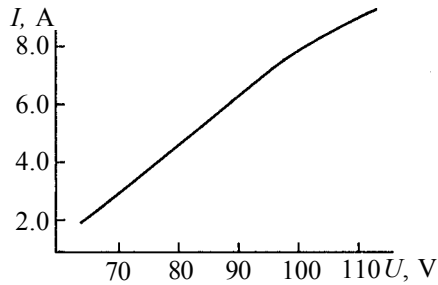
**Figure 4.10.** Volt–ampere characteristic of a lanthanum chromite heater [17].
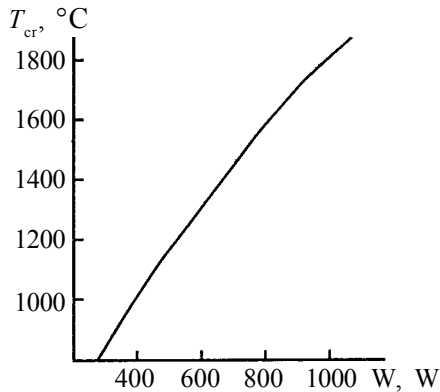


**Figure 4.11**. Dependence of the brightness temperature of the active part of a heter on the required power [17].

is the relatively low specific electrical resistance at room temperature (≈10 ohm·cm) and, consequently of these, heaters can be used starting from 20°C. The high resistance of chromite heaters results in stable operation not only in the continuous but also quasi-periodic regime at high heating and cooling rates [17]. The high thermal resistance of the electrodes is the result of application of porous ceramics (approximately 25%) with the granular structure. This type of ceramics is characterised by high strength, low elasticity modulus and, consequently, is used for the production of heaters. Figures 4.10 and 4.11 show respectively the volt–ampere characteristic and the dependence of brightness temperature on the required power of the heaters produced from lanthanum chromite illustrating the high physical parameters of the electrodes produced from lanthanum chromite.

The furnaces with heaters produced from lanthanum chromite require efficient high-temperature thermal insulation. Disruption of thermal insulation results in overheating and failure of the heaters.

**Table 4.5.** Main parameters of a lanthanum chromite heater

| Parameter | Numerical value |
|---|---|
| Total length, mm | from 350 to 700 |
| Length of active part, mm | to 250 |
| Diameter, mm | from 16 to 35 |
| Scatter of resistivity, % | ± 20 |
| Ratio of resistance of leadouts and active part | 1:5 |
| Total porosity, % | ~25 |
| Coefficient of linear thermal expansion (20-1000°C)·$10^{-6}$ /deg | 8.0 |
| Permissible working temperature on internal surface of heater, °C | 1850 |
| Permissible working temperature in furnace, °C | 1750 |
| Change of resistivity in the first 600 h of operation, % | ≤ 15 |

The heat-insulating materials in the furnaces are represented by layers of dense corundum, low-dense alumina, or caolin cotton based material. The main parameters of heaters produced from lanthanum chromite are presented in Table 4.5.

**References**

1.  Foex M., *Rev. Haute temp. Refract.,* 1966, **3**, 309.
2.  Cohn W., Braught G., *J. Opt. Soc. Amer.*, 1954, **44**, 45.
3.  Foex M., Third Colloque National du Centre National de la Recherche Scientifique Sur la Chimie des Hautes Temperature, Paris, 1963, 117.
4.  Ol'shanskii L.Ya., Pryanishnikov V.P., Chemical electro-chemistry, Moscow and Leningrad, Goskhimizdat, 1962.
5.  Aleksandrov V.I., et al., *Usp. Khim. Nauk*, 1978, **10**, No. 3,385–427.
6.  Aleksandrov V.I., et al., *Izv. Akad Nauk SSSR, Neorgan. Mater.,* 1973, **9**, 236.
7.  Petrov Yu.B., et al., *Vysokochistye Veshchestva,* 1989, No. 3, 136.
8.  Ganyuchenko V.M., et al., *Steklo i Keramika*, 1975, No. 9.
9.  Petrov Yu.B., et al., *Ogneupory*, 1980, No. 10, 41–46.
10. Cichy P., *Interceram.*, 1974, No. 4, 1975, No. 1.
11. Toropov N.A., et al., Equilibrium diagrams of silicate systems, Moscow and Leningrad, 1965.
12. Barta R., Barta Ch., *Zh. Prikl. Khimii*, 1956, **29**, No. 3.

13.   Petrov Yu.B., Ratnikov D.G., Cold crucibles, Moscow, 1972.
14.   Aleksandrov V.I., et al., *Vestn. AN SSSR*, 1973, No. 2, 29.
15.   Sokolov A.N., et al., *Ogneupory*, 1979, No. 9, 35–39.
16.   Aleksandrov V.I.,et al., Synthesis and crystal growth of refractory mate-
      rials by RF melting in a cold container, Curr. Top. Mater. Sci., Amster-
      dam,  421–480, 1978.
17.   Balkovich V.L., et al., *Elektron. Prom-st',* 1981, No. 7/8, 103–104.

# 5

# Growth of single crystals

## 5.1. GROWING CORUNDUM, RUBY AND OTHER CRYSTALS, USING A SEED (THE CZOCHRALSKI METHOD)

To grow single crystals by drawing using a seed crystal, by the Czochralski method, it is necessary to:

1. Produce a strictly determined distribution of temperature in the melt and at the solidification front, in particular in the central part of the melt surface the temperature should be lower than at any other point of the melt;

2. Ensure high stability of temperature at the solidification front. The application of the Czochralski method for the growth of crystals from a cold crucible is of considerable scientific and applied interest. However, in this case, there are difficulties of the principal nature, caused by specific features of direct melting using high-frequency current in a cold crucible, which include: 1. The need for superheating the melt to ensure its stable maintenance in the crucible; 2. The regulation of melt temperature to compensate phase instability in direct high-frequency heating; 3. The formation of radial temperature gradients on the surface and in the volume of the melt; 4. The existence of turbulent convection flows in the melt due to steep temperature gradients in the volume of the melt and the presence of internal heat generation sources.

The previously presented isotherms (Fig. 2.6 and 2.7) provide information on the nature of temperature distribution in the melt and show that the change of the position of the induction coil in relation to the surface of the melt and the variation of the power supplied to the melt have strong effects on the temperature gradients in the

melt. The factors affecting the formation of temperature gradients in the melt also include the following technological parameters: the dimensions of the crucible, the working frequency of the generator, the presence of thermal screens or additional heat sources, the configuration of the induction coil, and other.

The efficiency of a specific method of the formation of thermal fields in the melt is determined mainly by the physical characteristics of the melt and the growing crystal. Therefore, there is no universal recipe for obtaining the required temperature distribution in the melt and for every specific case it is necessary to select appropriate technological conditions.

The formation of the required radial temperature gradient and the stabilization of convective flows in the melt are achieved by increasing the generator frequency and the diameter of the melt surface. Figure 6.3 shows the temperature distribution on the surface of a $Al_2O_3$ melt in a crucible with a diameter of 80 mm at a frequency of the field of 5.28 MHz. Such radial temperature distribution corresponds to the condition necessary to grow crystals by the Czochralski method. However, even in this case, the fluctuations of the convective flows with time remained significant. The majority of produced melts are characterised by low viscosity and only some of them, which include glass-forming components in their composition, such as $SiO_2$, are viscous. The absence of the convective flows on the surface of the melt is associated with high melt viscosity.

Using a number of examples, special attention will be given to the application of different technological procedures in the growth of single crystals from a cold crucible using a seed crystal. For example, the authors of [1,2] described the growth of dislocation-free silicon crystals from a cold crucible. The optimum thermal conditions were achieved by selecting the size of the crucible, the frequency of the generator, and the position of the inductor in relation to the surface of the melt. It should be mentioned that as a result of the electromagnetic interaction of the silicon melt with the high frequency field, the melt is displaced from the walls of the crucible and the surface of the melt becomes sferical. According to the authors of [3], the growth of silicon by this method is highly promising because it is possible to obtain a high degree of purity in comparison with the crystals produced by the Czochralski method from a conventional crucible and a higher uniformity in comparison with the crystals produced by zone melting.

One of the simplest methods of the formation of temperature
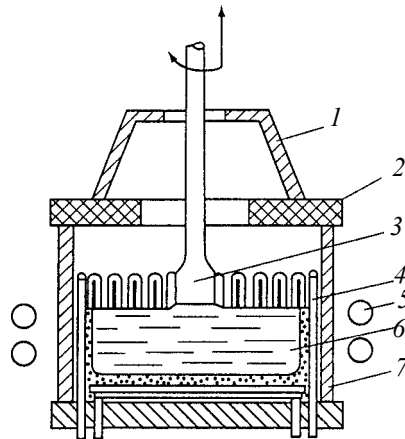
**Figure 5.1.** Schematic of a cold crucible for growing SrTiO$_3$ crystals [4,5]/ 1,2) heat screens; 3) growing crystal; 4) cold crucible; 5) inductor; 6) melt; 7) quartz pipe.

gradients on the surface of the melt is the application of thermal screens which were used successfully in [4,5] in the growth of crystals of strontium titanate. The diagram of the thermal section for the growth of crystals is shown in Fig. 5.1. The cold crucible is accurately centered in relation to the induction coil and the thermal screens are positioned in such a manner that the thermal convection flows on the surface of the melt converge in the centre, forming a melt spot with a slightly reduced temperature. The melt temperature is regulated by the variation of the power supplied to the melt by the high-frequency generator. The stability of generator power is ensured by stabilising the anodic current of the generator lamp.

A further development of the method of growth of crystals from the cold crucible by the Czochralski method is the combination of direct high-frequency melting with radiation heating of the surface of the material [6,7]. The diagram of equipment for this process is shown in Fig. 5.2. Powerful optical concentrators with arc xenon lamps as light sources are used for starting heating. Equipment provides for vertical displacement and rotation of the crucible. The presence of the light sources makes it possible to control the configuration of the thermal fields in the melt by varying the distance of the focal spot from the axis of rotation of the crucible and by regulating of the power of the light flux. In order to reduce the temperature gradients in the growing crystals, and also for subsequent annealing, a platinum electrical resistance furnace and
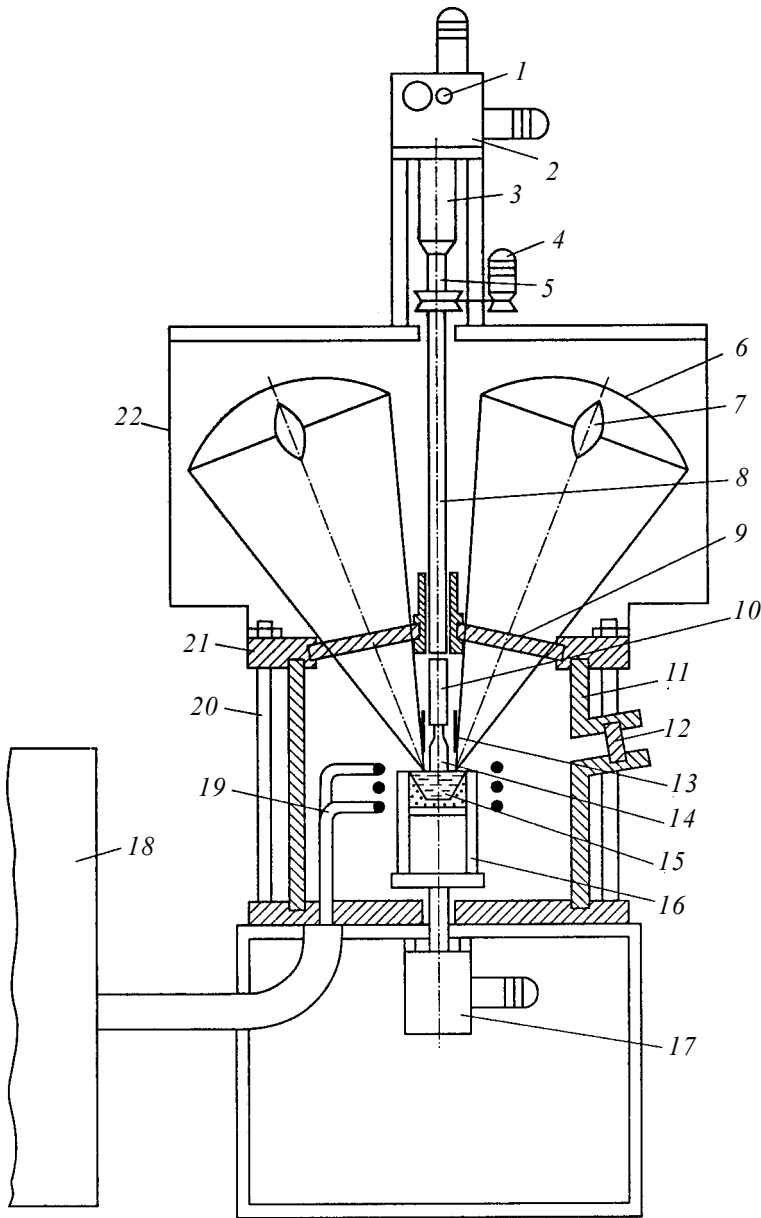
**Figure 5.2.** Principal diagram of equipment for growing single crystals by the Czochralski method with combined HF and radiation heating [6,7]. 1) changeable reductor; 2) drive of the upper rod; 3) coupling; 4) drive for rotating the upper rod; 5) magnetic coupling; 6) elliptical reflector; 7) source of light radiation; 8) upper rod; 9) quartz glass; 10) seed holder; 11) chamber; 12) quartz window; 13) annealing furnace; 14) crystal; 15) melt; 16) cold crucible; 17) drive for the lower rod; 18) HF oscillator; 19) inductor; 20) pin; 21) chamber lid; 22) jacket.

heat screens made of aluminium oxide are placed above the melt.

In the investigated system, the presence of radiation heat sources at the effective ratio of the powers of the high-frequency fields and light radiation makes it possible to produce thermal fields in the melt for stable growth of the crystals on a seed. The experimental results show that convection becomes the dominant mechanism of heat transfer in the melt. Changing the direction of movement of the melt flows, it is possible to control the configuration of the thermal fields and the shape of the solidification front. However, it should be mentioned that the control of the heat flows in order to obtain the required structure of the thermal fields remains the most complicated process and further work is required to solve this problem.

One of the first crystals grown successfully by drawing on a seed crystal from a cold crucible were leucosapphire and ruby crystals [8]. The process of growth of these crystals from the cold crucible is controlled by: 1. Relatively low electrical conductivity of the $Al_2O_3$ melt; 2. The low viscosity of the melt; 3. The high solubility of gaseous oxygen in the melt, and 4. High heat conductivity of solid corundum. The first two features lead to the formation of a fluctuating convection pattern, associated with the variation of temperature at the solidification front. The third specific feature leads to the release of oxygen at the liquid–solid interface of the oxygen-saturated melt. Hence, even the smallest fluctuation of temperature, small oxygen bubbles are trapped by the growing crystals and form light-scattering inclusions.

The high heat conductivity of corundum, on the one hand, is favourable for supports stable growth of the crystal because it ensures rapid removal of heat and prevents tangential growth. On the other hand, rapid removal of heat from the melt through the skull to the walls of the cold crucible resulting in the spatial instability of the interface between the melt and the skull and requires extensive superheating of the melt. Therefore, to ensure stable long-term growth of the sapphire and ruby crystals, it is necessary to use crucibles and induction coils shown in Fig. 3.2b. This configuration of the crucible results in uniform heating of the melt not only from the side but also from the bottom. Figure 5.3 shows the photograph of a sapphire crystal growing from the cold crucible. The diameter of the crystal was regulated by changing the position of moving screens, situated above the melt. The rate of withdrawal was 10–30 mm/h, the speed of rotation was varied in
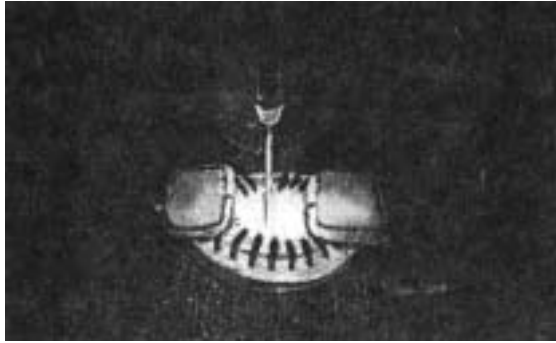
**Figure 5.3.** Photograph of a growing sapphire crystal [8].

the range 20–140 rpm. In cases in which the convection pattern greatly fluctuated, it is necessary to employ the planetary rotation of the crystals. In this type of rotation, the crystals intersect a large number of areas with different temperatures which are averaged-out at the solidification front. In this case, there is no capture of the oxygen bubbles. In these crystals, the solidification front is almost completely flat.

This method was used to produce single crystals of leucosapphire and ruby with different orientations, up to 160 mm long, with a diameter of up to 35 mm. The grown crystals were characterised by special features determined by the features of preparation.

The density of dislocations in the basal plane was $10^2$–$10^3$ cm$^{-2}$. The flat solidification front resulted in the uniform radial distribution of chromium atoms in the ruby crystals. However, the distribution of chromium along the length of the crystals was non-uniform, the chromium concentration decreased during drawing. This was associated with the evaporation of chromium oxide from the overheated melt in superheating. The concentration of chromium along the length of the crystal was equalised using the programmed 'saturation' of the melt with chromium oxide powder from a special hopper.

## 5.2. DIRECTIONAL SOLIDIFICATION OF THE MELT IN A COLD CRUCIBLE

In most cases, single crystals are produced from the cold crucible by the directional solidification of the melt. This preference is associated with the relatively simple procedure of the method because it does not require an additional heating source and

complicated design features of the thermal section.

As already mentioned, the method is based on the production, by means of direct high frequency heating, of a relatively large volume of the melt in a cold crucible with subsequent solidification at a specific rate. Crystallisation can be initiated most efficiently by lowering the crucible with the melt in relation to the induction coil. With exit of the lower part of the melt from the induction coil, the efficiency of coupling of this part with the high-frequency field decreases and, consequently, less power is supplied to the melt. The crystallisation process takes place as a result of gradual cooling of the bottom part of the melt. Less frequently, the melt is cooled by a programmed decrease of the generator power. However, the latter method is less reliable because it may result in the formation of a spatial instability and uncontrolled solidification of the melt. Consequently, the solidification method is only suitable for melts characterised by high stability in relation to the variation of the temperature of the melt which is determined by its physical–chemical properties [9].

In comparison with other methods of preparation of refractory single crystals (Verneuil method, zone melting), the method of directional solidification in the cold crucible has a number of advantages. The large volume of the melt facilitates convective mixing of the matter and impurities during growth. Crystals can be grown in any atmosphere. In addition to this, the open surface of the melt makes it possible to regulate the composition of the melt by adding components and also supports the removal of highly volatile impurities and gases from the melt.

However, the method has also shortcomings. The most important shortcoming is that it is not possible to examine visually and control the crystallisation process by measuring the temperature of the melt and the crystal directly during growth. The possibility of regulating the melt temperature in a relatively wide range by regulation of the power supplied to the melt is relatively limited because it is determined by the conditions of equilibrium and stability of the phase boundary [8,10]. In addition to this, it is not possible to anneal and cool to room temperature the crystal immediately after growth without using additional heating devices.

The feasibility of using the method for the growth of single crystals of refractory oxides is determined by the physical–chemical properties of the materials in the melt and the solid phase. In particular, this relates to the materials whose high melting point and

corrosive effect do not make it possible to select a suitable crucible material.

The possibility of application of the examined method also depends on the electrical and thermophysical properties of the material. They determine the very possibility of the formation and stable maintenance of the melt, as already mentioned in Chapters 1 and 2. For example, to ensure a stable process, a low conductivity of the solid phase of the material is desirable. High rates of evaporation of the components of the melt may become a reason for a decrease in the volume of the melt and this may also disrupt the stability of the system and of the crystallisation process. The volatility of the individual components also disrupts the stoichiometry of the grown crystals. In this case, it is necessary to correct the composition of the melt or use an atmosphere preventing evaporation.

In most cases, a cold crucible consists of several sections, separated by small gaps. When the skull is melted through the crucible melt may be poured out thus disrupting the process of growth of the crystals. Pouring out of the melt depends on the surface tension of the melt, the width of the gap between the sections and the forces of molecular bonding of the melt with the material of the crucible wall. Consequently, it is necessary to use melts with a relatively high viscosity.

The directional solidification of the melt in the cold crucible greatly differs from the growth of crystals in a conventionally heated crucible, for example, by the Bridgman method. Firstly, this is associated with the existence of a skull layer on the water-cooled sections of the crucible with which the melt is in contact; secondly, it is linked with the specific distribution of temperature inside the cold crucible which is determined by the absorption of the HF power directly in the melt and the directional heat removal from the solidification front to the cold walls of the crucible.

These special features will now be discussed in greater detail. As a result of directional crystallisation of the melt in a cold crucible without the application of special seed crystals, one obtains ingots consisting of a large number of crystals. The design of the cold crucible does not restrict the amount of nuclei formed. However, during growth, the number of these crystals decreases as a result of selection on the basis of the growth rate. Competition of this type results in the survival of crystals in which the direction of 'rapid' growth is close to the normal to the solidification front. In

this case, the crystals in the ingot are elongated and distributed parallel to each other, forming a columnar structure. Attempts have been made to use seed crystals. However, difficulties in controlling the melting of the charge and the absence of any means of checking that the 'seed' has not melted, make this process unreliable. Thus, the number and, correspondingly, size of the crystals depend on the composition of the melt and growth conditions.

The growth of large and high-quality crystals is based on solving problems of controlling temperature and its gradients in the melt and the solid phase. Therefore, the distribution of temperature fields in the cold crucible is extremely important. However, as already mentioned, high temperatures (>2000°C) and the high-frequency field prevent direct measurement of the melt temperature by contact methods. Only the radiation method can be used in the present case, i.e. in the growth process only the temperature of the melt surface can be measured. The qualitative pattern of the radial distribution of temperature in a viscous glass melt was indicated in [11]. In [12], temperature fields in an oxide melt upon direct high-frequency heating were experimentally studied, and the effect of several technological factors on the temperature distribution was also investigated. This melt is characterised by high viscosity and relatively low-temperature (≈1500°C) and the results of the experiments provide a characteristic pattern of the temperature field in the melt in which the energy of the high-frequency field is directly converted into thermal energy.

Figure 2.7 shows the distribution of temperature in a melt for different positions of the induction coil in relation to the surface of the melt and the variation of the absorbed power. It may be seen that by changing these parameters it is possible to form efficiently the temperature fields in the volume and on the surface of the melt. The nature of the temperature distribution, shown in Fig. 2.7, is in agreement with the results published in [13] in which the conditions of crystallisation are linked with the distribution of the components of the $ZrO_2$–$Y_3O_3$ solid solution and defects affecting the optical homogeneity of these single crystals. The pattern of the temperature distribution in the melt (Fig. 2.7) explains qualitatively the mechanism of formation of these defects and is in agreement with the experiments carried out on a modelling melt [12].

Very high melt temperatures in the growth of the crystals by the method of the cold crucible result in large thermal losses from the

surface of the melt. Intensive radiation heat removal from the surface of the melt results in the formation of a layer of the sintered charge whose presence has a positive effect decreasing the heat losses and increasing the stability of the solidification process [14, 15]. However, when correcting the composition of the melt in the growth process, the sintered layer prevents the pouring of the charge on the surface of the melt. Mechanical failure of this layer reduces the stability of the equilibrium of the melt–crystal system and has a negative effect on crystal growth. A screen-reflector has been proposed for reducing this undesirable effect, Fig. 3.2, which prevents the formation of a 'roof'' above the melt surface and which reduces the heat losses due to radiation of the melt.

The method of directional solidification has been used for growing a large number of single crystals of simple and complicated oxides and also solid solutions based on them (see Table 5.1). The most successful application of this method is the synthesis of a new class of single crystals – fianites (cubic zirconia). The technology and properties of this material are described in detail in Chapter 7. The first reports on the production of the single crystals of zirconia with a size of several millimetres using the cold crucible methods were published in [16,17]. At the same time, Russian investigators produced large single crystals of different compositions with a number of applications in practice. This technology is used extensively throughout the world and has stimulated the application of the method of direct high-frequency melting for the growth of other single crystals.

In addition to the crystals based on $ZrO_2$ and $HfO_2$, this method has been used successfully for the production of large crystals of oxides of transition elements [18–20] and for growing a large number of complex oxides [8, 10, 20–23]. Investigations of the oxides of the transition elements show that, at high temperatures, many of these elements are characterised by the electrical and thermophysical properties that permit efficient heating by high-frequency current, melting, maintenance in the molten condition and solidification of the melt in the cold crucible. The cold crucible method has been used for growing, in the air atmosphere, crystals of CoO, $Fe_2O_3$ and $TiO_2$ with a volume of up to 3 $cm^3$ [19]. The colour of produced $TiO_2$ crystals indicates a disruption of stoichiometry with respect to oxygen which, however, is completely restored by annealing at temperatures of 1000–1300°C in an oxygen atmosphere.

**Table 5.1.** Single crystals grown from a cold crucible

| Material | $T_m$, °C | Methods and growth parameters* | Crystal dimensions |
|---|---|---|---|
| $Al_2O_3$ | 2046 | Czochralski method, crucible with heated bottom<br>$D_c$ = 80 mm,<br>$V_g$ = 10÷30 mm/h<br>$V_r$ = 20÷140 rpm<br>Directional solidification | Diameter<br>$d$ = 10÷35 mm<br>length $l$ = 160 mm<br><br>Several millimetres |
| $TiO_2$ | 1855 | Directional solidification<br>$W$ = 60 kW, $f$ = 5.28 MHz<br>$D_T$ = 50÷80 mm, air | Volume 1-3 cm³ |
| $Fe_3O_4$ | 1560 | Directional solidification<br>$W$ = 60 kW, $f$ = 5.28 MHz<br>$D_T$ = 50÷80 mm, air<br>$W$ = 20 kW, $f$ = 3 MHz<br>$D_T$ = 60÷85 mm, CO/CO$_2$<br>(flow-through) | Volume 1-3 cm³<br>Columnar crystals<br>$l$ = 2 mm |
| $M_{1-x}O$<br>(M = Mn, Co,<br>Fe, Ni) | ~2000 | Directional solidification<br>$W$ = 20 kW, $f$ = 3 MHz,<br>$D_T$ = 60÷85 mm, CO/CO$_2$<br>(flow-through), $V_p$ = 7.5÷15 mm/h | Columnar crystals<br>$l$ = 1 cm |
| CoO | 1805 | Directional solidification<br>$W$ = 60 kW, $f$ = 5.28 MHz,<br>$D_T$ = 50÷80 mm, air | Volume 1-3 cm³ |
| $CeO_2$ | 2700 | Directional solidification<br>$W$ = 60 kW, $f$ = 5.28 MHz,<br>$D_T$ = 50÷80 mm, air | Volume 1-3 cm³ |
| $Pr_2O_3$ | 2250 | As above | Plate-shaped crystals |
| $Nd_2O_3$ | 2300 | As above | $l$ = 1.5 mm |
| $Sc_2O_3$ | 2405 | Directional solidification | Several millimetres |
| $Y_2O_3$ | 2410 | Czochralski method | Volume 1-3 cm³ |
| $Cd_2O_3$ | 2395 | As above | As above |
| $Er_2O_3$ | 2400 | As above | " |
| $ZrO_2(HfO_2)$-(8-50%)<br>MgO, CaO,<br>SrO, Sc$_2$O$_3$, | - | Directional solidification<br><br>$W$ = 20 ÷ 160 kW, $f$ = 0.44;<br>1.76; 5.28 MHz, air | Mass < 2 kg |

| Material | $T_m$,°C | Methods and growth parameters* | Crystal dimensions |
|---|---|---|---|
| $Y_2O_3$, $Ln_2O_3$ | | $V_p = 1 \div 40$ mm/h | |
| $Fe_3O_4$-<br>$Fe_2TiO_4$ | - | Directional solidification<br>$W = 20$ kW, $f = 3$ MHz<br>$D_T = 60$; 85 mm, $CO/CO_2$ | Columnar crystals<br>$l = 1$ cm |
| $CaTiO_3$ | 1970 | Directional solidification | Columnar crystals |
| $CaWO_4$ | 1560 | $W = 60$ kW, $f = 5.28$ MHz | $5 \times 5 \times 10$ mm |
| $BaWO_4$ | 1490 | $D_T = 80$; 120 mm, air,<br>$V_p = 1 \div 10$ mm/h | |
| $SrTiO_3$ | 1910 | As above<br>Czochralski method<br>$D_T = 130$; mm, air,<br>$V_p = 5 \div 10$ mm/h<br>$V_{BP} = 40 \div 60$ rpm | As above<br>$d = 15$ mm<br>$l = 30$ mm |
| $Ln_2Ti_2O_7$<br>(Ln = Sc, Y,<br>La, Nd, Sm,<br>Eu, Dy, Tb,<br>Gd, Ho, Er,<br>Yb) | 1600-<br>1900 | Directional solidification<br>$W = 60$ kW, $f = 5.28$ MHz<br>$D_T = 80$; 120 mm, air,<br>$V_p = 1 \div 10$ mm/h | 2-12 mm |
| | | Czochralski method | $d = 3$ mm<br>$l = 8$ mm |
| $Ln_2NiO_4$<br>(Ln = La, Pr,<br>Nd) | - | Directional solidification<br>$W = 20$ kW, $f = 3$ MHz<br>$D_T = 60$; 85 mm, $CO/CO_2$ | $4 \times 4 \times 6$ mm |
| $LaCrO_3$ | 2430 | Directional solidification | Needle crystals |
| $YCrO_3$ | 2290 | | |
| $ErCrO_3$ | 2300 | $W = 60$ kW, $f = 5.28$ MHz<br>$D_T = 80$; 120 mm, air, | $1 \times 1 \times 10$ cm |
| $Y_3Al_5O_{12}$ | 1930 | Directional solidification | Several millimetres |
| $Sc_2Zr_2O_7$ | 2700 | As above | As above |
| $Bi_{12}GeO_{20}$ | 930 | Czochralski method<br>$W = 5$ kW, $f = 1 \div 10$ MHz,<br>$V_p = 1 \div 150$ mm/h<br>$V_{BP} = 0 \div 100$ rpm | $d = 20$ mm<br>$l = 70 \div 80$ mm |
| $MnZnFe_2O_4$ | - | Czochralski method with<br>additional light heating | $d = 10 \div 17$ mm<br>$l = 100$ mm |

| Material | $T_m$, °C | Methods and growth parameters* | Crystal dimensions |
|---|---|---|---|
| $Nd_3Ga_5O_{12}$ | - | Czochralski method $W_1 = 100$ kW, $f_1 = 1 \div 7$ MHz, $W_2 = 75$ kW, $f_2 = 7 \div 10$ kHz, $D_T = 80$ mm, $V_p = 4$ mm/h $V_{BP} = 0 \div 100$ rpm | $d = 35$ mm $l = 92$ mm |
| Si | 1417 | Czochralski method $f = 470$; $250 \div 400$ kHz, $D_T = 31$; 75 mm, argon, $V_p = 12 \div 168$ mm/h | $d = 15$ mm $l = 25$ mm |

*Growth parameters: power of HF generator $W$, frequency $f$, crucible diameter $D_T$, atmosphere, growth rate $V_p$, speed of rotation of the seed $V_r$

Up to the present time, high-quality crystals of magnetite $Fe_3O_4$ have been efficiently grown by the Bridgman in platinum crucibles. However, this method is expensive, because after growth, the crucible must be sectioned in order to release the crystal and, in addition to this, iron diffuses into platinum and disrupts this metal. Consequently, the method of direct high-frequency melting has a number of obvious advantages in this case. From the viewpoint of the retention of the stoichiometry of magnetite with respect to oxygen, it is important to create an oxygen-enriched atmosphere in the solidification chamber and control its composition. A $CO/CO_2$ buffer mixture has been used for this purpose. The process of crystal growth consists of two stages. The first stage consists of the production of the required volume of the melt in air, and the second stage is the evacuation of the solidification chamber and passage of the gas mixture through the chamber. The melt is held in this atmosphere for 90 min, in order to establish equilibrium and, subsequently, the crucible is lowered. In order to retain the equilibrium of the melt with the solid and gas-forming phases, the rate of growth is reduced to 7.5 mm/h, this also increases the size of the crystals.

In the cold crucible, it is also possible to grow successfully crystals of oxides of transition metals $Mn_{1-x}O$, $Co_{1-x}O$, $Fe_{1-x}O$ and $Ni_{1-x}O$ [20], characterised by interesting electrical, optical and magnetic properties. Equipment for the growth of single crystals in the cold crucible was the same as in the previous case. As a result of examination of the effect of the atmosphere used for the growth process on the phase composition of the single crystals it was

established that the presence of the inclusions of $M_3O_4$ is associated with a surplus of oxygen in the melt. In a reduction atmosphere, the oxide is reduced to metal. The investigations [20] also showed the significant role of the subsolidus annealing of the crystals which improves the homogeneity of the crystals and results in the complete disappearance of the $M_3O_4$ phase.

After selecting a suitable buffer oxygen atmosphere, single crystals of titano-magnetite $(Fe_3O_4)_{1-x}(Fe_2TiO_4)_x$ were grown in the chamber. The size of the crystals reached 1 cm$^3$ [21,24]. The atmosphere was controlled throughout the process, including melting. Examination of the phase composition of the crystals grown in different atmospheres showed that this method is suitable for producing single crystals of ferrites of complicated composition. In addition to the previously mentioned groups of materials, the same equipment and procedure was used for the growth of crystals of $Ln_2NiO_4$, where Ln = La, Pr, Nd [23].

The above examples of the growth of single crystals by directional solidification in the cold crucible show that the method is highly promising. As an example, Table 5.1 shows the far from complete list of the single crystals, produced by the cold crucible method.

In many cases, the application of single crystals depends greatly (and in some cases almost completely) on their geometrical dimensions, the shape, the homogeneity of the optical, mechanical and other properties in the volume of the crystal. The simplest method of increasing the size of the crystals grown by solidification from the melt and of increasing their homogeneity is to increase the volume of the solidifying melt. However, this method has its limitations determined by the possibilities of processing equipment and economic efficiency. In addition to this, the increase of the volume of the melt on its own does not solve the problem of producing single crystals of the required shape and dimensions and the reproducibility of the growth process.

Another method of increasing the size and improving the quality of single crystals is the formation of the optimum conditions for crystal growth. However, the solution of these problems is made more complicated by the shortcomings typical of the cold crucible method, with the main disadvantages being the fact that it is not possible to examine visually the process of melting and solidification, and the absence of reliable methods for obtaining complete information on the state of the melt directly during the

solidification process. In order to control the process, it is necessary to determine the dependence of the condition of the melt on the operating conditions of the high-frequency generator.

Both examined directions of the development of directional crystallisation in the cold crucible supplement each other in terms of increasing the size and improving the quality of crystals. However, only the second direction results in a principal improvement of the method and offers extensive possibilities for producing large crystals in the automatic regime.

A special feature of the process of directional solidification in the cold crucible is that, with lowering of the crucible with the melt in relation to the induction coil, the block of the crystals grows. For crystal technology, it is interesting to investigate the technological factors affecting the number, size and shape of the crystals forming the block, *i.e.*, the block structure changes.

Initially, attention will be given to the effect of the shape of the solidification front on the structure of the block. In the cold crucible method, this factor is very important because the melt in the entire surface of the phase interface is in contact with the polycrystalline phase of the same composition. This surface contains ready solidification centres on which crystals begin to grow already in the stages of formation of the volume of the melt and its homogenising.

It is assumed that the crystals grow in the direction normal to the solidification front, and the boundaries between the crystals are also perpendicular to the solidification front. In the initial variant of the model, the phenomenon of displacement of some crystals by others is not taken into account. Under the given assumptions, the schema demonstrating the growth of a block of crystals in the cold crucible for different shapes of the solidification front is shown in Fig. 5.4*a, b, c*. The concave and convex solidification fronts (SF) are indicated by arcs of circles, and the flat front is indicated by a straight line. The solid lines indicate the initial state of the solidification front and the position in which the front is found a certain period of time after the start of crystal growth. The dotted lines indicate the intermediate position of the solidification front during the crystal growth, with the radius of the curvature of the front remaining constant.

For a concave solidification front (Fig. 5.4*a*), the crystals nucleated on the side surface of the phase boundary grow into the volume of the melt during lowering of the crucible. The number of growing crystals consequently increases and the cross sections of

the crystals decrease. The block forms from the crystals grown both from the bottom of the crucible and on its side. In this case, all crystals grow in the final analysis to the upper surface of the melt.

If the solidification front is convex (Fig. 5.4*b*), the number of crystals growing from the bottom of the crucible decreases during growth an d the transverse dimensions of the crystals increase. The crystals, growing at the periphery of the front gradually reach the side surface of the phase boundary and stop to grow. Thus, not all the crystals that started their growth from the bottom of the crucible with the melt reach the upper surface of the block. In the final analysis, the block consists of two regions, *i.e.* the skull a region of the crystals, grown on the side surface prior to the start of lowering of the crucible, and the central region, consisting of crystals grown from the bottom during lowering of the crucible. In both cases, with the concave and convex solidification fronts, the growth of crystals is distorted. In the case of the concave solidification front, it is distorted in the direction of the surface of the melt, and in the case of the convex front, in the direction of the side wall of the crucible. In the presence of a flat solidification front (Fig. 5.4*c*) there is no bending of the axis of growth of the crystals and the number and size of the crystals remain constant. In the final analysis, the block consists of a cluster of parallel columnar crystals (Fig. 5.5).

In practice, the shape of the solidification front is more complicated as a result of the generation of heat directly in the melt in the vicinity of the crucible wall. The number and shape of the crystals formed in the entire solidification front may differ, but in every separate region the crystals grow in accordance with the previously examined cases. The shape of the solidification front may change as a result of the variation of thermal conditions during the growth process. For example, the front may be initially concave and gradually transform into flat and then into convex. Consequently, in addition to the change of the number and transverse dimensions of the crystals, there may also be extensive bending of the axis of growth of the crystal as a result of the effect of the sum of heat flows. In practice, it is always necessary to try to produce a flat or slightly convex solidification front.

Thus, the shape of the solidification front has a strong effect on the number and, consequently, the size of crystals in the grown block. With the concave solidification front, the lowering of the
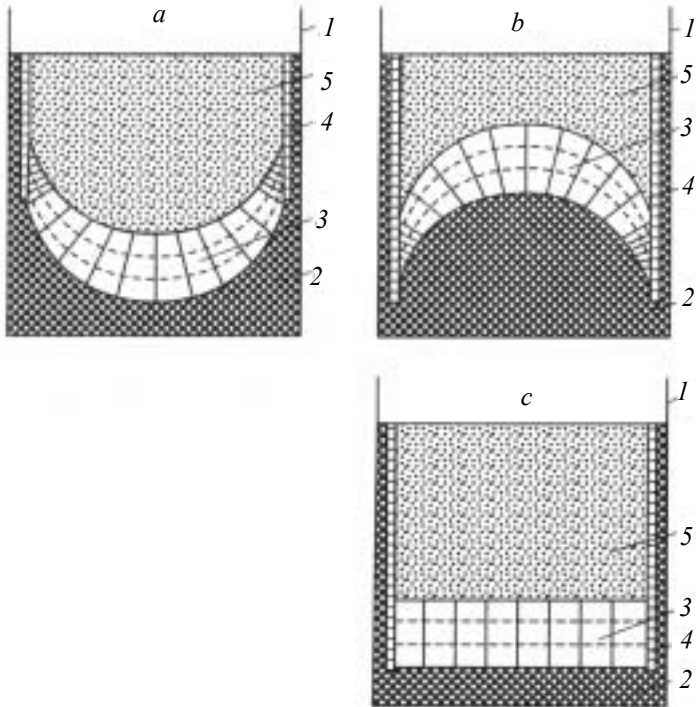
**Figure 5.4.** Growth of a crystal block in a cold crucible [18,25]. a) with the concave solidification front, b) with the convex solidification front, c) with a flat solidification front, 1) crucible, 2) skull, 3) crystals growing from the crucible bottom with the melt, 4) crystals growing from the side surface of the crucible with the melt, 5) melt.
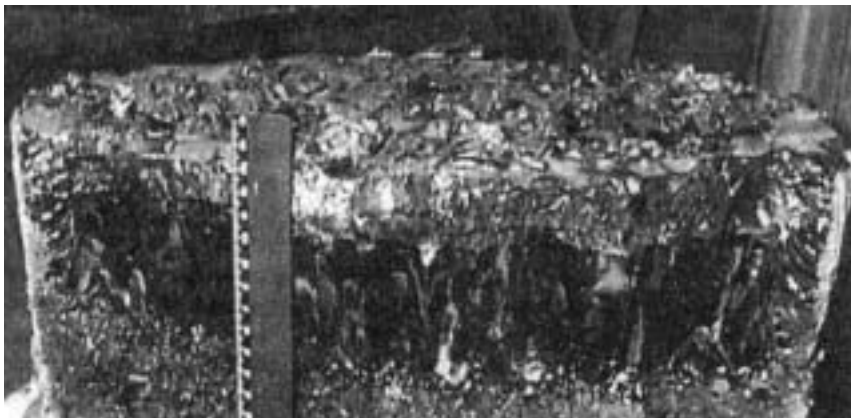


**Figure 5.5.** Block of crystals of cubic zirconia produced in a cold crucible.

crucible is accompanied by an increase in the number of growing crystals and in the case of a convex front, some of the crystals cease to grow as a result of the limited volume of the melt.

Previously, it was shown that if the boundaries between the crystals are oriented in the direction of heat transfer, then independently of the shape of the solidification front the crystals continue to grow until the crucible contains a melt. However, the transverse dimensions of the crystals decrease in this case. A second reason for the decrease in the transverse dimensions of the crystals may be the process of degeneration, associated with a deviation of the boundary between the crystals from the direction perpendicular to the direction of the solidification front. Degeneration is accompanied by a decrease in the transverse dimensions of only a part of the crystals which in the final analysis cease to grow, whereas the adjacent crystals increase in the transverse size (Fig. 5.6). Thus, the number of growing crystals in the block decreases and the dimensions of these crystals increases. Only some of the crystals nucleated on the bottom of the melt reach the upper surface of the block.

In the growth of cubic zirconium dioxide crystals it was established that one of the factor affecting the degeneration process is the degree of superheating of the melt in the stationary condition. The degree of superheating of the melt is determined by the density of the power generated in the melt in the stationary condition:

$$Q_{stat} = P_{m.stat} / M_{stat} \qquad (5.1)$$

where $P_{m.stat}$ is the power generated in the melt in the stationary state; $M_{stat}$ is the mass of the melt in the stationary condition. Parameter $Q_{stat}$ determines the level of superheating of the melt in the crystallisation process. In order to determine the effect of $Q_{stat}$ on the degeneration process, a number of experiments was carried out with the growth of $ZrO_2$ crystals stabilized with $Y_2O_3$ from melts at different values of $Q_{stat}$. These experiments were carried out using the measuring-calculation complex described in Chapter 2, controlling the state of the generator–load system. Consequently, it was possible to calculate the value of $P_m$ directly during the melting process and determine the value of $P_{m.stat}$ and also control the change of the melt volume. In order to ensure the reproducible crystallisation conditions, the dimensions of the crucible and the induction coil, the level of the load and the rate of lowering of the
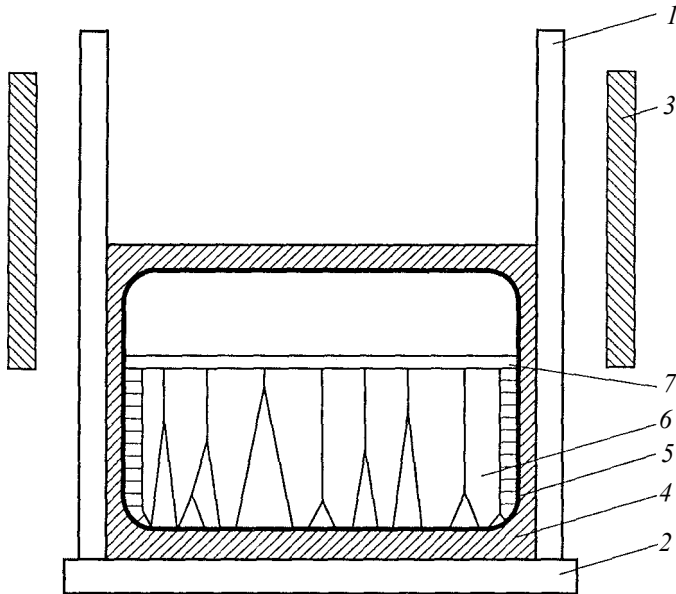
**Figure 5.6.** Cold crucible with a grown block of a cubic zirconia crystal [26]. 1) wall and 2) bottom of the cold crucible, 3) inductor, 4) charge, 50 solidified melt, 6) crystals growing from the bottom of the crucible with the melt, 7) the single crystal grown from the upper surface of the melt.

cruciblet, and also the purity of the charge were maintained constant in all experiments. In this case, the technological parameters were selected in such a manner that the solidifying melts where similar in the mass and the absorbed power of the melt $P_m$, and the bottom of the crucible was flat in order to eliminate the effect on the shape of the solidification front on the experimental results. In the crystallisation process, anodic voltage was stabilized. The values of $P_m$ and $P_{m.stat}$ in all experiments were varied in almost the same manner and at the end of the process the shape of the solidification front was distorted only slightly.

After completion of the growth process, the height of the block of the crystals was measured and the number of crystals starting to grow from the bottom of the crucible with the melt that reach the upper surface of the block was determined. The solidified melt was weighed and the value of $Q_{stat}$ calculated. In [25], to investigate the process of degeneration of part of the growing crystals, the number of these crystals was counted at different distances from the start of growth. In order to characterise the process of degeneration of crystals throughout the entire block, a
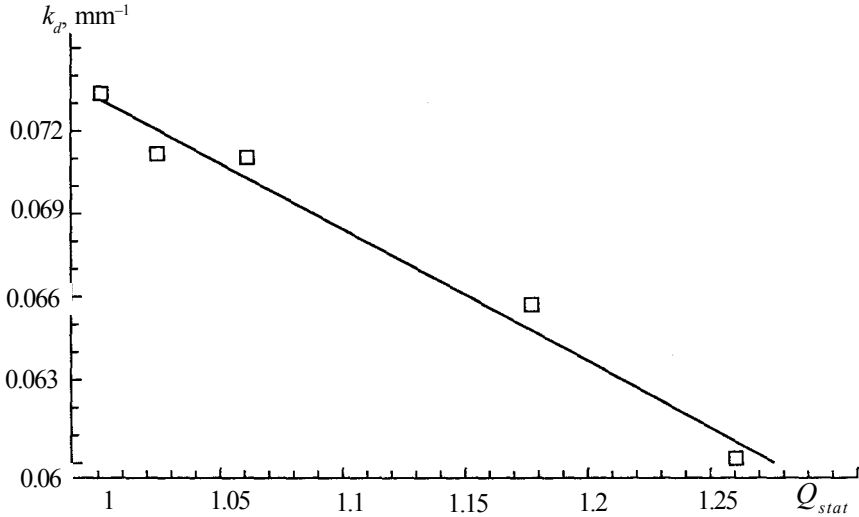
**Figure 5.7.** Dependence of the coefficient of degeneration on the density of power generated in the melt prior to the start of the solidification process [26].

generalised parameter, i.e. the degeneration coefficient, was introduced:

$$k_d = (n_1 - n_2)/n_2 h, \tag{5.2}$$

Here $n_1$ and $n_2$ are respectively the number of crystals which started to grow from the bottom of the crucible and the number of crystals which reached the upper surface of the block; $h$ is the height of the block of the crystals. This coefficient characterises the mean (with respect to height and radius) number of the degenerated crystals normalised to the unit height of the block per a single crystal that reached the upper boundary of the block. Parameter $k_d$ also characterises the mean angle of growth of the crystals, under the condition that degeneration takes place uniformly along height $h$. The larger $k_d$ increases, the larger the angle of growth of crystals.

Figure 5.7 shows the experimental dependence of $k_d$ on $Q_{stat}$ in relative units. The minimum value of $Q_{stat}$ differs from the maximum value by ~25%. It is evident that the application of the linear dependence as an approximating function is in agreement with the experimental data. Figure 5.7 also shows that the value of $k_d$ increases with decreasing $Q_{stat}$. The latter circumstance indicates

that for a lower degree of superheating of the melt the rate of degeneration is higher and the crystals are characterised by a larger growth angle.

A satisfactory explanation of the process of degeneration of cubic zirconia crystals with a flat solidification front may be provided on the basis of Tiller's theory [27]. According to this theory, grooves form at the boundary between the growing crystals. These grooves are formed by the surfaces of the boundaries of the crystals and, consequently, the free energy per unit volume in them is higher than in the sections of the crystal outside these boundaries. Consequently, the temperature of the liquid–solid phase transition inside the grooves is lower and the surface on which the crystals join has a lower temperature in comparison with the remaining interfacial surface and, consequently, a cavity forms between the crystals. The dimensions of the cavity depend on the temperature gradients in the melt and the solid phase and on the direction of growth of the contacting crystals.

According to Tiller's theory, the slope of the edges of the grooves depends on the orientation of crystals. The steepest slope is characteristic of a crystal oriented in the <111> direction in relation to the growth axis. Figure 5.8 shows two intergrown crystals, a bicrystal, with the misorientation of these crystals being the result of rotation around the axis of growth. The crystals were in the same growth conditions, but one of them had the interfacial surface in the plane <hkl> and the other one in the (111) plane. The distance $\delta x$ of the base of the groove of the <hkl> bicrystal in relation to the base of the <111> groove is the consequence of the wedge-shaped form of the <hkl> groove. The growth of the
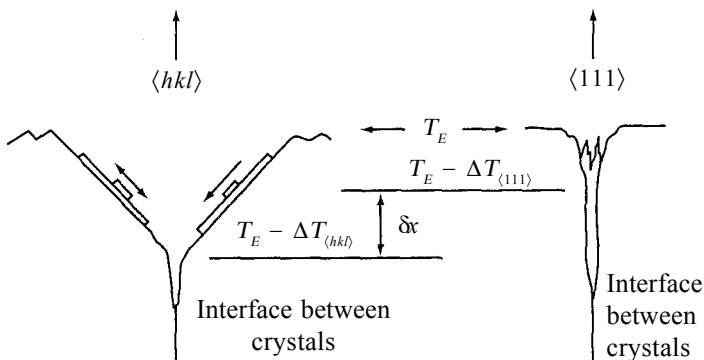


**Figure 5.8.** Bicrystals, formed in the same growth conditions: the orientation of the left crystal is <hkl>, of the right crystal <111> [27].
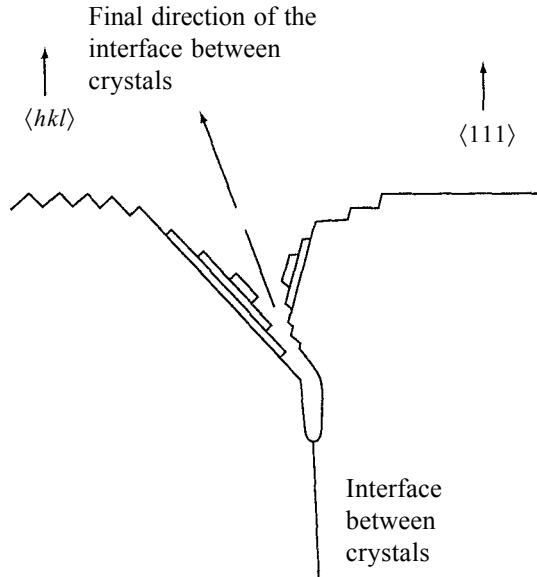
**Figure 5.9.** Bicrystal consisting of two crystals with the orientations *<hkl>* and *<111>*. The scheme indicates how the crystal *<111>* displaces the *<hkl>* crystal [27].

layers of the walls of the groove of this bicrystal occurs faster than the growth of the <111> layers of the crystal. This may take place if the mean temperature of the layers of the *<hkl>*-crystal is lower in comparison with that of the <111> crystal, because the rate of implantation of the atoms into the crystal lattice is a function of supercooling of the melt.

However, if the bicrystal forms from *<hkl>* crystal and <111> crystals, then the groove at the boundary of the crystals is asymmetric (Fig. 5.9). The normal growth of the layers on the walls of the groove results in the sagging of the <111> crystal above the *<hkl>* crystal. Thus, the <111> crystal will 'step' on the *<hkl>* crystal and in the final analysis will displace this crystal.

Taking into account this mechanism, an increase of $k_d$ with a decrease of $Q_{stat}$ may be explained as follows. A decrease of $Q_{stat}$ results in a decrease of the mean temperature of the melt and, consequently, in a decrease of the axial temperature gradient in the layer of the melt adjacent to the growing crystals. This in turn results in an increase in the depth of the groove by $\delta x$ (Fig. 5.9) and, consequently, the crystals with the preferential orientation displace the adjacent crystals which will result in their degeneration.

Detailed examination of the grown crystals shows that the grooves actually form at the boundary between the cubic zirconia crystals. They form either during rapid solidification of the remainder of the melt when the solidification front is exposed, or during the crystallisation of the melt when the single crystals, growing in the upper part of the melt in the direction from top to bottom, come into contact with the crystals growing from the bottom (Fig. 5.6). In this case, the front of growth of the crystals, growing from the bottom, 'imprints' on the lower surface of this single crystal, covering the entire surface of the melt. Figure 5.10 shows the photograph of a fragment of such a single crystal indicating the imprint of the groove. Figure 5.11 shows the cross-section of the upper crystal by the plane normal to the boundary between the crystals (the arrow indicates the point of joining of the crystals).
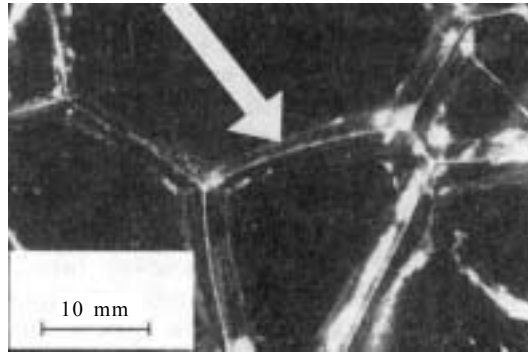


**Figure 5.10.** Photograph of the lower surface of the fragment of a single crystal grown from the surface of the melt. Prints of the grooves indicating elongated cavities with a rib along the joint line of two adjacent crystals can be seen [26].
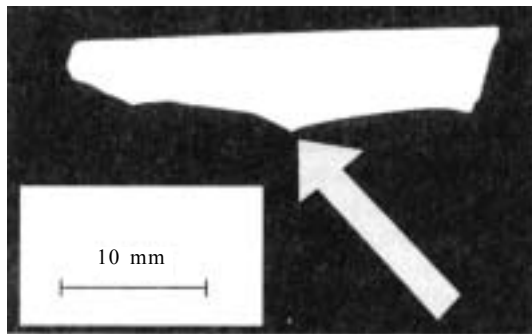


**Figure 5.11.** Photographs of the section of the upper single crystal in the vertical plane normal to the interface between two lower crystals. The arrow indicates the point of contact between the crystals [26].

Thus, the experiments show that in the growth of crystals in the cold crucible by the method of directional solidification with a flat solidification front, the process of degeneration takes place by the mechanism proposed by Tiller [27]. On the basis of this theory, it is also possible to explain the increase of the transverse dimensions of the crystals with a decrease of the rate of growth [27] or a decrease of these dimensions with an increase in the content of impurities in the melt. If the content of the impurities in the melt is insufficient for achieving concentrational supercooling resulting in the formation of a cellular structure, the interfaces between the crystals play the role of a sink of impurity atoms and supercooling in the groove is released. The deposition of the impurities, in particular $Al_2O_3$, on the side surfaces of the cubic zirconia crystals was reported in [28]. The (111) planes trap the impurities and keep them at the base of the groove consequently delaying their growth and resulting in complete interruption of growth at a specific impurity concentration. Consequently, the groove becomes deeper because of the poisoning of the (111) planes by the impurities thus preventing their sagging above the *<hkl>*-crystal. In this case, displacement is less intensive or is completely interrupted.

The effect of the power supplied to the melt on the process of degeneration of the crystals was investigated in [25]. The results show that in the examination of the process of degeneration on the basis of Tiller's theory, a decrease of the power generated in the melt results in a decrease of the mean temperature of the melt and, consequently, in a decrease of the axial gradients at the solidification front thus resulting in an increase in the depth of the groove between the growing crystals and supporting the degeneration process. A decrease of the growth rate also increases the size of the crystals causing their degeneration [27, 29]. From the viewpoint of Tiller's degeneration theory, the ratio of the rate of displacement to the rate of growth in the axial direction in the case of low growth rates is higher and the efficiency of displacement should be higher.

The size of the crystals is also affected by the volume of the cold crucible. In large crucibles (diameter > 200 mm), it is possible to grow larger crystals [30]. In small cold crucibles (diameter ~90–100 mm) it is necessary to superheat the melt in order to maintain it in the crucible because the ratio of the area of the cooling surface to the volume of the melt increases. Superheating has also a detrimental effect on the shape of the solidification front and on the degeneration conditions.

In addition to the technological conditions, the degeneration process is affected by the presence of secondary impurities and also by the type and concentration of the stabilizing oxide. It is well known that in the case of the directional solidification of multicomponent melts with the distribution coefficients of the components differing from 1 the component which decreases the crystallisation temperature is displaced into the melt and accumulated ahead of the solidification front (at $K < 1$). As already mentioned, the grooves at the boundaries between the crystals operate as sinks for certain impurities, decrease the rate of lateral growth of the crystals, increase the depth of the grooves and reduce (or completely interrupt) the degeneration process. The effect of several secondary impurities on the size and quality of single crystals will be considered in Chapter 7.

## 5.3. MODIFICATION OF THE PROCESS OF CRYSTALLISATION IN THE COLD CRUCIBLE

To grow crystals of neodymium–gallium garnet $Nd_3Ga_5O_{12}$, Mateika *et al* [31] have improved the method of the cold crucible introducing into the melt a bottom heater and an additional crucible immersed in the melt. A schematic of the modified cold crucible is shown in Fig. 5.12. A cylindrical crucible was produced from 40 water-cooled copper tubes. The bottom of the crucible consists of tubes spaced at 0.3 mm from each other and coated with metallic rhodium. A ring of aluminium oxide is used for maintaining the cylindrical shape of the crucible when the volume of the charge increases during heating. Springs are used for protecting the quartz sheet against failure during compensation of vertical pressure. The external appearance of the crucible with the water-cooled bottom, with the height and internal diameter of 120 mm, is shown in Fig. 5.13. The cylindrical induction coil, surrounding the crucible, was connected to a high-frequency generator operating in the frequency range (1–7) MHz. The maximum power of the generator was 100 kW. The second induction coil of the helical shape, situated below the bottom of the crucible, was connected to a 75 kW generator, operating at a frequency of 10 kHz. Inside the crucible there was an iridium ring placed on pins and resting on a quartz sheet. The iridium crucible, which will be referred to as the growth crucible, was suspended on a support in the upper part of the cold crucible. Its internal diameter is 80 mm and the crucible has a conical bottom
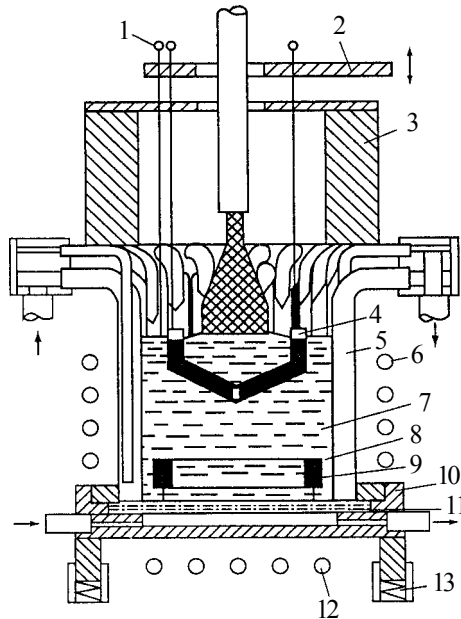
**Figure 5.12.** Schematic of a double crucible [31]. 1) detector of the melt surface;
2) crucible support; 3) thermal insulation; 4) growth crucible; 5) cold crucible; 6)
HF heater (1–7 MHz); 7) melt; 8) skull; 9) bottom heater; 10) quartz ring; 11)
quartz sheet; 12) HF heater (7–10 kHz); 13) shock absorbers.



**Figure 5.13.** External view of a double cold crucible [31].

with a hole in the centre. The walls of the crucible contain several diametrical slits. The support of the crucible moves in the vertical direction by means of an electric motor. An iridium feeler measures the lowering of the surface of the melt in the crucible during crystal growth by contacting the voltage source with the growth crucible. A ceramic tube in the upper part of the crucible decreases the extent of radiation losses. The iridium ring on the quartz sheet is heated with a field with a frequency of 8 kHz by an induction coil below the bottom of the crucible. As soon as a melt appears in the region of the ring, the field of the cylindrical induction coil with a frequency of 2 MHz is activated and the volume of the melt increases. When the free surface of the melt is produced, the melting stage is completed. The growth crucible is lowered into the melt and filled through the slits and the hole in its bottom section. The temperature of the melt during seeding of the crystal is regulated by controlling the power of the two generators. The growth process takes place by the well-known Czochralski method. The diameter of the growing crystal is controlled by regulating the power of the high-frequency generator, and the power of the generator at a low frequency is maintained constant. In the growth of the neodymium–gallium garnet, a gas mixture, consisting of 98% of nitrogen and 2% of oxygen, is continuously pumped through the chamber. During crystal growth, the detector continuously controls the level of the melt. The growth crucible is lowered using the mechanism for maintaining the level of the melt constant. When the required length is reached, the crystal is separated from the melt and withdrawn from the growth crucible. The generator power decreases to 0 during 10 hours.

The melts, heated directly by high-frequency currents, are characterised by a tendency for spontaneous solidification. This takes place if the volume of the melt decreases below the critical level required for coupling the high-frequency field with the melt. In order to prevent these effects, it is necessary to use the iridium ring (Fig. 5.12) situated at the bottom of the cold crucible. It is also used as a heating element at the start of the melting process. In subsequent stages, the hotter ring is used as an additional heating element in order to stabilize the required volume of the melt. This operation makes it possible to control the crystal diameter by changing the power supplied by the high-frequency generator. Thus, the melt remains stable throughout the entire process of crystal growth. Figure 5.14*a* shows the flow pattern on the surface of the

melt of the neodymium–gallium garnet prior to lowering the growth crucible into the melt. Examination shows small irregular bubbles moving in different directions. This indicates the presence of turbulent convection of the melt and the radial distribution of temperature with a minimum in the centre of the surface. The turbulent convection of the melt in the immediate vicinity of the growing crystal is an unexpected phenomenon observed when using the growth crucible. The melt inside this crucible is heated mainly as a result of the melt surrounding it. Only a small volume of the melt is poured out through the slits in the wall of the internal crucible. The application of the internal crucible creates suitable conditions for the growth of the crystal by the traditional Czochralski method and a regular pattern should form on the surface of the melt. Figure 5.14*b* shows the patterns of the flow lines in the growth crucible. The patterns, identical with those in Fig. 5.14*a*, were detected on the surface between the two crucibles, and inside the growth crucible the flows of a specific shape travelled into the centre of the melt. This clearly indicates the radial temperature gradient with a minimum in the centre. The hole in the bottom of the growth crucible is used as an output hole for the melt in order to ensure the stability of circulation of the melt from one crucible into another (Fig. 5.15). This disposition of the crucibles stabilises the circulation of the melt flows from the walls of the hotter crucible to the centre of the surface.

A significant special feature of this modified technology is the possibility of regulating the growth process. The height of the melt in the growth crucible is maintained constant as a result of the presence of a large volume of the melt in an external crucible. This is combined with the efficient restriction of the volume of the melt in the zone of the growing crystal. The proposed method also
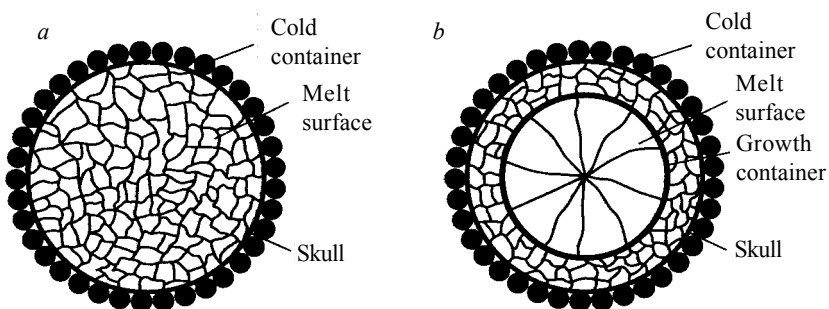


**Figure 5.14.** Schematic of the flow lines on the surface of a neodymium–gallium garnet melt [31]. a) without the growth crucible; b) with the growth crucible.
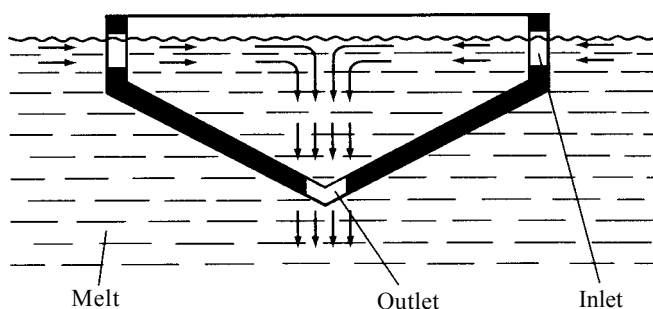
**Figure 5.15**. Forced convection of the melt inside the growth crucible [31].
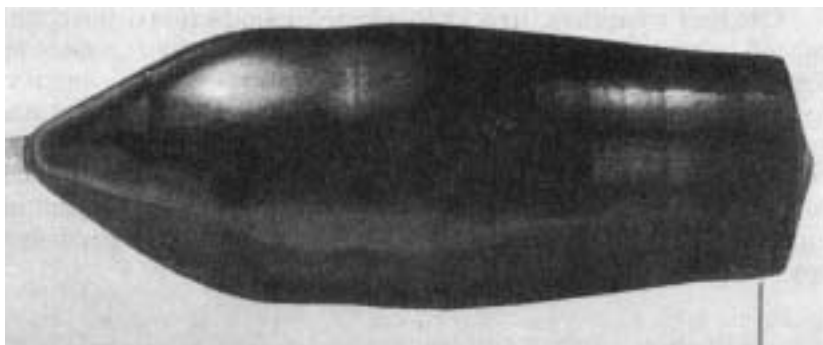


**Figure 5.16.** Neodymium–gallium garnet grown in a double crucible, scale 1 cm [31].

makes it possible to save noble metals. The iridum ring and the growth crucible are produced from sheet metal. Consequently, this technology has several advantages in comparison with the conventional method of growing large single crystals.

A single crystal of the neodymium–gallium garnet 92 mm long with a diameter of 35 mm was grown at a withdrawal rate of 4 mm/h, the speed of rotation was 10 rpm. The growth surface of the end part of the crystal was conical. The drawn crystal is shown in Fig. 5.16.

From the viewpoint of crystal technology, it is important to note that the proposed method is very complicated because the synchronisation of simultaneous operation of two high-frequency generators is a complicated technical task.

The presented review of the methods for growing single crystals from the cold crucible makes it possible to propose the most promising directions of further development of the method.

The method offers extensive possibilities of producing high-temperature non-metallic single crystals. The authors investigated

mainly the crystallisation of oxide materials, but the method is also used efficiently for a wide range of non-metallic, in particular refractory, materials, such as nitrides, carbides, and borides and others, and also standard crystals, produced by other methods, as well as new high-temperature compounds and solid solutions which cannot be produced by standard methods.

Undoubtedly, further investigations in this area will lead to the production of new interesting materials which will be used in different areas of science and technology. The most convincing example is the development of a new family of crystals, i.e. fianites (cubic zirconia).

It should be mentioned that the method of production of single crystals should be selected for each specific material taking into account the physical–chemical, electrophysical and thermal characteristics of the melt and the crystal. In this case, in addition to the already investigated methods (directional crystallisation, the Czochralski method), it is evident that special interest is attracted by the combination of the method of the cold crucible with growth methods such as the Stepanov method, growth from the solution in the melt, and other methods.

## References

1.  Ciszek T.F., *Cryst Growth*, 1984, Vol. 70, No. 1/2, 324–329.
2.  Wenckus J.F., Menashi W.P., Final technical report RADC-TR-82-171, Rome, Harsom. Air Develop. Cent., 1982.
3.  Kern E.L., Vaggy L.S., V$^{th}$ Amer. Conf. Crystal Growth, Abstracts. San Diego, 1981, 75–76.
4.  Aleksandrov V.I., Vishnyakova M.A., et al., *Izv. AN SSSR, Neorgan, Mater*., 1983, Vo.l. 19, No. 1, 104–107.
5.  Aleksandrov V.I., Barygov S.Kh., *ibid*, No. 2, 265–268.
6.  Balbashov A.M., Zavartsev Yu.D., *Tr. Leningrad Elektrotekhn. In-ta*, 1080. No. 455, 97–106.
7.  Egorov S.K., Zavartzev Yu.D., et al., Europ. Meeting Cryst. Growth 82, Mater. Electron. Abstr. Phaque, 1982, 205–206.
8.  Aleksandrov V.I., Osiko V.V., et al., *Usp. Khimii*, 1978, Vo. 47, No. 3, 385–427.
9.  Borik M.A., et al., Problems of crystallography, Nauka, Moscow, 1987, 165–189.
10. Aleksandrov V.I., Osiko V.V., Prokhorov A.M., Tatarintsev V.M., *Curr. Top. Mater. Sci*., 1978, Vol. 1, 421ª480.
11. Scott B., Rawson H., *Glass Technol*., 1973, Vol. 14, No. 5, P. 115–124.
12. Aleksandrov V.I., Blinov A.L., et al., *Izv. AN SSSR, Neorgan. Mater*., 1983, Vol. 19, No. 3, 443–447.
13. Aleksandrov V.I., et al., *ibid*, 1980, Vol. 16, No. 1, 99–104.

14. Marchall R.C., Larkin J.J., Armington A.F., Abstracts of Fourth Amer. Conf. on Crystal Growth, Gaitherburg, 1978, 66–67.
15. Petrov Yu.B., Induction melting of oxides, Energoatomizdat, Leningrad, 1983.
16. Michel D., Perez-Y-Jorba M., Collonques R., C. r. Acad. sci., 1968,Vol. 266, No. 23, 1602–1604.
17. Roulin Y., Vitter G, Deportes C., *Rev. Intern. Haut. Temp. et Refract.* 1969. Vol. 6, N 3, P. 153-158.
18. Harmon H.R., Aragon R., *Mater. Res. Bull.* 1978, Vol. 13, No. 11, P. 1097–1104.
19. Melekh B.T., Andreeva A.A., et al., *Izv. AN SSSR, Neorgan. Mater.*, 1983, Vol. 18, No. 1, 98–101.
20. Harrison H.R., Aragon R., Sandberg C.J., *Mater. Res. Bull.*, 1980, Vol. 15, No. 5, 571–580.
21. Harrison H.R., Aragon R., IV$^{th}$ Amer. Conf. Crystal Growth, Abstracts. Gaithersburg, 1978, 64–65.
22. Ershova L.M., Ignate'v B.V., et al., *Izv. AN SSSR, Neorgan. Mater.*, 1972, Vol. 13, No. 11, 2042–2945.
23. Buttrey D.J., Harrison H.R., Honig J.M., Schartman R.R., *J. Solid State Chem.*, 1984, Vol. 54, No. 3, 407–413.
24. Aragon R., Harrison H.R., McAllister R.H., Sandberg C.J., *J. Cryst. Growth*, 1983, Vol. 61, No. 2, 221–228.
25. Khaneev R.P. Development of a method for controlling and investigating processes of direct high-frequency melting and directional crystallization, Dissertation, Moscow, 1994.
26. Osiko V.V., Penyaz D.L., Khaneev N.P., *J. Cryst. Growth*, 1993, Vol. 128, 1193–1196.
27. Tiller W.A., *J. Metals*, 1957, Vol. 9, 847–855.
28. Lomonova E.E., Production and investigation of single crystals of solid solutions based on $ZrO_2$ and $HfO_2$, Dissertation, Moscow, 1980.
29. Aleksandrov V.I., et al., A method for producing single crystals based on solid solutions of refractor oxides, Author's Cert. 1048857, USSR, Publ. 15.06.1983.
30. Aleksandrov V.I., et al., A method for producing single crystals based on stabilised zirconia, Author's Cert. No. 1365739, USSR, Publ. 08.09.1987.
31. Mateika D., Laurien R., Liehr M.J., *Cryst. Growth,* 1983, Vol. 65, No. 1/3, 237–242.

# 6

# Production of refractory and special purity glasses

## 6.1. ELEMENTS OF GLASS PRODUCTION TECHNOLOGY

Glass is one of the most important artificial materials, used in various areas of science and technology. The range of application of glasses is continuously widening. The formation and development of branches such as quantum electronics, radioelectronics, missile and nuclear technology, semiconductor of physics, fibre optics, etc, has greatly widened the area of application of glasses. This has resulted in the development and production of new types of glass. They include laser glasses, activated with rare-earth ions; electric vacuum glass; semiconductor halide glasses; glasses transmitting or absorbing x-radiation, gamma radiation and also neutrons; glass-crystalline materials whose strength is considerably higher than the strength of commercial glass and can withstand steep temperature gradients; special purity glasses for fibre optics communication lines, and many other types.

The production of glasses of complicated composition, 'unsuitable' for the commercial technology of glass boiling, and also the increase in the requirements on optical homogeneity and chemical purity of glass present continuously new tasks to technologists such as, for example, the production of glasses with very high melting points and special-purity glasses.

High-temperature glasses, whose synthesis temperature is higher than 1600°C, are characterised by high temperatures of the start of the process of deformation and by heat resistance and,

consequently, they are irreplaceable for a large number of practical applications in high-temperature technology. Special attention is paid by investigators, in particular, to high-temperature systems of glasses: $R_2O_3$–$Al_2O_3$–$SiO_2$ (where R is Y, La, rare-earth elements). The experimental results show [1–5] that they are characterised by high refractive properties, high mechanical strength and resistance to the effect of alkali.

The glasses produced by industry at present are synthesised at temperatures below 1600°C. This limitation is associated with the possibilities of the currently available methods of synthesis in gas and electric furnaces. The development of methods of synthesis at higher temperatures will make it possible to produce optical materials with unique properties.

The glasses, satisfying stringent requirements on chemical composition, in particular, ultrapure glasses, are essential for fibre optics communication lines and laser technology. For example, in glasses for fibre optics communication lines, the content of impurities of transition metals should not exceed $10^{-5}$–$10^{-6}$ wt%. The problem of synthesis of glasses with a low content of OH⁻ hydroxyl groups has not as yet been solved completely in the technology of production of laser glass. This problem is especially acute in the technology of highly concentrated neodymium and erbium glasses. The content of OH⁻ groups in these glasses, of the order of $10^{19}$ cm⁻³, results in the quenching of luminescence of active ions. At present, the methods of purification of the initial materials for the glasses used in fibre optics communication lines makes it possible to produce materials satisfy the requirements on the content of the impurities. However, the commercial boiling methods increase the content of impurities by more than an order of magnitude. In the stage of synthesis of laser phosphate glasses which are boiled in platinum crucibles because of the corrosive effect of the melt, platinum penetrates into the glass. Platinum inclusions in glass greatly reduced the beam strength of the active elements produced from the glass of this type. It should be mentioned that the hydroxyl groups penetrate into laser glass in the synthesis stage.

To develop highly concentrated neodymium glass, it was necessary to develop a method for synthesis of laser glasses with the composition close to the stoichiometric compositions of crystals, i.e. the prototypes of glasses. In glasses of this composition, the neodymium content may reach $\approx 4 \cdot 10^{21}$ cm⁻³ whilst maintaining a higher quantum yield of luminescence of neodymium. These glasses

can be used to produce highly efficient small solid-state lasers.

The melts of these glasses are characterised by high crystallisation capacity. This greatly complicates the synthesis of these glasses. They include glasses with compositions similar to that of crystals M Nd $P_4O_{12}$ (here M is Li, Na, K, Rb, Cs). A change in the composition of a glass in order to reduce the crystallisation capacity is undesirable because of a decrease in the spectral-luminescence characteristics.

In this chapter, attention is given to the special features of the synthesis and boiling of high-temperature glasses in a cold crucible [6].

## Crucibles

Evidently, the first publication on the synthesis of glass by the method of direct RF melting was [7], published in 1968, describing the synthesis of glass in quartz crucibles cooled with water. The design diagram of the system is shown in Fig. 6.1. Induction heating of glass in cooled quartz or ceramic crucibles was also used for vitrification of radioactive waste [8].

The further development of the method of synthesis of glass was associated with the problem of synthesis of high-purity multicomponent glasses with small optical losses for fibre optics communication lines. In [9, 10], glasses were boiled in air-cooled quartz crucibles resulting in the formation of up to 600 g of glass. The method makes it possible to increase the yield of glass to several kilograms. A significant disadvantage of the application of quartz crucibles is the fact that it is necessary to regulate efficiently the temperature of the melt because at high temperatures and insufficient cooling the walls of the crucible may fail resulting in the penetration of water into the melt and in ejection of the latter. In addition to this, the application of quartz crucibles restricts the boiling temperature of glass and complicates the extraction of glass mass. Significant disadvantages also include the fact that quartz crucibles can be used only once.

The investigations show that the most promising method for the synthesis of glass is the application of metallic water-cooled crucibles described in [2, 11, 12]. The design diagrams of several crucibles are shown in Chapter 3.

Metallic crucibles, used for the boiling of glass, in contrast to crucibles for the growth of crystals and the synthesis of

polycrystalline materials, have a number of design features represented by the following [13]:

−a quartz vessel is placed in a copper crucible to prevent the contamination of the melt with copper. Aluminium crucibles are also used. The aluminium oxide does not colour the glass and is usually included in the main composition of the glass.

−assembled crucibles contain a large number of sections for preventing electric breakdowns in gaps.

−the crucibles are produced from split sections in order to be able to extract rapidly the glass block for annealing. An example of such a crucible produced from aluminium pipes is shown in Fig. 6.2.

**Starting melting**

As mentioned previously, the simplest and most efficient method of starting melting oxide materials is a method based on the introduction, into the charge, of small quantities of a metal which is included in the composition of the melted material. However, this method can not be used for glass boiling because of the uncontrollable contamination of the melt with metallic aluminium and products of production of aluminium, dispersed in the volume of the
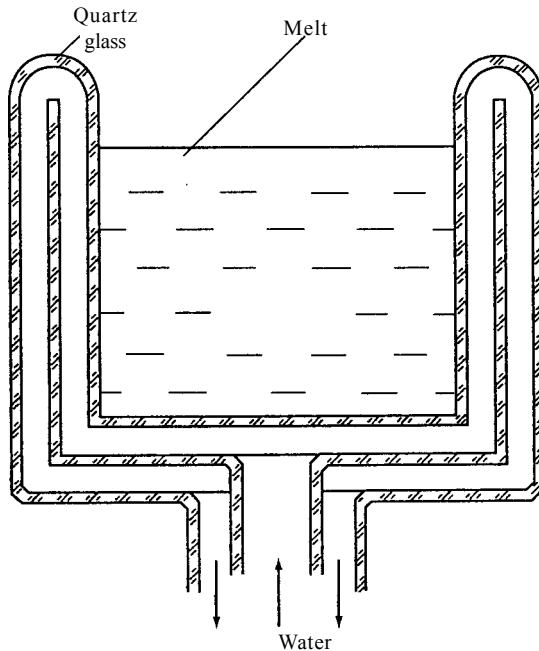


**Figure 6.1.** A water-cooled quartz crucible for boiling glass [7].

melt. Because of the high viscosity of glass forming melts, metallic aluminium is not oxidised during long periods of time [11]. Other metals show similar behaviour. Therefore, other methods of starting melting are used for boiling of glass. In [7], the starting volume of the melt was produced by melting a portion of a charge in a platinum crucible in a resistance furnace. Subsequently, the melt was poured into a crucible with the charge. In [9, 10, 12], starting melting was realised by introducing a secondary electrically conducting material, the heating body, into the charge. The heating body was represented as either by graphite or low-resistance silicon [8, 16], placed in a quartz capsule.

To prevent the evaporation of low-melting components of glass (salts of alkali metals), the authors of [16] have proposed to realise the process using the following procedure. The first stage consists of melting low melting components and, subsequently, refractory components are introduced into the melt and the melt temperature is gradually increased. Shortcomings of this method of loading the crucible include the high probability of production of glass with
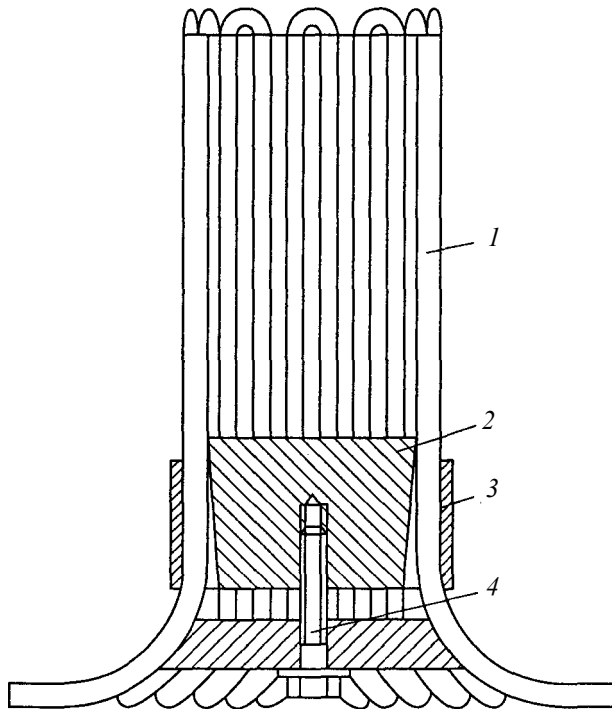


**Figure 6.2**. Aluminium water-cooled crucible [15]. 1) tubular sections, 2) spacing cone, 3) split supporting holder, 4) tightening bolt.

optical defects because the chemical composition of the skull (see Chapter 2) differs from that of the glass mass.

**Homogenising of the melt**

Homogenising of the melt is an important process essential for producing glasses with high optical quality. In [10], homogenising was carried out using either an air-cooled quartz stirrer or by the passage of a gas (oxygen or helium) through the melt. The melt of high-temperature glasses of the system $R_2O_3–Al_2O_3–SiO_2$ (where R is Se, Y, La) was stirred with a water-cooled stirrer. However, the application of the stirrer may have a negative effect on the quality of glass because it results in the formation of steep temperature gradients and increases the viscosity of the melt because of reducing its temperature [15]. The stirrer is therefore used at the beginning of the homogenising process, and in the final stage of homogenising takes place as a result of holding the melt at a high temperature. The presence in the melt of steep temperature gradients results in intensive convective mixing of the melt. However, experience shows that the efficiency of this stirring method is not sufficient for complete homogenising of the melt [17, 18].

**Extraction of a glass block from a crucible and annealing**

In the synthesis of glass in a glass boiling furnace, the glass block is annealed in the same crucible as the one used for boiling. This method can be used in boiling of glass using induction heating,. The point is that in cooling of the melt its electrical conductivity decreases and at a certain temperature the melt ceases to absorb the energy of the high temperature field. This is accompanied by rapid vitrification of the melt and, consequently, the glass cracks. Therefore, after cooling the block below some temperature which depends on the type of glass, the block must be transferred into a special annealing furnace [11, 15].

In melting in metallic water-cooled crucibles, the separation of the glass block from the crucible is relatively easy because a porous layer of the charge forms at the periphery of the block which is then easily separated from the crucible walls. When using quartz crucibles, a crucible together with the glass is placed in the annealing furnace. To prevent the formation of cracks in the glass

block, as a result of the difference in the coefficients of thermal expansion of the glass and quartz, it is usually recommended to use thin-wall crucibles [19]. In annealing, the quartz crucible cracks and separates and the glass blocks remains monolithic. If the glass block is used for withdrawal of the fibre, the quartz crucible with glass is transferred into the furnace for annealing and at a specific temperature glass rods with a diameter of up to 10 mm are drawn. On the outside, the rods are covered with a quartz layer [9, 10, 17].

In [6], the synthesis of glasses was carried out in Donets-4 equipment. The general operating principles of these systems and the main characteristics were presented in Chapter 3.

An important element of equipment is the water-cooled cold crucible whose design has a number of special features, resulting from the specific features of direct RF melting of glass. Glass mass is boiled using multisection tubular crucibles with a diameter of 130 mm and 90 mm, produced from aluminium or copper pipes. To extract a glass block from the crucible for subsequent annealing, two sections were replaced with U-shaped water-cooled elements which were easily removed from the crucible together with the glass block.

Water-cooled stirrers of different design, produced from aluminium tubes, are used for glass homogenising. The stirrer is secured to the upper rod. The speed of rotation of the stirrer is regulated smoothly from 0 to 100 rpm.

## Distribution of temperature in glass-forming melts

The distribution of temperature in the melt is an important technological parameter having a strong effect on all glass formation processes, clarification and homogenising of the glass mass [20]: the temperature distribution in the melt determines the heterogeneity of the viscosity of the melt which in turn determines the direction and intensity of flows in the volume of the melt [21].

The distribution of temperature in the melt was already partially discussed in Chapter 2, where the method of determination of the melt temperature was described. In this chapter, problems typical of the production of high-quality glass are examined.

A large number of investigations, for example [22–24], have been concerned with the calculation of temperature distribution in glass melts in industrial glass boiling furnaces of different types. On the other hand, the temperature fields in melts have been examined in

detail in the growth of crystals from the melt because this parameter is most important since it determines the conditions of growth of high-quality crystals. The investigations of temperature distribution and the hydrodynamics of the melt during the growth of crystals by the Czochralski method were carried out using the method of mathematical modelling [24–25], and experimental modelling was carried out on transparent liquids [28, 29].

The main special feature of the method of direct RF melting of materials in the cold crucible is the direct heating of material by the energy of the high frequency field. In this case, the material is in the water-cooled metallic crucible. Because of these circumstances, the thermal conditions in the melt greatly differ from the temperature distribution in the melt in the commercial methods of melting of materials in 'hot' crucible. The radial distribution of temperature on the surface of an $Al_2O_3$ melt is shown in Fig. 6.3 [10]. The given pattern of the radial distribution of temperature was obtained on the basis of the theoretical examination of direct RF heating assuming that the specific electrical conductivity is constant throughout the entire volume of the melt. The graph shows that the distribution of temperature along the radius of the crucible has a maximum whose position is determined by the depth of penetration of current into the melt. The temperature in the vicinity of the crucible walls decreases as a result of high thermal losses through the crucible walls. This pattern was obtained in
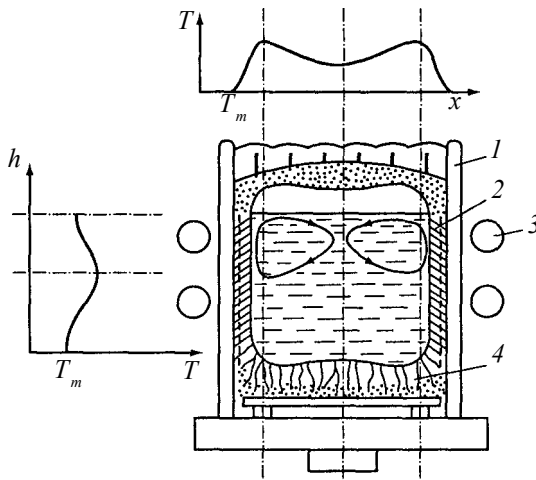


**Figure 6.3.** Distribution of temperature in a cold crucible [26]. 1) crucible; 2) skull; 3) inductor; 4) crystals.

examination of direct RF heating in a quartz crucible cooled with air.

## Effect of electrical conductivity and viscosity of the melt on temperature distribution

Table 6.1 shows the composition of glasses used for the determination of temperature distribution in the melt. Temperature dependences of the viscosity and electrical conductivity for the compositions of the $Na_2O$–$SiO_2$ system are available [30], and they are also available for industrial glasses of complicated composition which are of practical interest for fibre optics communication lines. Figure 6.4 shows the temperature dependences of the viscosity and electrical conductivity of the investigated melts.

The typical dependences of the temperature distribution in the direction of radius $T = f_r$ and the depth of the melt $T = f_z$ in a melt of sodium–boron–silicate glass (NaBSi) and also in melts of other glasses, are presented in Fig. 2.7. The identical dependences, obtained for melts of other glasses, have many common features with those shown in Fig. 2.7. All the curves of the radial distribution of temperature to a certain depth (in the examined case to $z = 70$ mm) show a maximum whose position remains constant for the investigated melts. The position of this maximum is determined by two factors: the nature of distribution of the active power absorbed by the melt and the special features of removal of heat through the watercooled crucible walls.

As shown in Chapter 1, the radial distribution of the power absorbed by the melt is determined by relationship (1.3) and for a crucible with the radius $r_0$ (in the investigated case $r_0 = 6$ cm) it is determined only by the value which depends on the electrical

**Table 6.1**. Composition of glass-forming melts

| Glass No. | Glass | Composition, wt% | | | | |
|---|---|---|---|---|---|---|
| | | $Na_2O$ | $SiO_2$ | PbO | $Al_2O_3$ | $B_2O_3$ |
| 1 | OM-1 | 20 | 58.5 | – | 1.5 | 20 |
| 2 | Zh-31 | 11.7 | 39.5 | 32.6 | 1.8 | 14.4 |
| 3 | $Na_2O$–$SiO_2$ | 45.6 | 54.4 | – | – | – |
| 4 | $Na_2O$–$SiO_2$ | 55.4 | 44.6 | – | – | – |
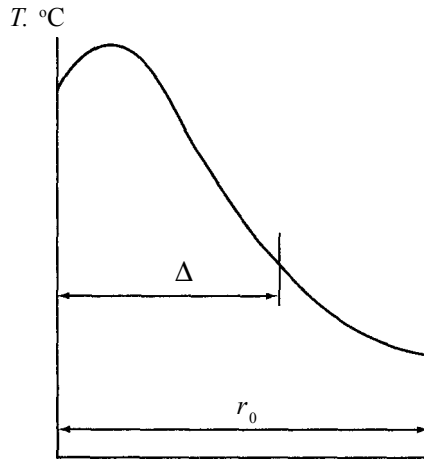
**Figure 6.4.** Radial distribution of temperature in a glass melt in direct HF heating [36]

conductivity of the melt. The removal of heat through the side walls of the cold crucible is determined by the thermophysical characteristics of the glass mass and the skull layer adjacent to the crucible wall.

The stability of the position of the temperature maximum of the glass mass of a specific composition in different conditions of the melting process indicates that the intensity of heat removal through the crucible walls is constant. The author of [6] investigated the temperature distribution in a melt in relation to two factors – the properties of the melt and the thermal conditions of the technological process. Figure 6.5 shows the radial temperature distribution in the melts of different glasses at $z = 0$ which indicates that the position of the maximum on the curve $T = f_r$ changes from $r = 35$ mm (melt Zh-31) to $r = 50$ mm (glasses 3 and 4). The dependence $T = f_r$ in the volume of the melt is the same.

According to the author of [6], the variation of the position of the maximum is determined mainly by different electrical conductivities of the investigated melts. This conclusion is confirmed by the similar position of the maximum for the glasses 3 and 4 characterised by almost the same electrical conductivity. Evidently, the change of the thermophysical characteristics of the melt and the skull layer for glasses of different composition is not very large and, consequently, the intensity of heat removal through the side surfaces of the crucible is not controlling for the radial distribution of temperature in the melt. It should be mentioned that the
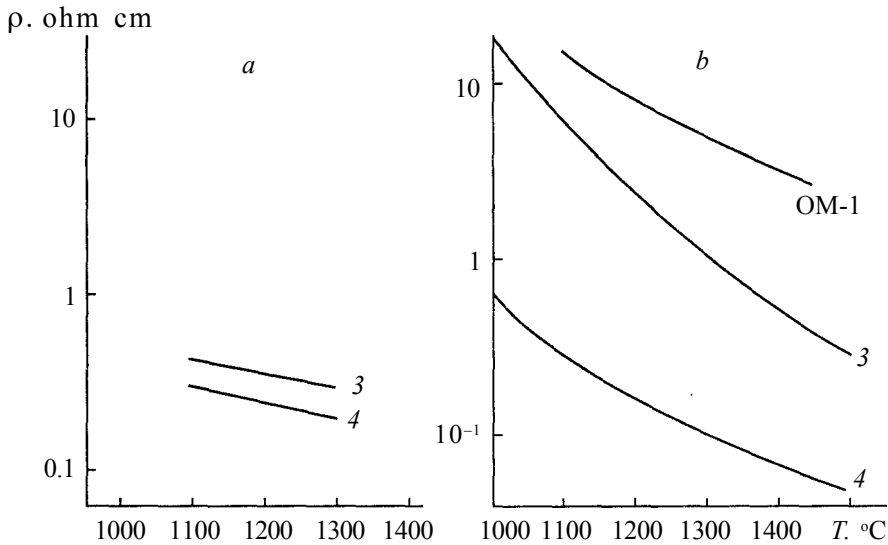
**Figure 6.5.** Temperature dependence of electrical conductivity and viscosity of glass melts [30]. Numbers of the curves correspond to glass compositions in Table 6.1.

temperature dependence of the electrical conductivity of glass-forming melts, in contrast to melts of simple oxides, has distinctive maxima and, consequently, by changing slightly the temperature of the melt it is possible to change the position of the maximum on the dependence $T = f_r$ However, it will be shown later that the author of [6] did not manage to record the displacement of the maximum of the radial distribution of temperature with the variation of the power absorbed by the melt. Possibly, the change of the position of the maximum was not greater than the error of determination of its position. Figure 2.7 shows that the magnitude of the detected maximum on the $T = f_r$ curves decreases with increasing depth $z$, and at any specific value of $z$ it completely disappears. This is determined by the rapid removal of heat through the water-cooled crucible bottom and also by a decrease in the efficiency of heating the layers of the melt situated below the induction coil. In the surface layer of the melt with a thickness of 10–15 mm, the distribution of temperature in the depth of the melt (Fig. 2.7) is characterised by the presence of temperature gradients reaching 150°C/cm caused by the removal of heat through the open surface of the melt.

The temperature distribution in the melt is strongly affected by the melt viscosity. Figure 6.7 shows the distribution of isotherms in
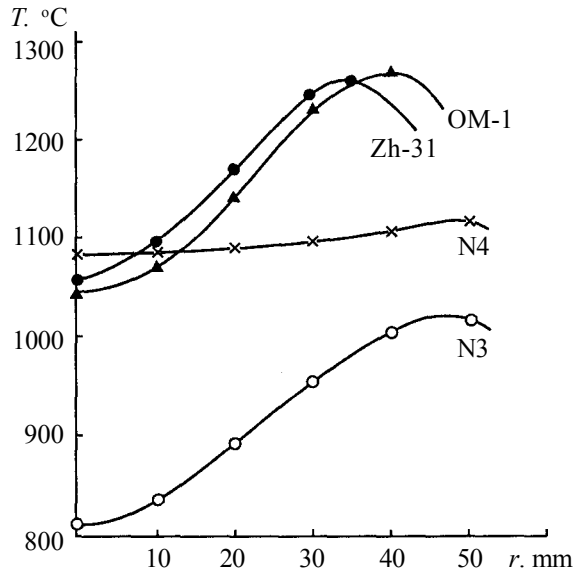
**Figure 6.6.** Radial distribution of temperature in glass melts of different composition on the melt surface [6]. Glass compositions are presented in Table 6.1.
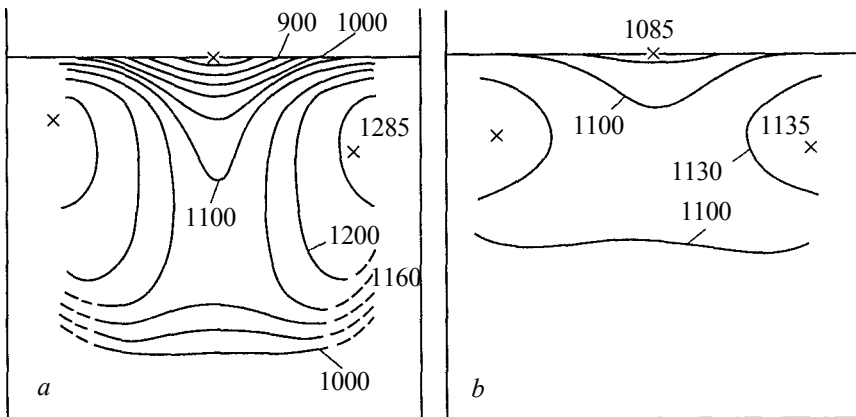


**Figure 6.7**. Temperature distribution in glass melts with different viscosity [6]: a) 45.6 $Na_2O \cdot 54.4\ SiO_2$ (No. 3); b) 55.4 $Na_2O \cdot 44.6\ SiO_2$.

the melts of glasses 3 and 4 which, having similar values of electrical conductivity, greatly differ in viscosity. For example, in the temperature range 1085–1140°C, the viscosity of the glass melt 4 changes from 0.4 to 0.2 Pa s, and the viscosity of glass 3 in the temperature range 1000–1285°C changes from 12 to 1 Pa s. Comparison of Figs. 6.7 (a) and (b) indicates that a decrease in the
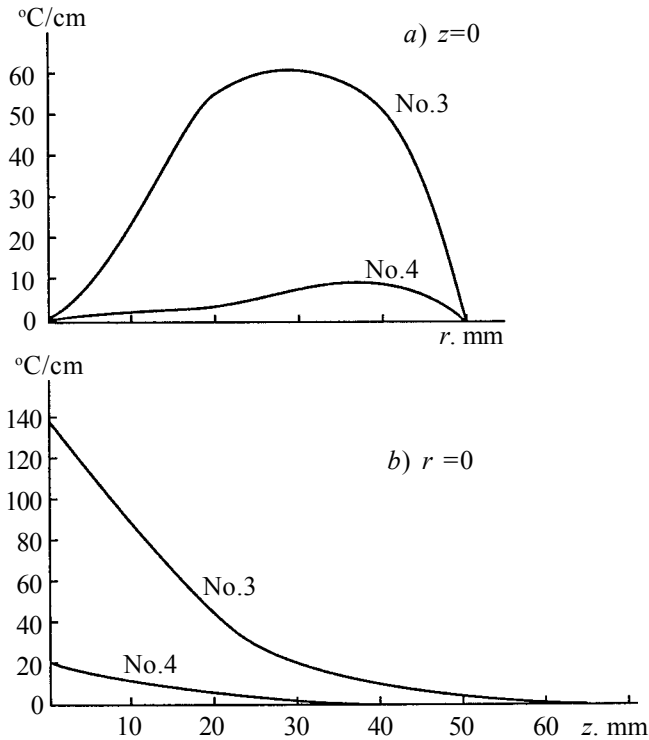
**Figure 6.8.** Radial (a) and axial (b) temperature gradients in glass melts No. 3 and 4 [6].

viscosity is accompanied by a rapid decrease of the temperature gradients in the volume of the melt. This is indicated by Fig. 6.8 which shows that with a decrease of viscosity, the maximum of the radial temperature gradient decreases from 60°C/cm to 10 °C/cm, and the axial gradient from 140° to 20°C/cm. The variation of the temperature gradients in the entire volume of the melt shows the same behaviour.

Evidently, the most probable reason for this large decrease of the temperature gradients in the melt with a decrease in melt viscosity is an increase in the intensity of convective mixing of the melt resulting in the equalisation of the temperature gradients.

Heat shields are used extensively in crystal growth for the shaping of the temperature gradients on the melt surface. In order to explain the effect of screening the surface of the melt on the distribution of temperature in the melt volume, experiments were carried out with the melt of glass 1. A heat shield made of fire clay was placed on the edge of the cold crucible. All other parameters:
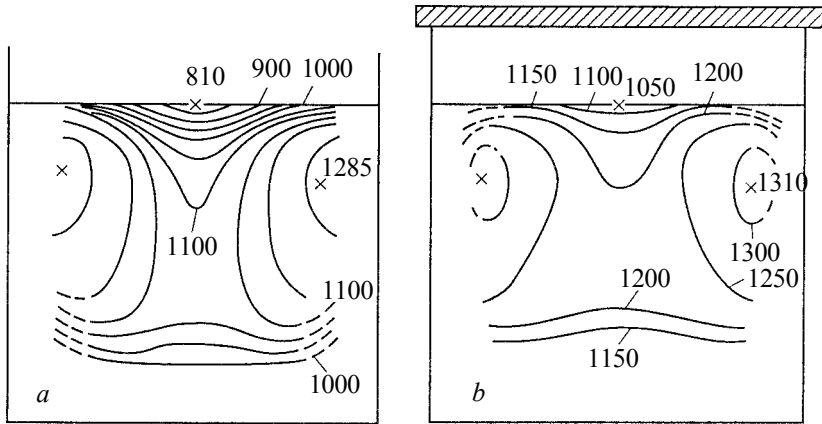
**Figure 6.9.** Temperature distribution in a glass melt with composition 45.6 Na$_2$O·54.4 SiO$_2$ with an open surface (a) and with a heat shield above the melt (b) [6]

the volume of the melt, the position of the induction coil in relation to the surface of the melt, the power, required by the RF generator, remained the same for all experiments. The measurement results are presented in Fig. 6.9. As indicated by the graph, the introduction of a heat shield has a significant effect on the temperature distribution in the volume of the melt:

–the maximum temperature on the surface of the melt increases by approximately 150°C;

–the temperature in the centre of the crucible on the surface of the melt greatly increases (≈250°C);

–the maximum temperature in the volume of the melt slightly increases, by ≈25°C;

–the region of the maximum temperature is slightly displaced into the bulk of the melt.

The measurements of the power, removed from the melt through the water-cooled crucible walls and the crucible bottom shows that the introduction of a shield increases this power from 6.8 to 8.1 kW. For the given crucible and the temperature of the glass melt of 1000–1200 °C the heat losses as a result of radiation from the free surface of the melt were ≈15% of the power absorbed by the melt.

The power of the heat flow of radiation ($q$) from the surface of the melt is calculated using the equation:

$$q = \{Q_{scr} - Q_O\} / \pi r^2, \tag{6.1}$$

where $Q_{scr}$ is the power generated in the melt when using a heat shield; $Q_0$ is the power, generated in the melt without the screen. For the radius of the investigated surface of 5 cm, $q = 17$ W/cm$^2$.

The density of the power of radiation of the surface of the melt may also be evaluated using the Stefan–Boltzmann law which is strictly valid for the absolutely black body:

$$Q = \sigma\varepsilon T^4, \tag{6.2}$$

Here $\sigma$ is the Stefan–Boltzmann constant, $\sigma = 5.67032 \cdot 10^{-8}$ W/m$^2 \cdot$ K$^4$ (in 1982), $\varepsilon$ is the emissivity of the melt, $T$ is the absolute melt temperature. For $\varepsilon = 0.6$ and $T = 1500$ K $q = 17.7$ W/cm$^2$, *i.e.* the calculated value of the density of the heat flow from the melt surface is in good agreement with the experimental value.

The effect of the position of the induction coil in relation to the melt and also of the value of the active power, generated in the melt, on the temperature distribution in the melt was investigated in a series of experiments with sodium–boron–silicate glass (NaBSi) at a constant volume of the melt. The main parameters, characterising the process conditions and also the temperature of the melt at certain points, are presented in Table 6.2.

To analyse the distribution of temperature in the melt, two regions should be selected: 1. The subsurface layer with a thickness of 10–15 mm, 2. The remaining volume of the melt. When the induction coil was lowered, the axial temperature gradients in the first region

**Table 6.2.** Main parameters of the process of melting and temperature distribution in the melt of sodium borosilicate glass [6]

| Parameter | Parameter value | | | |
|---|---|---|---|---|
| Position of induction coil in relation to melt, $z$, mm | −35 | −15 | +20 | −35 |
| Power absorbed by melt, kW | 12.1 | 12.1 | 12.1 | 9.9 |
| Maximum surface temperature at point $r$ mm, °C | 1200; 40 | 1190; 40 | 1275; 40 | 975; 0 |
| Temperature in crucible centre, $r = 0$, mm, °C | 1060 | 1090 | 1040 | 975 |
| Maximum temperature of melt at points $r$, $z$ mm, °C | 1355; 40; 50 | 1380; 40; 30 | 1425; 40; 20 | 1329; 37; 90 |

Comment: $r$ is the distance from crucible centre, $z$ is the depth of the melt
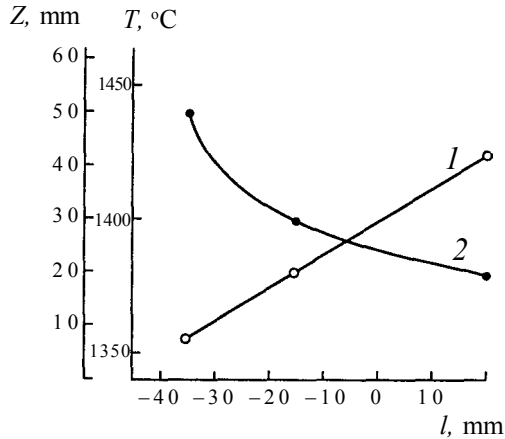
**Figure 6.10**. Dependence of the maximum temperature in the melt of sodium–borosilicate glass (1) and depth of the melt with maximum temperature (2) on the distance between the inductor and the surface of the melt: (+ – upper turn of the inductor above the melt surface) [6].

rapidly increased whereas the radial temperature gradients decreased. The distribution of temperature in the second region became more uniform and, in this case, the region of maximum temperature is displaced into the bulk of the melt and its size decreases (Fig. 6.10).

As already mentioned, the value Δ is linked with the specific electrical conductivity of the melt by the relationship:

$$\Delta = 5.03 \cdot 10^3 (\rho / \mu f)^{1/2} \tag{6.3}$$

Thus, the detected change in the position of the maximum of the radial distribution of temperature of the melt of glasses of different compositions (Fig. 6.5), within the framework of the investigated model which considers a cylindrical heat source instead of the induction coil, is determined by the variation of the diameter of the heat source $d_{hs}$.

A decrease in the level of the induction coil in relation to the surface of the melt corresponds to the displacement of the heat source into the bulk of the melt. In this case, the regional maximum temperature is also displaced into the bulk of the melt, the surface layers cool down and this results in an increase in the viscosity of the melt and convective heat transfer in the surface layers of the melt becomes more complicated. This results in a rapid increase of

the axial gradient in the first region. A decrease in the radial temperature gradient in the investigated region is also associated with a decrease in the strength of the effect of the heat source with movement of the source away from the surface.

The observed large change in the temperature distribution the melt with the variation of the power absorbed by the melt is also associated with the change of the viscosity of the melt. For example, with a decrease of the melt temperature of the (NaBSi) glass from 1300 to 1000°C, viscosity increases by more than an order of magnitude (Fig. 2.8). As a result of a relatively large distance between the heat source and the surface of the melt, the intensity of heating decreases and, consequently, the viscosity of the melt increases, especially in the first region. The convective heat transfer from the depth of the melt is complicated and the removal of heat through the watercooled walls of the crucible becomes controlling in the first region. This results in a change in the sign of the radial temperature gradient.

Thus, in cases in which the induction coil is situated well below the level of the melt, the variation of the power absorbed by the melt makes it possible to control the radial temperature gradient on the surface of the melt. This is very important in growing single crystals by the Czochralski method.

## 6.2. OPTICAL HOMOGENEITY OF GLASS

Optical glass may contain the following defects: crystallites, air bubbles and ripples [20]. In this section, special attention is given to the mechanism of formation of ripples in the glass produced in a cold crucible. The ripples have the form of the filament-like thin layers of glass with different refractive properties in comparison with the surrounding mass of the glass because of differences in the chemical composition. In boiling of glass in ceramic potters kilns and bath furnaces, there are two sources of formation of ripples: the boiling vessel and the free surface of the glass melt. At a high temperature, the glass melt interacts with the ceramic material of the vessel with the formation at the walls of a boundary layer enriched with interaction products. This layer is partially trapped by the moving melt, mixes with it, forming the ripples of 'ceramic' origin.

In the molten condition, glass becomes volatile. Some components of the glass evaporate very rapidly, others remain almost completely in the melt. Consequently, a layer of a melt with changed

composition, with the refractive index differing from the index of the main mass of the glass, forms on the surface. In the mixing, the surface layer is displaced into the volume of the melt and, consequently, ripples appear.

By analogy with the above, it is possible to define the sources of formation of ripples in the synthesis of glass by the methods of direct RF melting in the cold crucible. In the melt, the walls of the cold crucible are covered with a skull layer, consisting of a centre charge and viscous glass. As a result of the heterogeneity of the chemical composition of this layer, it may act as a source of ripples. However, it is important to note the principal difference in the formation of ripples in the methods used in commercial technology and in cold crucible technology. The point is that in boiling glass in a cold crucible, the formation of the boundary layer with the chemical composition different in comparison with that of the main mass may be avoided using, for example, a highly homogeneous charge, produced by the method of co-precipitation from solutions, or the boiling process is realised in such a manner that a relatively thick layer of viscous glass of the same composition as that of the main mass of the melt forms in the vicinity of the crucible walls in the homogenising stage.

The formation of ripples as a result of surface disproportionation takes place by the same mechanism during boiling of glass in ceramic and cold crucibles. (NaBSi) glass will be examined as an example: glass was boiled in a crucible with a diameter of 90 mm for 3 hours at a temperature 1400°C. The total losses of glass were 4.76 wt%. They consisted of the losses of 1.91 wt% $B_2O_3$ and 2.85 wt% $Na_2O$. Thus, in boiling, a layer depleted in boron and sodium oxides forms on the surface. Mixing with the remaining bulk of the glass, this layer results in the formation of ripples.

The optical quality of produced glasses was investigated in shadow equipment with a bright spot (Twayman equipment) [31]. In examination of shadow patterns it is necessary to note two aspects of the problems of the optical quality of glass. The first is the information on the distribution of convection flows in the glass mass, the second is the intrinsic optical quality of the produced glasses. The actual pattern of the ripples on shadow photographs characterises convection flows in the glass mass. However, when cooling a glass block in a cold crucible, the shape of the ripples is distorted because of the formation of the block (formation of a shrinkage cavity), and because of the distribution of flows during
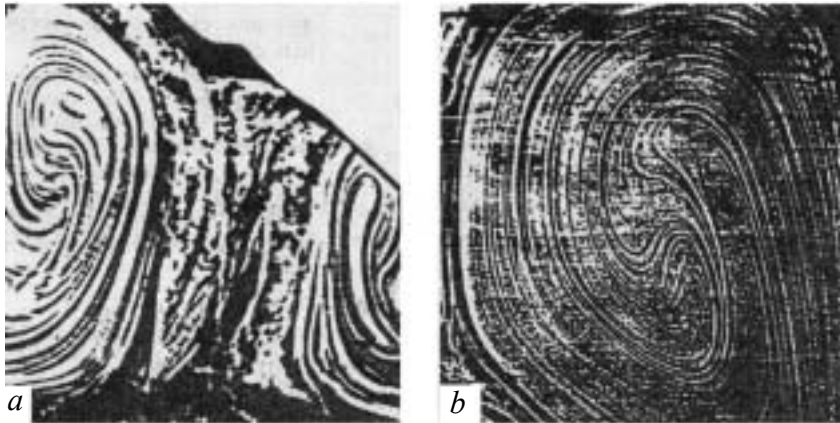
**Figure 6.11.** Schlieren photographs of glass containing lead [6]. a) without mixing the melt; b) the same glass with the melt mixed with a water-cooled stirrer. Speed of rotation 30 rpm, mixing time 3 h

nonuniform cooling, determined by the redistribution of thermal fields in the melt volume. The peripheral parts of the glass block are the first to cool down, i.e. the regions adjacent to the walls and bottom of the cold crucible. The pattern of the distribution of ripples in these regions reflects the direction of convection flows in the glass mass. The largest distortion is detected in the regions of glass solidifying last, i.e. the regions in the centre of the glass block. Since the cooling rate of the block is relatively high (the internal regions of glass are cooled to a temperature of 600–700 °C within 3–5 min), it is assumed that the shadow patterns provide relatively complete formation also on the convective flows in the glass mass. Figure 6.11 shows the shadow photograph of a glass containing lead, synthesised in a cold crucible for 4.5 hours without forced mixing of the melt. The photograph shows that the glass specimen is characterised by high optical heterogeneity and the nature of the ripples in the volume of the glass differs. Randomly distributed optical heterogeneities were found in the centre and at the periphery of the glass block, whereas in the remaining volume of the melt, the ripples are oriented according to the convection flows in the melt. This nature of distribution of the ripples is in good agreement with the temperature distribution in the melt (Fig. 2.6). For example, glass regions, distributed at of the periphery of the block are at a relatively low-temperature and, consequently, are characterised by high viscosity. Therefore, the convection stirring of the melt in these regions is difficult and this affects the optical
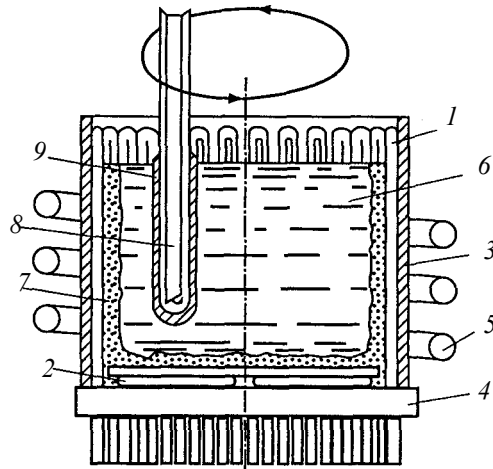
**Figure 6.12.** A crucible for producing high-temperature glasses. 1) a tubular water-cooled element; 2) water-cooled bottom; 3) insulating quartz cylinder; 4) securing ring made of an electrically insulating material; 5) inductor of HF generator; 6) melt; 7) charge; 8) water-cooled stirrer; 9) skull.

quality of glass. The central regions of the glass melt are characterised by small temperature gradients resulting in only slight convection mixing in this part of the melt. The remaining part of the melt has a higher temperature and is characterised by a steep temperature gradient. Therefore, in this region the ripples are oriented distinctively in the direction of convection flows. The formation of loop-shaped 'whirls' in this part of the block is evidently determined by the previously examined effects taking place during cooling of the glass block.

Thus, in boiling glass in the cold crucible, the melt contains 'dead' zones with insufficiently intensive homogenising of the melt. Therefore, the melt should be homogenised by means of forced stirring, using water-cooled stirrers. Figure 6.12 shows the method of production of high-temperature glass from a cold crucible using a water-cooled stirrer for homogenising the melt. The application of forced stirring results in the formation of high-intensity flows in the melt which determine the orientation of ripples. In this case, the volume of the 'dead' zones rapidly decreases, and only the 'column' in the centre of the crucible remains. The column is characterised by the formation of an ordered structure of ripples.

The application of forced stirring of the melt (within the limits of the given boiling and stirring conditions) is reduced to the ordering of ripples throughout the volume of glass. However, stirring of the

melt does not make it possible to produce glass completely free from ripples. The application of stirrers of the previously mentioned type also does not lead to any significant change in the nature of distribution of ripples in glass specimens. In the case of NaBSi glass forced mixing results in the local concentration of ripples in small volumes of glass and in the formation of large sections of glass almost free from ripples.

It is also necessary to note the large difference in the shadow photograph of specimens of glasses of type Zh-31 and OM-1 (Table 6.1). In the specimens of Zh-31 glass, the ripples are characterised by higher contrast in comparison with the OM -1 glass, as a result of differences in the chemical composition of the glass. Since PbO is characterised by a high partial contribution to the refractive index, even small local changes in the PbO content of the glass result in a large change of the refractive index. The optical properties of the NaBSi glass depend only slightly on its components and, consequently, local changes in the concentration of some component result in a less marked change of the refractive index.

The optical homogeneity of the glass is also affected by the grain size composition of the initial charge. A melt of a charge containing $SiO_2$ grains with a diameter of 1–2 mm contains lack of boiling defects, situated in the vicinity of the skull which are evidently the reason for the formation of distinctive randomly distributed ripples (Fig. 6.13).



**Figure 6.13.** Schlieren photograph of sodium–borosilicate glass, produced from a charge containing large (1–2 mm) $SiO_2$ grains [6].
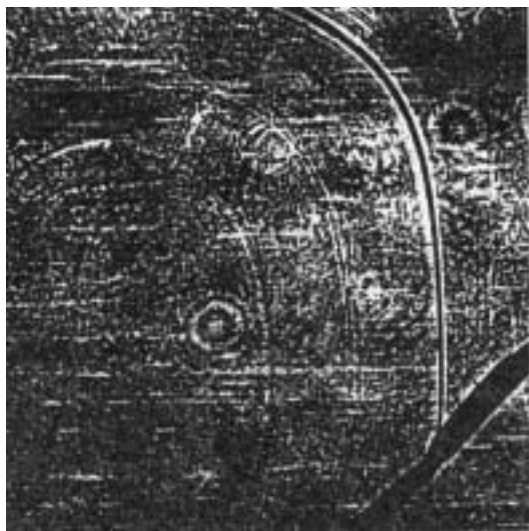
**Fig. 6.14.** Schlieren photograph of sodium–borosilicate glass produced using a water-cooled lid–cooler [6].

In order to improve the optical quality of glasses, the author of [6] proposed a method for removing ripples formed as a result of the selective evaporation of glass components from the melt surface. A melt of OM-1 glass was held at a temperature of 1400 °C to complete disappearance of particles of the charge and bubbles detected usually on the surface of the melt. The duration of melting of the charge and clarification of the melt should be minimum because in this stage the volume of 'surface' ripples increases. In the examined case, this time was 1.5 hours. Subsequently, the surface of the melt was cooled using a cover-refrigerator in the form of a coil consisting of water-cooled aluminium pipes. The power of the RF generator was reduced and the melt was homogenised below the cooled upper layer of the glass for 2.5 hours. As a result of this treatment, the quality of glass greatly improved and there were only single ripples in the bottom part of the melt (Fig. 6.14). Further improvement of the optical quality of glass is manifested in a decrease of the contribution of the skull bottom part of the melt to the formation of ripples. This may be achieved by 'freezing' the bottom part of the melt as a result of lowering slightly the crucible in relation to the induction coil.

**Chemically homogeneous impurities**

It is well-known that the main source of 'contamination' in the melting of initial powder components of glass and subsequent

**Table 6.3.** Physico–mechanical and electrical properties of high-temperature glass [2]

| Property | Glass composition, wt.% | |
|---|---|---|
| | Glass composition, wt.% | $SiO_2$: $Al_2O_3$:$Sc_2O_3$ = 60:30:10 |
| Density, g/cm³ | 2.20–2.21 | 2.578 |
| Refraction index | 1.4588 | 1.542 |
| Young modulus, kg/mm² | 7450–7140 | 12740 |
| Shear modulus, kg/mm² | 3200 | 5100 |
| Poisson coefficient | 0.16 | 0.249 |
| Microhardness, kg/mm² | 795 | 780 |
| Linear expansion coefficient, $deg^{-1}$ | $5 \div 7 \cdot 10^{-7}$ | $27 \cdot 10^{-7}$ |
| Temperature of start of softening, °C | 1250 | 1200–1250 |
| Specific resistivity, ohm·cm | | |
| at 20 ºC | $1 \cdot 10^{19} - 1 \cdot 10^{18}$ | $3 \cdot 10^{13}$ |
| at 600 ºC | $6 \cdot 10^{7} - 6 \cdot 10^{6}$ | $1.7 \cdot 10^{5}$ |
| at 1000 ºC | $1 \cdot 10^{6} - 2.5 \cdot 10^{5}$ | $1.1 \cdot 10^{4}$ |
| Dielectric permittivity at 20°C | 3.2 | 6.8 |
| Tangent of the angle of dielectric losses in the frequency range 30 kHz – 10 MHz | $2 \cdot 10^{-4}$ | $5 \cdot 10^{-4}$ |

homogenising of the melt is the crucible material. Contamination of the melt with the crucible material may take place by both the direct interaction of the crucible with the melt and by the transfer of material of the crucible into the melt through the gas phase. The dominant contamination mechanism is determined by the crucible material and the specific conditions of the boiling process (temperature, working atmosphere).

Platinum is a classic crucible material used widely in optical glass boiling. Platinum is resistant to the effect of the majority of

**Table 6.3** (continued)

| Glass composition, wt.% | | |
|---|---|---|
| $SiO_2:Al_2O_3:Y_2O_3$=50:20:30 | $SiO_2:Al_2O_3:La_2O_3$=54:21:25 | $SiO_2:Al_2O_3:Er_2O_3$=60:30:10 |
| 3.05 | 3.016 | 2.833 |
| 1.592 | 1.573 | 1.555 |
| 11040 | 9650 | 9080 |
| 4510 | 3940 | 3660 |
| 0.225 | 0.225 | 0.240 |
| 1050 | 735 | 930 |
| $70 \cdot 10^{-7}$ | $28 \cdot 10^{-7}$ | $10.3 \cdot 10^{-7}$ |
| 1000 | 1100–1200 | 1150–1200 |
| $2 \cdot 10^{13}$ | $4 \cdot 10^{13}$ | $1 \cdot 10^{13}$ |
| - | $1 \cdot 10^{5}$ | $1.7 \cdot 10^{7}$ |
| - | $5 \cdot 10^{3}$ | $5 \cdot 10^{3}$ |
| 7.0 | 7.1 | 6.9 |
| $2 \cdot 10^{-4}$ | $1 \cdot 10^{-4}$ | $2 \cdot 10^{-4}$ |

glass melt and, consequently, homogeneous glasses may be produced. However, in glasses synthesised in platinum crucibles there are often clusters of inclusions of metallic platinum.

As stressed a number of times, one of the advantages of the method of direct RF melting in the cold crucible is the high purity of the method determined by the absence of direct contact of the melt with the crucible material. Therefore, it was natural to investigate the variation of the chemical composition of glass in comparison with the composition of the initial reagents after boiling in the cold crucible. For this purpose, experiments were carried out with the boiling of OM-1 and Zh-31 glasses using initial reagents of high purity. The content of the main colouring elements in the initial reagents did not exceed several units, $10^{-6}$ wt%, and only the iron content was an order of magnitude higher. The boiling of glasses, carried out in a crucible produced from copper pipes,

showed that when using the initial charge containing nitrate salts, the glass becomes blue, with this colour typical of the presence of $Cu^{2+}$ in the glass. The absorption spectrum of the OM-1 glass is characterised by the presence of a wide absorption band with a maximum in the range 750 nm. When the initial materials are represented by oxides resulting in colouring of the glass, the absorption band does not form in this region of the spectrum. The comparison of these two factors was used for proposing a mechanism of contamination of glass with copper. When heating a charge, the initial stages of synthesis of glass are characterised by thermal dissociation of nitrate salts with the precipitation of nitrogen oxides. These components in the gas form react with the copper oxide film formed on the surface of copper pipes resulting in the formation of copper nitrate, with the latter falling into the melt when loading the charge into the crucible. Thus, copper is transferred from the crucible walls into the melt. Therefore, glass should be boiled in crucibles made of aluminium pipes. Aluminium is not a colouring addition in glass and is included in the main composition of many synthesised glasses. The aluminium oxide layer on the surface of pipes is resistant to the effect of nitrogen oxides. In [6] it was established that synthesised glasses are characterised by an increase in the content of iron, copper and vanadium in comparison with the initial charge. One of the possible channels of contamination of glass with iron and copper is the preliminary heat treatment of the charge. The need to carry out his operation was caused by special features of direct RF melting in the cold crucible because the initial charge contains $H_3BO_3$ which decomposes during starting melting, with the generation of water vapours. The vapours condense on the cold pipes of the crucible and close tubular sections, resulting in electrical breakdown and failure of the crucible walls. It is therefore necessary to introduce an additional operation: prior to loading into the cold crucible, the charge is baked in a resistance furnace at a temperature of ≈400 °C in order to remove water vapours.

The application of a quartz crucible for the baking process greatly decreases the content of undesirable impurities in glass. The quality of produced glass was inspected on the basis of measurements of absorption losses by the colourimetric method at a wavelength of 1.06 μm [32]. However, it should be noted that the absorption losses were slightly higher in comparison with multicomponent glasses. This was due to a relatively high content

of the impurities in the given reagents. The surrounding atmosphere in which glass synthesis is carried out may be a source of contamination of glass in heating with RF currents and, consequently, the synthesis of high purity glasses must be carried out in specially built facilities with the efficient removal of dust from the air.

## 6.3. REFRACTORY GLASSES OF THE $R_2O_3$– $Al_2O_3$– $SiO_2$ SYSTEM (R = Sc, Y, La, Nd, Er)

The glasses based on alumosilicate systems of yttrium and lanthanum are characterised by valuable properties for application. The combination of the high refractive index with high mechanical characteristics and deformation temperature and also the relatively low values of the thermal expansion coefficient and the very high resistance to the effect of alkali make these glasses promising optical materials capable of operation at high temperatures in chemically corrosive media.

The most promising method of production of these types of glass is the method of direct RF melting in the cold crucible. The method has no principal restrictions as regards the synthesis temperature and can also be used for producing glasses in volumes required for practical application without extensive contamination of glass with the crucible material.

The authors of [2] investigated glasses of the $R_2O_3$–$Al_2O_3$–$SiO_2$ system (here R is Y, Sc, La, Er) synthesized by the method of direct RF melting in the cold crucible. Glass synthesis was carried out at temperatures of approximately 2000°C for several hours. This resulted in the formation of glass blocks weighing up to 1.5 kg with almost no inclusions and components of the charge which have not managed to react. The compositions of the glasses corresponding to the section of the ternary phase diagram of the $Al_2O_3 \cdot 3SiO_2$–$R_2O_3 \cdot 3SiO_2$ system. The results show that at a content of up to 5 mol% ($R_2O_3 \cdot 3SiO_2$) glass remains transparent up to temperatures of 1100–1200 °C. With an increase of the content of $R_2O_3 \cdot 3SiO_2$, there is intensive crystallisation of glass at temperatures of 1050–1150°C. Crystallisation of a glass with a low content of oxides of rare-earth elements results in the formation of mullite ($3Al_2O_3 \cdot 2SiO_2$). An increase of the content of the rare-earth oxide after the formation of mullite leads to the formation of silicates of rare-earth elements, for example $Er_2(Si_2O_7)$ or

**Table 6.4.** Values of the coefficient of thermal expansion and temperature of the start of deformation and glass transition of $La_2O_3$–$Al_2O_3$–$SiO_2$ system

| Composition of glass, mol% | | | $\alpha_{20-800} \cdot 10^7$, deg$^{-1}$ | $T_{s.d.}$, °C | $T_g$, °C |
|---|---|---|---|---|---|
| $SiO_2$ | $Al_2O_3$ | $La_2O_3$ | | | |
| 50.1 | 32.8 | 17.0 | 64.0 | 855 | 820 |
| 55.0 | 28.4 | 16.6 | 62.5 | 860 | 825 |
| 59.1 | 34.7 | 6.3 | 43.2 | 895 | 850 |
| 71.6 | 26.4 | 2.0 | 33.7 | 920 | 900 |
| 72.0 | 21.5 | 6.3 | 38.9 | 910 | 865 |
| 68.3 | 25.6 | 6.1 | 39.1 | 905 | 860 |

alumosilicates with a complicated composition (Chapter 4).

Recently, high-temperature glasses have attracted attention because of possible use as laser materials. For example, the authors of [5] synthesised glasses with the composition 44.7 $SiO_2$–35.8 $Al_2O_3$–19.5[(1–$x$) $La_2O_3$ + $x$Nd$_3$O$_3$] and investigated their physical–chemical and spectral–luminescence properties. Glass from a charge prepared by the co-precipitation method was synthesised. The charge was baked in corundum crucibles in a gas furnace at a temperature of 1550°C for 1.5 hours. The physical and mechanical properties of the synthesised glasses are presented in Table 6.3 shows that the values of the refractive index, density, Young modulus, shear modulus and the Poisson coefficient for high - temperature glasses of this compositions are considerably higher than for quartz glasses. Figure 6.14 shows the dependence of the density, refractive index and microhardness on the lanthanum oxide content of glass. Table 6.4 shows the values of the thermal expansion coefficients in the temperature range 20–800°C. These values are important for practical application of the glasses.

Glass was synthesised in equipment Donets-4, which was described in Chapter 2. Crucibles were produced from copper or aluminium and their diameter was 130 and 90 mm.

The process of synthesis of glasses in the cold crucible may be divided into the following main stages: preparation of the charge and placing the charge in the crucible; starting heating and melting; clarification (holding) of the melt; cooling of the melt and annealing of the glass blocks. The initial reagents were baked in a silit-rod

furnace at a temperature of 1000–1100°C for 8–10 hours, weighed in corresponding proportions and thoroughly mixed in a china mortar. The amount of the prepared charge for crucibles with diameters of 130 and 90 mm was 4.5–7 kg and 1.5–2.5 kg, respectively.

The charge was placed in the crucible so that 80–90% of the volume of the crucible was filled. To produce a starting melt, a graphite rod with a diameter of 50 mm and 70 mm long was placed in the centre of the crucible. The rod was used as a heating source in order to produce the starting volume of the melt. The graphite rod was heated and melted the charge which was in direct contact with it. During melting of the charge a cavity formed around the rod which was then filled with the next portions of the charge up to obtaining the critical volume of the melt sufficient for the effective absorption of the energy of the RF field directly by the melt. This was controlled on the basis of the variation of the intensity of anodic current $I_a$. In the conventional operating conditions of the RF generator, the intensity of the anodic current in the idling regime is 2.5 A, and the increase of current to 3.5–4 A indicates the start of direct RF melting of the charge. The critical value of current $I_{a\ cr}$ depends on the composition of the synthesized glass, mainly on the $SiO_2$ content. For example, for glasses with 70–75 mol% of silicon oxide, the critical current is $\approx 4$ A, and for glasses with a lower content of $SiO_2$ it is $\approx 3.5$ A. It may be assumed that the melts of the glass with a high content of silicon oxide have a lower specific electrical conductivity than the glasses with a lower content of $SiO_2$ and, consequently, the starting volume of the melt in the first case should be larger (or it should be heated to a higher temperature). This also results in an increase of $I_{a\ cr}$.

The moment of the start of direct RF heating of the melt is determined visually when the temperature of the melt in the vicinity of the crucible walls becomes higher than in the central part of the crucible. When the critical volume of the melt has been reached, the graphite heater is removed and small portions (100–200 g) of the charge are poured into the crucible, up to obtaining the required volume of the melt. The duration of starting melting is usually 15–20 min and the melting process of the charge lasts approximately 1 hour.

Starting melting and placing of the charge are characterised by complicated physical–chemical processes: melting of the individual components of the charge, the formation of the liquid phase whose composition corresponds to the eutectic with the lowest melting

point on the equilibrium diagram, the occurrence of solid-phase reactions and reactions in the melt leading to the formation of silicates, dissolution of $SiO_2$ grains in the resultant mixture of the silicates.

The next stage of the process is the clarification of the melt usually represented by the removal of gas bubbles from the melt [20]. In the stage, the chemical composition of the melt is equalised. After loading the charge, the melt contains a large number of bubbles and insoluble particles of the charge. In order to accelerate the dissolution of charge particles and remove the bubbles, it is necessary to increase the power of the RF generator up to the temperature of the melt (1600–1700)°C. As already mentioned, a characteristic feature of direct RF melting of glasses is the presence of a steep temperature gradient in the melt.

The condition of the melt in the cold crucible is characterised by the maximum temperature which is usually measured with an optical pyrometer. The nonuniform distribution of temperature in the melt has a strong effect on the processes of clarification of the glass mass and dissolution of solid charge particles. The initial process is the removal of bubbles from the zone with the maximum temperature situated at a distance of 10–20 mm from the crucible walls. After holding for 20 min this zone of the melt no longer contains any bubbles. The remaining bubbles are concentrated in the vicinity of the crucible centre.

An important consequence of the steep temperature gradient in the melt is the high-intensity convection of the melt resulting in the clarification of the latter. Figure 6.13 shows the direction of the convection flows in the vicinity of the melt surface decorated with the trajectories of movement of the bubbles in the melt. The layer of the melt, adjacent to the crucible walls, contains charge particles that are in direct contact with the walls of the cold crucible and with the layer of viscous glass whose thickness depends on the operating regime of the generator and is usually 3–5 mm. Because of small variations of the generator power, the skull melts periodically with the generation of bubbles which either 'freeze' in the layer of viscous glass or penetrate into its main volume. In order to eliminate this potential source of bubbles, after holding the melt for 1–1.5 hours, the generator power is slightly reduced. This results in an increase in the thickness of the layer of the viscous glass melt and, consequently, in a decrease of the probability of penetration of bubbles from the skull into the melt. The presence

of the skull layer increases the probability of crystallisation of the glass because the charge particles are potential nuclei situated in direct contact with the melt and, under specific conditions, may initiate the crystallisation of the whole volume of the glass. Thus, if a glass has a high crystallisation capacity, it is very difficult to produce this glass in the cold crucible.

The conditions of production in the cold crucible of glasses with higher crystallisation capacity depend on a large number of factors: the melt volume, the thickness of the layer of viscous glass adjacent to the crucible walls, the viscosity and electrical conductivity of the melt, and also the cooling rate of the melt and the rate of crystallisation of the melt. In practice, it is very difficult to take all these factors into account. However, it may be concluded quite confidently that if the rate of crystallisation in the 'dangerous' temperature range is sufficiently high to ensure that during cooling of the melt the crystal can 'grow through' the entire volume of the glass, then a solidified ingot is produced.

The melt is homogenised using a rod copper water-cooled stirrer, with the speed of revolution being 30–40 rpm. After clarification and homogenising of the melt, the stirrer is withdrawn from the melt and this is followed by a slower decrease of the generator power and the temperature of the melt resulting in a decrease of the electrical conductivity of the melt and, consequently, in an increase of the value of $\Delta$ (for the explanation of the value $\Delta$ see Chapter 1). When $\Delta$ becomes comparable with the crucible radius $\Delta \approx r_0$, the energy absorbed by the melt rapidly decreases and the melt cools down spontaneously as a result of heat transfer through the walls and bottom of the crucible.

A glass with a specific composition has a characteristic temperature dependence of electrical conductivity which determines the lower temperature up to which the cooling rate of the glass may be regulated. For the majority of investigated high-temperature glasses, this temperature is in the range 1400–1500°C. When the temperature is reached, RF equipment is switched off and the glasses cooled in the cold crucible. Cooling of the glass is nonuniform: the peripheral section of the block cools at a considerably higher rate than the central part of the block. The duration of withdrawal of the glass from the crucible is determined by two mutually excluding circumstances: in order to prevent cracking, the glass block must be withdrawn from the crucible as soon as possible; however, this operation may result in heating of
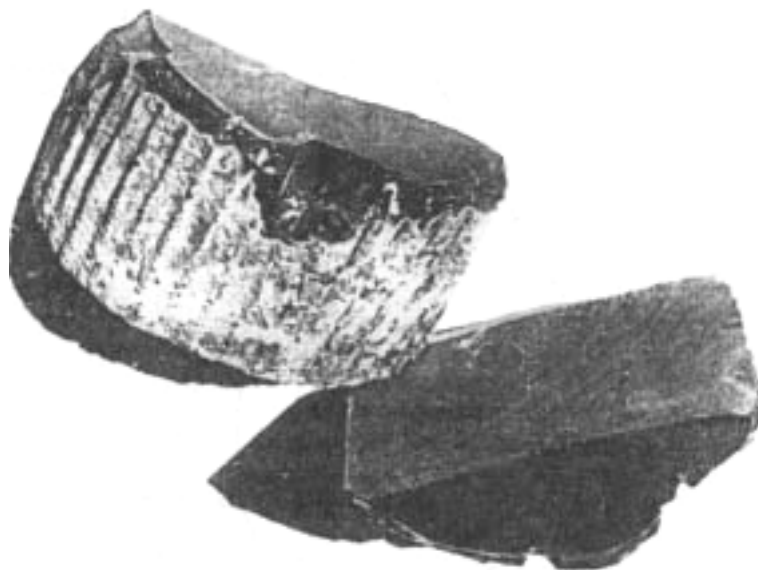
**Figure 6.15**. A block of alumosilicate glass, active with neodymium produced in a cold crucible [6].

the peripheral part of the ingot as a result of the internal hot region. This may result in softening of the peripheral part of the block and escape of glass mass. Experiments show that in extraction of the glass from the crucible at the surface temperature (700–800°C the block does not crack and is not deformed. The glass, withdrawn from the crucible, is annealed in a furnace at a temperature of 800°C for 4–6 hours and is then cooled by inertia in the furnace to room temperature.

The distribution of ripples in the produced glasses was identical with that in NaBSi glass, but the ripples were characterised by a lower contrast, probably as a result of less extensive evaporation of the glass components during synthesis. This technology was used to produce glass blocks weighing 5–7 kg free from lack of boiling defects and bubbles. Figure 6.15 shows a typical casting of neodymium–alumosilicate glass.

## Examination of the range of glass formation in the $La_2O_3$–$Al_2O_3$–$SiO_2$ and $Y_2O_3$–$Al_2O_3$–$SiO_2$ systems

The method of direct RF melting in the cold crucible was used in [6] for the determination of the ranges of glass formation in the $La_2O_3$–$Al_2O_3$–$SiO_2$ and $Y_2O_3$–$Al_2O_3$–$SiO_2$ systems. It should be

mentioned that the method of synthesis in the cold crucible proved to be highly suitable for this purpose because it makes it possible to examine the range of glass formation in no more than two experiments.

The following procedure was used for the preparation of experimental specimens. The two–component $SiO_2 + Al_2O_3$ mixture of a specific composition was loaded into the cold crucible. For starting melting, 3–5 g of aluminium in the form of powder was placed in the initial charge. The powder melted the surrounding charge. After formation of the critical volume of the melt, the melt was heated directly by the energy of the RF field. The melt was held at a temperature of 1800°C up to complete burning-out of the metal floating on the surface of the melt. Usually, this time is ≈ 1 hour. Subsequently, the prepared $SiO_2 + La_2O_3(Y_2O_3)$ mixture of the required composition was added in small portions to the melt (30–50 g). After adding each portion of the charge, the melt was held for 10 min. Subsequently, several droplets of the melt weighing 1–3 g were taken using a quartz stick. The droplets were subsequently quenched on a water-cooled metallic plate. Using this method, it was possible to produce specimens of glasses with compositions in different ranges of the investigated phase diagram.

The proposed method can be used to produce specimens for investigations of the three-component system. It is important to mention one significant principle which must be taken into account in the preparation of specimens for the examination of glass formation ranges. The initial composition of the phase diagram should have a higher liquidus temperature than every following portion. Otherwise, a crust forms on the surface of the metal preventing the averaging of the chemical composition of the melt and the production of specimens with a homogeneous composition. The range of glass formation was determined by the methods of x-ray and microscopic analysis of the specimens and also by visual examination. Figures 6.16 and 6.17 show the areas of glass formation in the investigated systems. In these systems at an $SiO_2$ content in the range 65–75 mol%, an addition of approximately 2 mol% of lanthanum or yttrium oxides results in the formation of transparent glasses. At an $SiO_2 \leq 60$ mol%, the boundary of the range of glass formation is limited by the compositions characterised by surface crystallisation, and at a higher silicon content, the range of glass formation borders with the compositions of glasses characterised by luminescence. The detected widening of the ranges of glass formation in investigated systems is caused evidently by a
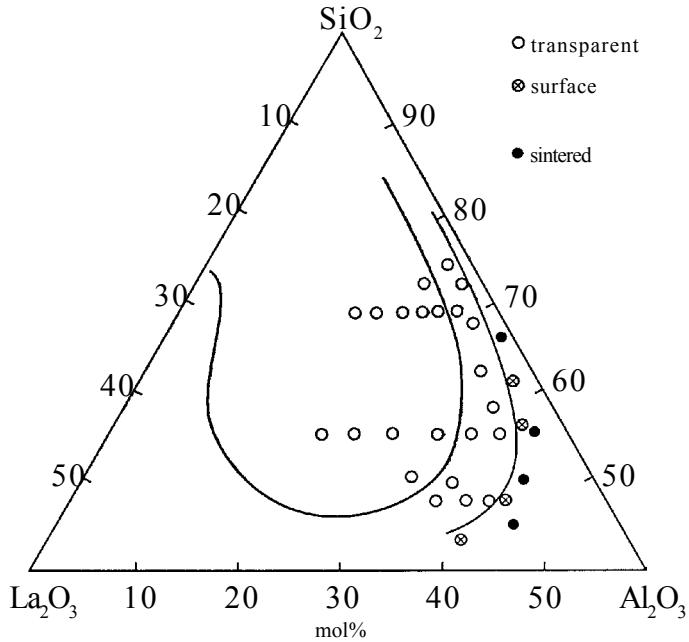
**Figure 6.16.** Region of glass formation in the $La_2O_3$–$Al_2O_3$–$SiO_2$ system. Thick line – synthesis temperature 2000°C [6]; thinner line – synthesis temperature higher than 1600°C [35].
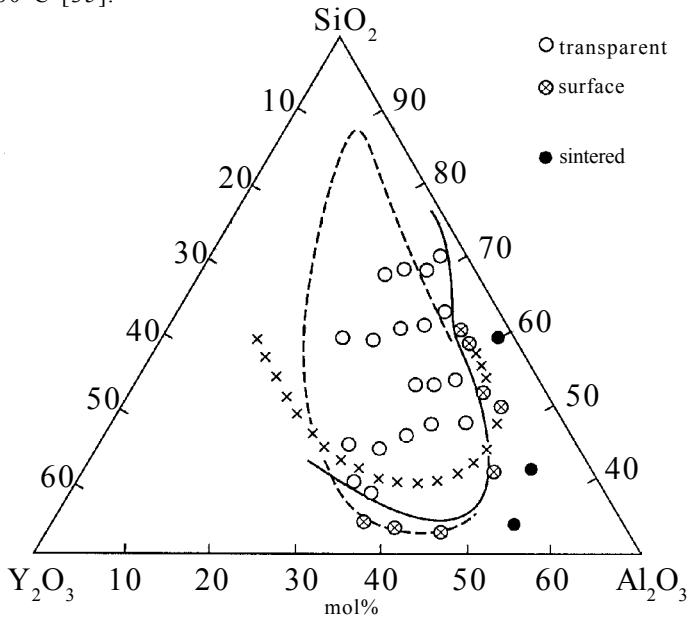


**Figure 6.17.** Region of glass formation in the $Y_2O_3$–$Al_2O_3$–$SiO_2$ system. Data from: - - - - - [6]; ×××× [3]; ——— [1].

**Table 6.5.** Boiling conditions for glass of different compositions

| Glass composition | Anode voltage, kV | Anode current, $I_a$, A | Grid current, $I_c$, A | Melt temperature, °C | Diameter of cold crucible, mm |
|---|---|---|---|---|---|
| $50SiO_2 \cdot 25Al_2O_3 \cdot 25Tb_2O_3$ | 7.0 | 5.5 | 1.15 | | 130 |
| $49.5SiO_2 \cdot 24.7Al_2O_3 \cdot 25.8Nd_2O_3$ | 7.4 | 5.2 | 0.95 | 1730 | 130 |
| $49.5SiO_2 \cdot 24.7Al_2O_3 \cdot 25.8Y_2O_3$ | 7.8 | 5.2 | 1.1 | 1820 | 130 |
| $47.3SiO_2 \cdot 27.5Al_2O_3 \cdot 22.7Yb_2O_3 \cdot 2.5Ho_2O_3$ | 7.8 | 5.5 | 0.85 | 1750 | 130 |
| $54SiO_2 \cdot 27Al_2O_3 \cdot 19Y_2O_3$ | 8.0 | 5.0 | 0.8 | 1770 | 130 |
| $54SiO_2 \cdot 27Al_2O_3 \cdot 19La_2O_3$ | 8.4 | 5.0 | 1.15 | 1770 | 130 |
| $10Sm_2O_3 \cdot 30Al_2O_3 \cdot 60SiO_2$ | 9.0 | 4.0 | 1.2 | 1950 | 90 |
| $10La_2O_3 \cdot 30Al_2O_3 \cdot 60SiO_2$ | 9.7 | 5.2 | 1.1 | 2100 | 90 |
| $10Nd_2O_3 \cdot 30Al_2O_3 \cdot 60SiO_2$ | 9.5 | 4.7 | 1.0 | 2050 | 90 |
| $15Y_2O_3 \cdot 20Al_2O_3 \cdot 65SiO_2$ | 8.5 | 4.3 | 1.1 | 2000 | 90 |
| $15Dy_2O_3 \cdot 20Al_2O_3 \cdot 65SiO_2$ | 8.9 | 5.1 | 0.9 | 2300 | 90 |

high synthesis temperature and a high cooling rate of the analysed samples. The compositions and conditions of boiling of the synthesised glasses are presented in Table 6.5.

## References

1. Sakharov B.A., Sedykh G.S., Ranevskaya E.P., *Trudy Giredmeta*, 1974, Vol. 52, 83–87.
2. Aleksandrov V.I., et al., *Fizika i Khimiya Stekla*, 1977, Vo. 3, No. 3, 177–180; 1980, Vol. 6, No. 2, 170–173.
3. Makishima A., Tamura Y., Sakuino T., *J. Am.Ceram.Soc.,* 1978, Vol. 61, No. 5–6, 247–249.
4. Makishima A., Shimohira T., *J. Non.-Crystaline Sol.*, 1980 Vol. 39/40, part 11, 661–666.
5. Malashkevich G.E., et al., *Zh. Prikladnoi Spektroskopii,* 1982, Vol. 37, No. 2, 261–265.
6. Borik M.A., Development of technology and examination of oxide glasses for electronics, Dissertation, General Physics Institute, Moscow, 1985.
7. Synthesis of laser materials from the melt by direct HF heating ina cold container, Institute of Physics, Russian Academy of Sciences, Moscow, 1985.
8. Moulin J., Reboux I., *Verres et Refractaires*, 1972, Vol. 26, No. 4–5, 123–127.
9. Scott B., Rawson H., *Glass Technology*, 1973, Vol. 14, No. 5, 115– 124.
10. Scott B., Rawson H., *Opto-electronics*, 1973 Vol. 5, No. 4, 285–288.
11. Aleksandrov V.I., et al., *Uspekhi Khimii*, 1978, `Vol. 47, No. 3, 385–427.
12. Nezhentsev V.V., et al., *Izv. LETI, Nauchnye Trudy*, 1980, No. 273, 51–56.
13. Petrov Yu.B., Cold crucibles, Metallurgyia, Moscow, 1972.

14.  Aleksandrov V.I., et al., *Current Topics in Materials Science*, 1978, Vol. 1, 421–479.
15.  Petrov Yu.B., Induction melting of oxides, Energoatomizdat, Leningrad, 1983.
16.  Nezhentsev V., et al., A method of boiling refractory glass and an induction furnace for this purpose, Author' Cert. No. 872 465, USSR, Byul.. Izobr. 1981, No. 38, 123.
17.  Gossink R.G., 11 International Congres on Glass,  Prague, 1977, 114–157.
18.  Gossink R.G., Topical Meeting on Optical Fiber Transmission, Williamsburg, 1975, TaB 4, 1–5.
19.  Parent I. P., LeSergent C., Lerner P., Galay S., Brehan C., Second European Conference on Optical Fibre Communication, Paris, 1976, 33–35.
20.  Demnika L.I. (editor), Physico-chemical fundamentals of production of optical glass, Khimiya, Leningrad, 1976.
21.  Rawson H., *Physics in technology*, 1974, Vol. 5, No. 2, 91–114.
22.  Mase H., Ocda K., *J. Non-Crystalline Solids*, 1980, Vol. 38/39, part 2, 807–817.
23.  Rawson H., J. Non-Crystalline Solids, 1977, Vol. 26, 1–25.
24.  Plumat E., *J. Non-Crystalline Solids*, 1977, Vol. 26, 179–201.
25.  Kobayashi N., *J. Crystal Growth*, 1978, Vol. 43, 337–363.
26.  Kobayashi N., Arizumi T., *J. Crystal Growth*, 1980, Vol. 49, No. 3, 419–425.
27.  Kobayashi N., *J. Crystal Growth*, 1981, Vol. 52, No. 2, 339–344.
28.  Shiroki K., *J. Crystal Growth*, 1977, Vol. 40,  No. 1, 129–138.
29.  Brandle C.D., *J. Crystal Growth,* 1977, Vol. 42, No. 1, 400–404.
30.  Mazurin O.V., et al., Properties of glasses and glass-forming melts, Handbook, Vol 1, Nauka, Leningrad, 1973.
31.  Doladugina V.S., Equipment and methods fo rexamining the homogeneity of quartz, in: Growth of crystals, Institute of Crystallography, Vol. 3, Moscow, 1961, 481.
32.  Bryushkova T.I., et al., *Kvantovaya elektronika*, 1976, Vol. 3, No. 11, 2500–2503.
33.  Bogdanova G.S., Kozel'skaya E.S., Glass-forming systems and new glasses, Khimiya, Moscow, 1971, 49–50.

# A family of crystals – fianites

Single crystals – large crystals of simple and complicated substances, play a significant role in science, technology and industry. They are used in the development of lasers and optical devices, electronic circuits and sections of computers, and different analytical devices. In the group of single crystals important for practice, an important position is occupied by the crystals based on oxide and complex oxide compounds with high melting points and exceptionally high chemical resistance. These are crystals of quartz, corundum, yttrium–aluminium and gadolinium–gallium garnets, lithium niobate or tantalate, and other compounds. Many of crystals of this type are present in the nature in the form of appropriate minerals and follow their traditional names: ruby, garnet, alexandrite, apatite, and so on. However, others have no natural analogues and are known only as artificially produced crystals. In the group of synthesized crystals, new crystals, fianites, are of considerable importance. In recent years, the production of fianites in Russia and throughout the world has reached the level of the production of the 'mass-produced' synthetic crystals.

Fianites is the name for the entire family of the crystals. Their chemical base is represented by dioxides of rare metals, zirconium (Zr) and hafnium (Hf), and the stabilising components are represented by oxides of other elements: yttrium (Y), calcium (Ca) and rare-earth elements characterised by high melting points. The properties of fianites are truly unique. The exceptionally high melting point (depending on composition, the melting point varies in the range 2700–2850°C) is combined with high hardness and chemical resistance. Fianites are optically isotropic because of the

highly symmetric cubic structure. They are characterised by higher transparency in a wide wavelength range, highly refractive index values (2.0–2.2) and high dispersion. Because of their unique properties, fianites are used in technology, medicine, jewellery production since they efficiently simulate diamonds.

## 7.1. POLYMORPHISM AND THE STRUCTURE OF PHASES OF PURE ZIRCONIA

Pure zirconia has three polymorphic modifications: monoclinic ($m$–$P2_1/C$), tetragonal ($t – P4_2/nmc$) and cubic ($c–Fm_3m$). The region of thermal stability of the monoclinic phase extends up to 1140°C, the tetragonal phase from 1160 to 2370°C, and the cubic phase from 2370 to the melting point of 2680°C.

The cubic phase $ZrO_2$ is a non-distorted structure of the fluorite type (Fig. 7.1). The spatial group is $Fm_3m$; the coordination number of oxygen is 4, the coordination number of zirconium in relation to oxygen is 8 [1, 2].

The structural type of fluorite is one of the most widely encountered types of inorganic crystalline materials [3]. The main reason for such large occurrence of the fluorite motive $MX_2$, is the high stability of its cation sublattice, resulting from the distribution of all metallic atoms by the type of the densest cubic packing-in the nodes of the face-centred F-lattice. In particular, this cation structural motive changes constantly in all derivatives of the structure of $CaF_2$, whereas the oxygen matrix often undergoes extensive transformations. The cation sublattice usually has no vacancies, i.e., it is completely filled.

The second special feature of this structural type is the constancy of the coordination of the anions each of which is always surrounded by four metallic atoms, forming together a tetrahedron distorted to various degrees. In Fig. 7.2$a$ the fluorite structure is depicted in Pauling polyhedrons showing clearly the primitive cubic packing of the anions distributed in the form of layers in the nodes of the quadratic cell. Half of all anion cubes is populated in accordance with the three-dimensional checkered law. The cations are characterised by the eightfold coordination. Each node of the cation cell has four filled and four empty polyhedrons.

If some atom X of the anion packing is eliminated from the investigated motive, the four polyhedrons of the cube, previously situated in the close vicinity of the selected node, loose one apex
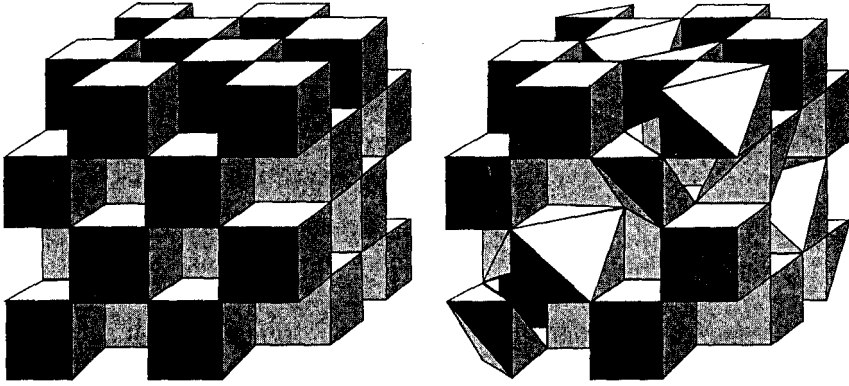
**Figure 7.1.** Structural type of fluorite [2].
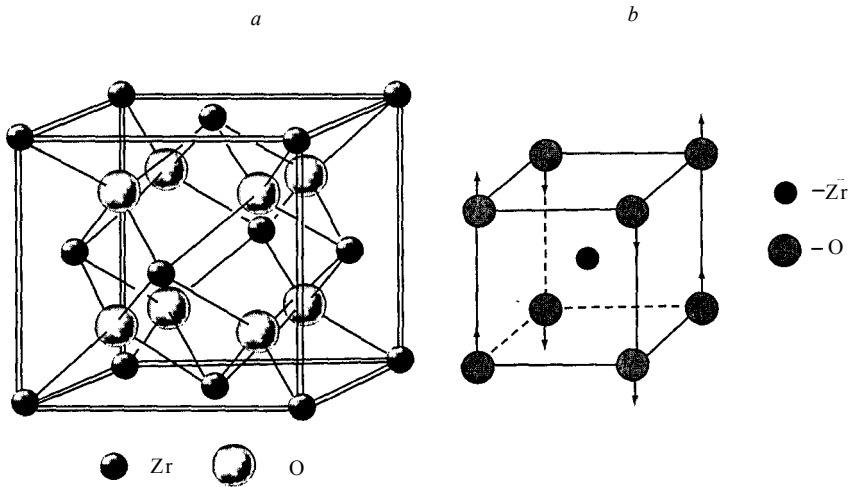


**Figure 7.2.** Structural type of fluorite (a) and the structure of pyrochlore derived from it (b).

each and transform to the heptahedron (Fig. 7.3*b*). Neither the face-centred distribution of the cation nor the coordination of the remaining anions change. Finally, such a derivative deduction structure is favourable fo incorporation of the metal ions with different chemical nature and geometrical parameters. As a result of the transformation of the vacancies in the X-sublattice, the initial M-cube may be transformed into new polyhedrons (Fig. 7.3*a–e*). Investigations of specific structures have confirmed the existence of cubes (*a*), hexahedrons (*b*) and also of polyhedrons of the type (*d*) and (*e*), with the octahedrons found most frequently in the two

latter types. The possibility of formation of trigonal prisms (*c*) has not as yet been explained [7]. The Pauling polyhedrons, shown in Fig. 7.3, have the limiting (idealised) form. In the real structures, these polyhedrons are distorted to various degrees which is the result of a large number of compromises in the produced crystal lattice. The largest movement is shown by the oxygen atoms which usually move in the direction of the vacancies, resulting in a more isometric form of the M-polyhedrons. In particular, the 'flattened' octahedrons (*d*) acquire their usual configuration, observed in the majority of the known inorganic compounds.

The tetragonal phase $ZrO_2$ has a crystal structure of slightly distorted fluorite (Fig. 7.4). The spatial group is P4$_2$/*nmc*, the lattice parameters are *a* = *b* = 5.085A, *c* = 5.166; *a/c* = 1.016 [4–6].

When the temperature is reduced to 2370°C, the cubic phase becomes unstable and transforms to tetragonal modification as a result of the distortion of the fluorite structure. Due to small movement of the atoms, the oxygen ions are displaced in relation to the ideal position (1/4, 1/4, 1/4) in the fluorite lattice. However, this does not result in any change of the coordination number of zirconium in the Pauling octahdera, which transform into dodecahedrons. Four oxygen ions are situated at a distance of 2.065 A in the straightened tetrahedron, four other ions – at a distance of 4.455 A in the distorted tetrahedral positions. On the whole, the lattice of the tetragonal phase slightly increased in the length in the direction of the *c* axis in comparison with the cubic lattice.

The monoclinic phase $ZrO_2$ belongs to the spatial group P2$_1$/*c*, the lattice parameters are *a* = 5.169 A, *b* = 5.232 A, *c* = 5.341 A, β= 99°15', *Z* = 4 [1–3, 7–10].

The next phase transition, observed when the temperature is reduced below 1200°C, transforms the tetragonal structure to monoclinic, stable in the normal conditions. In particular, the crystals of this modification are found in the Earth's crust and are known as baddeleyite. Their structure is the result of further distortion of the cubic structure of $ZrO_2$, whose rearrangement is so extensive that a completely new structural type forms. The coordination number of zirconium decreases to 7 (Fig. 7.5*a*) but not as a result of the previously mentioned 'truncation' of the M-cubes, and is due to the unique packing of the oxygen atoms whose number corresponds to the initial stoichiometry $MO_2$. In this packing, half of all the square networks remains unchanged (only slightly deformed), and the anion motive of the fluorite structure may be
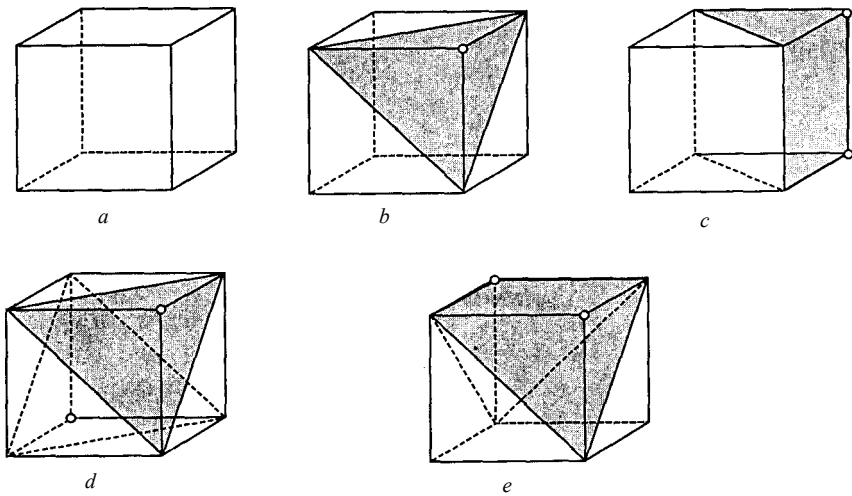
**Figure 7.3.** Pauling polyhedra formed from the cube as a result of 'truncation' of its tips (anion vacancies) [3]. a) cube; b) heptahedron; c) trigonal prism; d) octahedron; e) hexahedron with a single quadratic face.
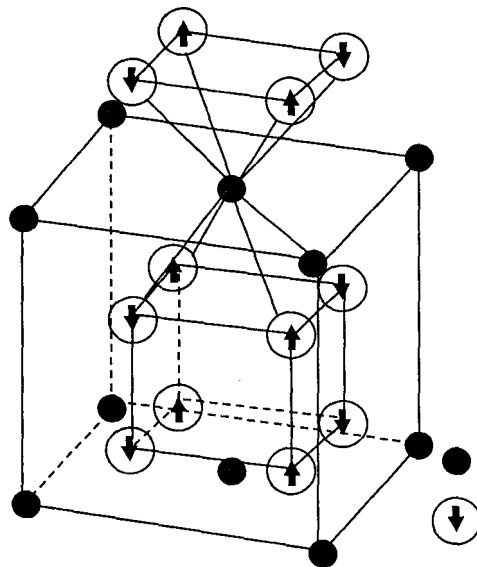


**Figure 7.4.** Tetragonal structure of $ZrO_2$.

located on them (Fig. 7.5*b*). The remaining anion networks, alternating with the former ones, are greatly distorted and their loops are represented by oblique squares with the double number of the triangles. As a result of monoclinic shift of the layers
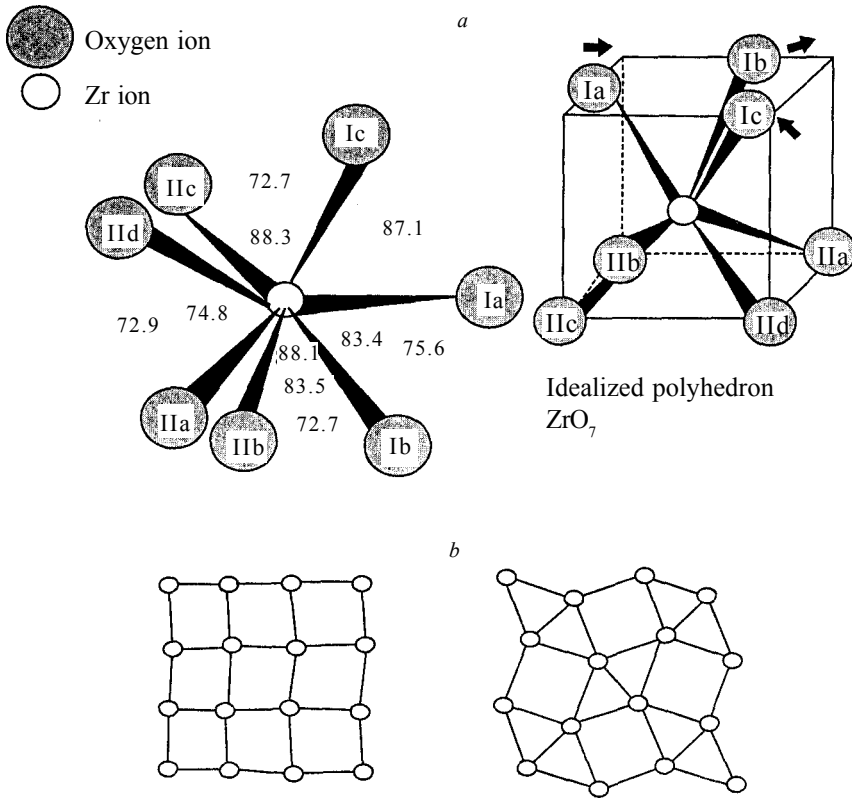
**Figure 7.5**. Structure of monoclinic zirconia (a) and two types of alternating anion networks (b).

zirconium atoms, retaining the checkered order of alternation, appear between loops of adjacent networks with different configuration: one square and one triangular. All the cations greatly deviate (by 0.2 Å) from their ideal positions, coinciding with the nodes of the F-lattice. In the final analysis, one of the main criteria which determine the structural type of fluorite and its derivatives – tetrahedral coordination of all anions, is violated. In the crystal structure of baddelyite only half of the oxygen atoms is characterised by quatenary coordination, whereas the remaining atoms have the coordination number 3.

The crystal structure of monoclinic $ZrO_2$ is characterised by very high stability, as indicated not only by the wide temperature range of existence of the monoclinic phase but also by the uncommon stability of baddelyite in the natural conditions. The monoclinic structure is characterised by twinning whose planes $\{100\}m$ or $\{110\}m$ are formed by the oxygen ions.

## 7.2. PHASE DIAGRAM OF THE SYSTEM $ZrO_2$–$R_2O_3$ (WHERE R – Y, Eu, Gd, Yb)

The equilibrium diagrams of the $ZrO_2$–$R_2O_3$ system, where R are the rare-earth elements (REE), are complicated systems of intermediate phases whose stability and length are not governed by simple relationships [11]. The allied structures of the phases, formed in these systems, change from the structure of the type of fluorite to the structure of the type $Ti_2O_3$ with the increase of the content of the REE oxide. This continuous transition is characteristic of high temperatures. At lower temperatures, there are phases of P-pyrochlore and $H_1$, $H_2$, $H_3$ and hexagonal phases. All these phases are derivatives of the structure of fluorite and their formation is the result of establishment of different degrees of structural order [12].

Some systems based on zirconia are characterised by a long history of investigations but, regardless of this, the results are highly contradicting. This is associated with a large number of difficulties resulting from the special features of the structure of zirconia and also from establishment of true equilibrium in these systems [13]. Firstly, at temperatures above 2000°C it is difficult to examine directly the crystal structure and, therefore, a large number of x-ray investigations were carried out at room temperature on specimens quenched from high temperatures. However, even with very fast cooling, there may be changes in the ratio of the phases and this complicates the interpretation of the results. Secondly, at temperatures below 1200°C, a reverse problem appears: the diffusion of ions is so slow that equilibrium is difficult to establish.

In these conditions, the process of construction of accurate equilibrium diagrams of several most important 'zirconium' systems has been very slow and the results have been contradicting. However, certain successes were achieved in the 60s and 70s of the previous century: the existence of a high-temperature cubic phase [14], discovery of the ordered phases in the $ZrO_2$–MgO [15,16], $ZrO_2$–CaO [17], $ZrO_2$–$Y_2O_3$ [18–20] systems, and the accurate determination of the field of stability.

**The $ZrO_2$–$Y_2O_3$ system.** In the system, the yttrium oxide is one of the main stabilisers of the cubic structure of $ZrO_2$. The system was investigated for the first time by Ruff and Ebert [21]. The system is characterised by the presence of wide areas of solid
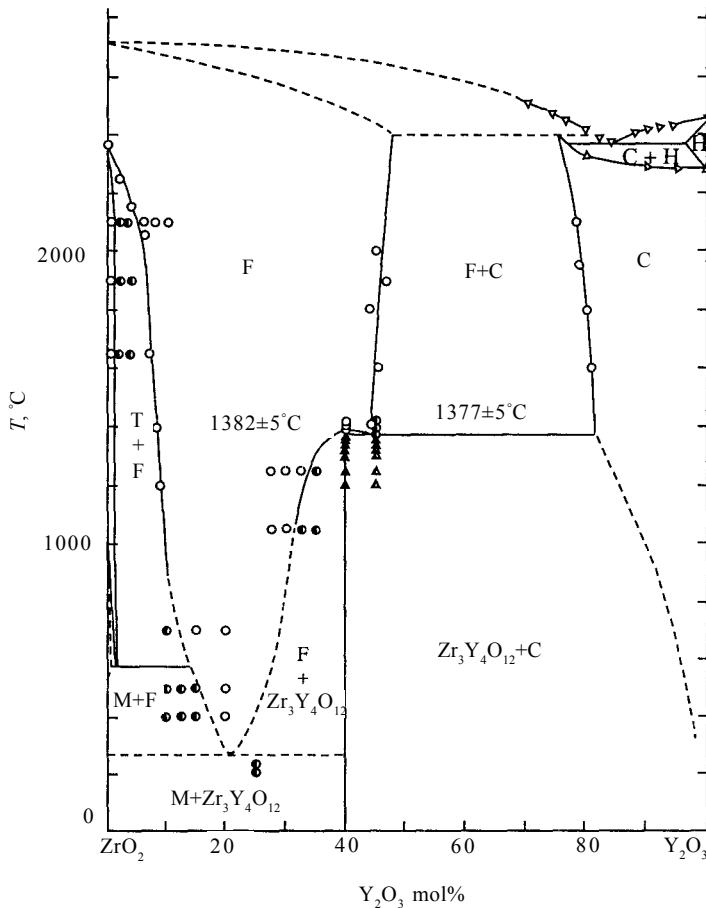
**Figure 7.6**. $ZrO_2$–$Y_2O_3$ equilibrium diagram [22].

solutions, both on the side of zirconia and on the side of yttrium oxide. Later, the equilibrium diagram of the zirconium systems were studied in detail by Stubican [22], Scott [23], Pascual and Duran [24] and the results are shown in Fig. 7.6.

All these diagrams show that in addition to the solid solutions, the system is characterised by the stable compound $Zr_3Y_4O_{12}$ which forms at a content of 40 mol.% $Y_2O_3$ and was synthesised for the first time and described by Ray and Stubican. Scott also detected a long area of ordering at 40 mol.% of yttrium oxide. According to Scott's data, $Zr_3Y_4O_{12}$ is stable below 1370°C and is characterised by a narrow region of homogeneity [23]. According to Stubican, the δ-phase forms as a result of the disruption of the order in the distribution of the ions in the cubic solid solution at temperatures
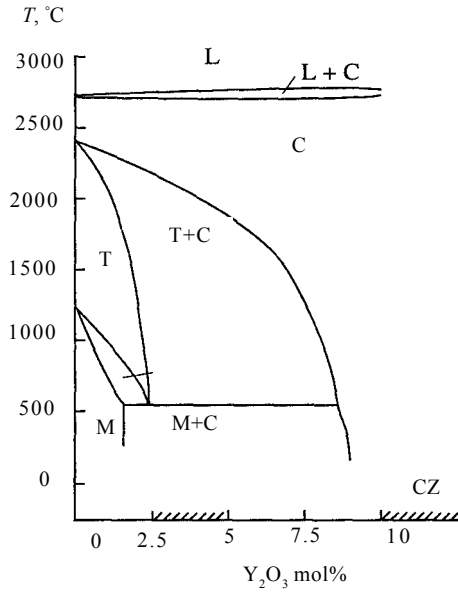
**Figure 7.7.** Part of the equilibrium diagram of the $ZrO_2$–$Y_2O_3$ system on the side rich in zirconium oxide [12].
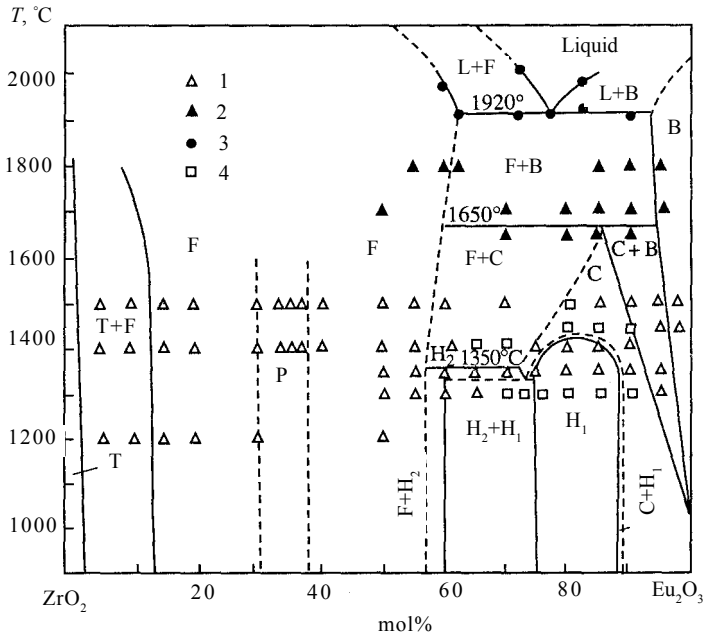


**Figure 7.8.** Diagram of the $ZrO_2$–$Eu_2O_3$ system [29]

above 1382+5°C [5]. The structure of the δ-phase is a derivative of the fluorite structure with ordered distribution of the oxygen vacancies and the formation of a rhombohedral cell. However, there are also contradictions between the three proposed diagrams.

Since the part of the phase diagram on the side of zirconium is very important from the practical viewpoint, the subsolidus equilibrium in this part of the diagram has been studied by many authors. The most detailed study was published by Scott (Fig. 7.7). The characteristic property of the phase diagram in this region is the decrease of the temperature of the tetragonal–monoclinic transition with increase of the yttrium content.

With increase of temperature above the region of stability of the monoclinic phase there is a narrow two-phase monoclinic-tetragonal region which is followed by the region of the so-called transformed tetragonal phase (*t'*). The transformed tetragonal solid solution which undergoes transformation to the monoclinic phase in cooling, exists in the composition range from 0 to 5 mol.% $Y_2O_3$. At higher yttrium oxide concentrations, there is a two-phase region of the non-transformed tetragonal (t) and cubic solid solutions. A further increase of the concentration of yttrium oxide results in the formation of the single-phase cubic solid solutions. The nature and property of the untransformed tetragonal phase and also the formation of the cubic phase from the tetragonal phase during a phase transition, have been studied in detail by Anderson [25].

Investigations of the subsolidus equilibrium at a low content of yttrium oxide in the $ZrO_2$–$Y_2O_3$ system were carried out by Ruh et al [26]. They found that approximately 1.5 mol.% of $Y_2O_3$ dissolves in monoclinic zirconia at 500°C, whereas the two-phase region (monoclinic solid solution + cubic solid solution) exists at temperatures below 500°C to 7.5 mol.% $Y_2O_3$. The agreement with the results obtained by Stubican is relatively good with the exception of the existence of a region of cubic solid solutions below temperatures of 1200°C. The difference forms owing to the fact that it is almost impossible to establish equilibrium at these temperatures. The results obtained by Stubican were recorded at low temperatures and using the hydrothermal method of synthesis of the compound in order to increase the reaction rate. In this case, a eutectic composition forms at temperatures below 400°C in the range 20–30 mol.% $Y_2O_3$: cubic $ZrO_2$ (solid solution) (monoclinic phase $ZrO_2$) +$Zr_3Y_4O_{12}$. It is assumed that the equilibrium phases below the eutectoid transformation temperatures are the monoclinic solid solution based on zirconia and $Zr_3Y_4O_{12}$ compound.

The regions of the two-phase mixture of the solid solutions based on zirconia and yttrium oxide are in the ranges: 64–76; 69–79; 73–86 mol.% $Y_2O_3$ at temperatures of 1400, 1700 and 2000°C, respectively.

In [27] in the investigations of the process of evaporation of the $ZrO_2$–$Y_2O_3$ solid solution it was found that the composition with the yttrium oxide content of approximately 20 mol.% behaves as an azeotrope.

### The $ZrO_2$–$Eu_2O_3$ system

The phase transformations in the systems were investigated in [28, 29]. A solid solution with the cubic lattice of fluorite was identified in the $ZrO_2$–$Eu_2O_3$ phase diagram shown in Fig. 7.8. It is characterised by a wide range of homogeneity from 10 to 55 mol.% of $Eu_2O_3$. In the composition range 27–39 mol.% $Eu_2O_3$ a $Eu_2Zr_2O_7$ phase forms on the basis of the solid solution F. This phase is characterised by the ordered crystal structure of the pyrochlore type. The boundary of the region of homogeneity of this compound on the $ZrO_2$–rich side ($T$ = 800–1400°C) is situated close to $x$ = 1.48 mol.% $Eu_2O_3$ [29].

**The $ZrO_2$–$Gd_2O_3$ system**. The system was investigated in [30–33]. Specimens were synthesised by the solid phase method and a compound with the structure of pyrochlore was found in a wide homogeneity range (Fig. 7.9). Several types of solid solutions were also found in the system: 1 – the tetragonal solid solution based on zirconia in the subsolidus range (above 1000°C); 2 – the cubic solid solution of the fluorite type; 3 – the cubic solid solution of the $Tl_2O_3$ type; 4 – the solid solution with the pyrochlore structure ($a$ = 10.527 Å with the composition $Gd_2Zr_2O_7$); 5 – the hexagonal phase existing in narrow ranges in the vicinity of 57 mol.% $Gd_2O_3$, with the lattice parameters: $a$ = 10.002 Å, $c$ = 18.644 Å; 6 – the hexagonal phase, stable below 1600°C and containing 77–78 mol.% of $Gd_2O_3$: $a$ = 10.032 Å, $c$ = 18.814 Å. The authors of [33] investigated the equilibrium diagram of the $ZrO_2$–$Gd_2O_3$ system with the gadolinium oxide content up to 10 mol.% (Fig. 7.9).

In the investigations of the system by the 'annealing and quenching' method it was established that there are solid solutions based on both $Gd_2O_3$ and $ZrO_2$ at a temperature of >2000°C. The wide region of the solid solutions based on zirconia is characterised by a continuous transition of the tetragonal solid solution to the
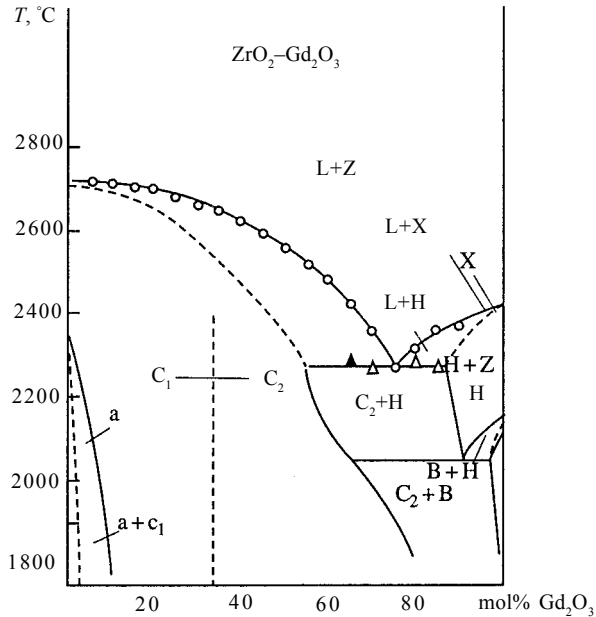
**Figure 7.9.** Diagram of the $ZrO_2$–$Gd_2O_3$ system [33].
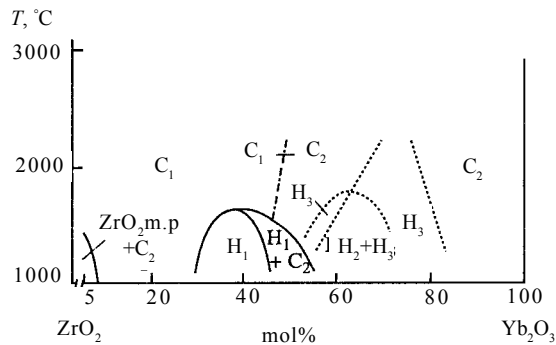


**Figure 7.10.** Diagram of the $ZrO_2$–$Yb_2O_3$ system [34].

cubic type of fluorite and of the latter to the cubic solid solution of the type $Tl_2O_3$.

## The $ZrO_2$–$Yb_2O_3$ system

In the system (Fig. 7.10) investigations showed the existence of several types of solid solutions: 1) the solid solution based on tetragonal zirconia at temperatures above 1000°C; 2) the cubic solid

solution of the fluorite type; 3) the cubic solid solutions of the $Tl_2O_3$ type. The latter should be regarded as solid solutions of zirconia in the cubic ytterbium oxide [31, 32]. The system is characterised by the presence of a rhombohedral phase (H) and two hexagonal phases. The parameters of the elementary cell were determined for the phase H. For the compositions with 33 mol.% $Yb_2O_3$: $a = 8.178$ Å, $\alpha = 72°32'30''$, and for the compositions with 40 mol.% $Yb_2O_3$: $a = 8.259$ Å, $\alpha = 72°40°20''$. The phase with the pyrochlore structure was not found in the system, but the existence of the $Zr_3Yb_4O_{12}$ compound was detected on the $ZrO_2-Yb_2O_3$ equilibrium diagram [34], Fig. 7.10.

Examination of the structural and phase transformations of nominally pure zirconia, stabilised by yttrium oxide, and also of rare-earth elements shows that there are three types of crystals, differing in the structure, physical and mechanical properties, which form three independent branches of development of new directions. These are the completely stabilised zirconia with the stable cubic structure whose crystals are referred to in Russia as fianites and are used efficiently in technology and jewellery industry. These are crystals with an incompletely stabilised cubic lattice, whose crystal structure depends on temperature, the nature and amount of the stabilising oxides. In this group of the crystals, it is necessary to mention the crystals with a partial phase transition from the cubic to tetragonal phase. This transformation results in the formation of domains of complicated geometry which fill the entire volume of the crystal. The high mechanical properties have been the main interesting points of these crystals in recent years: the strength and toughness of the material. The experimental results show that the increase of the concentration of the stabilising oxide above specific values, for example, for $Y_2O_3 > 20$ mol.%, results in a change of the local environment of the admixture cations; the crystals retain the cubic structure of the fluorite type. Thus, a new optical matrix, the C-OX single crystals, form. In doping with ions of the transition metals, the C-OX single crystals are characterised by greatly differing optical properties in comparison with the fianites. In the following chapters, all the three types of the crystals will be studied in detail.

The stability of the solid solutions based on zirconia depends on the nature and concentration of the stabilising oxide, temperature, annealing time and chemical purity of the initial reagents. The specimens, produced by crystallisation of the melt, as indicated by

the equilibrium diagram, are not equilibrium at room temperature.

The stability of the solid solutions based on $ZrO_2$, produced by the directional solidification of the melt, was investigated in [35]. Crystalline specimens, containing 1–33 mol.% of the stabilising oxides, and powders prepared from them were annealed in air at a temperature of 1000°C for 10 days and at 1200°C for 45 days.

After annealing, no changes were detected in the x-ray diffraction patterns of the crystals. No turbidity was observed in the cubic single-phase crystals. Annealing of the powders of the same composition at 1000°C also caused no changes. In annealing for 45 days at 1200°C, examination showed the partial decomposition of the solid solutions of several compositions, shown in Table 7.1. A monoclinic phase appeared at low concentrations of the stabilising oxide: at a concentration of the stabilising oxide of 10–33 mol.%, the cubic phase in the solid solutions remained also after annealing.

Thus, the single crystals of the cubic solid solutions, produced by directional solidification of the melt, are stable at high temperatures. Annealing for 45 days at 1200°C of the crystals, refined into powder, show the formation of the monoclinic phase only for the composition the $ZrO_2$–8 mol.% $Eu_2O_3$. No monoclinic phase formed after annealing in the compositions $ZrO_2$–(8–33) mol.% $R_2O_3$, where R is Gd, Y, Yb and $ZrO_2$–(10–33) mol.% $Eu_2O_3$.

In [35], a series of experiments was also carried out with the growth of crystals with a low solidification rate (1–2 mm/h) followed by long-term annealing (14–40 *h*) by a smooth decrease of the power of the generator; the temperature in the crucible was varied from 2600 to 1200°C (Table 7.2).

The crystals with the composition $ZrO_2$–12 mol.% $R_2O_3$ (R–Y, Gd), and $ZrO_2$–8 mol.% the $Gd_2O_3$, grown in these conditions, were turbid, although no significant changes are detected on the x-

**Table 7.1.** Phase composition of powders after annealing at 1200°C for 45 days

| Composition of crystals | $R_2O_3$ content, mol% | | | | | | | |
|---|---|---|---|---|---|---|---|---|
| | 1 | 2 | 3 | 5 | 8 | 10 | 12-20 | 33 |
| $ZrO_2$–$Eu_2O_3$ | M | M+T | M+T | T+M | F+M | – | F | P |
| $ZrO_2$–$Gd_2O_3$ | M | M+T | M+T | T+M | F | F | F | F |
| $ZrO_2$–$Yb_2O_3$ | M | M+T | M+T | T+M | F | F | F | F |

ray diffraction diagrams of these crystals. The examination by the Raman scattering method did not show the presence of a second phase in the crystals. Nevertheless, in investigations using a laser ultramicroscope, it was established that the scattering of the light in the crystals is caused by the particles of the second phase with the size of 1–0.1 μm. The crystals with the composition $ZrO_2$–$R_2O_3$ (R–Y, Yb) with the concentration of 14–33 mol.% and $ZrO_2$–16 mol.% $Gd_2O_3$, grown in the same conditions remained transparent. The appearance of the scattering particles may be associated both with the presence of secondary admixtures in the charge whose solubility decreases with decreasing temperature, and with the decomposition of the fluorite solid solution.

The direct determination of the composition of the second phase and of its structure is difficult because the content of this phase is very low and the particle size is very small. It should be mentioned that after heating the specimens to 2100°C (in vacuum) for 30 *h* and subsequent rapid cooling at a rate of 1000°C/h there was almost no scattering of the light in the crystals with the composition $ZrO_2$–12 mol.% $Y_2O_3$.

In slow crystallisation and subsequent slow cooling of the crystals with the composition $ZrO_2$–(8–12) mol.% $R_2O_3$ (R–Gd, Y, Yb a) a second phase appeared (Table 7.2), but the amount of this phase was small and its nature could not be determined by x-ray diffraction analysis. The single crystal nature of the specimens is not disrupted, but they intensively scatter the light. The crystals with the composition $ZrO_2$–(16–33) mol.% $R_2O_3$ (R–Gd, Y, Yb) do not show any changes in the same growth and annealing conditions. Thus, in directional crystallisation of the $ZrO_2$–$R_2O_3$ melts, depending on the type and concentration of the stabilising oxide and also on the growth regime, the process yields either non-transparent crystals, containing scattering particles of the second phase, or optically homogeneous single crystals (Table 7.2).

The phase composition of the crystals $ZrO_2$–$R_2O_3$ (R–Eu, Gd, Y, Yb), grown from the melt, is not thermodynamically equilibrium in relation to room temperature. For the crystals with the concentrations of the stabilising oxide of 1–5 mol.% $R_2O_3$, the characteristic feature is the presence of several phases. This problem will be examined in greater detail in Chapter 8, concerned with partially stabilised crystals of zirconia. At the concentration of the stabilising oxides 8–40 mol.% $R_2O_3$ (R–Eu, Gd, Y, Yb) the solid solution with the fluorite structure undergoes the order–disorder

**Table 7.2**. Effect of composition and growth conditions on the stability of solid solutions (growth rate 1–2 mm/h, cooling directly in crucible to 1000°C for 12–40 h) [35]

| Composition | External appearance of crystals | XDA data on phase composition |
|---|---|---|
| $ZrO_2$–12 mol% $Y_2O_3$ | Slightly scattering | Single-phase cubic solid solution with fluorite structure |
| $ZrO_2$–16 mol% $Y_2O_3$ | No scattering | |
| $ZrO_2$–8 mol%$Gd_2O_3$ | Strong scattering | |
| $ZrO_2$–12 mol%$Gd_2O_3$ | Slight scattering | |
| $ZrO_2$–16 mol%$Gd_2O_3$ | No scattering | |
| $ZrO_2$–14 mol%$R_2O_3$(Y,Yb) | No scattering | |

transition with increase of the $R_2O_3$ concentration. It has been established that at the content of the stabilising oxide of > 8 mol.% $R_2O_3$, solid solutions are produced in the form of transparent single-phase single crystals, characterised by high phase stability at temperatures up to 1200°C in air for at least 45 days.

Examination of the process of decomposition of the solid solutions in high-temperature annealing shows that large single-phase, optically homogeneous single crystals can be produced only when using the conditions of slow solidification at a rate of 1–2 mm/h followed by a slow decrease of temperature to 1200°C (at a rate of 10°C/h) at the content of the stabilising oxides: $R_2O_3$ more than 14 mol.% for Y, Yb and more than 16 mol.% for R–Eu, Gd.

## 7.3. PRODUCTION OF FIANITES

As mentioned previously, the method of direct HF melting in a cold crucible is at present the only method of producing large single crystals of stabilised zirconia and hafnia–fianites.

The initial reagents for the growth of fianites are dioxides of zirconia, hafnium, yttrium, and also oxides of certain alkali-earth and rare-earth elements used as stabilising or colouring additions. In most cases, high-purity reagents are used.

Fianite technology includes several main stages. The first stage is the process of start melting. Start melting is usually realised by introducing, into the volume of the molten material, a metal included in the composition of the components of the material. For example, to produce $ZrO_2$–$Y_2O_3$ crystals, metallic yttrium is added to the

charge, and for the $ZrO_2–R_2O_3$ (R–Eu, Gd, Yb) crystals it is metallic zirconium or the appropriate rare-earth element, for $HfO_2–Yb_2O_4$ it is metallic hafnium. Usually, the amount of starting metal is approximately 10–15 g per kilogram of the weight of the charge.

Heating of the metal and the surrounding charge in the process of start melting takes place as a result of the absorption of the energy of the HF field and was also the result of the exothermic reaction of oxidation of metal by atmospheric oxygen. In every specific case, the special feature of the process depends on the physical–chemical properties of the metal used. Another important factor in the conditions of the starting process: atmosphere, the depth of the starting metal in the charge, the degree of refining of the metal, dispersion of the charge. These factors determine to a certain degree the duration of the starting period. The physicochemical properties of the metal used for starting were published previously in Table 2.2.

In the fianite crystals with the composition $ZrO_2–R_2O_3$, where R is Eu, Gd, Yb, the concentration of the oxides of the rare-earth elements changes in the range 8–33 mol.% [33].

The main and stabilising oxides are mixed in plastic cuvettes. Thorough mixing of the charge, subsequent sintering and grinding of the mixture prior to melting has no significant effect on the quality of the ground crystal. Therefore, after mixing, the charge is directly loaded into the container. The melting of these compositions is carried out in a container with a diameter of 130 mm, height 160 mm. Equipment Donetsk-4 is used for melting and growth of the crystals. Zirconium oxide crystals, stabilised with yttrium oxide, were also grown in other systems, described in Chapter 2. Usually, the diameter of the crucible was 220 mm, height 300 mm. In growing $ZrO_2–Y_2O_3$ in large containers, the charge produced from powder reagents was used together with crystal waste of the same composition in the ratio of 4/3, and the total weight of the charge was 14 kg. The application of compacted material shortens the loading time and reduces the amount of waste. It should also be mentioned that directional crystallisation is accompanied by additional purification of the initial charge. The use of the crystalline material also improves the quality of grown crystals.

The loading of the container is the important stage of the technological process which controls the dimensions and optical homogeneity of the crystal. Prior to loading, a layer of the sintered

charge several centimetres thick is placed on the bottom of the container and this is followed by loading the charge with the crystals. The shavings of starting metal are deposited at the top in the depths of 2–4 cm and compacted. The melting of the charge starts 5–20 min after activating the generator. Indication of melting is the high-intensity glow between the sections of the crucible. At the start of melting, the working parameters of the generator rapidly change. The power generated in the load in Donetsk-4 equipment is controlled using a calibrated constantan–copper thermocouple measuring the temperature of water at entry into and exit from the container. The temperature difference is proportional to the power removed from the container. The temperature of water is determined with the accuracy of ±0.1°C. The consumption of water, flowing through the container, is controlled by a contact pressure gauge. The power in the melt, is calculated from the equation:

$$p = V/t(T_2 - T_1)C, \qquad (7.1)$$

where $V$ is the volume of the water flowing through the container, m³; $t$ is time, $s$; $\Delta T = T_2 - T_1$ is the temperature difference of water at entry into and exit from the container, deg; $C$ is the heat capacity of the water, J/(m³ · K).

During melting, the power, absorbed by the melt increases as a result of the increase of the melt volume. Thus, by varying $\Delta T$ it is possible to control the melting process. For example, when the next portion of the charge is placed on the surface of the melt, the value $\Delta T$ rapidly decreased (Fig. 7.11), since part of the energy is used for heating the charge. This results in partial solidification of the melt, a decrease of the volume of the melt and, consequently, weakening of the inductive bond resulting in the instability of the parameters of the generator ($U_a$, $I_a$); with a subsequent gradually increase of the volume of the melt, the value of $\Delta T$ increases.

The charge is also added in the crucible to ensure that the volume of the melt reaches the required value. At the end of loading, the charge forms a cupola-shaped 'roof' above the melt which baked under the effect of intensive radiation of the melt. The 'roof' reduces the heat losses from the surface of the melt. The duration of starting up the container with the diameter of 220 mm with the charge is 1–1.5 h.

At the stable level of the supplied power the container with the
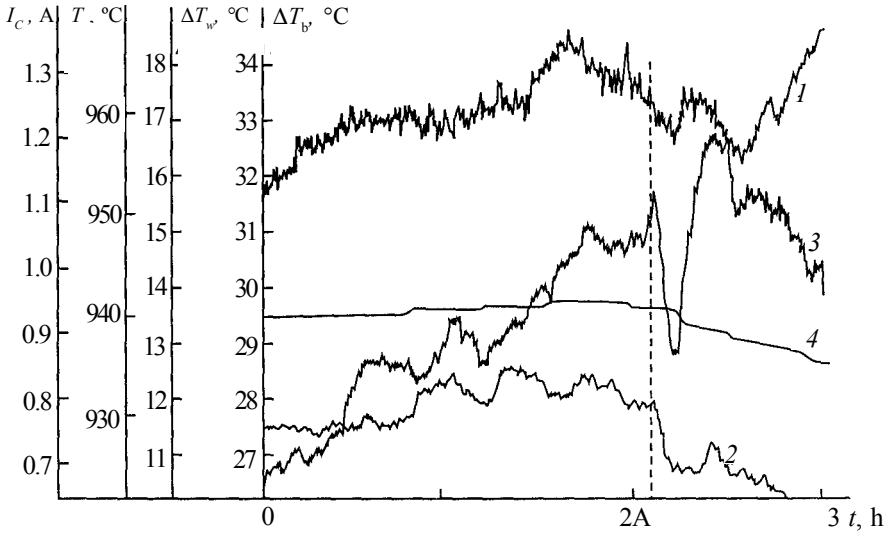
**Figure 7.11.** Time dependences of: 1) $\Delta T_b$; 2) $\Delta T_w$; 3) $\Delta T_p$; 4) $l_C$ [37].

melt is held for 30–40 min to establish phase equilibrium. Solidification is initiated by lowering the container with the melt in relation to the induction coil. With exit of the lower part of the container from the induction coil, the bonding of the melt with the induction coil decreases and, correspondingly, the supply of energy to the melt becomes smaller. As a result of the gradual cooling of the lower part of the container, the process of solidification of the melt starts spontaneously.

The anode ($I_a$) and grid ($I_{gc}$) currents are the parameters sensitive to the variation of the melt volume. Therefore, it is possible to carry out objective control of the phase equilibrium between the melt and the solid phase in the course of the process. Figure 7.12 shows the time dependences of $I_{gc}$ and $I_a$ in the processes of homogenisation, solidification of the melt, and annealing of the grown crystals. $U_a$ was maintained constant.

In addition to the anode and grid currents, another sensitive parameter is the frequency of generation which is sensitive to the variation of the load. Donets-4, Fianit and Kristall-401 can be used for producing 1.5–6 kg of crystals in a single process.

To evaluate the effect of the conditions of directional solidification on the phase composition and optical homogeneity of the crystals, the rate of loading of the crucible was varied in the range 1–40 mm/h. The results show the increase of the size of the single crystals with a decrease of the lowering rate of the container
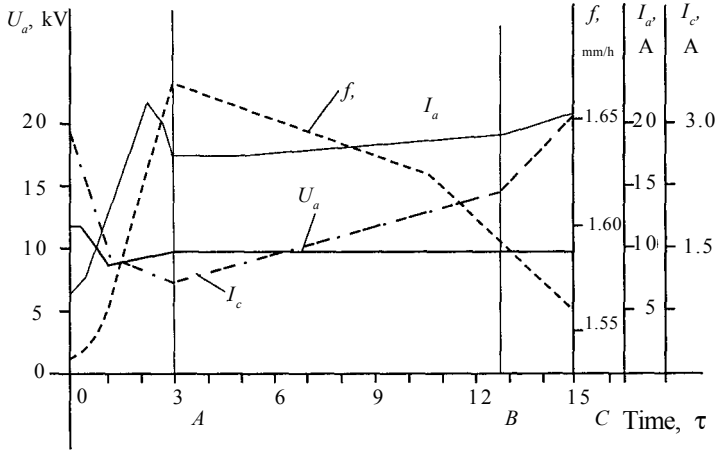
**Figure 7.12.** Drift of the electrical parameters of Kristall-401 equipment in real melting and solidification processes of cubic zirconia. $I_a$ – anodic current; $f$ – the frequency of HF generator; $I_c$ – grid current; $U_a$ – anodic voltage; (O–A) – process of homogenizing the melt; (A–B) – growrth of the crystal block; (B–C) – annealing.
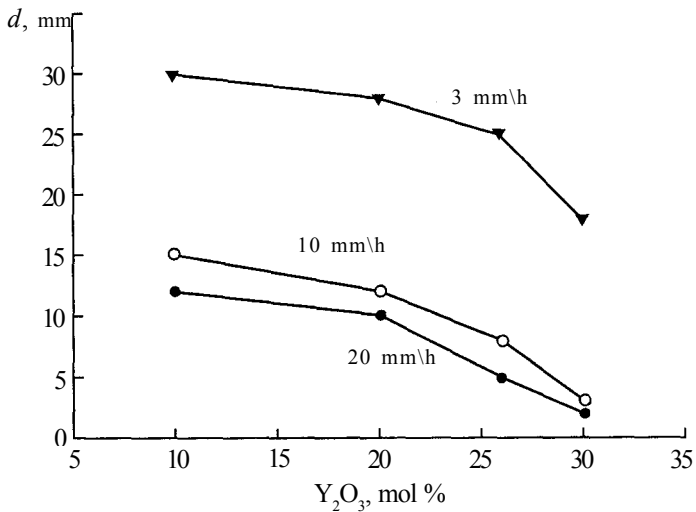


**Figure 7.13.** Dependence of the size of cubic zirconia crystals on the content of the stabilizing oxide $Y_2O_3$ and solidification rate (indicated at the curves).

[37, 38]. This is due to the fact that the polycrystalline layer of the solid shell contains a large number of crystallisation centres, and slow growth is sufficient for spatial selection as a result of which only the crystals with optimum orientation in the growth direction 'survive'. For example, at a container diameter of 130 mm and a growth rate of 2 mm/h, only 2–3 large crystals were grown. At a rate of 60 mm/h, the number of crystalline blocks was more than

20. The slow growth rates also resulted in the improvement of the quality of the crystals and increase of optical homogeneity. Figure 7.13 shows the dependence of the dimensions of the grown crystals on the rate of lowering of the container with the melt and the content of stabilising yttrium oxide. Table 7.3 shows the effect of rare-earth oxides on the yield and dimensions of the crystals which also makes it possible to predict the optimum technological parameters for obtaining the crystals of the required dimensions [39].

To examine the effect of mass transfer in the melt on the quality of crystals, investigations were also carried out into the effect of reverse rotation of the container. At a growth rate of 8–16 mm/h reverse rotation of the container has no significant effect on the quality of the grown crystals, but at a growth rate of 1–2 mm/h, the quality of crystals noticeably improves [40]. Evidently, reverse rotation results in the disruption of the diffusion layer ahead of the solidification front. The large crystals, grown at low rates and in

**Table 7.3.** Effect of composition and cooling rate on the dimensions of crystals (*d*) of zirconia $ZrO_2$ stabilized with $R_2O_3$ (R = Ce–Lu)

| C, mol % | Crystal dimensions *d**, mm | | | | |
|---|---|---|---|---|---|
| | $R_2O_3$ (R-Ce–Nd) | | | $R_2O_3$ (R-Eu–Lu) | |
| | V=16 mm/h | V=2 mm/h | V**=16 mm/h | V=16 mm/h | V=2 mm/h |
| 0 | 2–3 | – | 10 | 2–3 | 1–2 |
| 0.1 | 2–4 | – | – | 3–5 | – |
| 0.3 | 10–12 | – | 15 | 10–15 | – |
| 1.0 | 10–12 | – | – | 10–15 | – |
| 5.0 | 4–5 | 8 | 5 | 12–15 | 15–20 |
| 10-20 | 2–3 | 4–5 | 2–3 | 12–15 | 20–40 |
| 25 | – | – | – | 8–10 | 12–15 |
| 33 | 1-2 | – | – | 2–3 | 8–12 |
| 40 | – | – | – | 2–3 | 8–10 |

*Crucible diameter 130 mm
**Thermal screens were used

small containers, usually crack. At a large number of small blocks the stresses are removed as a result of the formation of boundaries between blocks. However, the formation of a small number of large blocks results in the formation of high mechanical stresses in the volume of the crystals causing failure of the latter.

The experimental results show that the most justified method of increasing the dimensions of fianite crystals and their optical homogeneity is the increase of the volume of the crystal melt and a decrease of temperature fluctuations at the solidification front. The increase of the optical homogeneity is also supported by a decrease of the rate of growth of the crystals and by the application of intensive forced mixing of the melt. The decrease of the linear growth rate to 1 mm/h and the application of the system for reverse rotation of the container makes it possible to reduce the gradients of the refractive index of the crystals to $10^{-4}$ cm $^{-1}$. The increase of the volume of the solidifying melt makes it possible to produce large single crystals as a result of reducing temperature gradient and increasing heat capacity. During cooling in the temperature range 2800–1000°C the crystals still have sufficiently high electrical conductivity and continue to absorb the energy of the HF field and, consequently, the integrity of the crystals is not disrupted.

To produce colour crystals, it is necessary to use small additions (≈0.5 wt%) of rare-earth and transition metals to the melt. The technological scheme of the production of fianite crystals by the technology developed at the General Physics Institute of the Russian Academy of Sciences is described below.

The technology of the fianite crystals includes the following main stages: a) preparation of the charge; b) loading the charge into the container; c) melting; d) growth of single crystals by the method of directional solidification of the melt; e) extraction of the crystals from the crucible; f) machining and grading of the crystals; g) cleaning of crystal waste for subsequent melting and crystallisation. The diagram of production of the fianite crystals and equipment used at the General Physics Institute is shown in Figs. 7.14 and 7.15 [35].

The industrial technology of growth of zirconia-based crystals, used widely in many countries, is almost completely based on the results of investigations of Russian scientists obtained in the last 30 years [42, 43, 44–47].

The quality of the charge and the purity of the initial reagents
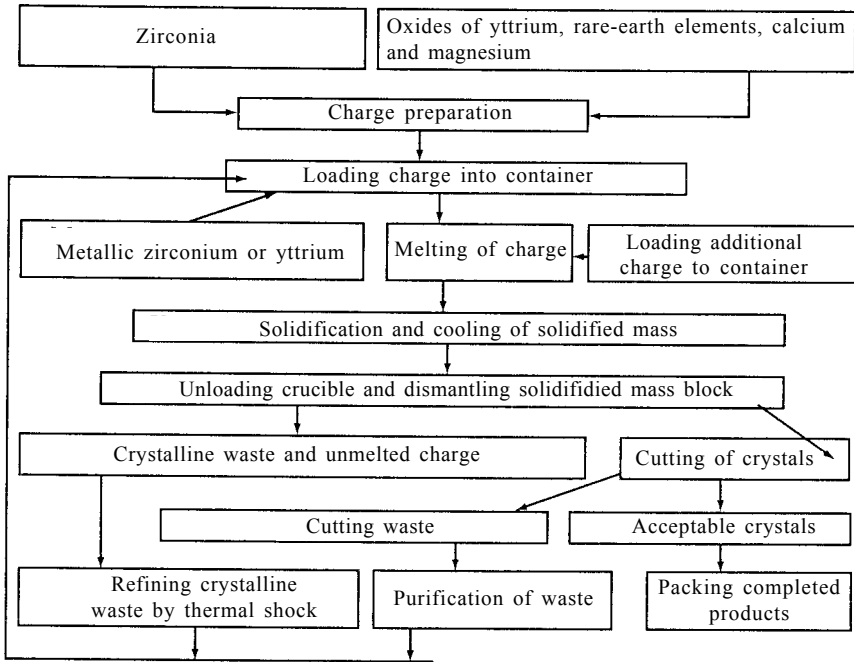
**Figure 7.14.** Flow chart of production of cubic zirconia crystals (fianites) at the General Physics Institute of the Russian Academy of Sciences [35].

have a controlling effect on the entire technological process of crystal production. The oxides in the proportion, corresponding to the given composition, are thoroughly mixed in a mechanical mixer and loaded into a container. Crystal waste of the same composition from the previous melts is added to the charge [43, 45]. This makes the technology almost completely waste-free and results in a considerable saving of expensive reagents, shortens the loading and melting time because the crystalline material has higher density. In directional solidification, there is also additional purification of the melt to remove a number of impurities and this improves the quality of the grown crystals.

The presence of a number of uncontrolled impurities in the initial oxides, used for the growth of single crystals by directional solidification, is highly undesirable. These impurities influence the both the growth process and the quality of the crystals. As shown later, the crystal growth is negatively affected mainly by the impurities such as Si, Al, Ti, Nb; the effect of Fe, Co, Ni, Mn, Cr, V, W, Mo is slightly less marked. The effect of these impurities is
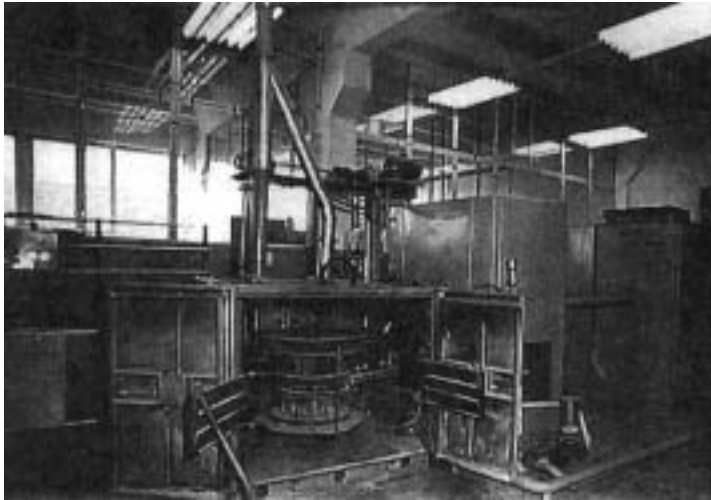
**Figure 7.15.** Kristall-403 equipment for growing fianites.

reflected in the formation of inclusions, the formation of a cellular substructure, promotes the formation of cracks and reduces the size of the single crystals. The growth defects, caused by the presence of microimpurities, reduce the optical homogeneity and strength characteristics of the crystals. In addition to this, there is a number of requirements on the purity of the initial material in relation to the application of the final product. For example, special requirements are imposed on the fianites used as substrates for the epitaxial growth of semiconductors (Si, Ge, $A^{III}B^V$, $A^{II}B^{VI}$, etc) as regards the content of the elements which may influence the electrophysical characteristics of the films. When producing a film-forming material based on zirconia, special attention is given to the impurities influencing radiation resistance, beam strength, and also impurities influencing the technological properties of the material in spraying (volatile impurities). Thus, these factors require careful analysis of both the components of the initial materials and the produced single crystals.

The composition of the impurities of the initial oxides and grown single crystals has been investigated by the method of atomic emission spectral analysis because the standard methods of atomic emission analysis cannot be used for zirconia because of its high thermal stability (Table 7.4).

Table 7.4 gives the content of microimpurities in the crystal grown from the given charge. The analysis results indicate that the

**Table 7.4.** Content of uncontrolled impurities in charge and in crystals [40]

| Element | Impurity content, % $\times 10^{-5}$ | | | |
| | In initial charge | In crystal | | |
| | | bottom | centre | top |
|---|---|---|---|---|
| Fe | 2.0 | <0.1 | <0.5 | 1.0 |
| Ca | 3.0 | 1.1 | 1.6 | 1.8 |
| Si | 5.1 | 0.1 | 0.5 | 1.0 |
| Mn | 0.2 | <0.1 | <0.1 | <0.1 |
| Cu | 1.0 | <0.1 | <0.1 | <0.1 |
| Mg | 1.2 | 0.5 | 1.1 | 1.4 |
| Al | 0.5 | <0.1 | <0.1 | <0.1 |
| Nb | 0.4 | 0.1 | 0.1 | 0.3 |
| W | <0.1 | <0.01 | | |
| Ti | 0.5 | <0.1 | 0.1 | 0.4 |
| Be | <0.1 | <0.01 | <0.01 | 0.01 |
| Sr | 4.3 | 1.5 | 2.1 | 3.3 |

purity of the produced crystals is 5–100 times higher as regards the content of the impurities in comparison with the initial oxides. This effect is a direct consequence of the application of technology of directional solidification in the cold crucible because the crystals are not contaminated during growth which takes place in other methods of crystal growth characterised by contact of the melt with the crucible material. In the present case, the melt and the crystals are greatly purified as a result of the displacement of the microimpurities to the upper part of the crystal and evaporation of a number of impurities (As, Pb, Cu, etc.) as a result of the high temperature of the melt.

Filling of the crucible with the charge is an important stage of the technological process which controls the yield, dimensions and quality of crystals. The distribution of the material in the crucible determines the formation of the volume of the melt and the thermal

conditions in which the melting of the material and solidification of the melt take place. Special features of loading of the cold crucible consist of the need for the formation of the lower bulk thermal screen in the form of rings produced from powder-like materials and crystal waste.

The lower thermal screen plays the following functions: 1– reduces heat losses through the bottom of the crucible; 2 – equalises the temperature fields in the diameter of the crucible; 3– reduces the axial gradients in the growing crystals; 4 – reduces the number of seed crystals and this increases the dimensions of the single crystals in the grown block.

The ring-shaped loading scheme has the following advantages: 1–saves the powder material, 2–reduces the duration of the process of starting melting; 3–supports the formation a high–density, sintered layer of the solid phase, 4–increases the stability of the melting process, 5– simplifies the process of loading large diameter crucibles.

## 7.4. CRYSTAL CHEMISTRY OF THE CUBIC PHASE OF SOLID SOLUTIONS BASED ON ZIRCONIA

The zirconia single crystals have a unique combination of the properties resulting in the special interest in this material. However, the presence of the monoclinic–tetragonal transition, accompanied by a sharpe change in the volume, results in the failure of the grown zirconia crystals and prevents their use in practice. In order to facilitate the production and used of zirconia crystals of the highest-temperature cubic modification, it is necessary to stabilise the modification in the entire temperature range, up to room temperature.

Examining the geometrical stability criteria, Goldsmith, Magnus and Pauling used the fluorite lattice as an example to shows that the critical parameter is the ratio of the ionic radii of the cation and the anion. At $R_c / R_a \geq 0.736$, the densest packing of the anions in the $Fm3m$ lattice is likely to exist. When this parameter is lower than this value, the ion crystals do not form the cubic lattice because at short distances between the anions the forces of electrostatic repulsion unavoidably distort the structure. For zirconia, this ratio is 0.66 [2].

The cubic structure may be stabilised by increasing the radius of the cation (*i.e.*, replacing zirconium by cations with a larger

diameter) or by the formation of vacancies in the anion sublattice (*i.e.*, by introducing the cations with a smaller charge or by heterovalent substitution). The solid solutions, formed in this case, are denoted as follows: $Zr_{1-x}^{+4}R_x^{3+}O_{2-x/2}^{2-}(V^O)_{x/2}$ where $V^O$ is the vacancy in the oxygen sublattice.

To obtain the necessary increase of the ratio of the radii of the cation and the anion in the zirconia lattice, it is necessary to change the geometrical parameters by ~4% [48]. The lattice constants of stabilised zirconia are characterised by different values in relation to the nature and concentration of the stabilising oxide.

In a number of cases, stabilisation takes place during the introduction of the oxides whose cations have a smallert ion radius than the radius of zirconia. Consequently, the controlling factor for the formation of the cubic structure of $ZrO_2$ is not only the cation radius [49]. Thermodynamic considerations show that the crystal lattice is stable if its state is characterised by the minimum free energy. To reach this state, in addition to the radii of the cation and the anion, it is also important to consider the nature of interaction between the electron shells of the components of the lattice. According to the authors of [50, 51], the relationship between the secondary cation and oxygen should be more heteropolar than between the ions of zirconium and oxygen. In this case, the structure of fluorite is formed. However, in the establishment of the equilibrium state in the system, it is also necessary to take into account the kinetic factor.

In most cases, oxides structurally similar to zirconia are used. In this case, according to crystallochemical considerations, stable solid solutions may form. These oxides are, in particular, oxides of rare-earth elements, yttrium, and also the oxides of the group of alkali-earth elements.

Since the cubic solid solutions are stable in the entire temperature range from melting point, they are often referred to as the completely stabilised zirconia.

There is obviously a large number of intermediate states between the random and ordered distribution of cations and vacancies in the sublattice sites. The actual state has a very complicated nature and cannot be calculated [49].

The $ZrO_2$–$R_2O_3$ solid solutions with the general formula $Zr_{1-x}^{4+}R_x^{3+}O_{2-x/2}V_{x/2}^O$ in the vicinity of the composition 33 mol.% $R_2O_3$ (R–La–Gd) undergo the 'order-disorder' type transformation leading to the formation of a phase with the pyrochlore structure. Ordering

takes place simultaneously in the cation and anion sublattices [52].

The structure of the pyrochlore mineral has the general formula $A_2B_2X_7$, where the position A may be replaced by the ions Na, Ca, Th, U, Ln; the position B by Nb, Ta, Ti, in positions X by O, OH, F. This structure is a derivative of the fluorite-type structure [53], whose spatial group is $O_h^7$–$Fd3m$, $Z = 8$, $a = 10.35$–$10.45$ Å. The structure is stable at the ratio of the ion radii $R_A/R_B = 1.2$. In transition of the fluorite structure to the pyrochlore structure, one of the eight anions, surrounding the cation, is removed from the nodes of the anion sublattice, and the other are displaced from their ideal positions. The displacement is characterised by parameter $x$ [53–57]. Large ions A are coordinated by eight oxygen ions which surround them in the tips of the distorted cube. The ions B are distributed inside the oxygen cubes two tips of which situated at the ends of the spatial diagonal, remain free (coordination number 6), (Fig. 7.3*b*). Thus, the anion motive of the structure of pyrochlore is to some extent intermediate between the motive of the structure of fluorite where all polyhedrons are cubes and the motive of the structure of senarmontite where all polyhedrons are flattened octahedrons [57]. The breakdown of the polyhedrons into two types of components results in doubling of the identity period and in a change of the symmetry: the spatial group of symmetry Fd3m replaces *Fm3m*). The transition from the fluorite to pyrochlore structure is accompanied by the formation of superstructural reflections on the x-ray diffraction patterns corresponding to the establishment of an order in the distribution of the cations and distortion of oxygen polyhedrons. These reflections have odd indexes of the type (311), (331), (511), (531), etc, and low intensity whose value depends mainly on the difference of the values of the scattering capacity of the cations of the groups A and B of the structure. If this difference is small, the odd reflections (*hkl*) may not be detected. Thus, an indeterminacy forms in the identification of the structure by the method of x-ray diffraction analysis and it is necessary to examine the structure of pyrochlore by other methods.

The 'order–disorder' transformation in solid solutions takes place at critical temperature $T_C$ [52,58]. At temperatures higher than $T_C$, the cations of zirconium and rare-earth elements are distributed randomly, like the anions and vacancies of oxygen. Below this temperature, the cations $Zr^{4+}$ and $Y^{3+}$ are distributed in an ordered manner. At temperature $T > T_C$ the fluorite structure forms and the

**Table 7.5.** Ordering temperatures in $ZrO_2$–$R_2O$ systems [52]

| System | $r_{R3+}$, A | $T_C$, °C |
|---|---|---|
| $ZrO_2$–$La_2O_3$ | 1.14 | Order at all temperatures |
| $ZrO_2$–$Nd_2O_3$ | 1.04 | As above |
| $ZrO_2$–$Sm_2O_3$ | 1.00 | 2400 |
| $ZrO_2$–$Gd_2O_3$ | 0.97 | 1550 |
| $ZrO_2$–$Dy_2O_3$ | 0.92 | Disorder at all temperatures |

pyrochlore structure forms at $T < T_C$. The transformation temperature increases with increase of the ion radius of the rare-earth element, as indicated by the data presented in Table 7.5 [52].

The composition of the non-stoichiometric phase is written in the general form: $R_{2\pm x}Zr_{2\pm x}O_{7\pm x/2}V^O_{1\pm x/2}$.

In addition to the ordered compounds of the type of pyrochlore, the system based on zirconia contains compounds of the type $A_7O_{12}$ containing three- and four-valent cations, characterised by a chain of oxygen vacancies along the direction <111> of the initial structure [18–20, 34]. In the range 40 mol.% $R_2O_3$ the compounds $Zr_3Y_4O_{12}$ and $Zr_3Yb_4O_{12}$ with rhombohedral symmetry were found. The ordering process in the compound $Zr_3Y_4O_{12}$ takes place at $T <1200$°C [20]. For example, at a temperature of 1180°C, the ordered phase is formed only after annealing for 13 weeks.

The decrease of the amount of stabilising oxide is accompanied by the formation of a tetragonal solid solution based on zirconia. However, single-phase tetragonal specimens are produced only in strictly specific synthesis conditions [59–62]. For sintered ceramic specimens, the stability of the tetragonal structure of zirconia depends on various factors, such as density, composition, grain size and sintering temperature. Since the upper temperature boundary of phase stability of the solid solutions is the temperature of the phase tetragonal–cubic transition and it is lower than the melting point, these materials are referred to as partially stabilised zirconia (PSZ).

It has been established that there are two forms of tetragonal zirconia which may form in the $ZrO_2$–$Y_2O_3$ system [23, 63–65]: yttrium oxide-rich 'non-transformable' $t'$-$ZrO_2$ phase and the $t$-$ZrO_2$ phase depleted in $Y_2O_3$ which is capable of martensitic

transformation to the monoclinic phase *m*. The *t'*-$ZrO_2$ phase is the main component in the rapidly quenched cubic solid solutions. It forms by a diffusion-less mechanism as a result of a shear phase transformation and is characterised by the presence of antiphase domain boundaries clearly visible in a transmission electron microscope.

$ZrO_2$ ceramics with a low content of the stabilising agent (2–9 mol.% $Y_2O_3$), produced by solid phase sintering, consists mainly of two (or three) phases, depending on the previously mentioned factors. The monoclinic tetragonal zirconium oxide exists in these materials in the form of coherent precipitates in the tetragonal or cubic matrix.

In directional solidification of the melt in the cold crucible, the optimum conditions of production of the specimens consisting only of tetragonal zirconia are: the yttrium oxide concentration 3 mol.% and rapid cooling of the melt (> 400°C/h) [65]. These results are in good agreement with the experimental conditions determined by Lefevre [30] for retaining the tetragonal phase. With a decrease of the cooling rate or when adding the sesquioxide oxide in the concentration of less than 3 mol.%, in addition to the tetragonal phase, the specimens also contains the monoclinic phase. The mixture of the cubic and tetragonal phases is obtained in the same experimental conditions, if the amount of the sesquioxide is more than 5 mol.%.

In pure zirconia, the cubic–tetragonal transition takes place at temperatures above 2300°C, depending on the partial pressure of oxygen. This transition is paraelastic ↔ ferroelastic *(m3m ↔ F4 /mmm)* [65]. In the phase diagram of the $ZrO_2$–$Y_2O_3$ systemt in the concentration range rich in zirconia (Fig. 7.7), the cubic and tetragonal phases are separated by the two-phase region (*c+t*) [12]. In growth of a crystal from the melt, the crystals with the cubic structure of the fluorite type are the first to grow, and the transition to the tetragonal phase takes place at a temperature below critical temperature $T_C$. These temperatures for a number of compositions were determined in [66]. The structural types of the zirconia crystals, partially stabilised with the yttrium oxide, are presented in Table 7.6. Figure 7.16*a* shows an elementary tetragonal cell whose nodes are denoted by the solid circles. The position ½, ½, ½ (empty circle) corresponds to the node equivalent to the fluorite lattice. The zirconium (or yttrium) cations, are surrounded by the oxygen anions that form the same coordination polyhedrons as in the case of the

**Table 7.6.** Structures of tetragonal zirconia (3 mol% $Y_2O_3$) [65]

| | Tetragonal $Zr_{1.94}Y_{0.06}O_{1.94}$ | Cubic fluorite $MO_2$ |
|---|---|---|
| Spatial group | $P4_2/nmc$, $Z = 2$ | $Fm3m$, $Z = 4$ |
| Cell parameters | $A_t = 0.3610$ nm; $c_t = 0.5168$ | $A_c = 0.5126$ nm |
| Atomic positions | 2(a) Zr (or Y) 000B = 0.002 $nm^2$ | Z=0.025 |
| | 4(d) O (or vacancies) 01/2Z | |
| | $Z = 0.199$, $B = 0.025$ $nm^2$ | |
| Cation environment | 4Zr–O 0.208 nm | 8M–O 0.222 nm |
| | 4Zr–O 0.238 nm | 12M–M 0.362nm |
| | 4Zr–O 0.361nm | |
| | 4Zr–O 0.363 nm | |
| Anion environment | 2O–Zr 0.208 nm | 4O–M 0.222 nm |
| | 2O–Zr 0..238 nm | 6O–O 0.256 nm |
| | 2O–O 0.258 nm | |
| | 2O–O 0.261nm | |

Comment. The cubic fluorite structure of $MO_2$ with the elementary cell of the same volume is given for comparison [68]

cubic lattice, but with the orientation different from 000 and ½, ½, ½ positions, as shown in Fig. 7.16.

The main difference between the tetragonal structure and the fluorite structure is that in the tetragonal zirconia there are two types of the metal–oxygen bond. The difference in the strength of the M–O bonds is determined by their lengths of 0.208 and 0.238 nm, which correspond to the binding forces of $s = 0.72$ and $s = 0.30$, respectively [65].

The consequence of this change in the structure is the transformation of cleavage planes in the tetragonal crystals on which preferential separation of the single crystals takes place. The cleavage planes for the fluorite structure belong to the family of {111} planes. The separation of the tetragonal crystals takes place mostly along {001} planes, normal to the fourth-order axes [65].

The special features of the formation of phases and structure of

a



b
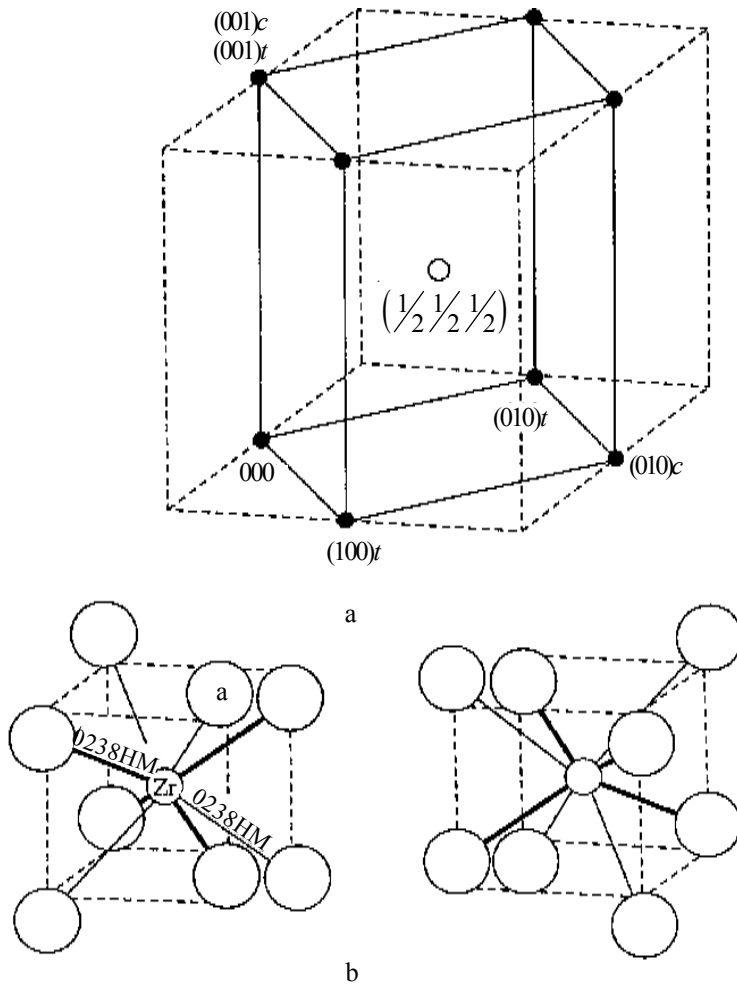
**Figure 7.16.** Elementary cell of tetragonal zirconia stabilised with 3 mol.% $Y_2O_3$ (a) and the distribution of ions in the cell [65].

the $ZrO_2$–$Y_2O_3$ solid solutions (1–33 mol.%), produced from the melt by directional solidification, have been investigated by a number of authors [65–69].

Experimental results are presented in Table 7.7. The solid solutions with the concentration of the yttrium oxide of 10–15 mol.% are characterised by some disordering which become smaller at higher and lower concentrations of the oxide [70].

The problem of the difference of the content of the cubic and tetragonal *t'* (pseudo-cubic) phases in the crystals of partially stabilised zirconia has not as yet been solved. For example, the

**Table 7.7.** Phase composition of crystals grown by directional solidification of the melt [65,68,70]

| Mol% $Y_2O_3$ | Number of phases | Composition of phases | Spatial group |
|---|---|---|---|
| 1–2 | 2 | Monoclinic +tetragonal | $C_{2h}^5$–$P2_1/c$<br>$P4_2/nmc$ |
| 3 | 1 | Tetragonal | $P4_2/nmc$ |
| 3–8 | 2 | Tetragonal + cubic | $P4_2/nmc$<br>$O_h^5$–$Fm3m$ |
| 8–35 | 1 | Cubic | $O_h^5$–$Fm3m$ |

phase analysis of the crystals with 4.7 mol.% of $Y_2O_3$ shows that they consist of ~35 wt% of the trigonal *t*-phase and 65 wt.% of the pseudo-cubic *t'*-phase [71, 72].

The conclusions on the nature of the solid solution formed in solidification of the melt have been made on the basis of comparison of the x-ray density calculated from the crystal lattice parameter, and the density determined by experiments. Calculations were carried out usually using the model of the solid substitutional solution with oxygen vacancies which results in good agreement between the calculated and the experimental densities. When the experimental density was higher than the calculated values, it was assumed that a small fraction of interstitial ions may exist in the lattice of the investigated solid solutions [49, 73–77].

The results of phase analysis in these investigations slightly differ. The characteristic special feature of the single crystals, produced from the melt, is the existence, in the crystals, of the metastable phases at room temperature. The quantitative composition of the phases corresponds to the composition of the melt from which they were produced. The diffusion processes, taking place in cooling in the solid phase in accordance with the equilibrium diagram, even at the same synthesis conditions, may take place by different mechanisms depending on the technological conditions (for example, solidification rate, cooling rate, temperature gradients, additional heat treatment, etc). This may be the reason for the difference in the data obtained by different authors. Table 7.8 presents the comparative results of phase formation in the $ZrO_2$–$R_2O_3$ system.

Comparison of the results, obtained by the RS method, with the results of traditional methods of analysis of the phase composition

**Table 7.8**. Phase compositions of $ZrO_2$–$R_2O_3$ systems (R – Eu, Gd, Yb, Y) determined by the method of Raman scattering of light (RS), x-ray phase (XPA) and crystallo-optical analysis [35]

| Composition of crystals, mol% | Phase composition | | |
|---|---|---|---|
| | RS method | XPA | Crystallo-optical analysis |
| | $ZrO_2$–$Eu_2O_3$ | | |
| 1 | M + T | M + T | M + T (small amount) |
| 3 | M + T | M + T | M + T |
| 5 | T | M + T | M + T + K |
| 8–10 | T | F | T + K |
| 10–12 | F | F | K |
| 15–20 | DP | F | K |
| 33 | F | F | K |
| | $ZrO_2$–$Gd_2O_3$ | | |
| 1 | M + T | M | M + T (small amount) |
| 3 | M + T | M + T | M + T |
| 5 | T + M | M + T | T + M + K |
| 8 | T | F | T + K |
| 10 | K | F | K |
| 12–33 | F | F | K |
| | $ZrO_2$–$Yb_2O_3$ | | |
| 1 | M + T | M | M + T (small amount) |
| 3 | T | M + T | M + T |
| 5 | T | T | T + K + M |
| 8–33 | F | F | K |
| | $ZrO_2$–$Y_2O_3$ | | |
| 6–8 | T | F + T | F + T |
| 10 | F | F | F |
| 12 | DF | F | F |
| 15–20 | OF | F | F |
| 33 | DF | F | F |

Notations: F – fluorite, DF – disordered fluorite, OF – ordered fluorite, DP – disordered pyrochlore. Phases: P – cubic pyrochlore, T – tetragonal, M – monoclinic, K – cubic

show that the RS method provides the largest amount of information. For example, in investigation of the phase compositions and phase transitions in the materials with the low concentration of the stabilising oxides, investigations were carried out directly on the crystals, whereas powder x-ray diffraction analysis requires grinding of the specimens, activating the phase transformations in the specimens. In addition to this, in the investigations of the processes, associated with the ordering of the cubic solid solutions determined mainly by the ordering of the oxygen vacancies, formed in heterogeneous substitution, the sensitivity of x-ray diffraction analysis is low. Crystal-optical analysis is not capable of separating the cubic phases with different types of structure.

Only the complex approach is most reliable. In a number of cases (for example, for the inspection of the formation of the second phase in the range of cubic solid solutions), the sensitivity of the conventional x-ray diffraction and crystal-optical methods, is sufficiently high.

## Parameters of the crystal lattice of fianites $ZrO_2-Y_2O_3$

Investigation of the structure of fianite single crystals is of both independent interest and of interest in connection with investigations of the polycrystalline stabilised zirconia synthesised by different methods: co-precipitation [78, 79], melting [49], plasma spraying [80] and sintering.

The authors of [81] carried out detailed x-ray diffraction examination of the $ZrO_2-Y_2O_3$ cubic phase. Single crystals were produced by directional solidification of the melt in air. The cubic structure was stabilised with $Y_2O_3$ in the amount of 6–40 mol.%.

X-ray diffraction analysis was carried out in a diffractometer with filtered $CuK_\alpha$-radiation. The lattice constant was determined from the (531) peak with the accuracy of 0.001 Å. The degree of ordering of the single crystals was characterised by two quantities: the ratio of the intensity of the lines (600) and (200) to the normalised width of the peaks (531) at half height in relative units.

According to the results of x-ray diffraction analysis, all the single crystals were characterised by the stabilised high-temperature crystalline form of the cubic structure of the fluorite type. The spatial group $O_h^5 - Fm3m$. Figure 7.17a shows the dependence of the lattice parameter on the content of the stabilising oxide in the crystal. The equation for the calculation of the lattice parameter of
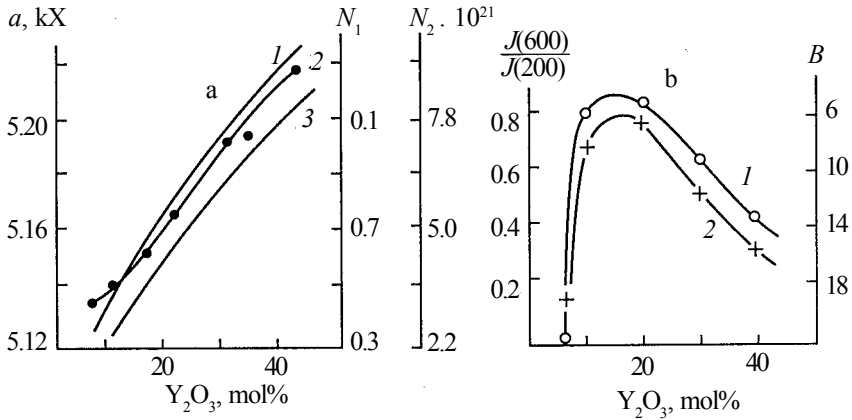
**Figure 7.17.** Variation of the lattice spacing and number of vacancies in relation to $Y_2O_3$ content [82]. a) 1 – lattice spacing calculated from equation (7.2); 2 – experimental values of the spacing; 3 – number of vacancies in the anion sublattice; $N_1$ – in the elementary cell; $N_2$ – in 1 cm³. b) disorder as a function of the $Y_2O_3$ concentration: 1 – half-width of the (531) line and 2 – intensity ratio of the (600) and (200) lines

zirconia, stabilised simultaneously by *n* different elements, taken at different ratios, was obtained on the basis of considerations of the spherical packing of the ions in the crystal structure [81]:

$$D = A\left[ R_{Zr} + R_O + \sum_{k=1}^{n} P_k m_k \Delta R_k /100 + \sum mk(P_k - 1) \right], \qquad (7.2)$$

where $A = 2.31$; $R_{Zr}$ and $R_O$ are the radii of the ions of zirconium and oxygen; *n* is the number of various stabilising additions; $P_k$ is the number of ions of each stabilising element per one molecule of the oxide; $m_k$ is the amount of the *k*-th stabilising oxide, expressed in mol.%; $\Delta R_k$ is the difference of the radii of the ions of the *k*-th stabilising element and zirconium. For the binary system, in which $n = 1$ and $P = 2$,

$$D = 2.31\{R_{Zr} + R_O + 2m\Delta R /(100 + m)\}. \qquad (7.3)$$

As shown by equation (7.3) and the graph (Fig. 7.17*a*), the dependence of the lattice spacing on the $Y_2O_3$ content is non-linear. The calculated and experimental curves have the same form and are in numerical agreement for the composition 10 mol.% $Y_2O_3$. A
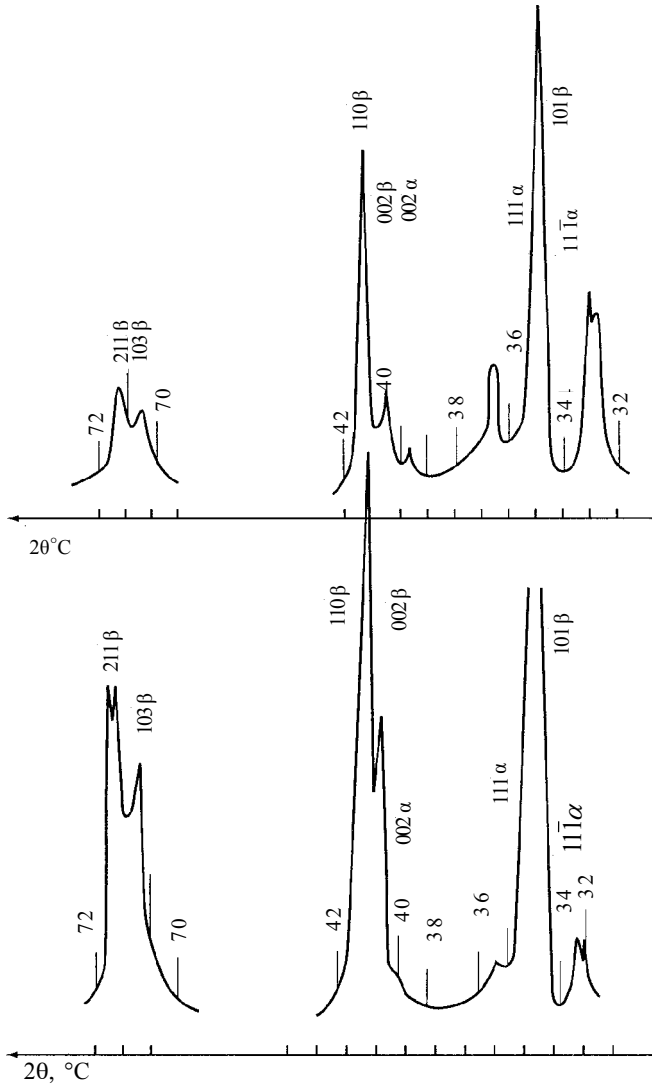
**Figure 7.18.** X-ray diffraction patterns of a crystal with composition $ZrO_2$–3 mol.% $Y_2O_3$ [82].

large deviation is detected for the specimen with 6 mol.% because of the special features of its structure.

   As a result of incomplete stabilisation, some elementary cells are characterised by changes in the coordinates of the oxygen ions, leading to the formation of the tetragonal lattice. In this case, the parameter *a* of the cubic lattice decreases, and the size on the *c* axis greatly increases. The rearrangement of the structure results in the splitting of some lines and in the formation of doublets. The

diffraction pattern of the specimen with 3 mol.% $Y_2O_3$ is shown in Fig. 7.18.

The increase of the lattice spacing may be associated with the presence in the crystal of two phases: cubic and distorted tetragonal. The main role of the stabilising addition in this case is played only by the cubic phase and this increases the yttrium concentration in this phase. The lattice spacing, equal to 5.136 A, corresponds to the specimen with the content of 8 mol.% $Y_2O_3$. The amount of the tetragonal phase in the investigated specimen is, according to the estimate, ~25%, which is in agreement with the intensity of peaks on the diffraction patterns.

At the content of the stabilising additions greater than 10 mol.% $Y_2O_3$, there is a small difference between the theoretical and experimental curves. The deviation of the experimentally determined spacings of the crystal lattice to low values is caused by the formation of vacancies. The mean number of the anion vacancies for a single elementary cell is calculated from the equation:

$$V = \sum 4P_k m_k (2 - P_{ok} / P_k) / [100 + \sum m_k (P_k - 1)], \qquad (7.4)$$

where $P_{ok}$ is the number of the oxygen ions in the molecule of the stabilising oxide. The other notations are the same as previously. For the investigated system, the equation (7.3) is greatly simplified:

$$V = 4m / 100 + m. \qquad (7.5)$$

As indicated by the graph (Fig. 7.17*a*), in the specimen with 33 mol.% of yttrium oxide, one vacancy is formed in each elementary cell or $7.1 \cdot 10^{21}$ vacancies form in 1 $cm^3$. This large number of the vacancies in the anion sublattice influences the regrouping of the ions and reduces the lattice spacing. The characteristics of the degree of ordering of the investigated single crystals are presented in Fig. 7.17*b*. The most disordered structure is the composition with 6 mol.% of yttrium oxide. A possible explanation was presented previously. The increase of the content of the stabilising oxide to 10 mol.% results in the complete stabilisation of the cubic lattice and a large increase of the degree of ordering which tends to increase with the increase of the concentration of the stabilising oxide to 20 mol.%. A further increase of the content of the stabilising oxide results in a monotonic decrease of the degree of

**Table 7.9.** Density of zirconia single crystals in relation to the concentration of stabilizing oxide $Y_2O_3$ [82]

| [$Y_2O_3$], mol% | $\rho_1$ g/cm³ | $\rho_2$ g/cm³ | [$Y_2O_3$], mol% | $\rho_1$ g/cm³ | $\rho_2$ g/cm³ |
|---|---|---|---|---|---|
| 10.3 | 5.930 | 5.910 | 19.8 | 5.661 | 5.655 |
| 13.8 | 5.868 | 5.863 | 31.2 | 5.596 | 5.603 |
| 16.3 | 5.766 | 5.800 | 35.9 | 5.538 | 5.543 |

Comment. $\rho_1$ is the distance according to x-ray data; $\rho_2$ is the distance determined by hydrostatic weighing.

ordering as a result of the gradual transition from the lattice of zirconia to the lattice of the solid solution of oxides of zirconium and yttrium.

The calculation of the density of the substitutional solid solution taking into account the vacancies formed in the given composition is carried out using the equation:

$$\rho = [818.050 - 136.920m/100 + m]/d^3. \tag{7.6}$$

The values of the density of the single crystals with different yttrium content, calculated using equation (7.6), and the experimental results, obtained by the method of hydrostatic weighing, are presented in Table 7.9.

Figure 7.19 shows the calculated and experimental values of the density of the single crystal solid solutions of hafnium dioxide in
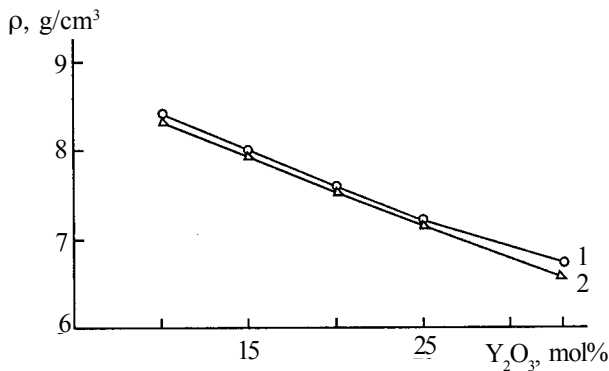


**Figure 7.19.** Pycnometric (1) and calculated (2) densities of crystals of solid solutions of the $HfO_2$–$Y_2O_3$ system versus the yttrium oxide content [83].

relation to the yttrium oxide content.

With the increase of the yttrium oxide content, the density of the crystals rapidly decreases. The main reasons for the decrease of the density is the increase of the volume of the elementary cell and the formation of anion vacancies. Small differences between the calculated and experimental values indicate the high perfection of the crystal structure.

## 7.5. DEFECTS IN THE STRUCTURE OF FIANITE CRYSTALS

Crystal structure defects include any deviation from the ideal periodicity of the atomic structure. Defects form in the solidification process under the effect of thermal, mechanical, electrical, and radiation influences and also when adding admixture elements to the melts.

Defectiveness influences many structure-sensitive properties of the crystal. The dislocations, vacancies, impurity atoms, phase precipitates and other elements of the real structure of the crystal determine all phenomena of plasticity and strength of the crystals. The detected optical absorption is mostly of the impurity type. The crystals, containing a large number of macroscopic ($\approx 10^{-4}$ cm or more) or even colloidal ($10^{-6}$–$10^{-5}$ cm) inclusions and cracks are not suitable for practical application. Defects influence many physical and chemical properties of the crystals. The formation of defects is linked genetically with the phase transformations and the coefficients of distribution of the impurity atoms in the crystals. This circumstance makes it possible to restore the prior history of formation of the crystal on the basis of the morphology, form, dimensions, chemical composition and physical properties of crystals with the defects. Investigations of the defects, formed in the process of growing fianites with different stabilising additions in a wide range of the composition, enabled the definition of two more classes of compounds with the properties differing from those of the fianites.

The interest in the defects, formed during growth, is associated with the non-repeatability of the defective structure and, consequently, the variations of the structure-sensitive characteristics of the crystal not only from specimen to specimen but also within the limits of the same crystal. Therefore, high-quality crystals should be perfect from 'birth'.

The following growth defects are found most frequently:
–heterogeneous inclusions–inclusions of a second phase of the

macroscopic dimensions from colloidal to several centimetres;

–point defects–impurity atoms and ions, vacancies and their aggregates;

–twins, stacking faults, dislocations, block boundaries;

–internal stresses;

–heterogeneities in the distribution of the previously mentioned defects–zonal, sectorial, 'pencil' and other structures [84].

## Coefficients of distribution of impurities in the $ZrO_2$ crystals

The equilibrium coefficient of distribution of the impurities and components is one of the main parameters of the crystallisation process and it is also the parameter of the equilibrium between the solid and liquid phases. The distribution coefficient $K$ is the ratio of its concentrations in the solid and liquid phases, having the common interfacial surface. In practice, it is necessary to consider the distribution coefficients determined for equilibrium ($K_0$) and non-equilibrium ($K_{eff}$) conditions. An objective relationship exists between the values of the equilibrium and effective coefficients.

The distribution coefficient for the equilibrium conditions $K_0$ characterises the ratios of the concentrations corresponding to the liquidus and solidus lines of the equilibrium diagram. The factor which determines the transition from the nonequilibrium to equilibrium conditions is the solidification rate.

The dependence of the effective distribution coefficient on the solidification rate is described by the Barton–Prim–Slichter formula which treats crystallisation as a heterogeneous process at the interface and the transfer of excess atoms of the second component (at $K_0 < 1$) or the main component (at $K_0 > 1$) in the liquid phase [85].

If the solidification rate is high, the impurity component is displaced (at $K_{eff} < 1$) or it may be trapped by the solid phase if the solidification rate is higher than diffusion rate in the volume of the liquid phase. A concentration gradient forms in the liquid phase ahead of the solidification front. This region, enriched at $K_{eff} < 1$ (or depleted at $K_{eff} > 1$), controls the process of implantation of the component in the solid phase in non-equilibrium crystallisation. If the liquid phase is mixed mechanically or by thermal convection, the concentration differences in the volume of the liquid are equalised. The flow in the liquid layer in the vicinity of the interface between the liquid and solid phases remains laminar. Diffusion in this layer

remains the controlling factor and results in the distribution of the concentration of the component in the solid phase with the coefficient $K_{eff}$ in the range $K_0 < K_{eff} < 1$ or $K_0 > K_{eff} > 1$. In a general case δ, the thickness of the layer in which the diffusion plays the controlling role, depends on the mixing rate. Assuming the purely diffusion transfer of the components in the melt and the stationary solidification conditions, the effective distribution coefficient is described by the equation:

$$K = \frac{K_0}{K_0 + (1 - K_0)\exp(-f \cdot \delta / D)}, \qquad (7.7)$$

where $D$ is the diffusion coefficient of the component in the liquid; $f$ is the solidification rate.

This equation is used widely in describing the solidification processes. The value of $K_{eff}$ varies continuously from $K_{eff} = K_0$ at low growth rates to $K_{eff} = 1$ at high growth rates.

In the initial stage of crystallisation, the conditions of removal of the impurity or its capture are unstable. In this stage, a diffusion layer with thickness δ forms in the liquid. The concentration of the impurity in the diffusion layer changes from the mean concentration in the liquid phase to some stable concentration in the solid phase [86]. On reaching the stationary crystallisation regime, the distribution of concentrations in the solid phase is described by the Gulliver–Pfann equation in which the equilibrium coefficient of distribution is replaced by the effective coefficient $K_{eff}$ [87]:

$$C(g) = KC_0(1 - g)^{K-1}, \qquad (7.8)$$

where $g$ is the fraction of the solidified substance.

In the crystallisation process, a diffusion layer forms in the liquid phase. The diffusion layer is enriched with the low-melting component of the solution which has the temperature higher than the equilibrium temperature of crystallisation of the given system. The remaining mass of the liquid phase solidifies at this temperature. This phenomenon is referred to as the concentrational supercooling as a result of which the surface of the solidification front loses its stability.

The morphology of the interfacial surface must be taken into account in interpretation of the experimental data, characterising

directional solidification. It is evident that different degrees of concentrational supercooling correspond to different effective distribution coefficients. The concentration dependence of the effective distribution coefficient in directional solidification may also be ambiguous. This is caused by the fact that with the increase of the concentration of the impurity component $K_{eff}$ may approach unity in accordance with the variation of the equilibrium coefficient $K_0$ (isomorphous capture or displacement of the impurity), and also because of the development of concentrational supercooling (non-isomorphous capture or displacement). The ambiguity of $K_{eff}$ may also be associated with the instability of the thermal conditions of directional solidification. Small variations of temperature at the solidification front result in a situation in which the main translational movement is supplemented by additional reciprocal movement. The variations of the growth rate result in the periodic heterogeneity of the composition of the crystals in the growth direction. The periodic or banded heterogeneity often forms in drawing the crystals from the melt as a result of the heterogeneities of the temperature field. Banded heterogeneity, like the cellular structure, displaces the effective coefficient to unity. Banded heterogeneity may be removed only by the stabilisation of the thermal, mechanical and hydrodynamic conditions of the solidification process and this is difficult to achieve. However, it

**Table 7.10.** Effective coefficients of distribution of $Y_2O_3$ in $ZrO_2$ crystals [35]

| $Y_2O_3$ concentration, % | Rate of lowering cold crucible, mm/h | $K_{eff}$ |
|:---:|:---:|:---:|
| 5 | 16 | 1.08±0.05 |
| 8 | 16 | 1.06±0.05 |
| 10 | 1 | 1.12±0.03 |
| 10 | 5 | 1.05±0.02 |
| 10 | 8 | 1.02±0.02 |
| 10 | 30 | 1.07±0.02 |
| 15 | 16 | 1.02±0.20 |
| 20 | 16 | 1.00±0.01 |
| 30 | | 1.01±0.02 |

**Table 7.11.** Composition of grown crystals and effective coefficient of distribution of components in zirconia [35]

| Composition of crystals, $ZrO_2$–$R_2O_3$–$R'_2O_3$–$R''_2O_3$ wt.% | | | Effective distribution coefficient | | |
|---|---|---|---|---|---|
| $ZrO_2$ | $R_2O_3$ | $R'_2O_3$ | $K_{R2O3}$ | $K_{R'2O3}$ | $K_{R''2O3}$ |
| $ZrO_2$–$Y_2O_3$ ($V_r$=16 mm/h) | | | | | |
| 89.49 | 10.51 | | 1.07±0.02 | | |
| 84.91 | 15.09 | | 1.08±0.01 | | |
| 81.29 | 18.21 | | 1.6±0.03 | | |
| 80.13 | 19.87 | | 1.06±0.0.02 | | |
| 77.63 | 22.37 | | 1.03±0.01 | | |
| 70.02 | 29.98 | | 1.02±0.03 | | |
| 53.93 | 47.09 | | 1.01±0.02 | | |
| $ZrO_2$–$Gd_2O_3$ ($V_r$ = 16 mm/h) | | | | | |
| 84.00 | 16.00 | | 0.99±0.01 | | |
| 79.62 | 20.38 | | 0.98±0.04 | | |
| 76.00 | 24.00 | | 1.03±0.03 | | |
| 72.05 | 27.95 | | 1.02±0.02 | | |
| 66.68 | 33.32 | | 1.02±0.03 | | |
| 60.96 | 39.04 | | 1.01±0.04 | | |
| 46.52 | 53.48 | | 1.02±0.01 | | |
| $ZrO_2$–$Y_2O_3$ $Nd_2O_3$ ($V_r$ = 5 mm/h) | | | | | |
| 79.4 | 19.9 | 0.74 | 1.04±0.01 | 0.57±0.07 | |
| 77.9 | 19.7 | 2.44 | 1.08±0.01 | 0.60±0.02 | |
| 75.0 | 22.6 | 2.41 | 1.01±0.01 | 0.67±0.01 | |
| 73.0 | 22.3 | 4.74 | 1.04±0.01 | 0.59±0.01 | |
| 60.4 | 37.4 | 2.23 | 0.99±0.01 | 0.66±0.02 | |
| 58.7 | 36.9 | 4.40 | 1.01±0.01 | 0.64±0.01 | |
| $ZrO_2$–$Y_2O_3$–$Nd_2O_3$–$Ce_2O_3$ ($V_r$ = 5 mm/h) | | | | | |
| 76.1 | 17.8 | 4.83 | 1.24 | 1.09±0.01 | 0.51±0.02 | 0.39±0.02 |
| 76.2 | 16.2 | 6.03 | 1.54 | 1.09±0.01 | 0.52±0.01 | 0.42±0.01 |
| 77.2 | 16.3 | 5.30 | 1.24 | 1.12±0.01 | 0.55±0.02 | 0.39±0.03 |
| 78.2 | 16.4 | 4.28 | 1.13 | 1.09±0.01 | 0.66±0.01 | 0.40±0.01 |
| 78.2 | 16.4 | 4.28 | 1.13 | 1.07±0.01 | 00.71±0.01 | 0.47±0.02 |
| 79.0 | 14.8 | 4.90 | 1.25 | 1.08±0.01 | 0.60±0.03 | 0.49±0.04 |
| $ZrO_2$–$Y_2O_3$–$Nd_2O_3$–$Ce_2O_3$ ($V_r$ = 10 mm/h) | | | | | |
| 93.2 | 5.28 | 0.89 | 0.59 | 1.13±0.01 | 0.87±0.01 | 0.78±0.02 |

should be mentioned that the effect of banded heterogeneity on $K_{eff}$ is far less marked than the effect of cellular or dendritic heterogeneity.

Diffusion-less crystallisation, i.e. crystallisation without diffusion displacement of matter leading to the separation of the components may take place at high cooling rates and high solidification rates with a steep temperature gradient [86].

The values of the concentrations of the stabilising oxides in the crystals of the $ZrO_2$–$R_2O_3$–$R_2'O_3$–$R_3''O_3$ system (where R is Gd, Y; R' – Nd; R'' – Ce) and effective coefficients of distribution for different growth conditions and compositions are presented in Tables 7.10 and 7.11.

Comparison of the distribution curves of yttrium for the $ZrO_2$–$R_2O_3$ single crystals, taken from different sections of the ingot, shows that the distribution of yttrium along the length of the crystals is periodic. The waves on the concentration curves taken from different parts of the ingot may not coincide and this indicates differences in the crystallisation conditions in the cross-section of the ingot (not a flat solidification front).

The variation of the solidification rate (1–16 mm/h) and the concentration of the yttrium oxide has only a slight effect on the form of the distribution curves. Figure 7.20 shows the characteristic curve of the distribution of yttrium oxide along the length of a single crystal with the $ZrO_2$–$Y_2O_3$ cubic structure. As indicated by
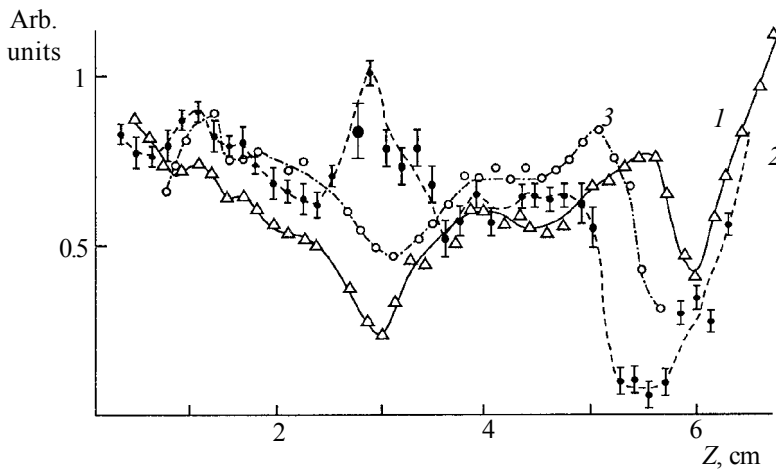


**Figure 7.20.** Distribution of yttrium in $ZrO_2$–10 mol.% $Y_2O_3$ single crystals in different sections of the ingot, growth rate 1 mm/h (centre – 1, periphery – 2, intermediate region – 3).

Tables 7.10 and 7.11, the effective distribution coefficients of the yttrium oxide, calculated using these data, are close to 1 and depend only slightly on the growth rate and the initial concentration of the yttrium oxide. For example, for the $Y_2O_3$ concentration of 10 mol.% (16.95 wt.%) the decrease of the growth rate increases the value of the distribution coefficient; at a rate of 16 mm/h, the increase of the concentration is accompanied by a small decrease of $K_{eff}$.

For the crystals $ZrO_2$–$Gd_2O_3$ at growth rates ($V_P$ = 60 mm/h), the distribution coefficients of the stabilising oxide are also close to unity and slightly increase with increase of the oxide concentration.

The authors of [35] also determined the nature of penetration of oxides of rare-earth elements with high ion radii (Ce, Pr, Nd) into the crystal lattice of zirconia. The range of the compositions, which produce single-phase crystals in crystallisation of the melts, is very narrow as a result of the nature of phase formation in these systems, differing from $ZrO_2$–$R_2O_3$ system (R–Y, Gd, Yb). Therefore, the oxides of caesium, praseodymium and neodymium were added in the form of an additional mixture to the solid solutions $ZrO_2$–$Y_2O_3$. The distribution of the concentration of the ions of rare-earth elements along the length of the crystal greatly differs from the values calculated from the Gulliver–Pfann and Barton–Prim–Slichter equations.

In addition to admixtures, especially introduced into the melt to stabilise the crystal structure or activate laser generation, the crystal usually contains uncontrollable impurities from the charge. The content of the impurities varies in the range $10^{-3}$–$10^6$ wt.% and is determined by the purity of the initial reagents and the effective distribution coefficient. The amount of the impurities in the charge and in the crystals grown from the charge is presented in Table 7.4.

**Characteristics of defects in fianites**

In most cases, the fianite single crystals contain macro- and microdefects which often have a controlling effect on the properties and quality of the crystals. The aim of the present section is to describe the characteristic defects of large single crystals, explain the nature and reasons for their formation, and determine methods of removing them. The larger defects, which are already present in the crystal, can be eliminated only by a mechanical method, i.e.

by removing the defective part of the crystal.

Crystal technology should be such as to ensure that defects do not form during growth and cooling of the crystals. It should be mentioned that the defects, detected in fianites, are also found in other crystals, grown from a cold crucible and their formation mechanisms are similar.

Characteristic defects in fianites are growth bands, inclusions of secondary phases, the cellular substructure and also residual mechanical stresses. These defects cause the optical heterogeneity of the crystals. Undoubtedly, the formation of these and other defects is influenced by the impurities of secondary elements,
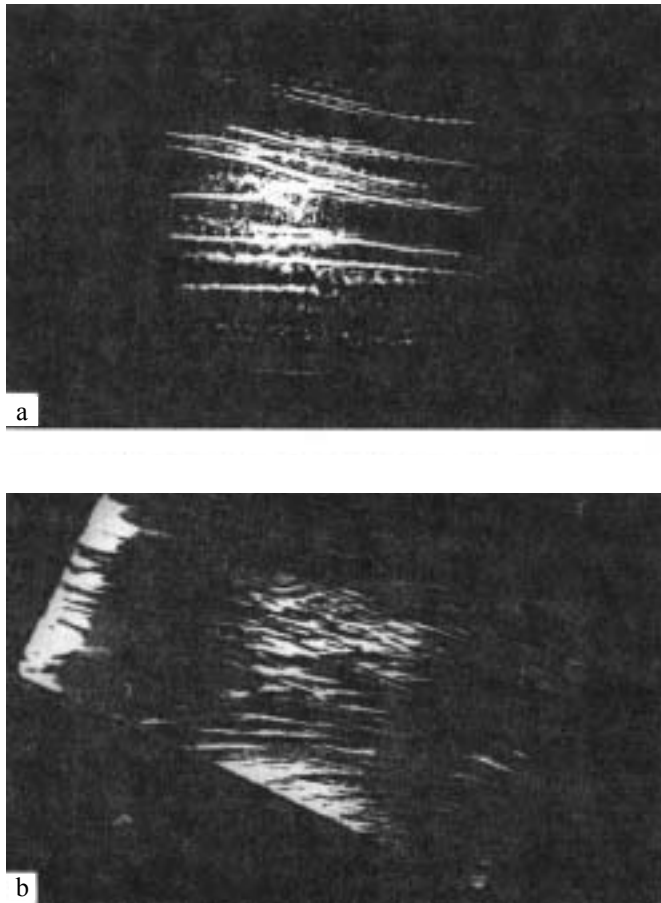


**Figure 7.21.** Growth bands: in the $ZrO_2$–33 mol.% $Y_2O_3$ single crystals, the growth rate 16 mm/h (a) and in single crystals grown in the 'lid' of the crystalline block (b) [40].
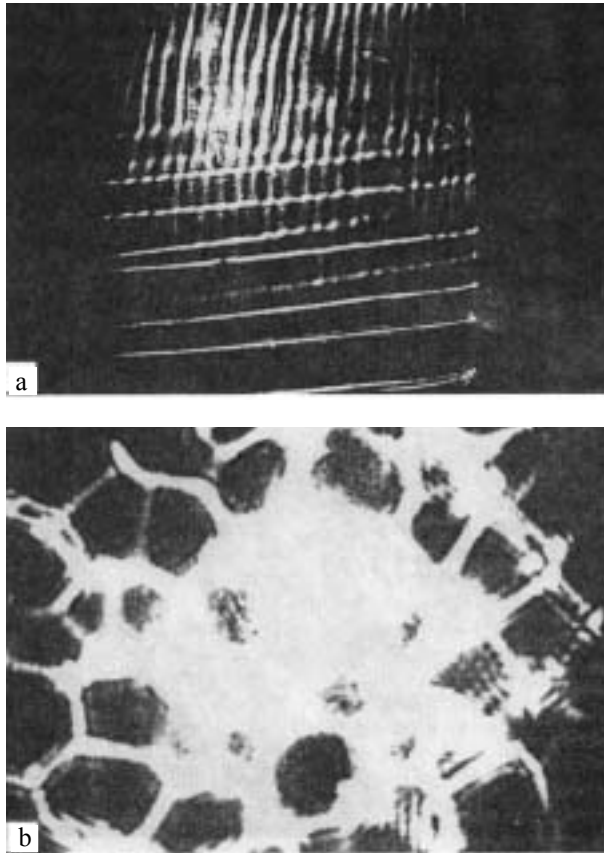
**Figure 7.22**. The cellular structure in the $ZrO_2$–33% $Y_2O_3$ crystals [40], a) the direction parallel to the gross axis, ×300; b) in the direction normal to the growth direction, ×15.

present initially in the reagents. As indicated by Table 7.4, the content of the main impurities is relatively low but in some cases (for example, in drawing light fibre optics) the content of the impurities is outside the permissible range and the initial reagents must be additionally purified.

**The growth bands** are layers with different refractive indices found in all crystals. They are manifested in the form of bands normal to the direction of growth of crystal blocks (Fig. 7.21*a*). In the crystals, growing on the surface of the melt, the growth bands are represented by randomly distributed deformed layers (Fig. 7.21*b*).

**The cellular structure** is found in crystals in the central part of the ingot, usually in its upper part (Fig. 7.22). The upper end
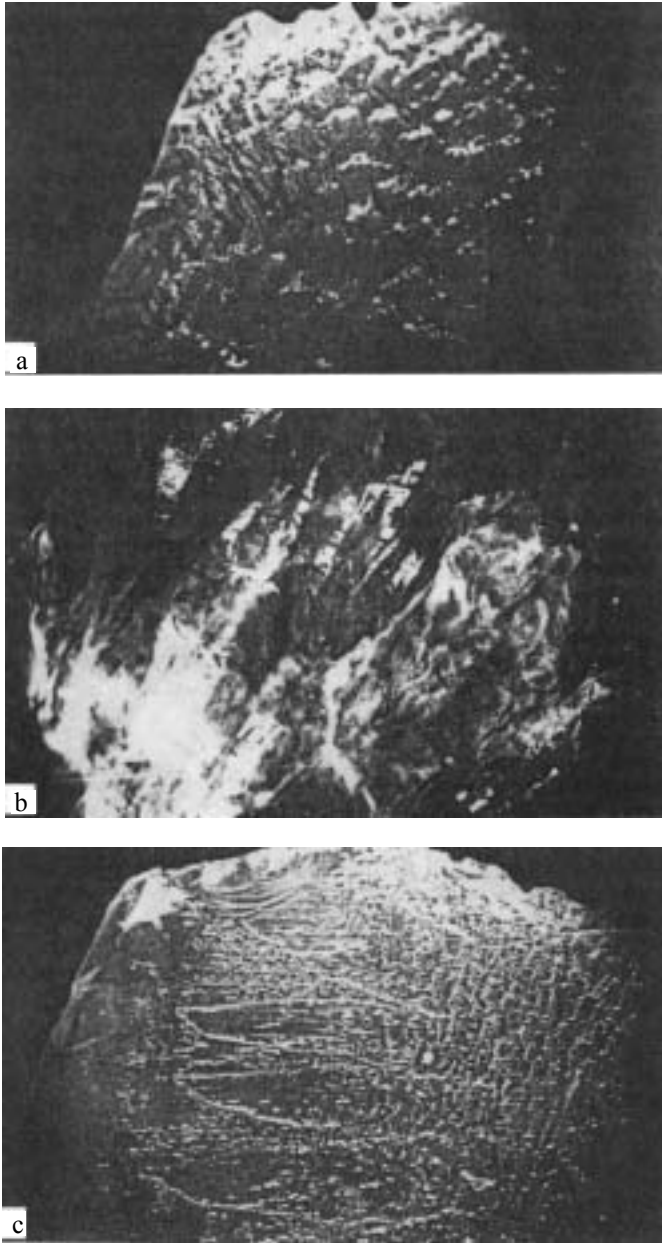
**Figure 7.23.** The end surface of crystals, grown from the bottom of the crucible [40]. a) the region with the cellular structure, b) peripheral region, c) transition region of the crystal.
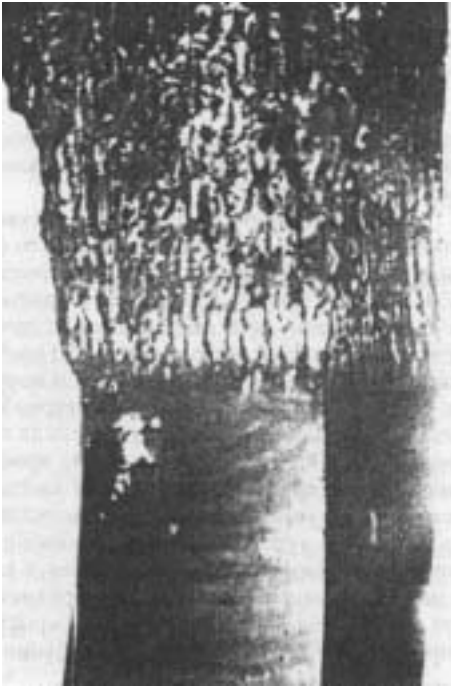
**Figure 7.24.** The side surface of the crystal with a highly developed cellular structure.

surface of the crystals in which the similar structure formed has a characteristic rough form (Fig. 7.23*a*). On the side surface of the structure there is a distinctive boundary between the smooth surface with strong shine and the uneven surface (Fig. 7.24). Figure 7.22*a* shows that the number of bands decreases with the formation of the cellular structure. The same crystal may contain alternating regions with distinctive bands and cellular structures. The dimensions of the region of the ingot with the cellular structure, extending to the surface of the ingot, reached 120 mm in diameter (using a crucible with a diameter of 220 mm and a high purity charge). The crystals distributed around the periphery are characterised by a smooth surface, and those in the transition region have a rough surface (Fig. 7.23). Table 7.4 gives the content of the impurity elements in the initial reagents and in the crystals grown from them. In most cases, the impurity content of the crystals is lower than in the melt. This may be explained by the partial evaporation of highly volatile oxides, and also by the presence of impurities with the distribution coefficient $K < 1$.
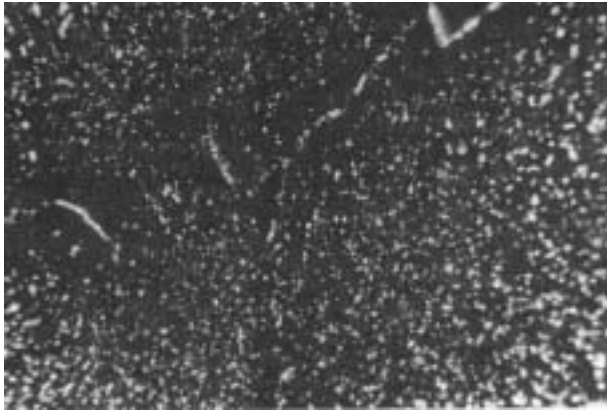
**Figure 7.25.** Inclusions of the second phase in the $ZrO_2$–$Y_2O_3$ 10 mol.% + $N_2O_3$ 0.5 mol% (electron microscopy) [40].

## Inclusions of secondary phases

Large single inclusions of the solid phase and bubbles are found only seldom. The inclusions of the second phase in the form of particles with the size of 0.08–10 µm are found more frequently, cause scattering of light and can be detected visually (Fig. 7.25) or using a microscope. There are cases in which all the crystals of the ingot were 'turbid' to various degrees. The intensity of light scattering was the highest in the crystals taken from the central part of the ingot. However, the crystals contained areas with scattering particles in the form of a layer covering the entire block or its part.

Light scattering depends on the purity of initial reagents. Optical investigations with glowing points show that the scattering regions coincide with the regions of the cellular structure characterised by a large increase of the intensity of the glow of the Tindall cone. In addition to the inclusions in the volume of the crystal, the second phase is detected in the form of deposits on the surface of blocks. The individual sections, usually smooth with strong shine of the side surface, are covered with a matt deposit.

The formation of the inclusions causing light scattering in fianites, may take place both in the process of solidification of the melt at the phase boundary, at the boundaries of the cellular structure, and in cooling of the ingot in the process of high-temperature annealing of the crystals in the growth chamber with a decrease of the generator power [40].

## Heterogeneities of chemical composition

The distribution of the stabilising oxide and the heterogeneity of the composition were investigated on the example of solidification of the solid solutions: $ZrO_2–Y_2O_3$ [7], $ZrO_2–Y_2O_3–CaO$ [89]. The crystals were grown by directional solidification of the melt in air with lowering of the crucible with the melt at a rate of 1–20 mm/h. The initial charge was prepared by thorough mixing of the powders of zirconium and yttrium oxide. The concentration of the yttrium oxide was varied in the range 8–33 mol.%. In lowering the crucible, solidification of the melt started in the lower part of the crucible on crystalline grains of the skull. The solidified ingot consisted of several columnar single crystals. Solidification of the melt also started by means of a slow decrease of the generator power with the crucible in the stationary position. The rate of decrease of the generator power corresponded to the mean linear growth rate of 16–20 mm/h. In addition to the main solidification process from the bottom of the crucible, a 'roof', i.e. a single crystal layer, also formed on the surface of the melt, growing into the bulk of the melt as a result of high-intensity radiation. The solidified layer reached the maximum thickness (up to 3 cm) in solidification by decreasing the generator power.

The grown crystals were characterised by three types of optical heterogeneities: growth bands (ripples), light scattering and the cellular substructure. The ripples, alternating layers with the changed refractive index, were detected in all crystals. They are manifested in the form of straight bands, normal to the direction of growth of the crystals growing from the bottom of the crucible (Fig. 7.26*a, b*) or in the form of distorted bands in the 'roof'. The variation of the refractive index in the ripples is caused by the variation of the yttrium concentration determined by examination of the distribution of yttrium along the length of the crystals. Figure 7.20 shows the curves of distribution of yttrium $C(z)$ in the crystals taken from different parts of the ingot. The concentration of yttrium in the melt was 10 mol.%, the rate of growth of the crystals 1 mm/h. The figure shows that the distribution of yttrium $C(z)$ is wave-shaped. The waves in different parts of the crystals differ in amplitude and frequency, indicating different solidification conditions in the cross-section of the crystal. The concentration of yttrium at the end of the crystals is lower. This is characteristic of the impurity with the distribution coefficient $K_{eff}$ higher than unity.
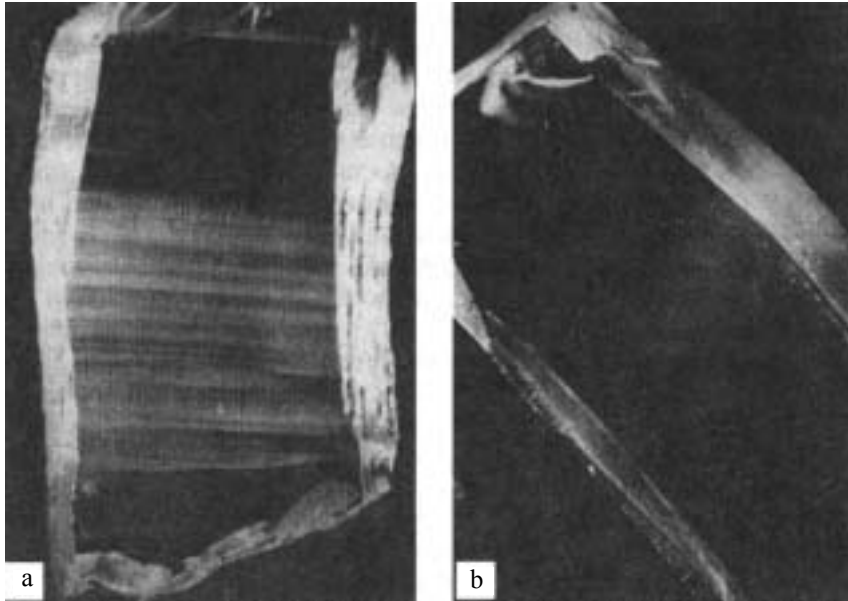
**Figure 7.26.** Scattering of light in $ZrO_2 - 12\%$ $Y_2O_3$ crystals in the region of the cellular structure [40]. The region includes the entire crystals; b) part of the crystal, $\times 3$.
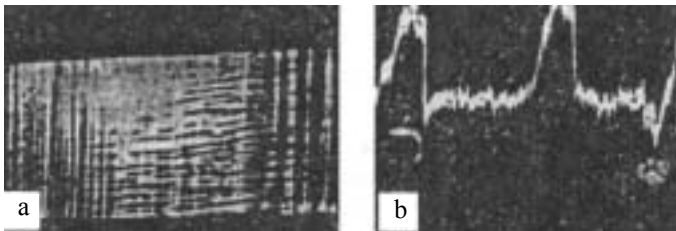


**Figure 7.27.** Crystal with a cellular structure [88]. a) side view, b) distribution of yttrium in the region between the cells.

Similar phenomena are also found in other crystals and depend only slightly on the solidification rate and the concentration of the impurity in the melt. The effective coefficients of distribution of yttrium, calculated using these data, are presented in Table 7.10. Comparison of Figs. 7.20 and 7.27, relating to the same crystal, shows that the presence of the ripples in the crystal is independent of the yttrium distribution $C(z)$. Evidently, the variation of the composition corresponding to the ripples is insufficient to be detected by the x-ray spectral method. The difference in the yttrium concentration between the sections with different refractive indices is smaller than 1%. In the crystals, growing from the bottom of the crucible, the number of ripples decreased with a decrease of the

rate of lowering the container with the melt and when using reversing motion. The decrease of the growth rate also increases the size of the crystals in the ingot. At the rate of lowering of the crucible of 1 mm/h, an ingot with a diameter of 130 mm consisted of 4–5 blocks. Large blocks, grown at this rate, contained high stresses and cracked during cooling. After thermal annealing, the crystals remained without fracture.

Another type of heterogeneity is the cellular structure, usually detected in the upper part of the crystals, grown in the middle of the ingot at a lowering rate of the crucible with the melt of 60 mm/h and higher. An example of the crystal with a cellular structure is shown in Fig. 7.27*a*. The formation of the cellular structure is accompanied by the decrease of the ripples. The same crystal may contain alternating regions with ripples and a cellular substructure. The determination of the composition in the cross-section of the crystals with the cellular substructure shows that the concentration of yttrium in the centre of the cells is 2% higher in comparison with the concentration at the boundaries of the cells.

The particles, scattering the light, are grouped in ripples or at the boundaries of the cells, but crystals with uniform scattering throughout the entire volume were also grown. The layer distribution of the inclusions, coinciding with the banded structure, formed at a relatively low concentration (8–9%) of the yttrium oxide, and the crystals also showed light scattering.

One of the types of inclusions – large (~10 µm) particles, concentrate in the crystals at the boundaries of the cells. Local x-ray spectral microanalysis shows that the chemical composition of these particles is heterogeneous and they consist of silicon, yttrium, but do not contain any zirconium.

The formation of this cellular substructure is usually linked with concentrational supercooling (CS) [90, 91]. In solidification, the melt is enriched with the component which decreases the melting point. At a finite diffusion rate, the composition of the melt does not manage to equalise and a 'diffusion layer' forms in front of the solidification front. The solidification temperature in this layer increases in the direction into the bulk of the melt. The zone of the highest supercooling also travels into the bulk of the melt resulting in the instability of the flat solidification front: individual projections of the crystal, penetrating into the region of supercooling, grow at a higher rate than other regions of the solidification front.

Analysis of the distribution of temperatures in the melt shows

that the maximum temperature is obtained on the level of the induction coil. The temperature in the upper and lower parts of the melt is reduced because of a less effective absorption of the energy of the high-frequency field and more intensive heat removal. This distribution of temperatures complicates thermal convection in the melt above the crystals, growing from the bottom of the crucible. The extent of mixing of the melt by the high-frequency field is very low. In these conditions, the mass transfer in the melt is difficult and this results in the formation of a wide diffusion layer ahead of the solidification front and in the development of concentrational supercooling for crystals growing from the bottom of the crucible.

As mentioned previously [92, 93], the formation of the banded structure in crystals may be caused by concentrational supercooling and oscillations of the growth rate in the diffusion layer, and also by the failure of the layer in rapid solidification of the supercooled region of the melt. The instability of the growth rate results in the oscillations of the effective coefficient of distribution of the impurity. The decrease of the rate of growth and high intensity of mixing of the melt result in the equalisation of the impurity concentration in the melt and this reduces the probability of formation of concentrational supercooling and, consequently, reduces the extent of the banded structure. This mechanism explains the formation of growth bands in the crystals growing from the bottom of the crucible. For the crystals, growing in the 'roof', the formation of concentrational supercooling is unlikely because growth takes place in the conditions of strong convective mixing and a highly superheated melt is situated below it. However, the formation of the banded structure in the crystals, formed in the 'roof', may be caused by irregular convection, resulting in the fluctuations of temperature and the solidification front, as indicated by disordering of the ripples in the 'roof'.

As indicated by previous considerations, the same mechanism (concentrational supercooling) is used to explain different types of defects: the cellular substructure and the formation of the banded structure. It may be assumed that the transition from the banded to cellular substructure is determined by dimensions of the region of concentrational supercooling, and the formation of cells results in a decrease in the amount of the banded structure.

In addition to the variation of the growth rate associated with concentrational supercooling, the variations of the composition may

**Table 7.12.** Composition of inclusions in $ZrO_2$–$R_2O_3$ crystals (here R – Y, Eu, Gd, Yb)

| Composition of crystal | | Composition of inclusions | | | | | | |
| --- | --- | --- | --- | --- | --- | --- | --- | --- |
| | | Phase 1 (grey) | | | | Phase 2 (black) | | |
| $ZrO_2$, mol% | $R_2O_3$, mol% | $ZrO_2$, mol% | $R_2O_3$, mol% | $SiO_2$, mol% | CaO, mol% | $ZrO_2$, mol% | $R_2O_3$, mol% | $SiO_2$, mol% |
| 90 | $10Y_2O_3$ | 10.6 | 27.6 | 61.8 | – | 2.19 | 1.0 | 97.00 |
| In the zone of cellular structure | | | | | | | | |
| 88 | $12Y_2O_3$ | 8.15 | 28.14 | 62.69 | – | 10.06 | 7.65 | 97.23 |
| End of the crystal | | | | | | | | |
| 88 | $12Y_2O_3$ | 8.23 | 27.53 | 62.65 | 1.57 | 3.9 | 5.7 | 90.33 |
| 84 | $16Y_2O_3$ | 11.5 | 25.36 | 63.08 | – | 1.48 | 8.55 | 89.96 |

be caused by 'apparatus' effects: instability of the generator power, variation of the relationship between the induction coil and the melt, and the nonuniformity of movement of the crystal. As shown by the measurements of the power absorbed in the melt from the variation of the temperature of the cooling water at entry into and exit from the container, the growth process is accompanied by variations of the temperature of the melt which may cause heterogeneity of the composition of the crystal. These external instabilities are not the main source of the growth bands and can be eliminated by modifying the working conditions of equipment. At the same time, they may be responsible for the relatively large oscillations of the composition reflected in the form of concentration waves $C(z)$.

Silicon inclusions form as a result of the displacement of the silicon impurity by the growing crystal into the region between the cells. Yttrium oxide builds up in the $SiO_2$ phase whose acidity is higher than that of $ZrO_2$. The heterogeneity of the inclusions is caused by the fact that they are trapped by the growing crystal in the form of melt droplets, and the segregation processes already take place in the crystal matrix. The appearance of the second phase in the crystal is possible in cooling as a result of polymorphous transformations if the concentration of the stabilising addition is insufficiently high. The variations of the composition in the bands being formed take place in the vicinity of the boundary

of stability of the cubic phase.

In addition to the yttrium oxide, calcium oxide is also used as a stabilising addition. In [95], the crystals of the following systems were grown: $ZrO_2$–$CaO$, $ZrO_2$–$Y_2O_3$, $ZrO_2$–$Y_2O_3$–$CaO$. The distribution of $Y_2O_3$ and $CaO$ in the charge, the crystals and in the residual melt was determined by chemical analysis. The results are presented in Table 7.12 which shows that the $Y_2O_3$ content of the crystal is always lower than in the initial materials; the content in the residual melt is lower than in the crystal. This indicates that $Y_2O_3$ may evaporate and the coefficient of its distribution in the crystal is lower than unity. At the $Y_2O_3$ content of the melt of 20 mol.%, the growth of macroscopic crystals is more stable but they are darker. At 12 mol.% of $Y_2O_3$, the crystals are almost colourless and transparent.

Analysis of the crystals containing the calcium oxide shows that the amount of this oxide in the crystal is considerably smaller in comparison with the initial material. A large part of the oxide remains in the residual melt, i.e. the coefficient of distribution of the calcium oxide in the crystals $K_{Ca}$ is lower than 1. The crystals, containing 13 and 15 mol.% of $CaO$, are considerably smaller than the crystal stabilised by $Y_2O_3$; they are colourless and transparent but more brittle. The authors detected the same defects in the grown crystals and they will be described later. Etched specimens showed inclusions similar to pipes touching each other, and the form of the inclusions on the etched surfaces was tubular with a diameter of approximately 10 µm. The etching rate of the inclusions was considerably higher than that of the main matrix. The inclusions were concentrated at the ends of the crystal and removed by machining. The inclusions in the form of individual islands, detected in the centre of the crystal, were hexagonal. All the inclusions in the cubic crystals of stabilised zirconia had the same optical characteristics, but the refractive index and microhardness were clearly lower than those of the main matrix. Chemical analysis of the inclusions in the investigated crystal shows that the composition of the impurities is the same as that of the main matrix, and they consist mainly of a mixture of Si, Ca and Mg, with Si and Ca dominant. In polygonal inclusions in the form of polyhedrons, the content of Si and Ca was considerably higher, the content of Mg lower and that of Zr still lower. No silicon was found in the matrix of the crystal.

## 7.6. MECHANISMS OF FORMATION OF DEFECTS IN FIANITES

**Growth bands**

The appearance of the growth layers in fianites is caused by the presence of admixtures and, primarily, of the stabilising oxide. We have already mentioned an example of the distribution of the stabilising oxide along the length of the crystal (Fig. 7.20). Analysis of the results shows that the visually observed growth bands do not always correspond to the distribution waves of the concentration of the stabilising oxide. The discrepancy between the density of the concentration waves and visible growth bands are characteristic of the crystals with a high density of the layers. For low density of the layers (2–4 cm$^{-1}$), the agreement is quite good. Evidently, the amplitude of variations of the composition, corresponding to the growth bands, is below the sensitivity of the method of x-ray spectral analysis. In fact, the estimates of the composition made on the basis of the local measurements of the refractive index show that the difference between the absolute yttrium concentration in areas with different refractive indexes is usually approximately 1%. The density of the bands is unaffected by factors such as the concentration of the stabilising oxide, the rate of growth of the crystal, and the nature of mixing of the melt.

With increase in the concentration of the stabilising oxide, a large increase of the density of the bands was detected only in the range of the compositions close to 30 mol% $R_2O_3$ and a the lowering rate of the crucible of 16 mm/h. With a decrease of the lowering rate to 1mm/h, the density of the bands in the crystals decreased to 8 cm$^{-1}$. In forced mixing of the melt by reversing movement of the crucible and in the case of low growth rates, the density of the bands decreased to 1 cm$^{-1}$.

The growth layers are usually determined by two reasons: apparatus instability and special features of the mechanism of growth of crystals from the melt.

The determination of the heating power and the efficiency of removal of heat from the crucible with the melt shows that the maximum temperature is obtained on the level of the induction coil, and in the upper and lower volumes of the melt the temperature of the melt is usually lower because of the less extensive absorption of the energy of the high frequency field. Due to such a distribution

of temperature, the temperature in the layer of the melt above the crystal, growing from the bottom of the crucible, increases with the height and, therefore, heat convection is more difficult. The decreased in the concentration of the yttrium ions in the vicinity of the solidification front in comparison with the concentration in the melt (since $K_{eff} > 1$) results in an increase of the density of the melt at the solidification front and this also prevents convective mixing. The electrodynamic mixing of the melt by the high frequency field in the investigated case is insignificant because the working frequency is relatively high (5.28 MHz) and the electrical conductivity of the melt is relatively low (10–100 ohm cm) [94]. In addition to this, the solidification front is positioned well below the upper level of the induction coil. In these conditions, mass exchange in the melt is complicated, resulting in the formation of a thick diffusion layer and in the development of concentrational supercooling. Evidently, this is accompanied by the formation of spontaneous oscillations of the growth rate during the formation of the diffusion layer depleted in $Y_2O_3$, but the rate of crystal growth decreases since the crystallisation temperature increases. When the crucible is lowered into a region of lower temperatures, the partial or complete failure of the diffusion layer takes place as a result of the rapid crystallisation of the supercooled melt. Nonuniform growth leads to variations of the effective coefficient of distribution of the admixture. As indicated by experience, a decrease of the growth rate and intensive mixing of the melt cause the equalisation of the concentration of the admixture in the melt leading to a decrease of the probability of occurrence of concentrational supercooling and to a decrease in the extent of formation of the banded structure in the crystals.

Possible reasons for the formation of growth bands may also include: instability of the power of the generator, variations of the consumption of the heat carrier in the cooling system of the crucible, nonuniform movement of the crucible with the melt. The effect of these factors has been investigated in experiments in [6]. The nonuniform movement of the crucible was recorded using an indicating device with a sensitivity of 0.01 mm. The maximum 'jumps' were 0.05–0.07 mm, at a rate of lowering of the crucible of 1 mm/h, and these variations may be ignored.

In the growth of single crystals with the composition $ZrO_2$–12 mol.% $Y_2O_3$ in Donets-4 equipment with the crucible lowering rate of 2 mm/h, the parameters of the generator ($I_c$, $U_a$, $I_a$), working in

the conditions with stabilisation of $U_a$, were constantly controlled, together with the control of the power generated in the load and taken away by the cooling water throughout the entire growth process.

The recording of the heating power and the power, generated in the load, shows that the process of crystal growth is accompanied by variations of the melt temperature which may lead to heterogeneities in the composition of the crystals. Comparisons of the diagrams of temperature in the melt with the diagrams of distribution of yttrium along the length of the crystal at a growth rate of 1 mm/h shows that temperature jumps with time coincide with the jumps of the concentration of the stabilising oxide. Consequently, a mechanism of formation of concentration waves has been proposed. Disruption of the stability of the power of heating the melt leads to a disruption of the diffusion layer at the phase boundary and, consequently, to instability in the yttrium distribution. For the selected growth conditions, the number of bands formed throughout the entire growth process was 1–2.

Thus, the apparatus instability may lead to the formation of growth bands but it is not the main source of these bands. This position is confirmed by a decrease in the density of the growth bands with a decrease in the rate of lowering the crucible. The same relationships were also recorded for single crystals with other stabilising oxides (europium, gadolinium, ytterbium). It is important to note the anomalously low density of the growth bands in the crystals based on $HfO_2$. Evidently, the congruent crystallisation mechanism operates in this case.

For the crystals growing from the surface of the melt ('in the roof') the characteristic feature is the high density and considerable bending of the growth bands. The reasons for the formation of these bands differ from the reasons causing the formation of growth bands in the crystals growing from the bottom of the crucible. In these crystals, the formation of concentrational supercooling is unlikely because they grow in the conditions of strong convective mixing. The formation of the banded structure in these crystals is caused mainly by irregular convection, leading to the fluctuation of temperature at the solidification front. The irregular nature of convection flows is also the reason for the formation of the bent growth bands.

Thus, the formation of the banded structure in the fianite crystals is associated with small variations of the concentration of

the stabilising oxide as a result of concentrational supercooling. Crystal defects may be removed by decreasing the rate of lowering the crucible and by forced mixing of the melt.

**The cellular substructure**

Another type of admixture heterogeneity, often found in fianite crystals, is the formation of the cellular substructure. The determination of the chemical composition in the cross-section of the $ZrO_2$–10 mol.% $Y_2O_3$ crystals with a cellular substructure shows that the yttrium concentration in the centre of the cells is 2% higher in comparison with the periphery. This corresponds to the coefficient of distribution of yttrium in the crystal higher than unity.

The formation of the cellular substructure is usually associated with the concentrational supercooling of the melt. The formation of this defect during growth of fianite crystals was substantiated previously. During crystallisation, the melt is enriched with the component decreasing the melting point (zirconia), and at a low diffusion rate the composition of the melt does not equalise in the entire volume. In this case, a 'diffusion' layer forms ahead of the solidification front. The concentration of $Y_2O_3$ and, consequently, the solidification temperature in this layer increase in the direction from the surface of the crystal into the bulk of the crystal. This results in the instability of the flat solidification front.

Thus, the same mechanism – concentrational supercooling – is responsible for the formation of both the cellular structure and growth bands in the fianite crystals. Concentrational supercooling (CS) is an essential but insufficient condition for the formation of the cellular structure. The cellular structure forms only at some critical value of concentrational supercooling. Cells appear mainly in the upper part of the crystal, at a high crystallisation rate and without mixing of the melt. It is evident that the values of CS, required for the formation of the cellular structure, should be higher than those required for the formation of growth bands.

The formation of the cellular structure may be associated not only with the stabilising oxides but also with foreign admixtures, present in the initial charge. As in many other crystals, the most detrimental impurity for the crystallisation of fianites is the silicon oxide with the distribution coefficient considerably lower than unity.

## Inclusions of foreign phases

The light scattering in the fianite crystals, caused by the presence of the second phase, may be due to two reasons: a) decomposition of the cubic solid solutions; b) the presence of secondary phases in the initial reagents. The authors of [40] investigated the effect on the growth and perfection of single crystals of fianite of the most widely encountered admixtures in the form of oxides: $SiO_2$, $TiO_2$, $Al_2O_5$, $WO_3$, whose concentration in the initial reagents was approximately $10^{-2}$ wt.% and which had a significant effect on the properties of these crystals [101–103]. For example, it is well known that the presence of oxides of silicon, aluminium and titanium, found in the initial reagents, reduces the stability of the polycrystalline material. The $SiO_2$ impurity results in a large decrease of the strength and heat resistance of the crystals and decreases the softening temperature under load [103].

The formation of any specific type of admixture heterogeneity in the crystals is determined by the nature and concentration of the admixture. The previously mentioned admixtures are not isomorphous in relation to zirconia. In fact, the isomorphous inter-relationship of the atoms (ions) in the crystals is determined by a number of factors, namely: 1) chemical indifference; 2) similar ion radii; 3) identical nature of ion bonding; 4) isostructural nature of the produced crystals. The isomorphism conditions are not fulfilled for these ions with zirconia atoms already in the case of the first two parameters. Thus, these oxides should be displaced by the growing crystals and, depending on the crystallisation conditions and the concentration of the given admixture, they will cause the formation of different admixture defects.

We have investigated crystals with the composition $ZrO_2-R_2O_3$, where R = Eu, Gd, Yb, Y, and crystals with intentionally introduced admixtures in the concentration from 0.05 to 1 wt.%. The admixtures of aluminium, titanium and tungsten were introduced into a charge with the composition $ZrO_2-12$ mol.%$Y_2O_3$ in the amount of 1 wt.% [93].

## Effect of silicon dioxide on the crystallisation of fianites

The effect of the $SiO_2$ impurity on the nature of crystallisation and the optical homogeneity of the fianite crystals was investigated in [104]. Crystals of fianites with rare-earth stabilising oxides and a

batch of crystals with 12 mol.% of yttrium oxide and with the intentionally introduced silicon dioxide in the amount of 0.05–0.5 wt.% were grown. In the crystals without intentional addition of $SiO_2$ into the melt, the blocks were characterised by the typical appearance and the dimensions, and also by the presence of typical defects examined in detail in the previous chapter.

Examination of the crystals in a polarisation microscope showed
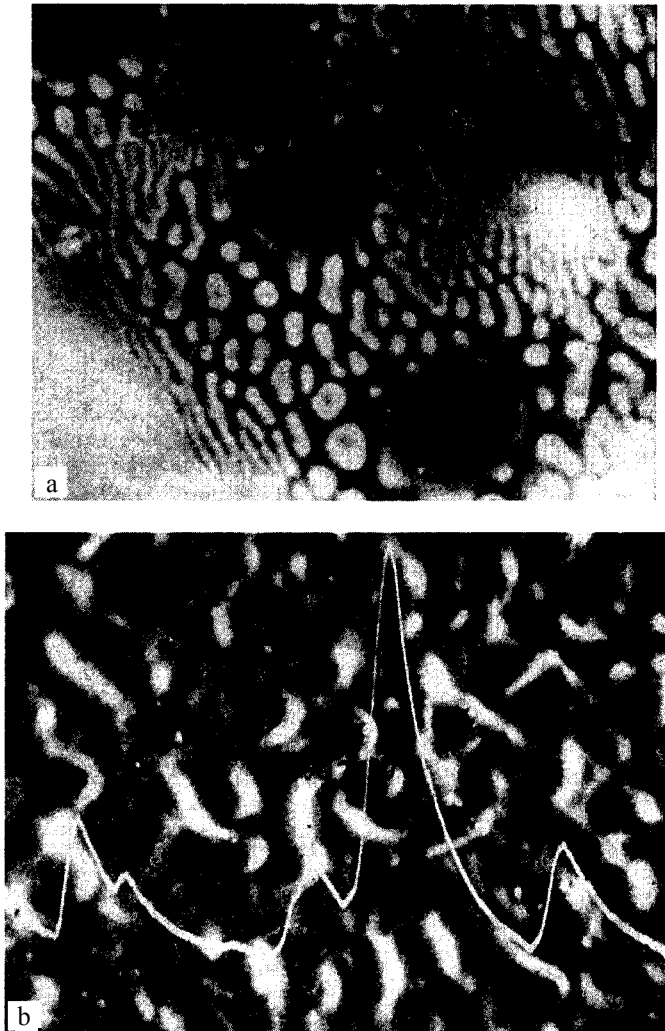


**Figure 7.28.** Deposits on the site surface, formed in the process of growth of $ZrO_2 – Y_2O_3$ 10 mol.% crystals [40]. a) the melt contained $SiO_2$ impurity, b) $Al_2O_3$ impurity.

**Table 7.13.** Composition of inclusions in crystals grown from a melt with the composition $ZrO_2$–12 mol% $Y_2O_3$ + 0.5 wt.% $SiO_2$ [40]

| Examined areas of crystal* | Composition, mol% | | |
|---|---|---|---|
| | $ZrO_2$ | $Y_2O_3$ | $SiO_2$ |
| 1 | 2.23 | 6.11 | 91.64 |
| 2 | 4.93 | 31.72 | 63.33 |
| 3 | 83.67 | 16.32 | - |
| 4 | 12.19 | 24.45 | 63.35 |
| 5 | 84.31 | 15.24 | - |

*Examined areas of crystal 1–5cm, in Table 7.14

that the cellular structure contained large (approximately 10 µm) inclusions of a second phase, distributed at the cell boundaries. Figure 7.25 shows a photograph of inclusions in the $ZrO_2$–$Y_2O_3$ crystals produced in scattered electrons. The shape of the inclusions was usually spherical or droplet shaped. Table 7.13 shows the composition of the inclusions of crystals with different concentrations of the stabilising oxide. Examination of matt areas of the surface of the crystals already showed the presence in them of individual clusters of phases with a high $SiO_2$ concentration (Fig. 7.28). With an increase in the silica concentration, the extent of light scattering increases, as indicated by an increase of the intensity and the diameter of the cross-section of the Tindall cone. Scattering was caused by small particles of the second phase with a size of ~0.1 µm. At an $SiO_2$ content in the melt of 0.2 wt.%, the crystals contained a columnar structure and growth bands. With an increase in the content of the admixture, this complicated structure of the defects was transformed into a cellular substructure. At 0.3 wt.% $SiO_2$, the crystals in the centre of the block were cellular and the blocks were polycrystalline. The periphery of the block was characterised by the growth of large single crystals with a high level of light scattering. In solidification of the melt, containing 0.5 wt.% $SiO_2$, examination showed the formation of a completely polycrystalline block. The phases, containing silicon dioxide in the polycrystals, were characterised by the form of continuous vertical columns passing through the entire length of the block. X-ray diffraction analysis showed that the crystals with a $SiO_2$

concentration of 0.05–0.5 wt.% have the cubic structure of the fluorite type.

According to the equilibrium diagram, the $ZrO_2$–$SiO_2$ system contains the $ZrSiO_4$ compound which decomposes in the solid phase into $ZrO_2$ and $SiO_2$ at a temperature of 1950 K, below the eutectic temperature. In directional crystallisation of the melt, the formation of a compound consisting of $ZrO_2$ and $SiO_2$ in the process of growth of crystals is unlikely to take place. Silicon dioxide, present in the investigated system, with a distribution coefficient lower than unity $K_{eff} < 1$, should be displaced during the growth of the crystal of the solid solution of $SiO_2$ with $ZrO_2$. The region of the phase diagram rich in $ZrO_2$ does not contain the $ZrSiO_4$ compound (the $SiO_2$ concentration in the crystal does not exceed $1.3 \times 10^{-2}$ [105, 106].

During growth of the crystals, the concentration of $SiO_2$ ahead of the solidification front increases because at a high growth rate the diffusion does not manage to reduce the concentration of $SiO_2$ because of the segregation process. This results in the formation of initially fine inclusions of the second phase and, subsequently, the formation of various morphological (columnar and cellular) structures forming large inclusions. The spherical shape and heterogeneity of the composition of large inclusions indicate that the capture of the admixtures takes place in the liquid state. Possibly, the unstable growth, taking place during the formation of the cellular structure, is accompanied by the capture of melt droplets from the boundary layer enriched with the silica. As a result of the lower (in comparison with $ZrO_2$) melting point, these droplets are enclosed in the hard matrix of the crystal. Thus, this phenomenon is associated with the concentrational supercooling [106]. The composition of the inclusions depends on the type and concentration of the stabilising oxide and also on the growth conditions of the crystal. The $SiO_2$ concentration in these droplets reaches more than 60 mol.%, and the droplets are characterised by the higher concentration of the stabilising oxides of rare-earth elements. Possibly, the $R_2O_3$ oxides, having the alkali nature, concentrate mainly in the droplets in which $SiO_2$ generates a more acid medium in comparison with the zirconia. The process of chemical differentiation takes place either during the formation of the droplet or during cooling of the droplet as a result of diffusion from the solid matrix. In order to explain the sequence of the distribution of the admixture in the droplet, it is convenient to use the $ZrO_2$–$SiO_2$ and $SiO_2$–$R_2O_3$ binary diagrams. The solidification of the droplet

takes place from the periphery to the centre and in accordance with the $SiO_2$–$Y_2O_3$ diagram, the first phase to form in the temperature range 1933–1973 K is the solid phase containing mainly $SiO_2$; the centre of the droplet is characterised by the crystallisation of the eutectic mixture of the solid phases $SiO_2 + Y_2O_3$ $2SiO_2$, together with the $ZrO_2$ component [107]. The composition of the inclusions in the $ZrO_2$–12mol.%$Y_2O_3$+0.5 wt.% $SiO_2$ crystals is presented in Table 7.13.

It is natural to expect that the composition and structure of the inclusions in crystals with other stabilising elements should be the same because these elements have the phase diagram is similar to $SiO_2$. However, Table 7.13 shows that this is not so in reality: the nature and compositions of the inclusions differ for different stabilising elements. Possibly, these differences are caused by the composition of trapped droplets or by the extent of exchange of components between the droplet and the solid matrix. It should be mentioned that the conditions of growth of the crystals, stabilised with the oxides of europium, gadolinium and ytterbium, differ from the conditions of growth of the crystal stabilised with yttrium (the volume of the crucible with the melt was considerably smaller). The high content of the stabilising oxide in the inclusions makes it possible to assume that in the case of relatively high concentrations of $SiO_2$ and a low content of the stabilising oxide, the silica may induce the decomposition of cubic solid solutions and the formation of the monoclinic phase $ZrO_2$, present in the polycrystalline materials [102].

Thus, the production of zirconia single crystals requires efficient purification of the components to remove silica, the content of silica in the melt should not exceed $\sim 5 \times 10^{-3}$ wt.%.

The presence of an admixture of aluminium oxide in the amount of 1 wt.% (1.2 mol.%) in the $ZrO_2$–2mol.% $Y_2O_3$ crystals at a growth rate of 10 mm/h did not disrupt the single crystal nature of the individual blocks, but the side surface of the crystals was characterised by the formation of a matt deposit. The crystals, growing from the surface of the melt ('the roof') were polycrystalline. Examination of samples in an x-ray microanalyser showed the presence of $Al_2O_3$ in the volume of the crystals and on the side surface (Fig. 7.28*b*). The distribution of oxides of zirconium, yttrium and aluminium in the cross-section of a single crystal block is shown in Fig. 7.29. The matt deposit on the side surface of the crystal blocks has the following composition: 85
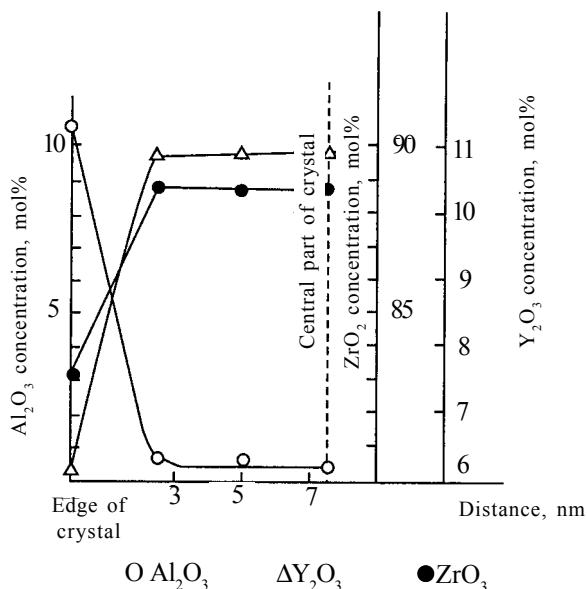
**Figure 7.29.** The radial distribution of the oxides of Zr, Y, Al in the $ZrO_2+Y_2O_3+Al_2O_3$ single crystals [40].

mol.% $Zr_2O_3$, 12.61 mol.% $ZrO_2$, 2.20 mol.% $Y_2O_3$. In the 'roof', the aluminium oxide precipitated between the blocks in the form of a second phase (Fig. 6.9*b*) with the composition $(86.02\pm2.19)Al_2O_3$; $(11.83\pm1.72)ZrO_2$; $(0.14\pm0.5)Y_2O_3$. The Debye patterns of the crystals did not contain additional lines. Thus, the aluminium oxide was rapidly displaced in the process of growth and accumulated mainly in the crystals which grew at the very end of the crystallisation process.

The admixtures of the oxides of titanium and tungsten ($TiO_2$ and $WO_3$) in the amount of 1 wt.% (1.5 and 0.5 mol%, respectively) do not disrupt the single crystal nature during the growth of crystals. After adding $WO_3$, the 'roof' of the ingot in the lower part formed in the form of a polycrystalline dense material. The single crystals in the upper part were characterised by slight colouring which, in the case of titanium, was yellow and for tungsten oxide it was green, with nonuniform distribution in the cross-section of the crystal. The crystals with titanium grown at a rate of 10 mm/h contained an area with a cellular structure formed at the end of growth and characterised by more intensive colouring. According to the results of x-ray diffraction microexamination, the content of tungsten in the volume of the crystals was considerably smaller than

**Table 7.14.** Distribution of $TiO_2$ in $ZrO_2$–12% $Y_2O_3$+1 wt.% $TiO_2$ crystals [40]

| Examined area of crystal | Concentration, mol% | | |
|---|---|---|---|
| Crystal growing from crucible bottom: | $ZrO_2$ | $Y_2O_3$ | $TiO_2$ |
| 1 – lower part | 86.00 | 13.92 | 0.06 |
| 2 – centre | 85.81 | 13.76 | 0.42 |
| 3 – upper part | 83.29 | 12.79 | 3.95 |
| Top of ingot: | | | |
| 4 – upper part | 86.2 | 11.35 | 1.93 |
| 5 – lower part | 84.93 | 12.01 | 3.04 |

the amount added to the melt, ~0.2 mol.%. The chemical composition of the single crystal part of the 'roof' of the ingot was: $ZrO_2$ 85.6 mol.%, $Y_2O_3$ 14.4 mol.%, $WO_3$ 0.2 mol.%, and the polycrystalline part was characterised by the presence of large inclusions with a size of 6–8 µm of irregular shape and containing large quantities of tungsten: $ZrO_2$ 34.2 mol.%, $Y_2O_3$ 23.0 mol.%, $WO_3$ 42.8 mol.%. The concentration of $TiO_2$ in the single crystals changed along the length with a gradual increase towards the end of growth of the crystal (Table 7.14). In the crystals of the 'roof', the $TiO_2$ content increased in the direction from top to bottom.

Polarisation–optical and electron microscopic examination of the regions with the cellular structure in fianite with the additions of titanium oxide showed that the cell boundaries are characterised by the presence of small (approximately 1 µm or smaller) spherical inclusions, consisting mainly of titanium, silicon, zirconium and yttrium. The titanium and silicon content of these inclusions was high but the quantitative composition could not be determined because of the small size of the inclusions.

The examination of the effect of the oxides of aluminium, titanium and tungsten shows that these oxides, like silicon dioxide, cause the formation of defects disturb the optical homogeneity and other properties of crystals. However, this requires higher concentrations than in the case of silicon.

Thus, of the investigated secondary impurities, the most

detrimental effect on the growth and perfection of the finite crystals is exerted by silicon. A small amount of silica (0.05 wt.%) disrupts the growth of crystals and increases the density of various defects and admixture heterogeneity. The experimental results show that all the previously mentioned admixtures are displaced by the front of the growing crystal during crystal growth. Therefore, a reduction in the rate of growth to 10 mm/h and the use of forced mixing of the melt increase the efficiency of the process of displacement of the admixtures and improve the optical homogeneity of the crystals.

**Formation of the microzonal structure**

The authors of [103] investigated the conditions of formation of a microzonal structure in refractory oxide crystals based on zirconia (fianite). As shown in previous chapters, the crystals contain growth bands, slight light scattering by submicron inclusions of the second phase, a cellular substructure and other defects [104, 105]. Crystals for the investigations were produced by the method of direct RF melting in a 'cold' crucible. The concentration of the stabilising oxide $Y_2O_3$ in the charge was 12 mol.%, the content of the alloying admixture of titanium oxide was 0.01 wt.%.

Figure 7.30 shows the topography of the microzonal distribution of the admixtures of titanium in these crystals. The distribution was determined by the method of activation radiography, based on recording secondary β-radiation. The identification of radionucleotides, the evaluation of their content and the drop in activity were determined on the basis of γ-spectra of Ti[47]. The radiographs were interpreted by the method of digital image processing using an interactive system for image processing. The digital processing programs were prepared on the basis of the methodology of cluster analysis, used widely in object recognition problems.

As indicated by Fig. 7.30, the distribution of titanium is characterised by steep local gradients. Analysis of the topographs shows the following:

1. Examination showed the existence of a periodic microzonal structure (zones *1–3*) with a thickness of 300–400 µm, and with increase of the size of the crystal, the size of the microzones increases both with respect to the area and the total content.

2. The presence of a stochastic cellular structure was confirmed (zones *5–6*). The observed large decrease in the concentration of
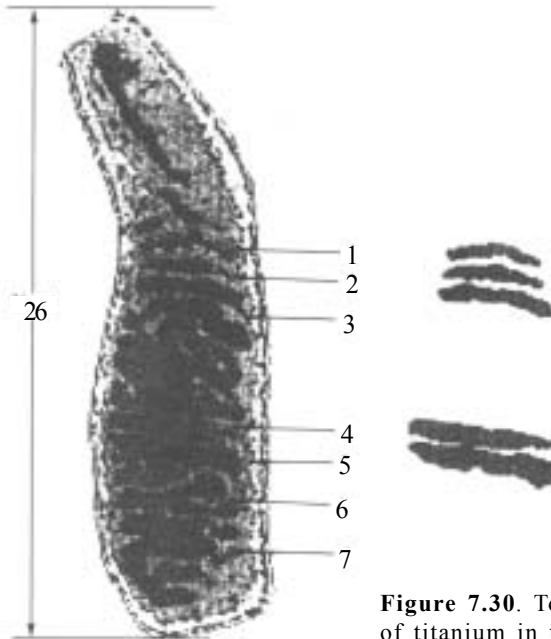
**Figure 7.30**. Topography of the distribution of titanium in the $ZrO_2+Y_2O_3$ crystal [96].

the admixture in the region of the cell boundaries is characteristic of an admixture with the effective distribution coefficient $K_{eff} > 1$.

The effective distribution coefficient of titanium calculated as the ratio of its total content in the single and polycrystalline regions, determined by the γ-spectra, is $K_{eff} = c_m/c_p = 2.2$,

3. A transition was found between the regions with the microzonal and cellular structures (zones *4, 7*).

The banded microzonal structure is described using various mechanisms based on: the variation of temperature at the crystallisation front, the variation of the speed of displacement of the front, and concentrational supercooling [106]. However, these models are restricted to diffusion–kinetic or thermodynamic approaches, determining the conditions of formation of an instability at the crystal–liquid interface [106]. The majority of the models, describing the formation of the banded microzonal structure, were developed for single-component crystals. Using these models, it is not possible to take into account correctly the kinetics of the chemical interaction between the admixture and the crystal material and describe the transition from the banded to cellular structure. It is important to take into account the kinetics of chemical interaction because in the majority of cases the process of growth takes place

at high temperatures and with participation of catalytically active components of the crystallising material.

The authors of [103] investigated the mechanisms of formation of the microzonal structure and its transition to a cellular structure which takes place as a result of the diffusion–transport catalytic reactions of oxidation of titanium on the surface of the crystal by the reaction of the type:

$O+E \leftrightarrow EO; \ Ti+E \leftrightarrow ETi; \ ETi+O \rightarrow TiO_2 +E,$

where E is the catalyst (in the present case, the role of the catalyst may be played by Y, Zr). The reactions of this type are well known in the case of fermentative catalysis and belong to the class of substrate–inhibitor reactions [108].

The mathematical analysis of the problem shows that there is a smooth transition from the unidimensional microzonal structure in the thin end of the crystal to the cellular structure of the microzones in the vicinity of the thicker part of the crystal. The length $l$ at which there is a transition is determined mainly by the geometrical factor (the ratio of the radii and the length of the modelling cone $r$, $r_0$ and $l$), and also by the diffusion and reaction-capable properties of the interacting components. The external appearance of the detected microzonal structure resembles domain structures investigated previously.

## 7.7. MECHANICAL STRESSES AND THERMAL ANNEALING OF FIANITES

The examination of the crystals of the $ZrO_2–Y_2O_3$ and $HfO_2– Y_2O_3$ solid solutions under a microscope in crossed polarisers showed a slight heterogeneity of extinction, caused by the presence of volume stresses in the crystals. Conoscopic images show that under the effect of the residual stresses, the isotropic crystals become biaxial, optically positive. The angle between the optical axes is close to 90°. The optical indicatrix of the crystals has the form of a slightly deformed sphere, elongated in the direction of the growth axis of the crystals [001]. The birefringence of the crystals is $\Delta n = n_2 - n_1 = 0.000707$ [109].

In order to relieve the internal stresses, the fianite crystals are subjected to high-temperature annealing in vacuum or nitrogen. Annealing in an oxidation atmosphere is carried out in gas flame or silit-rod furnaces.

In order to determine the optimum annealing conditions of the
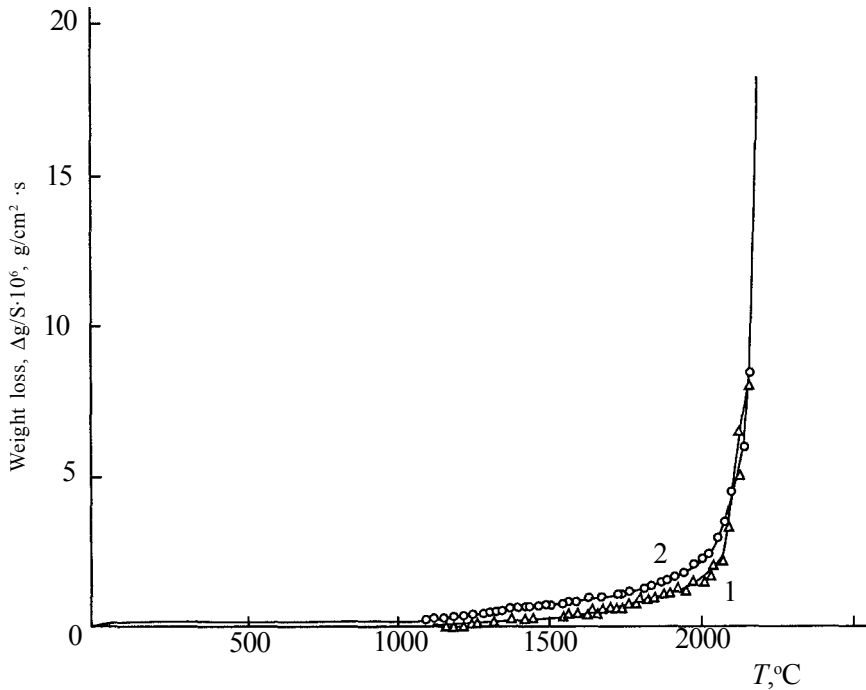
**Figure 7.31.** Curves of evaporation of the crystals of the $ZrO_2+Y_2O_3$ (1) and $HfO_2+Y_2O_3$ (2) solid solutions [101].

single crystals of $ZrO_2$–$Y_2O_3$ and $HfO_2$–$Y_2O_3$, the rate of evaporation of the crystals in vacuum was determined in advance. Evaporation was carried out in a vacuum of $10^{-4}$–$10^{-5}$ mm Hg on specimens in the form of disks with a diameter of 10–12 mm and a height of 1–2 mm. The extent of evaporation from the open surface was determined by continuous weighing. The minimum value of the recorded rate of evaporation was $10^{-8}$ g/cm² s. Figure 7.31 shows the temperature dependences of the weight loss of the investigated crystals in continuous heating at a rate of 8–10 deg/min. Extensive evaporation starts at a temperature of 2100°C. The rate of evaporation of the crystals of $ZrO_2$ and $HfO_2$ stabilised with 10 mol.% $Y_2O_3$ and measured at 2100 °C was respectively (7–8) and (3–5) $10^{-6}$ g/cm² s. Thus, vacuum annealing of the crystals–fianites should be carried out at temperatures not exceeding 2100°C.

The residual stresses were determined by the polarisation–optical method on the basis of birefringence. Figure 7.32 shows the interference patterns of the crystals in the crossed polarisers of the microscope prior to and after annealing. Annealing in the optimum
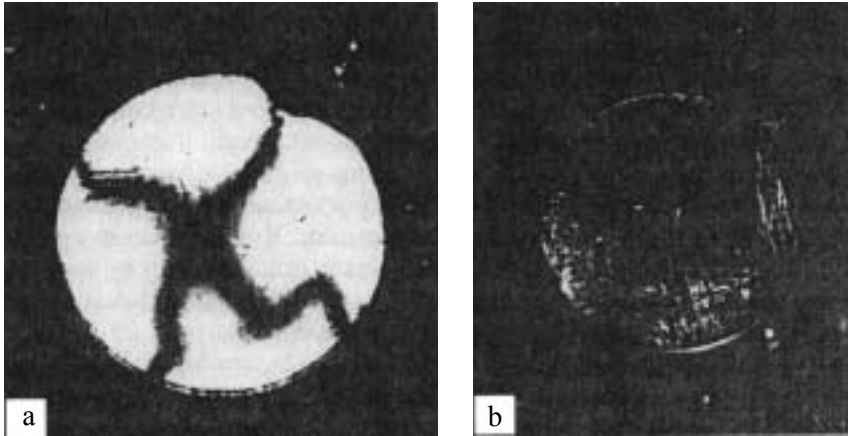
**Figure 7.32**. Interference patterns of the crystals of $ZrO_2 + Y_2O_3$ solid solutions with thermal stresses in the cross polarizers of the microscope (a) prior to and (b) after annealing [101].

conditions ($T_{max}$ = 2100°C, cooling rate 85 deg/h) almost completely eliminated the stresses. The light spots observed in the annealed crystals in crossed polarisers are associated with the inhomogeneous with the impurities present in the crystal.

The stresses in the crystal are also determined by the formation of dislocations, producing slip planes and the boundaries of mosaic blocks. It is interesting to investigate the effect of high-temperature annealing on the density of dislocations. The dislocation structure was developed by chemical etching. An efficient etching solvent for the fianite crystals is a mixture of nitric and hydrofluoric acids at a ratio of 2:3. Etch pits are triangular, with nonuniform distribution. The density of the etch pits greatly increased in the direction to the edges of the crystal, where thermal stresses evidently greatly increased. Annealing reduced the density of dislocations by approximately an order of magnitude.

The experimental results show that vacuum annealing at 2000°C and subsequent rapid cooling result in the blackening of transparent and colourless crystals, stabilised with 10 mol.% $Y_2O_3$. This phenomenon does not take place at low cooling rates. When heating dark specimens in air top 1200°C they lost colour. The darkening of the specimens is associated with the loss of oxygen at high temperatures and with quenching phenomena caused by a rapid decrease of temperature in vacuum. Vacuum annealing of the crystals reduces tetravalent cerium, praseodymium and terbium to

the trivalent condition and europium to the bivalent condition [110]. The annealing atmosphere also affects the microhardness of crystals which increases by 10–12%.

The optical heterogeneity and distribution of defects in the volume of crystals of Zr- and Hf-fianites was investigated in a laser ultramicroscope. The scattering of light was observed under an angle of 90° in relation to the direction of the incident light beam. The crystals of $ZrO_2$–$Y_2O_3$ with oxides of erbium, cerium and neodymium clearly show under the microscope microscopic and submicroscopic particles with a density of $10^6$ mm$^{-3}$ and a diameter of several microns. Possibly, the particles of the admixture decorate the structural defects, the boundaries of the blocks and slip layers. Under the effect of long-term high-temperature vacuum annealing, the size of the particles greatly increased and the density of the particles dropped. In the nominally clean (unalloyed) fianites, the scattered light was detected in the form of the Tindall cone and the intensity of light scattering depended greatly on the purity of the initial materials and the technological growth conditions. The scattering of light by the crystals is caused by the particles with the size of the order of 0.1 μm. In block crystals and in crystals with volume stresses, the admixture is susceptible to aggregation. The concentration of the $Y_2O_3$ stabiliser in the range 10–20 mol% has almost no effect on the extent of light scattering. In the presence of a third admixture, scattering centres were detected in many cases.

Attention should be given in greater detail to the mechanism of high-temperature reduction of the crystals of fianite because this is of practical importance for application of these crystals.

High-temperature and electrolytic reduction of the polycrystalline sintered materials based on $ZrO_2$ was investigated in [104–107]. The experimental results show that the ions of $O^{2-}$ are removed from the crystal lattice and a phase nonstoichiometric in relation to oxygen forms:

$$Zr_{1-y}Y_yO_{(2-0.5y)} \rightarrow Zr_{1-y}Y_yO_{(2-0.5y)-x} + x/2O_2 \uparrow.$$
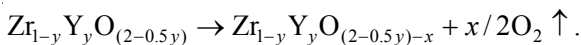
As a result of extensive reduction, the process may continue and lead to the precipitation of a metal-like phase, a solid solution of oxygen in α-Zr, suboxides $ZrO_6$ and $Zr_3O$ and metallic zirconium [113].

High-temperature reduction of the crystals was carried out in a
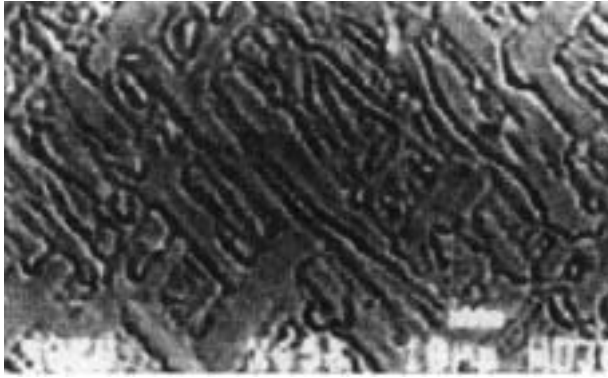
**Figure 7.33.** Electron micrograph of the surface of $ZrO_2+Y_2O_3$ crystals after thermal annealing.

vacuum furnace with a tungsten heating element at a temperature of 1400–2000°C for 10–30 hours, in a vacuum of $1.33 \times 10^{-2}$ Pa. Cooling was carried out at a rate of 20–100 deg/min [111]. After vacuum annealing the crystals became black. In heating in air, the reduced crystals lost their colour but the single crystal nature was not disrupted. In cooling at high rates, the surface of the crystals was characterised by the formation of a network of shallow cracks and thermal etch pits, Fig. 7.33. According to the results of x-ray diffraction analysis, a new phase does not appear in the material, but the parameter of the elementary cell decreases. In heating in air of the reduced specimens, examination showed small exothermic peaks in the range (200–500)°C. The formation of these peaks is associated with the oxidation process. The dependence of the degree of reduction on the composition of the solid solution is presented in Fig. 7.34. The maximum value of $\Delta P/P$ of the crystals corresponds to the two-phase region of the solid solutions, consisting of the monoclinic and tetragonal phases, at a content of the stabilising oxide of (3–6) mol.% [115, 116]. In the region of the cubic solid solutions, the degree of reduction decreases with increasing concentration of the stabilising oxide from 8 to 33 mol.%. The deficit of oxygen $x$ in the crystal $Zr_{1-y}Y_yO_{(2-0.5y)-x}$ changes in relation to the degree of reduction from $0.0003 \times 10^{-2}$ to $2.606 \times 10^{-2}$.

The amount of generated oxygen reaches the value $\Delta n_0/n_0 = 1.32\%$ for the crystals containing 3 mol.% of $Y_2O_3$. In the range of the cubic solid solutions, this value decreases and equals $\approx 0.4\%$. The density of the crystals increases during the reduction. An
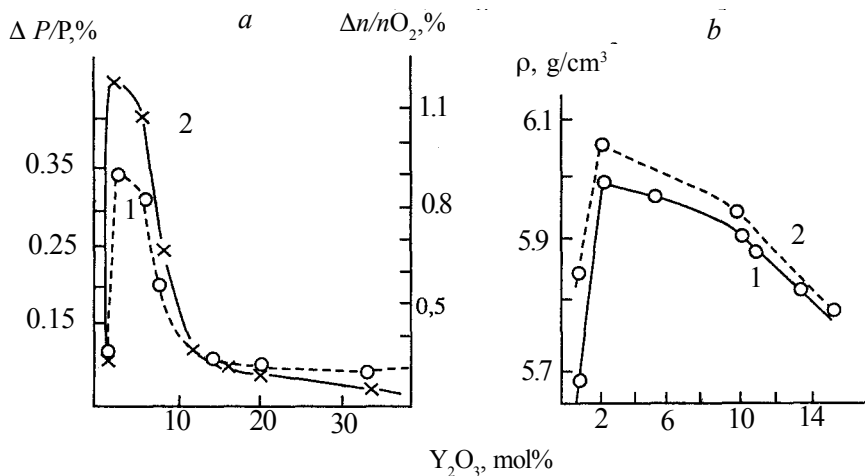
**Figure 7.34**. Dependence of the degree of restoration of the crystals of the $ZrO_2+Y_2O_3$ solid solution on the $Y_2O_3$ content after vacuum annealing (1400°C, 30 h) [104]. a: 1 – the fraction of lost oxygen, 2 – relative weight loss, b: – variation of the density of crystals: 1 – prior to annealing, 2 – after annealing.

increase in the amount of the generated oxygen (< 0.1%) [114] results in the compression of the crystal lattice as a result of the formation of vacancies. Possibly, at high temperatures and long holding times the metal may be transferred to the interstitial positions and shear structures may form as a result of the compression of the structure along some crystallographic planes during the loss of oxygen. An increase in the density of the crystals depends on the composition of the solid solution. The largest changes were detected in two-phase crystals containing from 1 to 6 mol.% of the stabilising oxide. The variation of the parameters of the elementary cell of the fianite single crystals is presented in Table 7.15.

A decrease in the parameter of the elementary cell and, correspondingly, increase in the density of the solid solutions increase the microhardness of the crystals after annealing. The values of microhardness of the crystals with the composition $ZrO_2$ (88 mol.%) $+Y_2O_3$ (12 mol.%) were as follows: (1360 + 60) prior to vacuum annealing, (1550 + 60) Pa for the reduced black crystals and (1390 + 50)Pa for the oxidised crystal.

Examination of the optical properties of the black fianites of the previously mentioned compositions shows that the edge of the absorption band is displaced to the longwave region of the spectrum and depends on the density of the reduced layer of the crystal. It
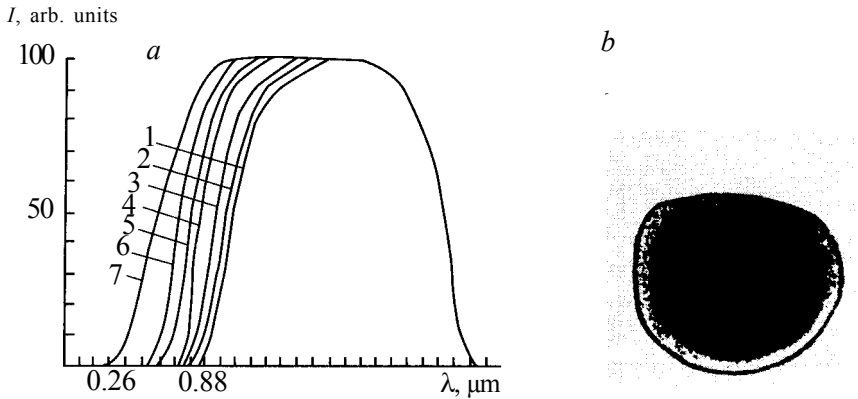
**Figure 7.35**. The transmission spectra of a sheet of black fianite in relation to the reduction conditions [104]. 1) annealing in a vacuum, $1.33 \cdot 10^{-2}$ Pa, 30 h, 2000°C; 2–7) in air at 350°C from 0.5 to 3 h (b).

**Table 7.15.** Variation of the parameters of the crystal lattice of single crystals of fianites $ZrO_2 - Y_2O_3$ after vacuum annealing (vacuum $1.33 \cdot 10^{-2}$ Pa, annealing temperature 2000°C, time 30 h) [104]

| $C_{ZrO_2}$ | $C_{Y2O3}$ | $a$, Å | | $\Delta a/a$,% |
|---|---|---|---|---|
| | | Prior to annealing | After annealing | |
| 89.70 | 10.30 | 5.1432 | 5.1390 | 0.08 |
| 87.20 | 12.80 | 5.152 | 5.143 | 0.17 |
| 84.8 | 16.2 | 5.158 | 5.154 | 0.11 |

may be assumed that the loss of oxygen by the crystal during reduction is accompanied by the formation of different electronic dye centres whose absorption spectrum overlaps the entire visible range of the spectrum. Figure 7.35*a* show that the process of oxidation of the single crystal starts on the surface and is caused by the diffusion of oxygen whose rate is determined by the annealing temperature. Figure 7.35*b* shows the transmission spectra of fianites for different degrees of reduction.

The partially reduced 'black' fianite is of considerable interest. In heating of the colourless fianite in vacuum at a temperature of 1800°C, the zirconia is reduced and, during this process, the crystal loses part of oxygen and the $Zr^{4+}$ ions transfer to the condition with lower degrees of oxidation. This process is accompanied by the formation of electronic dye centres whose absorption spectrum
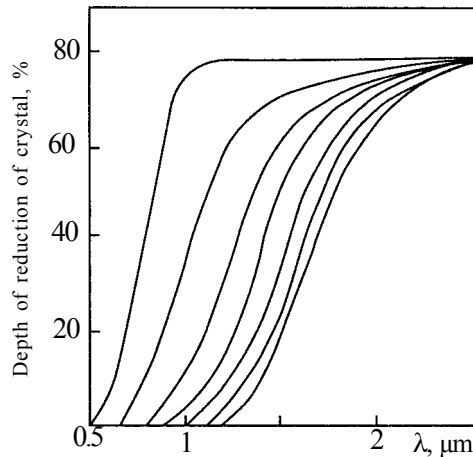
**Figure 7.36.** Long-wave edge of the absorption spectrum of 'black fianite (*d* = 1.2 mm) in relation to the depth of reduction of the crystals.

overlaps the entire visible range of the spectrum.

Figure 7.36 shows the long-wave edge of the absorption spectrum of black fianites, corresponding to different depths of reduction. It may be seen that the absorption spectrum can be varied in a wide range and, consequently, the black fianite may be used for infrared filters together with other well-known semiconductor materials, such as germanium and silicon.

In 'moderate' reduction of fianites, for example, in heating in a vacuum of $10^{-4}$ mm Hg at 1700°C for 30 hours, and subsequent cooling at a rate of 120 deg/h, the changes taking place in the crystals are fully reversible: in subsequent annealing in ar at 1000°C, the crystals are again colourless and optically homogeneous. This fact on its own is remarkable: regardless of the fact that the loss of oxygen in reduction, according to experimental data, reaches 0.02 wt.%, the phase homogeneity of the crystals is not disrupted. This results in the formation of a stable solid solution whose composition includes two or more valency forms of zirconium [117].

Figure 7.37 shows the absorption spectrum of the crystals prior to and after annealing in oxygen at 2000°C with subsequent quenching in air and in vacuum at 1250 and 1550 K at $v_{cool}$ = 6 deg/min. Annealing in air increases the absorption in the range $\lambda$< 350 nm (see also 7.37b), soft annealing (*T* ~1400 K) in vacuum results in clarification in this range. Vacuum annealing at high temperatures increases absorption in the entire examined range of the spectrum
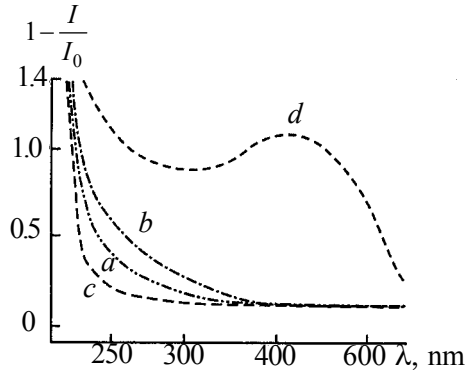
**Figure 7.37.** Absorption spectra of $HfO_2$–$Y_2O_3$ crystals prior to annealing (a) and after annealing: in air at 2000 K (b), in vacuum at 1200 K (c) and at 1550 K (d).
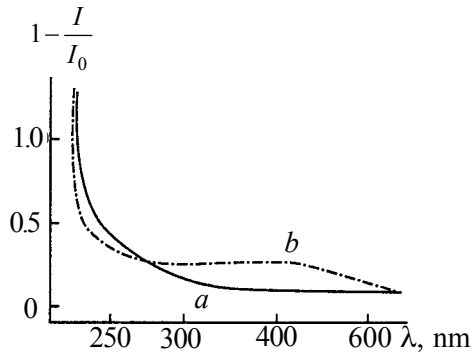


**Figure 7.38**. Absorption spectra a) initial, b) after γ-radiation, dose $10^6$ R.

230–800 nm, and the absorption spectrum shows a wide band with a maximum at approximately 500 nm (Fig. 7.37*d*).

Figure 7.38 shows the effect of γ-radiation at room temperature on the optical absorption of the $HfO_2$–$Y_2O_3$ crystals. In the non-annealed crystals, γ-radiation results in clarification in the range λ< 260 nm and in the appearance of additional absorption in the longer wave length range. The intensity of additional absorption increases with increasing dose and reaches saturation at a dose of $10^5$–$10^6$ roentgens. Qualitatively, these effects are caused by γ-radiation in the annealed crystals, but preliminary annealing affects the intensity of additional absorption and clarification. In the vacuum-annealed crystals, the intensity of radiation-induced additional absorption reaches saturation at higher doses and on a higher level, in comparison with the non-annealed crystals. Annealing in air with quenching has the opposite effect. Identical dependences of the

spectra of absorption on annealing and γ–gamma radiation were also detected in $HfO_2$ crystals, stabilised with other oxides $R_2O_3$ and also CaO.

The effect of heat treatment on the optical absorption of $HfO_2$–$Y_2O_3$ crystals is associated, as in the $ZrO_2$–$Y_2O_3$ crystals, with the variations of stoichiometry caused by the exchange of oxygen with the medium. Vacuum annealing results in the release of oxygen from the crystal which is accompanied by the formation of free electrons and oxygen vacancies. The electrons are distributed between the defects, filling mainly the deeper levels. Thus, vacuum annealing of the $HfO_2$–$Y_2O_3$ crystals is identical with the additive colouring of the alkali–halide crystals in the metal vapours. The main type of defects, capable of trapping the electrons in $HfO_2$–$Y_2O_3$ are the oxygen vacancies, both formed during the departure of oxygen and introduced by the stabilising $Y_2O_3$ admixture. The vacancies of oxygen, trapping one or two electrons, may be regarded as responsible for the additional absorption formed after high-temperature annealing (Fig. 7.37*d*). The formation of these intrinsic colouring centres is preceded by clarification in the ultraviolet range during vacuum annealing in comparatively 'soft' conditions (Fig. 7.37*b*). This indicates the existence of another type of defect characterised by deeper electronic levels in comparison with anion vacancies. These defects may be represented by uncontrolled admixtures of transition metals, containing in the higher valency state intense charge transfer lines in the ultraviolet range. In a crystal, containing admixtures of these metals in a higher valency state, vacuum annealing reduces the admixtures, resulting in disappearance of the charge transfer band (ultraviolet clarification). This is followed by the filling of less deep levels of the vacancies with the corresponding growth of the absorption of the intrinsic colouring centres. This is also clear from Fig. 7.37*c,d*. In annealing in air, the crystal absorbed oxygen and, consequently, the absorption of the admixture in the higher valency state increased (Fig. 7.37*a, b*).

The presence of two competing centres of capture of electrons – intrinsic, associated with vacancies, and admixture – may also be used to explain the nature of changes in the spectra caused by ionising radiation. In this case, additional absorption may be associated with the formation of the intrinsic colouring centres during capture of the electrons by anion vacancies, and the clarification in the ultraviolet range may be attributed to the

reduction of the uncontrolled admixtures of transition metals. In contrast to vacuum annealing in which the reduction of the admixtures and the formation of the intrinsic dye centres take place successively in the order of decreasing depth of the level, in γ–irradiation, both processes are parallel because the distribution of electrons between the levels of capture is regulated in this case not by the depth but by the kinetic parameters and concentration of the centres. Therefore, in the case of γ-irradiation, additional absorption increases together with the clarification in the ultraviolet range (Fig. 7.38) [118]. The charge state of the admixture ions and the appropriate absorption spectrum, formed after annealing crystals in different conditions, will be investigated in Chapter 8.

The crystals based on $ZrO_2$ are characterised, at elevated temperatures, by almost completely pure ionic conductivity. In the reduced condition, the crystals have a high fraction of electronic conductivity; in oxidation of the crystal and approaching the stoichiometric composition, the electronic component of electrical conductivity decreases [113, 119].

## 7.8. PHYSICOCHEMICAL AND MECHANICAL PROPERTIES OF FIANITES

Investigations of the fianites of different chemical composition show that they have properties not found in other available natural or synthetic crystals. It is important to note the physicochemical stability of fianites at high temperatures. They are characterised by a low degree of evaporation in vacuum, described by the value $7 \cdot 10^{-6}$ g/cm$^2$ and 2100°C. In air, the fianites do not change their chemical composition and structure up to the melting point (2700–2900°C). In this respect, the fianites are inferior only to the thorium dioxide which cannot at present be produced in the form of large single crystals and, in addition to this, the radioactivity of thorium must also be taken into account.

At room temperature, the fianites do not interact with alkali and acids, including hydrochloric, hydrofluoric and sulphuric acids. The chemical stability of fianites at high temperatures is characterised by, for example, the fact that they do not interact with melts of various corrosive metals, such as sodium, and melts of many semiconductor compounds. Especially high chemical resistance is typical of the crystals based on $HfO_2$. Not having porosity and disruptions in the structure of the surface, the single crystals are

greatly superior in chemical resistance to the sintered ceramics of identical composition. The hardness of the fianites is 8.5 on the Moos scale, and of the currently available natural crystals, only diamond and corundum are harder than fianites.

The electrical properties of the fianites are very interesting. At room temperature, the fianites are typical dielectrics. However, already at 300°C they show oxygen–ionic electrical conductivity which increases with increasing temperature and reaches 1 ohm$^{-1}$ cm$^{-1}$ at 2000°C.

As already mentioned, the fianites are solid solutions with a wide range of phase homogeneity. In addition to the oxide-stabilising agents, compounds of other elements, modifying the physical properties of the crystals, may be introduced into the composition of the fianites. The number of these compounds–modification agents is very large, and the concentration in which they can be added is several percent. The possibility of changing the chemical composition of the fianites in a wide range enables the physical properties of the fianites to be varied in a wide range.

**The density of fianites**

Density is one of the most important characteristics of the material and controls the majority of the mechanical, thermal, optical and other properties. Density is a physical constant of an individual substance. It is determined by the structure of the crystals, in particular, the density of packing of the atoms in the crystal lattice. The density of large crystals was measured by hydrostatic weighing based on the determination of the volume of the crystal on the basis of the mass of the liquid displaced by the crystal. The accuracy of measurement can be increased using high-density liquids. The results of measurement of the density of fianites are presented in Table 7.16 and Fig. 7.39. The presented data show that the density of the fianites depends on the concentration and nature of the stabilising oxide. The inflection point on the dependence of density on the concentration of the stabilising oxide corresponds to the phase transition from the region of two-phase solid solutions to the region of cubic solid solutions. The lattice parameters of the cubic solid solutions were used to determine the x-ray density which was compared with the density determined by hydrostatic weighing of the crystals.

The x-ray density was calculated from the equation: $\rho = 1.66020$

**Table 7.16**. Density of cubic solid solutions $ZrO_2$–$R_2O_3$ (R – Eu, Gd, Yb) [35]

| Stabilizing oxide | $RO_{1.5}$ concentration | Structure of solid solution | Lattice parameter | Density, $kg/m^3 \cdot 10^{-3}$ | |
|---|---|---|---|---|---|
| | | | | experimental | calculated |
| $Eu_2O_3$ | 19.02 | Fluorite | 5.172 | 6.415 | 6.411 |
| | 23.82 | As above | 5.185 | 6.471 | 6.461 |
| | 29.86 | " | 5.198 | 6.573 | 6.563 |
| | 37.04 | " | 5.219 | 6.675 | 6.662 |
| | 50.66 | Pyrochlore | 10.518 | 6.855 | 6.830 |
| $Gd_2O_3$ | 17.65 | Fluorite | 5.149 | 6.483 | 6.483 |
| | 20.84 | As above | 5.155 | 6.541 | 6.548 |
| | 25.32 | " | 5.162 | 6.651 | 6.617 |
| | 30.29 | " | 5.181 | 6.702 | 6.693 |
| | 43.82 | " | 5.186 | 6.906 | 6.893 |
| $Yb_2O_3$ | 16.82 | " | 5.132 | 6.659 | 6.655 |
| | 19.93 | " | 5.134 | 6.765 | 6.759 |
| | 22.79 | " | 5.136 | 6.867 | 6.856 |
| | 27.88 | " | 5.138 | 7.039 | 6.988 |
| | 35.62 | " | 5.174 | 7.167 | 7.161 |
| | 49.85 | " | 5.179 | 7.645 | 7.641 |
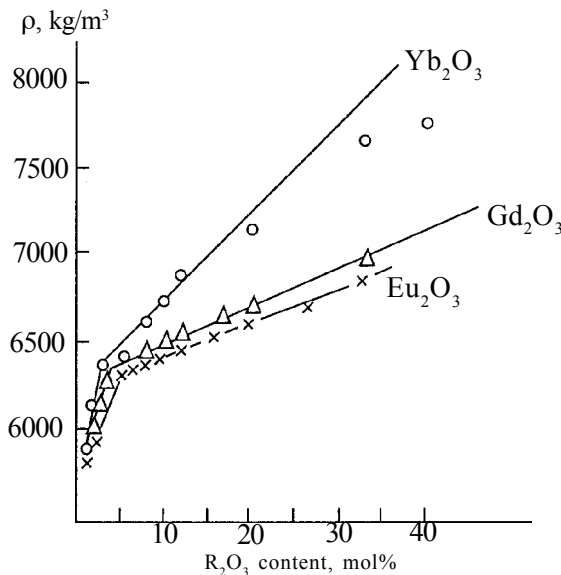


**Figure 7.39.** The density of $ZrO_2$–$R_2O_3$ fianite crystals in relation to the concentration of the stabilising oxide [40].

($\Sigma Z/V$), where $\rho$ is density, $\Sigma Z$ is the sum of the molecular weight of all molecules in the elementary cell; $V$ is the volume of the elementary cell. When calculating $\Sigma Z$, it was assumed that the heterovalent substitution of $ZrO_2$ by the oxides of rare-earth elements is accompanied by the formation of vacancies in the anion sublattice [121, 122], and the cation subsystem was assumed to be ideal. The following equation was used in the calculations: $\Sigma Z = xZrO_2 + yRO_{1.5}$, where $x$ and $y$ are the number of moles of $ZrO_2$ and $RO_{1.5}$ per the elementary cell of the structure, on the condition: $x + y = 4$; $x/y = $ mol.% $ZrO_2$/mol.% $RO_{1.5}$. According to the Debye patterns, the composition 33 mol.% $Eu_2O_3$ has a pyrochlore structure. X-ray density was determined for the $Eu_2Zr_2O_7$ compound. The results of the calculations are presented in Table 7.16, and the difference between the experimental and calculated values does not exceed 0.5%. However, in most cases, $\rho_{exp}$ is higher than $\rho_{cal}$ and this may be caused by the presence of a small number of interstitial atoms in the lattice of solid solutions.

It should be mentioned that for low concentrations of the stabilising oxide, the grinding of the crystals in an agate mortar into powder for x-ray diffraction examination results, due to the metastable state at room temperature, in the occurrence of phase transitions, and the powder x-ray diffraction patterns do not reflect the actual phase composition of the crystals. This problem will be investigated in greater detail in the chapter concerned with the crystals of partially stabilised zirconia (PSZ, Chapter 8).

**Microhardness of fianites**

The microhardness of the material is characterised by the elasticity of indentation of another body into the material at which there is no residual deformation or scratching. Microhardness is not a physical constant of material and depends on the measurement method. The microhardness of the fianites in the plane parallel to the direction of growth was determined in [120] using a microhardness meter. The optimum load was 70–100 g. The microhardness of fianites was investigated in relation to the nature and concentration of the stabilising oxides and the degree of ordering of the crystal structure. In [123, 124] was reported that a small amount of the stabilising oxide results in a large increase of the hardness of the specimens. For example, the hardness of pure zirconia is comparable with the hardness of quartz

(approximately 7 on the Moos scale or 700 kg/mm$^2$), and the hardness of stabilised zirconia is comparable with that of topaz (8 on the Moos scale or 1200 kg/mm$^2$ according to Vickers). The microhardness of the tetragonal solid solutions ($ZrO_2$–8 mol.% $Gd_2O_3$) is considerably higher than that of cubic solid solutions (20 mol.% $Gd_2O_3$). In addition, the experimental results show that the microhardness depends only slightly on the nature of the stabilising rare-earth oxide [125].

The value of microhardness in the series of solid solutions reflects the effect of the change in the spacing of the ions as a result of including the ions of the stabiliser in the composition of these solutions and also the disruption of the ordering of the structure. The solid solutions with the composition $R_2Zr_2O_7$ (33 mol.% $R_2O_3$) undergo the order–disorder transformation, and the temperature of this transition decreases with an increase in the atomic number of the lanthanide [126]. The microhardness of the solid solutions decreases in the same sequence as a result of disordering of the structure. The dependence of the microhardness of the specimens of $ZrO_2$–$R_2O_3$, where R = Eu, Gd, Yb, on the $R_2O_3$ content is shown in Fig. 7.40. The microhardness is maximum in the concentration range 5–7 mol.% $R_2O_3$, corresponding to the transition of systems from the single-phase cubic solutions to multiphase ones.

The large increase of the strength of the crystals in this range of the compositions is evidently determined by the mechanical inhibition of movement of the dislocations [127, 128, 129]. The crystals with these compositions are semi-transparent and greatly scatter the light because they consist of a mixture of the tetragonal

H, kg/mm$^2$
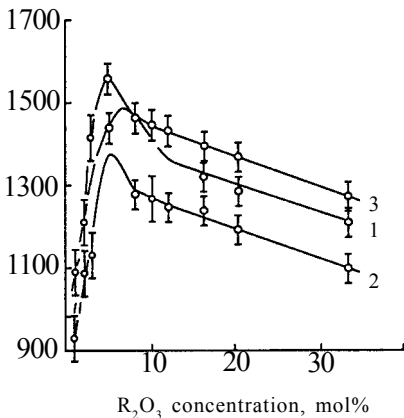


**Fig. 7.40.** Microhardness of fianite crystals in relation to the concentration of the stabilising oxide [40]. The number at the curves corresponds to the oxides: 1) $Y_2O_3$, 2) $Gd_2O_3$, 3) $Eu_2O_3$.

R$_2$O$_3$ concentration, mol%

and monoclinic phases. Hardening may be associated with the microscopic stress fields formed around particles during precipitation of the phase in the fine-dispersed condition. The subsequent decrease in the microhardness of the single crystals of cubic solid solutions with an increase in the content of the stabilising oxide is associated with the ordering of the structure of the solid solutions. An increase in the concentration of the stabilising oxide decreases the microhardness most markedly in the case of the $Eu_2O_3$ crystals and, to a lesser degree, in the crystals with $Gd_2O_3$ and $Yb_2O_3$. Attention should be given to the high microhardness values of the composition $ZrO_2$–8 mol.% $Gd_2O_3$ which may be associated with the presence of high stresses in these crystals.

The polished samples produced from the grown fianites were annealed in air at a temperature of 1200 °C for 10 hours. This heat treatment does not reduce the residual volume stresses, formed in the process of crystallisation, but eliminates the local stresses in the

**Table 7.17.** Microhardness of fianites $ZrO_2$–$Y_2O_3$ in directions of axes [111], [110], [100] (load 200 g) [40]

| Composition of crystals,mol% | | Microhardness $H$, kg/mm$^2$ | | |
|---|---|---|---|---|
| $ZrO_2$ | $R_2O_3$ | [111] | [110] | [100] |
| 88 | $12Y_2O_3$ | 1455±47 | 1532±60 | 1694±54 |
| 92 | $8Gd_2O_3$ | 1350±28 | 1472±30 | 1602±49 |

**Table 7.18**. Microhardness of fianites $HfO_2$–$Yb_2O_3$ in growth direction (load 100 g) [40]

| Composition of crystals, mol% | | Microhardness $H$, kg/mm$^2$ |
|---|---|---|
| $HfO_2$ | $Yb_2O_3$ | |
| 99 | 1 | 1067±36 |
| 98 | 2 | 1174±71 |
| 97.5 | 2.5 | 1346±46 |
| 95 | 5 | 1445±54 |
| 93 | 7 | 1631±60 |
| 88 | 12 | 1439±38 |

surface layer, formed during mechanical treatment of the crystals and increases their microhardness/.

The specimens of $HfO_2$ crystals, containing 1–7 mol.% of $Y_2O_3$, were not single-phased. The microhardness of these crystals increased with an increase in the content of the stabilising oxide to 7 mol.%, and in transition to the range of single-phase cubic solutions the microhardness decrease. The microhardness of the fianites based on the zirconia and hafnium dioxide, is presented in Tables 7.17 and 7.18. Attention should be given to the high brittleness of the crystals, containing small quantities of silicon oxide. The introduction of even as little as 0.05 wt.% of $SiO_2$ greatly decreases the microhardness.

## Thermal expansion of fianites

For technical applications of components produced from crystals of solid solutions based on zirconia, especially at high temperatures, it is important to know the coefficient of thermal expansion of these materials. These data for several compositions in the temperature range 20–900°C can be found in [35,40]

## 7.9. OPTICAL AND SPECTROSCOPIC PROPERTIES OF FIANITES

The optical properties of the zirconia crystals, stabilised by the oxides of yttrium and the rare-earth elements, are of considerable interest for optics and jewellery industries.

## Refractive index

The optical properties are extremely important characteristics of the cubic single crystals of zirconia: the refractive index, the dispersion in the visible range of the spectrum, the transmission band. The values of the refractive indices for the case of application of various oxides as stabilising agents are presented in Table 7.19 [40].

For the $ZrO_2$–$Y_2O_3$ cubic crystals, the dispersion of the refractive index is in the range 0.060–0.063 and the transmission band 0.26–7.5µm.

For the 11 spectral lines, the refractive indices of the transparent cubic crystals were measured by the prism method [120]. The values of the refractive index are presented in Fig. 7.41 *a–c* and

**Table 7.19.** Experimental and calculated parameters of refraction of single crystals of solid solutions based on zirconia [40] ($\lambda$ = 6328 Å)

| Stabilizer | Concentration, mol% | $n_{Dexp}$ | $n_{Dcalc}$ |
|---|---|---|---|
| MgO | 10 | 2.178 | 2.178 |
| CaO | 16 | 2.165 | 2.164 |
| | 24 | 2.104 | 2.116 |
| MnO | 10 | 2.21 | 2.20 |
| | 15 | 2.18 | 2.18 |
| $Y_2O_3$ | 10 | 2.173 | 2.178 |
| | 15 | 2.153 | 2.147 |
| | 20 | 2.121 | 2.129 |
| CeO | 25 | 2.244 | 2.194 |
| | 30 | 2.212 | 2.200 |

**Table 7.20.** Dispersion of the refractive indices of zirconia crystals [118]

| $\lambda$, μm | Refractive index, $n$ | | | |
|---|---|---|---|---|
| | $[Y_2O_3]$ = 9 | $[Y_2O_3]$ = 11 | $[Y_2O_3]$ = 15 | $[Y_2O_3]$ = 17 mol% |
| 0.4358 | 2.2224 | 2.2101 | 2.1783 | 2.1232 |
| 0.5461 | 2.1856 | 2.1737 | 2.1434 | 2.0949 |
| 0.5779 | 2.1790 | 2.1669 | 2.1372 | 2.0897 |
| 0.5893 | 2.1768 | 2.1653 | 2.1352 | 2.0881 |
| 0.6328 | 2.1718 | 2.1581 | 2.1287 | 2.0826 |

in Table 7.20. The resultant dispersion curves are measured in the wavelength range 400–650 nm. The reference value is represented by the refractive index of a crystal with the $ZrO_2$–12 mol%$Y_2O_3$ composition at a temperature of 77 K at a wavelength of $\lambda$ = 6328 Å, $n$ = 2.1546, the error of the measurement is +0.01 [35].

The refractive indices depend on the density of the crystals. The presence of oxygen vacancies decreases the density of crystals and,
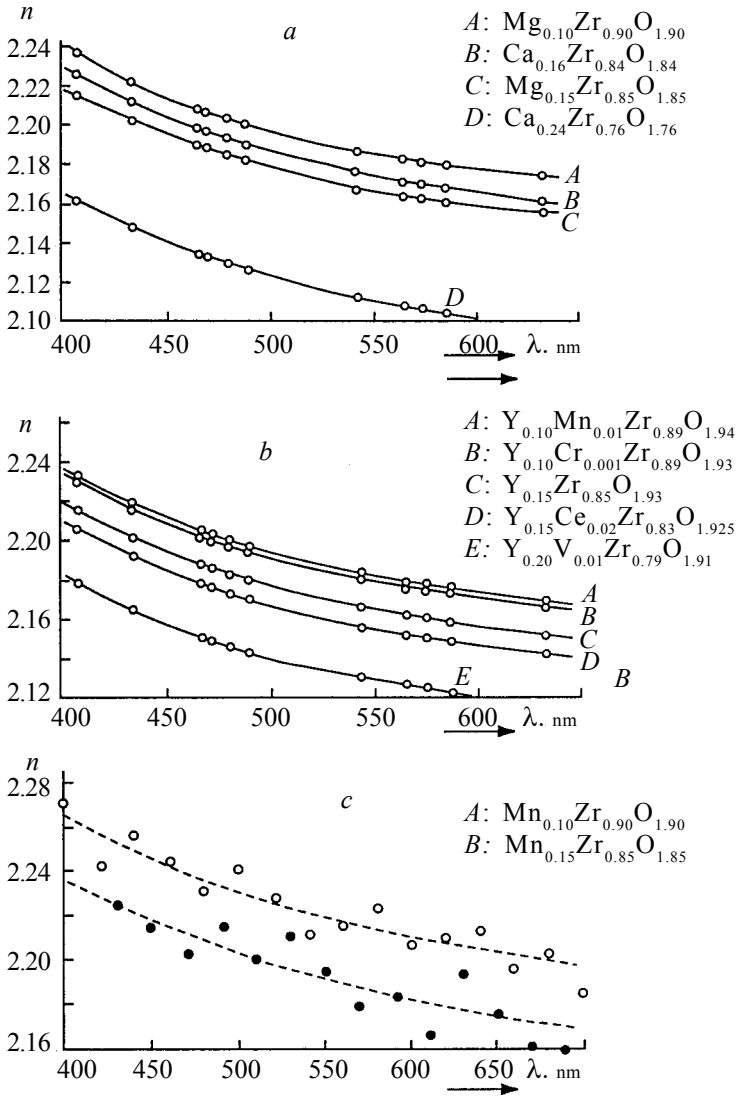
**Figure 7.41.** Dispersion curves of zirconia, stabilised with the oxides of magnesium and calcium in the wavelength range 400–650 nm (a); with yttrium oxide in the range 400–650 nm (b); with manganese oxide in the range 400–700 nm (c) [119].

consequently, the refractive index also decreases. The additions (Ce, Mn, Cr and V) in the crystal stabilised with the oxides of magnesium, calcium and yttrium, have only a small effect on the refractive index values. The concentration of the main stabilising

agent and its effective distribution in the crystal always have a considerably stronger effect.

**Molecular refraction and dispersion of fianites**

Molecular refraction ($R$) links the electronic polarisability of a substance ($\alpha_{el}$) with its refractive index ($n$) [115, 120]

$$R = [(n^2 - 1)/(n^2 + 2)](M/\rho) = 4/3\pi N_A \alpha_{el}, \qquad (7.7)$$

Here $M$ is the molecular mass of the substance; $\rho$ is the density, $N_A$ is the Avogadro constant.

   The molecular refraction is suitable for practical applications – it may be regarded as a sum of 'refractions' of the atoms or groups of atoms, forming the molecule of a complex substance. The additivity of $R$ enables the efficient application of the refractometric methods for examination of the structure of substances, and the determination of dipole moments and other important characteristics of compounds.

   It should be mentioned that the polarisability of a substance may be regarded as purely electronic only in the range of visible and ultraviolet radiation. Molecular refraction is directly associated with the polarisability of the ions and the molecules of the substance and is calculated from the following equation:

$$R = 4/3\pi N_A \alpha_{el} = 2.52 \cdot 10^{24} \alpha_{el}. \qquad (7.8)$$

On the basis of the measured values of the refractive index and the density of the crystals of $ZrO_2$–$R_2O_3$ solid solutions (here R = Eu, Gd, Yb, Y) in the concentration range 9–33 mol.% $R_2O_3$, calculations were carried out to determine the values of molecular refraction. The densities of the crystals of different compositions are presented in Table 7.21 and are also given below. The molecular mass of mixed crystals was calculated on the basis of the assumption that solid solutions are characterised by a filled cation sublattice with vacancies in the anion sublattice. The values of $R$ and $\alpha$ for the previously mentioned compositions are presented in Table 7.21 which shows that the values of the refractive index are determined by the nature and concentration of the stabilising oxide. An increase in the content of the stabilising oxide (Eu, Gd, Yb) increases the density of the crystals and the refractive index. In the case of stabilisation with the yttrium oxide, an increase of the

**Table 7.21.** Molecular refraction R and electronic polarizability of single crystals of $ZrO_2$–$R_2O_3$ (R – Eu, Gd and Yb) and $HfO_2$–$Y_2O_3$.

| $R_2O_3$, mol% | Molecular mass | Density. kg/m³·10⁻³ | Refraction index | Molecular refraction, R | Electronic polarizability, $\alpha_{el}$ $10^{39}$ C·m²/V |
|---|---|---|---|---|---|
| | | | $ZrO_2$–$Eu_2O_3$ | | |
| 11.06 | 133.560 | 6.4153 | 2.13 | 11.26 | 0.496 |
| 13.52 | 135.627 | 6.4712 | 2.14 | 11.40 | 0.502 |
| 17.55 | 138.821 | 6.5726 | 2.15 | 11.55 | 0.509 |
| 22.73 | 142.637 | 6.6750 | 2.18 | 11.87 | 0.523 |
| 33.92 | 149.807 | 6.8546 | 2.20 | 12.15 | 0.535 |
| | | | $ZrO_2$–$Gd_2O_3$ | | |
| 9.68 | 133.273 | 6.4913 | 2.11 | 10.99 | 0.485 |
| 11.63 | 135.079 | 6.5413 | 2.12 | 11.11 | 0.490 |
| 14.50 | 137.686 | 6.6510 | 2.14 | 11.26 | 0.496 |
| 28.01 | 148.421 | 6.9058 | 2.18 | 11.94 | 0.526 |
| | | | $ZrO_2$–$Yb_2O_3$ | | |
| 9.18 | 135.461 | 6.6588 | 2.03 | 10.37 | 0.457 |
| 11.07 | 137.749 | 6.7648 | 2.05 | 10.51 | 0.463 |
| 12.86 | 139.880 | 6.8669 | 2.11 | 10.90 | 0.481 |
| 16.20 | 143.630 | 7.0386 | 2.14 | 11.10 | 0.490 |
| 21.67 | 149.370 | 7.1674 | 2.16 | 11.46 | 0.505 |
| 33.20 | 159.850 | 7.6481 | 2.17 | 11.55 | 0.509 |
| | | | $ZrO_2$–$Y_2O_3$ | | |
| 8.00 | 121.510 | 5.9919 | 2.194 | 11.35 | 0.500 |
| 9.00 | 121.360 | 5.9385 | 2.1768 | 11.34 | 0.500 |
| 11.00 | 121.024 | 5.8990 | 2.1653 | 11.34 | 0.498 |
| 17.00 | 120.084 | 5.8204 | 2.1352 | 11.20 | 0.493 |
| | | | $HfO_2$–$Y_2O_3$ | | |
| 10.00 | 192.770 | 9.6500 | 2.0830 | 37.92 | 1.672 |

concentration of this oxide reduces the density and refractive index of the crystals. In the series Eu, Gd, Yb, the refractive index slightly decreases and this may be associated with a decrease in the polarisability of rare-earth elements included in the composition of the solid solution.

Colouring additions have no significant effect on the refractive index because of their low concentration in comparison with the main stabilising oxide. However, in certain cases, the nature of the third admixture affects the refractive index, for example, in the series mentioned below the following inequalities apply: $n$(Y+Nd) > $n$ (Y+Ho) > $n$ (Y+Er), $n$ (Y+Co²⁺) < $n$(Y+Co³⁺). The calculated

values of the electronic polarisability of the $ZrO_2$–$Y_2O_3$ system are close to the experimental data. The main contribution to the polarisability comes from the oxygen ions. An increase in the fraction of the oxygen vacancies with increasing concentration of the $Y_2O_3$ (yttrium oxide) results in a larger decrease of $\alpha_{el}$ in comparison with the increase of the concentration of the yttrium ions because of the low value of $\alpha_y$. The difference between the experimental and calculated values of the polarisability is evidently caused by a decrease of the averaged-out polarisability of the ions under the effect of the electric fields of the adjacent ions and the formation of oxygen vacancies.

For single crystals of the $ZrO_2$–$Y_2O_3$ and $HfO_2$–$Y_2O_3$ systems, investigations were carried out to determine the dispersion of refraction and to calculate the value of the dispersion coefficient (Abbe number):

$$v = (n_D - 1)/(n_F - n_C), \tag{7.9}$$

where $n_F$, $n_C$ are the refractive indices of the spectral lines $F$ and $C$, $n_D$ is the reference.

It should be mentioned that in the visible range of the spectrum, the dispersion has the normal form, *i.e.* the refractive index increases with a decrease in the wavelength, and the dispersion value is relatively high. In order to describe the dispersion in this wavelength range, it is sufficient to use the semiempirical Zelmayer relationship:

$$n^2 = n_\infty^2 + B/(\lambda^2 - \lambda_0^2). \tag{7.10}$$

The constant of the Zelmayer equation for the fianites with different contents of the oxide of yttrium and other activating elements are presented in Table 7.22.

The dispersion of the refractive index and the dispersion coefficient (Abbe number) of these crystals, calculated using the Zelmayer equation, are presented in Table 7.23. The temperature dependence of the refractive index of the fianites, stabilised by the yttrium oxide, in the temperature range 20–1000°C was investigated in [40]. The error of measurements was $\pm 2 \times 10^{-4}$ /deg, Fig. 7.42. The values of the refractive index change with temperature because of two reasons [135]. Firstly, because of the displacement of the

**Table 7.22.** Constants of Zellmayer equation for calculating the dispersion of refractive indices of the fianites [40]

| Composition of crystals | $n_\infty$ | B | $\lambda_0$, Å |
|---|---|---|---|
| $ZrO_2$–9 mol% $Y_2O_3$ | 2.137±0.06 | 4.82±2.45 | 0.24 |
| $ZrO_2$–11 mol% $Y_2O_3$ | 2.114±0.03 | 6.98±1 | 0.22 |
| $ZrO_2$–17 mol% $Y_2O_3$ | 2.088±0.002 | 6.36±0.1 | 0.20 |
| $ZrO_2$–10 mol% $Y_2O_3$ | 2.13 | 4.92 | 0.20 |
| $ZrO_2$–10 mol% $Y_2O_3$+0.5 wt% $Nd_2O_3$ | 2.12 | 8.03 | 0.22 |
| $ZrO_2$–10 mol% $Y_2O_3$+0.5 wt% $Er_2O_3$ | 2.11 | 6.58 | 0.19 |
| $ZrO_2$–10 mol% $Y_2O_3$+0.5 wt% CoO | 2.14 | 3.99 | 0.27 |
| $ZrO_2$–10 mol% $Y_2O_3$+0.5 wt% $Ho_2O_3$ | 2.12 | 7.34 | 0.20 |
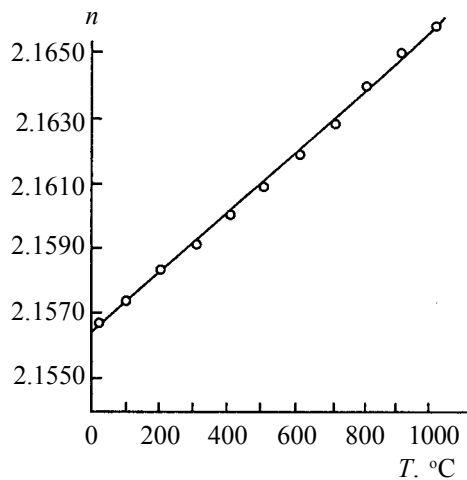


**Figure 7.42.** The temperature dependence of the refractive index of crystals with the composition $ZrO_2$–12 mol.% $Y_2O_3$, wavelength $\lambda = 6328$ Å [40].

absorption bands into the ultraviolet range of the spectrum, resulting in the displacement of the entire dispersion curve and in an increase of the refractive index; secondly, as a result of a decrease in the density of the substance with increasing temperature.

**The thermo-optical constant** is one of the important characteristics of the material and is determined by the following equation:

**Table 7.23**. Dispersion of the refractive indices of single crystals $ZrO_2$–$Y_2O_3$, $ZrO_2$–10 mol% $Y_2O_3$–0.5 wt.% $La_2O_3$, $HfO_2$–15 mol% $Y_2O_3$

| Composition | $n(\lambda)$, Å | | | | | Dispersion coefficient |
|---|---|---|---|---|---|---|
| | 4358 | 5461 | 5779 | 5893 | 6328 | |
| $ZrO_2$–9 mol% $Y_2O_3$ | 2.2224 | 2.1856 | 2.1790 | 2.1768 | 2.1718 | 31.50 |
| $ZrO_2$–11 mol% $Y_2O_3$ | 2.2101 | 2.1737 | 2.1669 | 2.1653 | 2.1581 | 30.72 |
| $ZrO_2$–17 mol% $Y_2O_3$ | 2.1783 | 2.1434 | 2.1372 | 2.1352 | 2.1287 | 33.89 |
| $ZrO_2$–9 mol% $Y_2O_3$ –0.5 wt% $CeO_2$ | 2.2285 | 2.1844 | 2.1778 | 2.1757 | 2.1691 | 33.88 |
| $ZrO_2$–9 mol% $Y_2O_3$ –0.5 wt% $Nd_2O_3$ | 2.2285 | 2.1916 | 2.1848 | 2.1759 | 2.1750 | 30.97 |
| $ZrO_2$–9 mol% $Y_2O_3$ –0.5 wt% $Ho_2O_3$ | 2.2189 | 2.1813 | 2.1744 | 2.1727 | 2.1658 | 34.80 |
| $ZrO_2$–9 mol% $Y_2O_3$ –0.5 wt% $Er_2O_3$ | 2.2061 | 2.1699 | 2.1634 | 2.1613 | 2.1547 | 34.87 |
| $ZrO2$–9 mol% $Y_2O_3$ –0.5 wt% $CoO$ | 2.2177 | 2.1804 | 2.1740 | 2.1722 | 2.1675 | 36.29 |
| $ZrO2$–9 mol% $Y_2O_3$ –0.5 wt% $CoO$ (annealed) | 2.2201 | 2.1835 | 2.1769 | 2.1748 | 2.1678 | 34.55 |
| $HfO_2$–15 mol% $Y_2O_3$ | 2.2132 | 2.0949 | 2.0897 | 2.0881 | 2.0826 | 39.14 |

$$\nu(\lambda) = \beta(\lambda)/[n(\lambda)-1] - \alpha, \tag{7.11}$$

where $n(\lambda)$ is the refractive index of the substance at the wavelength $\lambda$, $\beta(\lambda)$ is the relative increase of the refractive index of the material at the wavelength with the temperature changed by 1°; $\alpha$ is the mean coefficient of the linear expansion of the material in the same temperature range. The characteristic $\nu(\lambda)$ of the optical material is used in the calculation of thermo-optical aberration of the optical systems operating at temperatures other than room temperature. The calculated values of the thermo-optical constant in the temperature range 20–900°C are presented in Table 7.24.

**The spectroscopic properties of fianites**

The special feature of stabilised crystals of $ZrO_2$ and $HfO_2$ is that their crystal lattice may contain a large number of different impurities in high concentrations, reaching 10 mol.% whilst retaining the phase homogeneity. Rare-earth elements, elements of the iron group – chromium, vanadium, titanium and others, may be introduced into the fianites. Many impurity elements may exist in the solid solutions based on dioxides of zirconium and hafnium in different valency states. In principle, the solid solutions represent an entire class of substances which, retaining their microstructure

**Table 7.24.** Thermo-optical constants of the fianites $\lambda$ = 6328 Å, $n$ = 2.1567, $T$ = 20°C [40]

| Temperature range | $\beta \cdot 10^{-6}$ | $\alpha \cdot 10^6$ | $\dfrac{\bar{\beta}_\lambda}{n_\lambda - 1} \cdot 10^6$ | $\nu_\lambda \cdot 10^6$ |
|---|---|---|---|---|
| 20–100 | 8.75 | 8.48 | 7.56 | −0.92 |
| 20–200 | 8.89 | 9.44 | 7.73 | −1.75 |
| 20–300 | 8.57 | 9.66 | 7.41 | −2.25 |
| 20–400 | 6.68 | 10.03 | 7.50 | −2.52 |
| 20–500 | 8.75 | 10.24 | 7.56 | −2.67 |
| 20–600 | 8.96 | 10.38 | 7.75 | −2.63 |
| 20–700 | 9.12 | 10.63 | 7.88 | −2.59 |
| 20–800 | 9.36 | 10.68 | 8.09 | −2.53 |
| 20–900 | 9.43 | 10.68 | 8.15 | −2.62 |
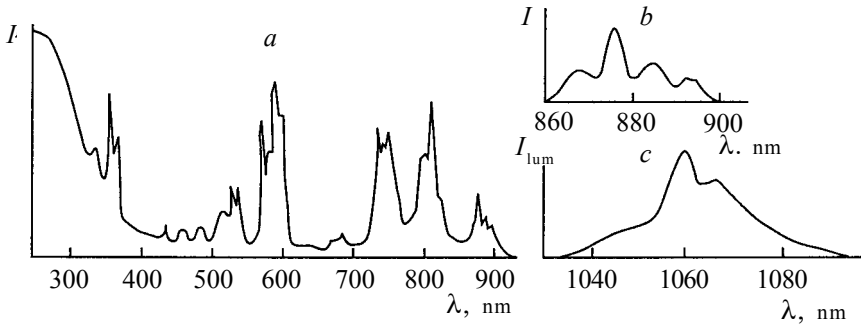


**Figure 7.43.** Optical spectra of $HfO_2$–$Y_2O_3$–$Nd^{3+}$ crystals [118]. a) the absorption spectrum of $HfO_2$–$Y_2O_3$–$Nd^{3+}$ crystals at 300 K; b) the absorption band of $Nd^{3+}$ corresponding to the $^4I_{9/2} \rightarrow {}^4F_{3/2}$ transition; c) the luminescence spectrum for the $^4I_{9/2} \rightarrow {}^4F_{3/2}$ transition at 300 K.

and phase homogeneity, may change their physical properties in a wide range. The spectroscopic properties of the solid solutions based on zirconium and hafnium dioxide with different impurities, illustrating the special features of these systems in comparison with other impurity crystals, used in optics and quantum electronics, have been investigated in [136].

## Colour fianites

Prior to discussing important technical aspects of the application of fianites, it is important to mention the application of fianites in the jewellry industry for which the main bulk of the crystals is produced [137]. As already mentioned, the crystal structure of the fianites is such as that a large number of different additional elements, in
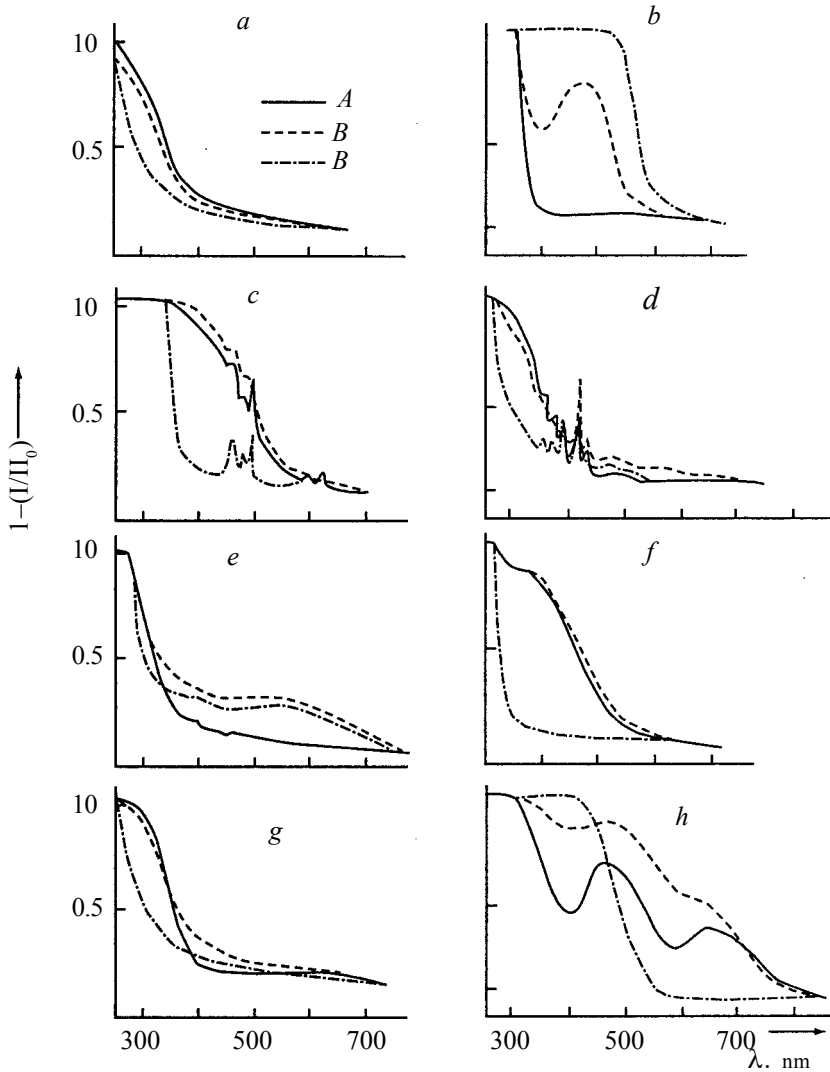


**Figure 7.44**. The absorption spectra of $ZrO_2+Y_2O_3$ crystals grown in air, after gamma irradiation and annealing in vacuum [118]: a) non-activated crystal, b) the crystal activated with the oxides of the elements: b) Ce, c) Pr, d) Sm, e) Eu, f) Tb, g) Yb, h) Cr.

particular, rare-earth elements, elements of the group of iron, chromium, vanadium, titanium and other chromophores, may be added to the crystal structure in the isomorphous manner and in large amounts. The introduction of stabilising additions such as the oxides of terbium, holmium, europium and thullium, colours the crystals correspondingly to the brown-green, yellow-green and white green colours. A small addition (0.1%) of the iron oxide results in a yellow shade of the crystal stabilised with the gadolinium oxide, and the cobalt oxide (0.01–0.5%) colours the crystals to dark violet colour, the nickel oxide (0.1–2%) to light brown colour, the vanadium oxide (0.1–1%) to green colour, the chromium oxide (0.1–2% cycle) to brown-purple colour, and the copper oxide (0.1–2%) makes the crystals to acquire yellow colour. The yellow-orange colour is typical of the fianites containing the addition of tetravalent cerium, and the trivalent cerium makes the crystals light red [137]. This wide range of the colours and shades enables many natural stones to be imitated, including diamonds and emeralds. Table 7.25 presents the elements whose oxides, added to the melt, result in the corresponding colour of the fianites.

## 7.10. ELECTROPHYSICAL, ACOUSTIC, ELASTIC AND PHOTOELASTIC PROPERTIES OF FIANITES

The authors of [126] established that the sintered ceramics of $ZrO_2$, stabilised with oxides CaO, SrO, $Y_2O_3$, $La_2O_3$, is characterised by ionic conductivity. The temperature dependences of the specific resistance in the temperature range 500–1300°C are presented in [127]. Figure 7.45 shows the temperature dependence of the specific resistance of single crystals of $ZrO_2$–$Y_2O_3$ (10 mol.%) and $HfO_2$–$Y_2O_3$ (10 mol.%), measured by the three-probe method [128]. In the low temperature range, the electrical conductivity is extrapolated by the equations: $\rho = 1.6 \cdot 10^{-4} \exp(1.20/kT)$ for $HfO_2$–$Y_2O_3$ (10 mol.%) crystals, and $\rho = 3.1 \cdot 10^{-5} \exp(1.12/kT)$ for $ZrO_2$–$Y_2O_3$ (10 mol.%), where $kT$ is expressed in eV, $\rho$ in ohm/cm.

The specific resistance of different specimens of zirconia single crystals, stabilised with yttrium oxide, of the same nominal composition greatly differs in the low temperature range. Evidently, this is associated with different concentration of the defects in the crystals, grown in different conditions. If an electrical field is applied to a crystal, heated to a temperature of 300°C or higher,

**Table 7.25.** Colours of cubic zirconium oxide after adding admixtures

| Admixture | Chemical symbol | Colour |
|---|---|---|
| Cerium | Ce | Yellow–orange–red |
| Chromium | Cr | Olive |
| Cobalt | Co | Lilac |
| Copper | Cu | Yellow |
| Erbium | Er | Rose |
| Europium | Eu | Rose |
| Holmium | Ho | Rose |
| Iron | Fe | Yellow |
| Manganese | Mn | Brown–violet |
| Neodymium | Nd | Lilac |
| Nickel | Ni* | Yellow–brown |
| Praseodymium | Pr | Amber |
| Thullium | Tm | Green |
| Titanium | Ti | Yellow–brown |
| Vanadium | V | Green |

*Typical colour for several tenths of a per cent; the colour may depend on the degree of oxidation of the admixture.

the negative electrode is characterised by the formation of a coloured region, spreading to the anode. In the absorption spectrum, a wide band appears in the vicinity of the fundamental absorption edge, determined by oxygen vacancies, neutralised by free oxides.

Investigations of the single crystals of zirconia in the temperature range 800–1900°C in vacuum and in air showed that the electrical conductivity of single crystals is 1.5 times higher in comparison with the ceramic specimens. When a second addition in the series of rare-earth elements was made, electrical conductivity increased in
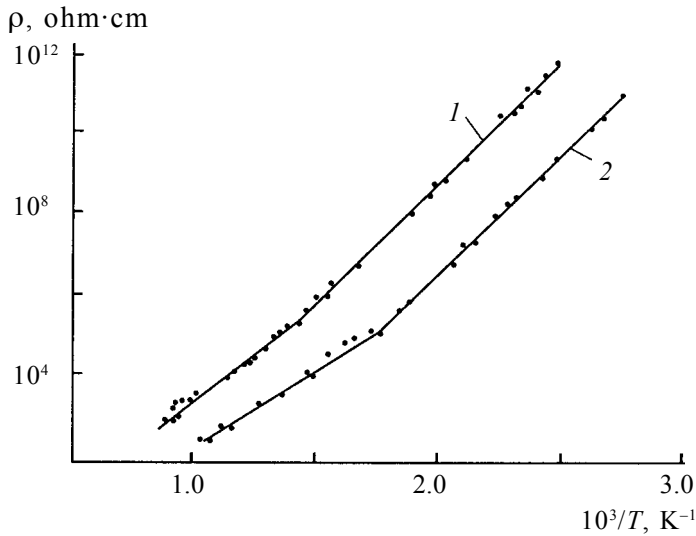
**Figure 7.45.** Temperature dependence of the specific resistivity of fianites $ZrO_2$–10 mol.% $Y_2O_3$ (curve 1) and $HfO_2$–10 mol.% (2) [127].

the direction from Ce to Pr, decreased in the case of Nd and again increased in the direction to Tb.

The frequency dependences of $\varepsilon$ and tg $\delta$ are presented in Fig. 7.46. The relatively low dispersion of dielectric permeability indicates that the polarisation of the investigated crystals is of the relaxation type and, possibly, is caused by the displacement of weakly bonded oxygen vacancies or admixture ions.

The temperature dependences of tg $\delta$ and $\varepsilon$ of the compositions $HfO_2$–10 mol.% $Y_2O_3$ and $ZrO_2$–10 mol.% $Y_2O_3$, presented in Fig. 7.47, are also of the relaxation type.

The authors of [129] investigated the elastic and photoelastic properties of single crystals of the $ZrO_2$–$Y_2O_3$ and $HfO_2$–$Y_2O_3$ solid solutions which depend on the concentration of the stabilising oxide $Y_2O_3$ and are characterised by the molecular scattering of light.

The investigations of the elastic properties of $ZrO_2$–$Y_2O_3$ crystals with 8 and 12 mol.% of $Y_2O_3$ by ultrasound methods were carried out in [130, 131]. The elastic and photoelastic properties of the crystals of $ZrO_2$–$Y_2O_3$ and $HfO_2$–$Y_2O_3$, containing 10 mol.% of $Y_2O_3$, were investigated by the Mandel'shtam–Brillouin methods and the patterns of molecular scattering of light by these crystals were determined. The investigations of the elastic properties of
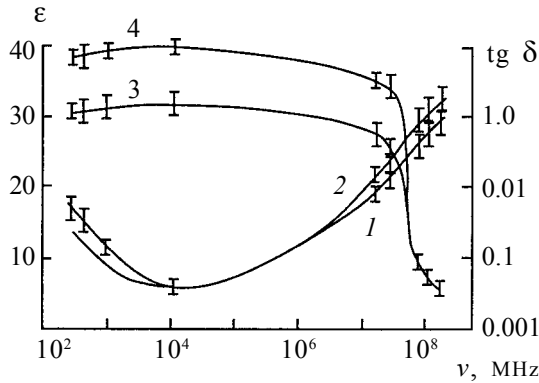
**Figure 7.46.** Frequency dependence of tg δ and ε of fianites [118]: the curves 1 and 3 – HfO$_2$–10 mol.% Y$_2$O$_3$; curves 2 and 4 – ZrO$_2$ – 10 mol.% Y$_2$O$_3$.
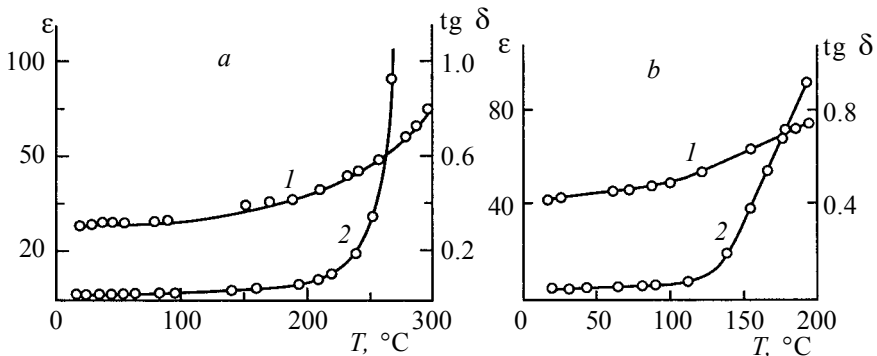


**Figure 7.47**. Temperature dependences of tg δ and ε of fianites [118].

ZrO$_2$–Y$_2$O$_3$ crystals as a function of the Y$_2$O$_3$ concentration, were carried out in [134].

Preliminary experiments on a large number of single crystal specimens of solid solutions showed that the results are highly sensitive to the accuracy of orientation of the crystal planes in relation to the crystallographic direction. The accuracy of the measurement methods was improved using the same method of light scattering on crystal specimens with accurately oriented planes. These results, together with other data [130–134], made it possible to improve the accuracy of determination of several properties of the dynamics of the lattice of ZrO$_2$–Y$_2$O$_3$ and HfO$_2$–Y$_2$O$_3$ crystals.

The speed of sound waves and the values of the elasticity constant, calculated from the speed of sound waves, show that in the ZrO$_2$–Y$_2$O$_3$ crystals, the speed of sound is considerably greater than that detected in the HfO$_2$–Y$_2$O$_3$ crystals. In both crystals, the

speed of longitudinal and transverse sound waves depends greatly on the direction of propagation of sound. Figure 7.48 shows the speed of the longitudinal and transverse sound waves in the $ZrO_2$–$Y_2O_3$ crystals as a function of the $Y_2O_3$ concentration. In order to facilitate comparison, the speeds of ultrasound waves $V_{L1}$, $V_{T1}$, $V_{T2}$, measured for the [110] direction, were reduced to the direction [100] and [11$\sqrt{2}$] for which the speed of ultrasound waves is available. Reduction was carried out using the relationships derived by Borcherds [135]. Figure 7.48 shows that the ultra- and supersonic speeds are similar and change only slighty with the $Y_2O_3$ concentration.

The speeds of sound *v* were used to calculate the elastic constants using equations [135]. The results are presented in Fig. 7.49

The photoelastic constants $P_{i,j}$ were calculated from the Mandel'shtam–Brillouin spectrum using the ratio of intensities and equations (7.11) and (7.12)

$$Z_1 = (p_{44}/P_{12})^2 c_{11}/(2c_{44}) \tag{7.12}$$

$$Z_2 = 2P_{44}/(P_{11} - P_{12})^2 c_{11}/(2c_{44}). \tag{7.13}$$

Here $Z_1$ and $Z_2$ are the ratios of the intensities of the transverse components to the longitudinal components for the $V\Sigma$ and $H\Sigma$ spectra, respectively, for the case of scattering of light on the
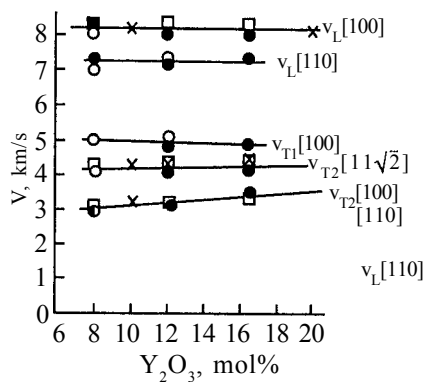


**Figure 7.48.** The speed of sound in $ZrO_2$+$Y_2O_3$crystals in relation to the concentration of $Y_2O_3$ for different crystallographic directions [130, 131]. ● – ultrasound measurements; O – ultrasound measurements for the direction [110] and the speed reduced to the direction [100]; □× – the hypersonic measurements (for explanation see the text).
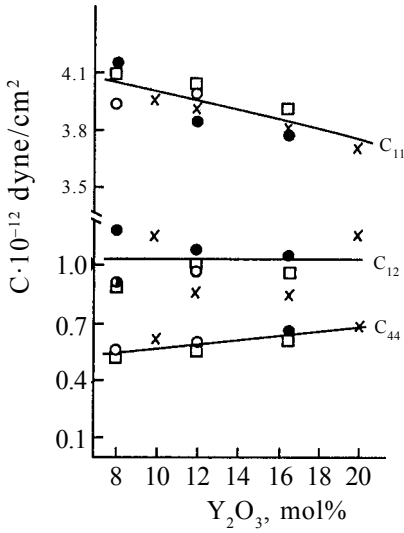
**Figure 7.49.** Elastic constants of the $ZrO_2+Y_2O_3$ crystals in relation to the $Y_2O_3$ content. The data are in complete agreement with Fig. 7.48.

photons passing along the [100] axis. The equations (7.11) and (7.12) form four combinations of the ratios $P_{11}$, $P_{12}$, and $P_{44}$. The authors selected orientations, providing the best agreement between the calculated and experimental spectra for the 2–4 orientation (Fig. 7.50). For the $ZrO_2$–$Y_2O_3$ crystals with 0.08, 0.1 and 0.156 mol.% $Y_2O_3$, only the parameters of photoelastic anisotropy ($P_{11}$–$P_{12}$)($2P_{44}$) were determined. The resultant relationships of the photoelastic constants and the parameters of photoelastic anisotropy are presented in Fig. 7.51.

The absolute values of the photoelastic constants were obtained in the examination of the diffraction of light on ultrasound. Directly measured acousto-optical parameters of quality $M_2$ are linked with $P$ using the equation $M_2 = n^6P^2/(\rho v^3)$. The value of $P$ is determined by the expression:

$$p = p_{ijkl}\alpha_i\beta_j\chi_k\gamma_l. \tag{7.14}$$

Here $P_{ijkl}$ is the tensor of the photoelastic constants of the material, $\alpha_i$ and $\beta_j$ are the unit verctors of the components of the electrical field ($E$) of the incident and scattered light waves, respectively; $\chi_k$ and $\gamma_l$ and the unit vectors of the components of the direction and of polarisation of sound, and $v$ is the speed of sound. For a longitudinal sound wave:

$$P_{11}, \text{ for } \alpha \text{ along [100]} \tag{7.15}$$
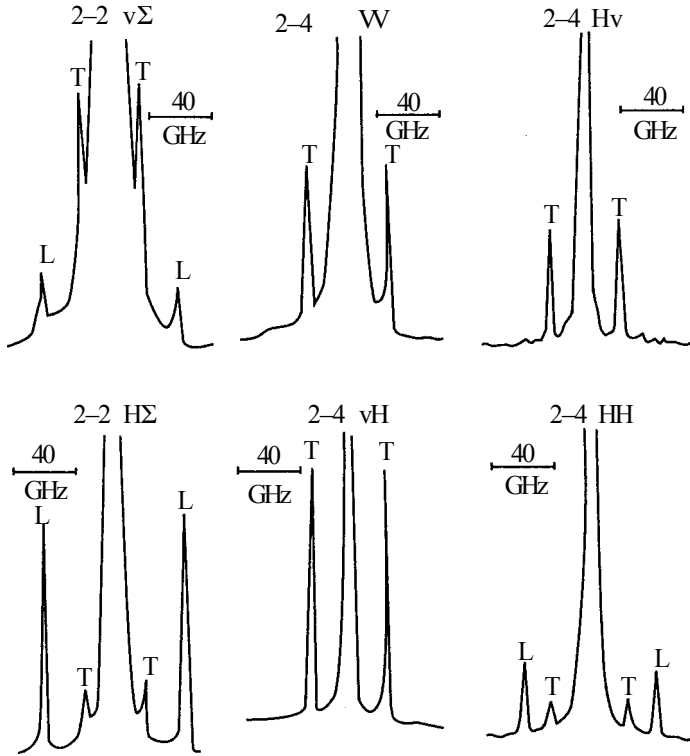
**Figure 7.50**. Mandel'shtam–Brillouin spectra for $ZrO_2+Y_2O_3$ crystals containing 20 mol.% of $Y_2O_3$.

$$P_{12}, \text{for } \alpha \text{ along } [001] \; \chi \text{ along} [100] \tag{7.16}$$

$$0.5(P_{11} + P_{12}) + P_{44} \text{ for } \alpha \text{ along} [100] \; \chi \text{ along} [110] \tag{7.17}$$

$$0.5(P_{11} + P_{12}) - P_{44}, \text{ for } \alpha \text{ along } [110]. \tag{7.18}$$

For the transverse sound wave, propagating along the [100] direction, the photoelastic constant $P$ is equal to $P_{44}$ and is independent of the orientation of the field $E$ in accordance with the vectors of propagation of light and sound

Figure 7.51 shows the photoelastic constants of the $ZrO_2$–$Y_2O_3$ crystals as a function of the $Y_2O_3$ concentration. In order to determine the dependence of the absolute values of the photoelastic constants on the $Y_2O_3$ concentration, the data of ultrasound measurements were used. Figure 7.51 also shows the parameters of the anisotropy $P_{12}/2P_{44}$ in relation to the $Y_2O_3$ concentration. The
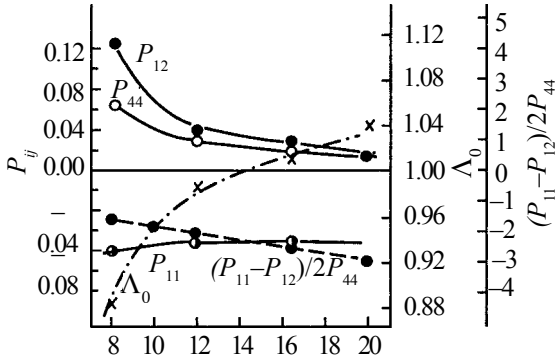
**Figure 7.51.** Photoelastic constants and the parameters of photoelastic anisotropy in relation to the $Y_2O_3$ content of the $ZrO_2+Y_2O_3$ crystals (for explanation see the text).

graphs indicate that the absolute values of the constants $P_1$ and $P_2$ decrease with increasing $Y_2O_3$ concentration, and $P_{11}$ is almost completely constant.

The mechanical properties of the material, especially cracking resistance and failure under welding, are controlled by the elastic properties of the material. Figure 7.49 shows the elastic constants for single crystals of solid solutions based on zirconia, which can be used to calculate the Zener relationships $Z = C_{44}/(C_{11}-C_{12})$, characterising the degree of anisotropy of the elastic properties in actual crystals (for $Z = 1$, the material is isotropic). The value of this ratio also determines the direction of the extreme value of the Young modulus: at $Z < 1$, the maximum value of the Young modulus is in the <100> direction, and at $Z > 1$ its maximum is found in the <111> direction [136].

Analysis of the results indicates the following:

1. Depending on the concentration of the yttrium oxide in the entire range of the compositions, including the multiphase composition, the constant $C_{11}$ monotonically decreases, $C_{44}$ monotonically increases, $C_{12}$ remains constant; the direction [100] is the high-modulus direction, $E \sim 360$ GPa, and {111} is the low-modulus direction, $E \sim 170$ GPa [136].

2. In the solid solutions $ZrO_2-Y_2O_3$ and $HfO_2-Y_2O_3$ there are directions of the exciting and scattered light for which the longitudinal waves provide almost no contribution to the scattering of light. Identical results were obtained previously for non-cubic crystals of sapphire and lithium niobate [136].

3. The speed of the longitudinal and transverse sound waves in the $ZrO_2-Y_2O_3$ and $HfO_2-Y_2O_3$ solutions depends strongly on the direction of propagation of the waves, *i.e.* the fianites are characterised by a strong anisotropy of the speed of sound.

4. The elastic and photoelastic anisotropy of the fianites are high and change in relation to the content of the stabilising oxide. The main physical properties of the fianites are presented in Table 7.26.

## 7.11. JEWELLERY QUALITIES OF THE FIANITES

The unique combination of the physical and physical–mechanical properties of the fianites is the reason why they are included in the class of valuable technical crystals. For the efficient application of these crystals in technology, it was necessary to develop methods of physical–chemical and physical–mechanical treatment: cutting, grinding and polishing to the 14th class of surface finish, drilling, optical clarification, brazing with metals, ceramics and glass, precision fractioning. The development of these methods of treatment has made it possible to produce components of complicated shapes from fianites and also join these crystals with other materials in sections of different devices and systems. The physical properties of the fianites are presented in Table 7.26.

The fianites are used on a large-scale in the jewellery industry. In particular, the fianites are regarded as an excellent imitation of diamonds.

The precious stones have been the subject of reproduction for many years. However, only at the end of the 19th century, the advances in chemistry and physics made it possible to develop synthetic stones whose properties do not differ at all from those of the natural precious stones and, in many cases, are higher.

A turning point in the production of synthetic precious stones was achieved by the French engineer V.A. Verneuil who in 1892 invented a method of production of synthetic ruby from a melt. His method was subsequently used for the growth of other synthetic crystals: sapphire, spinel, alexandrite and other 'precious' stones. In the period since Verneuil's invention, many methods have been developed for the growth of crystals and new types of crystals have been produced which have no analogues in nature, with the fianites occupying an important position [42, 43].

All synthetic crystals may be classified on the basis of the following features: 1. Synthetic jewellery stones, having no natural analogues, which include ruby, sapphire, spinel, rutile, diamond, isumrud, quartz, alexandrite, opal; 2. synthetic materials with no natural analogues, with suitable examples being strontium titanate, fabulite, lithium niobate, yttrium–aluminium garnet, fianite and other

**Table 7.26**. Physical properties of fianites [108]

| Characteristic | Value | Comment |
|---|---|---|
| Melting point, ºC | 2700–2850 | Depends on composition |
| Density, g/cm$^3$ | 5.85–9.65 | As above |
| Refractive indes, $n_o$ | 2.2 | $ZrO_2$–$Y_2O_3$–10 mol% |
| Mean dispersion of refractive index $n_{F-}n_c$ | 0.038 | " " |
| Transmission band | 0.26–7.6 | " " |
| Abbe number | 30 | " " |
| Hardness (mineralogical scale) | 8.5 | " " |
| Young modulus, kg/mm$^2$ | 3930 | " " |
| Shear modulus, kg/mm$^2$ | 10.87 | " " |
| Poisson coefficient | 0.374 | " " |
| Resistivity, ohm·cm$^{-1}$ | | " " |
| at 20 ºC | $1 . 10^{12}$ | " " |
| at 300 ºC | $1 . 10^4$ | " " |
| at 2000 °C | 1 | " " |
| Heat conductivity, kcal/m·h·deg | 2.2 | " " |
| Coefficient of linear thermal expansion at 20–1800°C, deg$^{-1}$ | $10.5 \cdot 10^{-6}$ | " " |
| Evaporation in vacuum, g/cm$^2$·s | $(7–9) \cdot 10^{-6}$ | " " |
| ($10^{-4}$ mm Hg at 2100 ºC) | $(3–5) \cdot 10^{-6}$ | $HfO_2$–$Y_2O_3$–10 mol% |

crystals; 3. imitations of the jewellery stones: glass, doublets and triplets. A special commission in 1970 published more accurate definitions of synthetic stones: 'Synthetic stones are crystallised produced completely or partially by the work of human hands. Their chemical composition, crystal structure and physical properties

coincide in a wide range with those of natural prototypes' [137].

The jewellery inserts from diamonds occupy a special position because of four properties:

1. Diamond (non-faceted ) has an exceptionally high refractive index ($n$ = 2.42) which enables the faceting in which a large part of the incident light is refracted, resulting in unusual sparkling.

2. Diamond is characterised by a high dispersion of the refractive index ($d$ = 0.044) resulting in the play of colours formed as a result of the decomposition of the white light into the components of the colour spectrum, with the beams reflected under different angles inside the stones.

3. Diamond has the highest hardness ($h$ = 10) and, consequently, after polishing with diamond powder, it is not scratched by other minerals (although the tendency to cleaving makes it susceptible to impacts).

4. The colourless diamond is characterised by the complete absence of colouring and this additionally increases the optical effect.

Any diamond substituent should be evaluated on the basis of these four properties. Although some synthetic and natural substituents are very close to diamond in respect of some properties, in other aspects they cannot be compared with diamond. For example, the dispersion of light in crystals such as strontium titanate ($d$ = 0.190) and rutile ($d$ = 0.280) is considerably higher than in diamond. However, these materials are characterised by low hardness ($h$ = 5.5–6.5) and, consequently, have insufficient wear resistance. However, even if they were harder, these stones could be easily identified due to their excessive sparkling ('fire') because their dispersion is considerably greater than that of the diamond.

More recent substituents of the diamond, aluminium–yttrium amd gadolinium–gallium garnets, have the hardness similar to that of the diamond ($h$ = 7.5–8.5) and intermediate values of the refractive index and dispersion (Table 7.27) and, consequently, they are characterised by a relatively high shine and sparkling ('fire'). Regardless of these properties, other characteristics of these stones are greatly inferior to those of the diamond.

At present, it is possible to grow fianite crystals weighing up to 5 kg. The colouring of the fianites and their density are determined by chemical composition. Small amounts of the impurities of rare-earth and transition metals result in different colours and shapes of the fianites: red, rose, violet, blue, yellow, etc. As regards the colour

range, the fianite is comparable with amethyst, garnet and zircon, and in the attractiveness it is compared with diamond.

The high refractive index of the fianites, which is close to that of the diamond, and the high dispersion result in special light effects. These properties, combined with different colouring, make it possible to simulate natural precious stones and also produce new ones with original colours. In the ultraviolet beams, the fianites in relation to the impurities may sparkle by blue, yellow, violet and other colours.

The fianites can be machined only in specific crystallographic directions. The fianites are relatively difficult to process, they easily crack and chip. The yield in the faceting of the crystals is usually not higher than 10–15%. In the production of juvenile inserts, the height of the lower part of the crystal should be deeper in order to improve its colour 'play', and the upper area should be wider in

**Table 7.27.** Diagnostic properties of diamond and its imitations [134]

| Name | Characteristic formula | Crystal system | Refractive index | Birefringence |
|---|---|---|---|---|
| Diamond | C | Cubic | 2.417 | Often anomalous |
| Fianite | $(Zr, Hf)O_2$ | " | 2.10–2.20 | None |
| Yttrium–aluminium garnet (YAG) | $Y_3Al_5O_{12}$ | " | 1.8834 | None |
| Synthetic rutile | $TiO_2$ | Tetragonal | 2.61–2.90 | 0.287 |
| Strontium titanate | $SrTiO_3$ | Cubic | 2.41 | None |
| Lithium niobate | $LiNbO_3$ | Trigonal | 2.20–2.30 | None |
| Zircon | $Zr[SiO_4]$ | Tetragonal | 1.920–2.010 | 0.036–0.059 |
| Scheelite | | Trigonal | | |
| natural | $Ca(WO_4)$ | Tetragonal | 1.918–1.934 | 0.016 |
| synthetic | | | | |
| Sphalerite | $ZnS$ | Cubic | 2.37 | None |
| Corundum | | | | |
| natural | $Al_2O_3$ | Trigonal | 1.757–1.776 | 0.008–0.009 |
| synthetic | | | | |
| Spinel, synthetic | $MgAl_2O_4$ | Cubic | 1.728 | Often anomalous |
| Evklaz | $Al_2Be_2[SiO4]_2(OH)_2$ | Monoclinic | 1.652–1.672 | 0.019–0.020 |
| Phenakite | $Be_2[SiO_4]$ | Trigonal | 1.654–1.670 | 0.019–0.020 |
| Tourmaline, achroite | $Na(Mg, Fe)_3(Al, Fe)_6[BO_3]_3[Si_6O_{18}](OH)_4$ | Trigonal | 1.614–1.634 | 0.016–0.024 |
| Topaz | $Al_2[SiO_4](F, OH)_2$ | Rhombic | 1.607–1.637 | 0.010 |
| Beryll, colourless | $Be_3Al_2[Si_6O_{18}]$ | Hexagonal | 1.566–1.600 | 0.004–0.010 |
| Mine crystal | $SiO_2$ | Trigonal | 1.544–1.553 | 0.009 |

comparison with the diamond. The faces of the inserts of the fianites are slightly rounded and this is another feature by which they differ from the diamonds.

The faceted stones produced from the fianites immediately attracted the attention of jewellers. As already mentioned, the initial batches of the fianite crystals were produced by the Lebedev Institute of Physics, Russian Academy of Sciences. Later, the production of similar crystals started in Switzerland by the company Grand Dzewahirdzhan which supplied the crystals to jewellery markets under the name djevalite. In the United States of America, the company Serez Corporation Corporation synthesized the material 'diamonesc' whose properties are very similar to those of the fianites. In Austria, Swarowski and Co produces 'zircon' using a Russian license [43] .

| Name | Dispersion | Shine | Density, $g/cm^3$ | Bonding | Hardness | Luminiscence colour in UV rays |
|---|---|---|---|---|---|---|
| Diamond | 0.063 (0.044) | Diamond-like | 3.52 | Perfect | 10 | Blue, yellow, green, rose, orange, colourless |
| Fianite | 0.060 | " | 6–10 | " | 7.5–8 | Green, blue, yellow, violet |
| Yttrium–aluminium garnet (YAG) | 0.028–0.038 | " | 4.57–7.09 | Imperfect | 6.5–8.5 | Green, blue, violet, yellow |
| Rutile, synthetic | 0.180–0.300 | " | 4.25–4.32 | Perfect | 6–6.5 | No luminiscence |
| Strontium titanate | 0.10–0.20 | " | 5.13–5.15 | " | 5.5–6.5 | No luminiscence |
| Lithium niobate | 0.120 | " | 4.64 | | 5.5 | No luminiscence |
| Zircon | 0.039 | " | 3.95–4.80 | Imperfect | 6.5–7.5 | Yellow |
| Scheelite natural | 0.026 | " | 6.1 | Mean | 5 | Blue |
| synthetic | | | | | | |
| Sphalerite | 0.156 | " | 4.09 | Highly perfect | 3.5 | No luminiscence |
| Corundum natural | 0.018 | Glassy | 3.99–4.05 | Imperfect | 9 | Sometimes slightly rosy |
| synthetic | | | | | | |
| Spinel., synthetic | 0.020 | " | 3.63 | Perfect | 8 | Green, blue |
| Evklaz | 0.016 | " | 3.02–3.10 | " | 7.5 | |
| Phenakite | 0.015 | " | 2.95–3.00 | Clear | 7.5–8 | |
| Tourmaline–achroite | 0.017 | " | 2.90–3.31 | Highly imperfect | 7–7.5 | |
| Topaz | 0.014 | " | 3.50–3.57 | Perfect | 8 | |
| Beryll, colourless | 0.014 | " | 2.50–2.90 | Imperfect | 7.5–8 | |
| Mine crystal | 0.013 | " | 2.65 | " | 7 | |

## Diagnostic properties of diamond and its imitations

It should be stressed that all possible imitations of the diamonds have been used in the jewellery industry for many years: transparent, colourless minerals: zircon, corundum, evklaz, phenakite, tourmaline–achroite, topaz, beryll, rock crystal, etc., and also various glasses with a strong dispersion of the refractive index because of various additions (mainly lead oxide). At present, the most effective imitations of the diamonds are the synthetic crystals such as yttrium–aluminium garnet (YAG), strontium titanate (fabulite), fianite, rutile, spinel, corundum, lithium niobate, etc. (Table 7.27) Some imitations are characterised by high dispersion, exceeding that of the diamond. These imitations differ from the diamonds by a number of properties. The main difference is the lower hardness. Up to now, there is no mineral or synthetic material with such a high hardness (10 on the Moss scale) like the diamond.

A significant role in the identification of the diamonds is played by the optical properties. Diamond is characterised by a high refractive index which cannot be measured by conventional optical methods. Some imitations with lower refractive indexes, presented in the table, can be easily distinguished from diamond on conventional refractometers. The minerals with high refractive indexes are characterised by a strong diamond shine, identical with that of the diamond; the shine of the minerals with low diffraction indexes is of the glassy type. This is especially clearly visible on the faceted stones. The recognition on the basis of the shine is carried out in a refractometer or in a 'magic eye' device used for distinguishing the diamonds from the crystals, characterised by less marked shine.

The property of birefringence of the crystal is often utilised in diagnostics. The presence of distinctive birefringence in the crystal makes it possible to separate diamond from the crystals of zircon, rutile, corundum, evklaz, phenakite, tourmaline, beryll, topaz, rock crystal. However, it must be remembered that the diamond may also sometimes be characterised by anomalous birefringence.

In the identification of the stones not secured in a holder, it is recommended to use the measurements of the density of the stone. Using a liquid with a density of 3.5 $g/cm^2$ (for example, the diluted Clerichi liquid) it is quite simple to separate the diamonds. All the imitations are characterised by higher or lower density. Density is also determined by hydrostatic weighing. Only the density of topaz is close to the density of the diamond. The densities of the most

widely used imitations are also presented in table 7.14. The density of the glasses changes in relation to the lead content of the latter, but the hardness of the glass is many times lower than that of the diamond and, consequently, they can be easily distinguished from the diamond. Additional diagnostic properties include the presence of the cleavage planes, luminescence and inclusions.

The universal method of identification of the diamond is to illuminate the insert by the x-rays. In the x-rays, the diamond is transparent, and the majority of minerals and glasses are non-transparent. The x-ray method can be used for the inserts, secured in the components. Recently, 'samplers' have been used widely for the identification of diamonds. The method is based on the measurement of the heat conductivity of diamond which differs by two orders of magnitude from the heat conductivity of the majority of imitations (Table 7.28). The method based on wetting the surface, with the determination of the contact wetting angle, is also used. Special black dyes are also used; they leave a continuous line on the diamond and a dotted line on other stones with high (more than 1.8) refractive indexes [121].

Because of the lower hardness and also as a result of less efficient polishing of less valuable materials, the substitutes of the diamonds contain unavoidably the faces which are not ideally flat and rounded edges. Consequently, the edges themselves are not so sharp and clear as in the diamond [45]. The diagnostic features of the diamond and of its imitations are presented in Table 7.27.

**Table 7.28.** Heat conductivity of diamond imitations

| Material | Heat conductivity (approximate) V/cm °K |
|---|---|
| Diamond | 10–26* |
| Corundum | 0.35 |
| Yttrium–aluminium garnet | 0.11 |
| Gallium–adolinium garnet | <0.1 |
| Strontium titanate | <0.1 |
| Rutile | 0.08 |
| Cubic zirconia (fianite) | 0.02 |

*Depends on the amount of the admixture.

# References

1. J. McCullough and K. Trueblood, *Acta Crystallogr.*, 18, 6, 983–991,1965.
2. G.B. Bokii, Crystallochemistry, Nauka, Moscow, 1971.
3. A.A. Voronkov, et al., Crystallochemistry of minerals of zirconium and their artificial analogues, Nauka, Moscow, 1978.
4. G. Teufer, *Acta Crystallogr.*, 15, 11, 1187, 1962.
5. Yu.M. Polezhaev, *Zh. Fiz. Khimii,* 41, 11, 2958–2959, 1967.
6. C.T. Lunch, et al., *J. Amer. Ceram. Soc.*, 44, 3, 143–147, 1961.
7. L.M. Komissarova, et al., *Zh.Neorg. Khimii,* 5, 7, 1413-1415, 1960.
8. R. Cupres and R. Wollast, *Ber. Deut. Keram. Ges.*, 40, 9, 527–532, 1963.
9. D.K. Smith and H.W. Newkirk, Acta Crystallogr., 18, 6, 983–991, 1965.
10. N.V. Belov, Kristallografiya, 5, 3, 460–461, 1960.
11. M. Perec-y-Jorba, High-temperature studies, Mir, Moscow, 1967.
12. H.G. Scott, *J.Mater. Sci.*, 10, 1527–1535, 1975.
13. V.S. Stubican and J.R. Hellman, Phase Equilibria in Some Zirconia System, pp.25–37, in: Advances in Ceramics, vol.3. Edited by A.H. Heuer and L.W. Hobbs, The American Ceramic Society, Columbus, OH, 1981.
14. D.K. Smith and C.F. Cline, *J. Am. Ceram. Soc.*, 45, 5, 249–50, 1962.
15. C. Delamarre, *C.R. Acad. Sci.*, C269, 113–115 (1965).
16. H.J. Rossell and R.H.J. Hannink, Phase $Mg_2Zr_5O_{12}$ in MgO Partially Stabilised Zirconia, pp.139–51, in: Advances in Ceramics, Vol.12. Edited by N. Claussen, M. Ruhle, and A.H. Heuer, The American Ceramics Society, Columbus, OH, 1984.
17. J.R. Hellman and V.S. Stubican, *Mater. Res. Bull.*, 17, 459–65 (1982).
18. R. Ray and V.S. Stubican, *Mater. Res. Bull.*, 12, 5, 549–556, 1977.
19. H.G. Scott, *Acta Crystallogr.*, B33, 1, 281–282 (1977).
20. V.S. Stubican, et al., *J. Am. Cer. Soc.*, 61, 1–2, 17–21, 1978.
21. O. Ruff and F. Ebert, *Z. Annorg. Allgem. Chem.*, 180, 19–41, 1929.
22. V.S. Stubican, et al., Phase Relationships in Some $ZrO_2$ System, pp.96–106 in: Advances in Ceramics, Vol.12, Edited by N. Claussen, M. Ruhle, and A.H. Heuer, The American Ceramics Society, Columbus, OH, 1984.
23. H.G. Scott, *J. Mater. Sci.*, 12, 2, 311–316 (1977).
24. J. Pascual and P. Duran, *J. Amer. Ceram. Soc.*, 66, 1, 23–27, 1983.
25. C. Anderson, et al., Diffusionless Transformations in Zirconia Alloys, p.78–85, Advances in Ceramics, Vol.12, Science and Technology of Zirconia II, The American Ceramics Society, Ohio, 1983.
26. P. Ruh, et al., *J. Amer. Ceram. Soc.*, 67, 9, A, 190–192, 1984.
27. A.I. Belov and T.A. Semenov, *Izv. AN SSSR, Neorg. Mater.*, 13, 10, 1817–1821, 1977.
28. I.A. Davtyan et al., *Izv. AN SSSR, Neorg. Mater.*, 5, 890–895, 1966.
29. S.S. Kiparsov, et al., *Izv. AN SSSR, Neorg. Mater.*, 12, 9, 1693–1694, 1976.
30. J. Lefevre, *Ann. Chem.*, 8, 1–2, 117–149, 1963.
31. M. Perez-y-Jorba, *Ann. Chem.*, 7, 479–511, 1962.
32. M. Perez-y-Jorba, et al., *C.R. Acad. Sci.*, 219, 22, 2329, 1959.
33. F. Sibieude and A. Rovanet, *C.R. Acad. Sci.*, 205, 459–468, 1972.
34. M.R. Thornberm, et al., *J. Solid State Chem.*, 11, 3–4, 536–544, 1970.
35. E.E, Lomonova, Dissertation, General Physics Institute, Moscow, 2001.
36. V.I. Aleksandrov, et al., *Pribory Tekh. Eksper.*, 5, 222–225, 1970..
37. V.I. Aleksandrov, et al., *Vestnik AN SSSR*, 1973, No. 12, 29–39.

38.  B. Scott and H. Rawson, *Glass. Technol.*, 1973. Vol.14. ! 5. P. 115-124.
39.  V.I. Aleksandrov, et al., Proc. Indian National Sci. Acad., V. 57, No. 2,1991, 133–144.
40.  Lomonova E.E., Production and examination of single crystals of solid solutions based on $ZrO_2$ and $HfO_2$, Disseration, FIAN, Moscow, 1980.
41.  H.J. Rossell, Ordering in Anion-Deficient Fluorite-Related Oxides, pp. 47-63, in: Advances in Ceramics, v.3, edited by A.H. Heuer and L.W. Hobbs The American Ceramic Society, Columbus, OH, 1981.
42.  V.I. Aleksandrov, et al., A method of production of single crystals based on solid solutions of refractory oxides, Author's Cert. No. 1048857, 15.06.1083.
43.  V.I. Aleksandrov, et al., A method of production of single crystals based on stabilised zirconia, Author's Cert. No. 1365739, 08.09.1987.
44.  V.I. Aleksandrov, et al., A method of production of coloured crystals of oxides  (its variants), Author's Cert. No. 1086833, 23.12.1983.
45.  V.I. Aleksandrov, et al., A method of production of dielectric crystals, Author's Cert. No. 1549123, 08.11.1989.
46.  V.I. Aleksandrov, et al., A method of production of single crystals based on stabilised zirconia, Author's Cert. No. 1568686, 01.02.1990.
47.  V.I. Aleksandrov, et al., A method of production of coloured crystals of refractory oxides (its variants), Author's Cert. No. 1112821, 08.05.1984.
48.  Mazdiysni K.S. and Brown L.M., *Journal Amer. Ceram. Soc.,* 54, 1, 43-45, 1970.
49.  V.P. Gorelov, et al., *Izv. AN SSSR, Neorg. Mater.*, 13, 1, 181–182, 1977.
50.  H.-H. Mobius, *Z.Chemie,* 4, 3, 81–94, 1964.
51.  I.I. Vishnevskii, et al., Nauch. Tr. Ukr. Nauch. Issled. In-ta Ogneuporov, 53, 6, 74, 1952
52.  R. Collongues, *Ann. Chem.*, 8, 7–8, 395–408, 1963.
53.  R.S. Roht, *J. Res. Nat. Bureau*, 56, 17–25, 1956.
54.  Yu.A. Pyatenko, *Kristallografiy*a, 4, 2, 204–208, 1959.
55.  Yu.A. Pyatenko, *Kristallografiy*a, 4, 5, 708–713, 1963.
56.  E. Alechin, R.Roy, *J. Amer. Ceram. Soc.*, 45, 1, 18–25, 1962.
57.  N.V. Belov, *Sb. L'vov. Geol. Ob-va*, 4, 21, 1950.
58.  R. Kollong, Nonstoichiometry, Mir, Moscow, 58–88, 1974.
59.  T.K. Gupta, et al., *J. Mat. Sci.*, 12, 2421, 1977.
60.  T.K. Gupta, *Science of Sintering*, 10, 205, 1978.
61.  C.A. Andersen and T.K. Gupta, Phase Stability and Transformation Toughening in Zirconia, in: Advances in Ceramics, V. 3, Sience and Technology of Zirconia, The Amer. Ceram. Soc., Columbus, Ohio, p.184, 1981.
62.  F.F. Lange, *J. Mater. Sci.,* 17, 10, 225–34, 1982.
63.  V. Lantery, et al., Tetragonal Phase in the System $ZrO_2$–$Y_2O_3$, pp. 118–130, in: Advances in Ceramics, v. 12, Sci. and Techn. II, The Amer. Ceram. Soc., Columbus, OH, 1984.
64.  T. Yagi, et al., *J. Amer. Ceram. Soc.*, 69, 1, A 3–4, 1986.
65.  D. Michel, et al., J.Mater. Sci., 18, 2618–2628, 1983.
66.  Yu.K. Voron'ko, et al., *Neorg. Mater.*, 34, 4, 439–443, 1998.
67.  D. Michel, et al., *J. Cryst. Growth*, 43, 4, 546–48, 1978.
68.  R.H. Ingel, et al., Physical, Microstructural and Thermomechanical Properties of $ZrO_2$ Single Crystals, in: Adv. in Ceram., V. 12, Science and Technology of Zirconia II, Ed. by N. Claussen, M. Ruhle and A.H. Heuer, Am. Cer. Soc., Columbus, OH, p.408–414, 1989.

69. V.I. Aleksandrov., et al., *Fiz. Tverd. Tela*, 20, 2, 528–534, 1978.
70. V.V. Osiko, et al., Spectroscopic Investigation of Defects Structure and Structure Transformations in Ionic Crystals, Crystals, Springer, 10, 37–86, 1984.
71. J. Martinez-Fernandez, et al., *Acta Metall. Mater.*, 43, 2, 593–601, 1995.
72. T. Noma, et al., *J. Ceram. Soc. Jpn.*, 94, 8, 887–90, 1986.
73. V.I. Aleksandrov, et al., *Fiz. Tverd. Tela,* 16, 8, 1456–1459, 1975.
74. V.I. Aleksandrov, et al., *Kr. Soob. Fiz.,* 3, 21–27, 1975.
75. I.L. Chistyi, *J. Raman Spectroscopy*, 6, 4, 183–192, 1977.
76. R.P. Ingel, D. Lewis III, *J. Am. Cer. Soc.*, 69, 4, 325–32, 1986.
77. R.P. Ingel, D. Lewis III, *J. Am. Cer. Soc.*, 71, 4, 265–71, 1988.
78. A.I. Ioffe, et al., *Dokl. AN SSSR*, 203, 657, 1973.
79. V.N. Filatova, et al., *Zh. Neorg. Mater.*, V. 11, 1427, 1975.
80. P.P. Budnikov, et al., Chemical technology of ceramics and refractories Stroiizdat, Moscow, 1972.
81. A.B. Ivanov and Yu.L. Krasulin, All-Union Conference on Chemistry, Technology and Application of Zirconium, Hafnium and their Compounds, Giredmet, Moscow, 1972.
83. J.M. Farley, *J. Mater. Sci.*, 7, 475 (1972).
84 Modern Crystallography, Vol. 3, Nauka, Moscow, 1980.
85. J. Barton, et al., in: Germanium, Izdatinlit, Moscow, 1955, 74–81.
86. V.M. Vigdorovich, et al., Directional Crystallisation and Physico-Chemical Analysis, Khimiya, Moscow, 1976.
87. G.. Pfann, Zone Melting, Mir, Moscow, 1970.
88. V.I. Aleksandrov, et al., *Neorg. Mater.,* 16, 1, 99–105, 1980.
89. D.B. Zhang, *J. Crystal Growth*, 79, 336–340, 1968.
90. M.G. Mil'viskii and V.B. Osvenskii, Problems of Modern Crystallography, Nauka, Moscow, 1975.
91. L.S. Milevskii, *Kristallografiya*, 6, 2, 249–255, 1961.
92. D.A. Petrov and B.A. Kolachev, Crystal Growth, Vol. 1, 159–169, 1957.
93. L.V. Tir and N.M. Smirnov, Proc. 4th Conference on Application of Magnetic Hydrodynamics in Industry, Donetsk, 1969.
94. E.K. Keler and A.B. Andreeva, *Ogneupory*, 4, 184–192, 1964.
95. G.P. Kalliga and L.A. Lyutsareva, *Ogneupory*, 9, 412–417, 1964.
96. M.Kh. Ashurov, et al., *DAN SSSR*, 313, 3, 590–593, 1990.
97. V.V. Voronov, et al., *Neorg. Mater.*, 21, 10, 1710–1714, 1988.
98. A.A. Chernov, Problems of Modern Crystallography, Vol. 3, Nauka,Moscow, 1980.
99. A.A. Chernov, *Usp. Fiz. Nauk*, 100, 2, 277–328, 1979.
100. F.F. Seelig, *Z. Naturforsch.*, 31, 731–738, 1976.
101. V.I. Aleksandrov, et al., *Neorg. Mater.*, 13, 2, 2192, 1971.
102. L.A. Krasikov, et al., *Fiz. Tverd. Tela*, 18, 12, 304, 1976.
103. L.A. Krasikov, et al., *Zavod. Lab.*, 46, 3, 242, 1980.
104. V.I. Aleksandrov, et al., *Neorg. Mater.*, 19, 1, 99, 1983.
105. P.A. Tikhonov, et al., *Zh. Fiz. Khimii*, 48, 3, 643, 1979.
106. A.K. Kuznetsov, et al., in: Electronic Structure and Physical Properties of Solids, part 2, Naukova Dumka, Kiev, 1972.
107. V.B. Glushkova, et al., *Izv. AN SSSR, Neorg. Mater.*, 13, 12, 2197–2201, 1977.
108. V.I. Aleksandrov, et al., *Vestnik Akad. Nauk SSSR,* 6, 65–72, 1980.
109. M.Kh. Ashurov, et al., *Dokl. Akad. Nauk SSSR*, 296, 1, 121–122, 1987.

110. F. Hund, *Z. Physikal. Chem.*, 199, 1/3, 142–151, 1952.
111. M. Spizbergen and P.M. Houpt, The British Ceram. Soc., 1968. Vol. 4. P. 247.
112. A.M. Leyus and M.R. Collounques, *C.R. Sci. Paris*, 1969. Vol. 269, 20, 1198–1200.
113. V.F. Kitaeva, et al., Experimental examination of the properties of $ZrO_2$–$Y_2O_3$ solid solution, Preprint No. 136, FIAN, Moscow, 1976.
114. B.F. Ormont, Introduction to Physical Chemistry and Crystal Chemistry of Semiconductors, Vysshaya Shkola, Moscow, 1973.
115. B.I. Ioffe, X-ray Diffraction Methods in Chemistry, Khimiya, Leningrad, 1976.
116. A. Anthony, *Rev. Hautes Temp. Refract.*, 2, 147, 1966.
117. D.W. Strikler and W.G. Carlson, *J. Amer. Ceram. Soc.*, 47, 122, 1966.
118. V.I. Aleksandrov, et al., *Usp. Khimii*, 47, 3, 385–427, 1978.
119. A. Baerman, et al., *J. Crystal Growth*, 79, 331–335, 1986.
120. L.I. Demkina (editor), Physical Fundamentals of Production of Optical Glass, Khimiya, Leningrad, 1976.
121. K. Nassau, *The Lapidary Journal*, 35, 6, 1194–1200, 1981.
122. K. Nassau, *The Lapidary Journal*, 35, 6, 1210–1214. 1981.
123. V.I. Aleksandrov, et al., Brief Comments on Physics, FIAN, Moscow, 2, 17, 1973.
124. V.I. Aleksandrov, et al., *Izv. AN SSSR, Neorg. Mater.,* 13, 12, 2192–2196, 1977.
125. V.I. Aleksandrov, et al., *Fiz. Tverd. Tela,* 26, 5, 1313–1318, 1984.
126. F. Krieger, Chemistry of Imperfect Crystals, Mir, Moscow, 1969.
127. V.I. Aleksandrov, et al., Brief Comments on Physics, FIAN, Moscow, 3, 3, 1975.
128. V.I. Aleksandrov, et al., Brief Comments on Physics, FIAN, Moscow, 6, 10, 1976.
129. I.L. Chistyi, *Journal of Raman Spectroscopy*, 6, 4, 183–192, 1977.
130. N.G. Pace, et al., *J. Mater. Sci.* 4 1106, 1969.
131. V.I. Aleksandrov, et al., *Kristallografiya*, 18, 1085, 1973.
132. P.H. Borcherds, *Opt. Acta*, 20, 147 (1973).
133. N.I. Kornilov and Yu.P. Solodova, Jewellery Stones, Nedra, Moscow, 1983.
134. V.S. Balitskii and E.E. Lisitrsyna, Synthetic Analogues and Simulation of Natural Precious Stones, Nedra, Moscow, 1981.

# Partially stabilised zirconia (PSZ) crystals

One of the current problems of materials science is the development of new structural nonmetallic materials in which the strength, low brittleness and chemical inertness are maintained in the oxidation of atmosphere in a wide temperature range.

These materials include partially stabilised zirconia (PSZ) which was previously produced only in the form of ceramic polycrystalline specimens. The method of direct high-frequency melting of dielectrics in the cold crucible has made it possible to produce for the first time partially stabilised zirconia in the form of nanostructured crystals and carry out investigations exposing the excellent properties of these materials.

## 8.1. PHASE TRANSFORMATIONS IN CRYSTALS OF PARTIALLY STABILISED ZIRCONIA

At present, it is regarded as established that the phase transitions in zirconia have the form of martensitic transformations, characterised by a number of features:

– diffusionless-shear mechanism of phase transition;
– the presence of a hysteresis
– the athermal nature of the process, i.e. the absence of the activation energy;
– quenching is not possible [1–6].

This nature of transition has been confirmed on single crystals of zirconia grown at low temperatures from the solution in the melt and by the hydrothermal method [6]. It has been shown that the

temperature range of the $m \leftrightarrow t$ transitions depends on the chemical composition of the specimen and its prior thermal history, in particular, on the synthesis method.

## Martensitic transformations in zirconia

The martensitic transitions take place in the solid state, in the absence of local changes in the chemical composition, i.e. without diffusion, and take place by a collective mechanism.

The development of the theory of martensitic transformations is based on the concepts proposed by G.V. Kurdyumov [4] on the regular nature of the rearrangement of the lattice and on the coherence of coexisting phases.

The $m \leftrightarrow t$ and $t \leftrightarrow c$ phase transitions in pure zirconia are martensitic transformations with athermal kinetics [1–12]. This means that the transition takes place with the speed of sound (the zero energy of activation) as soon as a viable nucleus of the new phase appears. This mechanism can be efficiently described using the model of the 'floating domino'. The process with the athermal kinetics cannot be prevented by rapid cooling (quenching) even at the temperature of liquid nitrogen or helium. However, the absolutely athermal mechanism is possible only in the presence of ideal interphase boundaries with no potential barriers, preventing the movement of the boundary. The situation completely changes even in the presence of point defects. In this case, the displacement of the interphase boundary is complicated by the barriers resulting from the presence of structural defects. The resultant energy of thermal activation differs from zero, the rate of the process rapidly decreases, and the kinetics of the process becomes isothermal. This circumstance indicates that it is possible to stabilise the metastable high-temperature phase by rapid cooling from the temperature of the equilibrium phase transition to a lower temperature. At cooling rates greatly exceeding the rate of transformation, the phase transition has no time to occur. From the thermodynamic viewpoint, the high-temperature phase is metastable and the absolute loss of stability may take place at some critical fluctuation of temperature. From the kinetic viewpoint, the fluctuation is the formation of a viable nucleus of the low-temperature phase. However, the probability of fluctuation formation of the nucleus with the critical volume decreases with decreasing temperature. At some relatively low temperature, this probability is actually equal to zero and the

metastable high-temperature phase may exist indefinitely long in the absence of external factors causing nucleation (for example, mechanical loading). These considerations qualitatively explain the process kinetics. Lattice defects lead to the formation of a potential barrier on the path of movement of the interphase boundaries. This is possible, for example, in the case of formation of the oxygen vacancies during the stabilisation of zirconia by the oxides of metals with the valency of the cations lower than that of zirconia. For example, with addition of yttrium oxide, one oxygen vacancy forms per two $Y^{3+}$ ions:

$$(1-x)ZrO_2 + xY_2O_3 \leftrightarrow Zr_{1-x}Y_xO_{2-x/2} + V^o_{x/2}$$
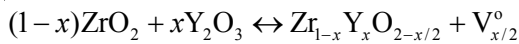
For better understanding of the processes of fully amorphous phase transformations in the solid solutions based on zirconia and the processes of phase formation in synthesis from melts of materials based on zirconia, it is essential to examine certain special features of the martensitic phase transitions.

## Crystallography and energetics of martensitic transformations

The crystallographic characteristics of the martensitic transition are the strict orientation relationships between two lattices: the habit form of the martensitic lath and the macroscopic form of the transformed part of the crystal [9–13]. In a martensitic process, the lattices are conjugated via coherent or semicoherent interphase boundaries.

Conjugation of the phases with different crystal lattices should provide for the mutual accommodation of the lattices [4,5]. The accommodation may result from elastic displacements of the atoms from equilibrium positions and from inelastic displacements due to misfit dislocations and vacancies condensed at the phase boundaries. Only elastic displacements are sources of internal stresses. The magnitude of these displacements is determined by two factors:

1. The mismatch of the crystal lattices of both phases in the contact plane

2. The mechanism of conjugation of the phases, determining the compensation of the mismatch.

A completely coherent phase conjugation is the one in which all crystal planes of one phase change continuously into the planes of

the another phase, thus forming the closed Burgers contour. This conjugation results in the maximum elastic stresses in the crystal.

A semi-coherent boundary forms when the lattices of the contacting crystals are elastically deformed in such a manner that some individual areas are characterised by coherence and other areas by the gradual buildup of the mismatch which is periodically eliminated by resultant breaks. The Burgers contour becomes open. The closing vector *b* is the Burgers vector of the mismatch dislocation. The mismatch dislocations consequently decrease the level of internal stresses [11].

The coherent conjugation forms in an early stage of the transition when the stored elastic energy is still insufficient for the formation of a mismatch dislocation. The increase in the size of the inclusion creates suitable conditions for the semi-coherent conjugation mechanism.

Polycrystalline materials and fine-grained ceramics (and also materials produced by means of nanotechnologies) may be characterised by the presence of completely non-coherent conjugation in which there is no friction between the matrix and the inclusion resulting in the failure of the material by the mechanism of intergranular sliding.

Khachaturyan [5] developed a theory which makes it possible to predict, on the basis of crystallographic and energetics relationships, the morphology of particles of the second phase, formed in the habit plane of the crystal matrix. The optimum form of the inclusion is determined by the opposite effects of two components of energy: volume and surface. In a general case, the form of the inclusion is determined by competition between the energy of elastic distortions, which is minimum for the infinitely thin and elongated plate, and the surface energy, minimum for the equilibrium form. In cases in which the contribution of surface tension is dominant, the equilibrium form of the plate in the habit plane is a circle, if the elastic energy is dominant, the plate is needle-shaped, representing in fact an infinitely prolate ellipse. In intermediate cases, inclusions have the form of a less prolate ellipse.

**Hysteresis of the martensitic phase transition**

The change of the volume during the $m \leftrightarrow t$ transition ($m \leftrightarrow t$ – compression, $t \leftrightarrow m$ –expansion) indicates that this transformation is the transition of the first type. In this case, the classic theory
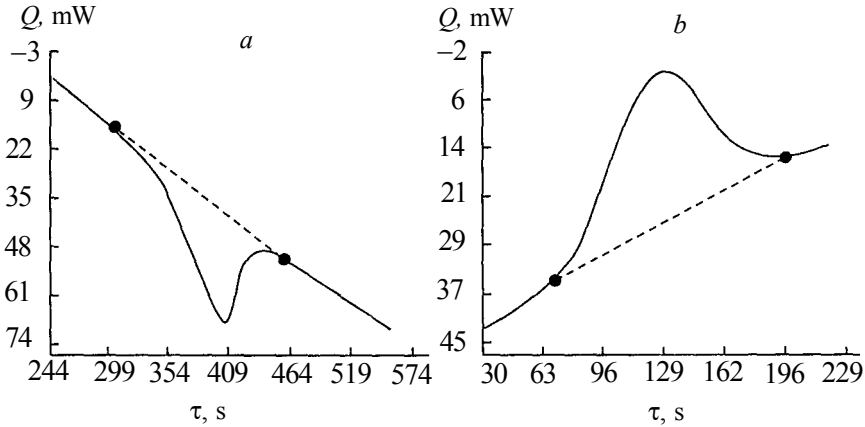
**Fig. 8.1.** Curves of differential scanning calorimetry of direct (a) and reversed (b) transirions of $ZrO_2$ crystals [19]

of allotropic transformations does not permit the existence of a transition with a temperature hysteresis.

The reason for hysteresis is assumed to be the change in the free energy of the crystal during the $m \leftrightarrow t$ transition [14–16]. From this viewpoint, the most probable case of a hysteresis is the stresses formed by a sudden change of the volume during the phase transition. For example, the introduction of the energy of the residual stresses into the equation for the internal energy of the phase decreases the temperature of the direct transition and increases that of the reverse transition.

The transformation temperature depends to a greater degree on the surface energy. The size of the particles (~100 Å), below which the transformation to the tetragonal modification is supported by the difference if the free energy of two polymorphous modifications, has been determined in [17]. In the determination of the critical size of the particles the potential energy of elastic deformation was not taken into account because it was assumed to be very small in comparison with the surface energy.

It was also assumed that the hysteresis is determined by different degrees of perfection of the structure of individual crystals present in the specimen [18, 19]. However, the existence of a hysteresis in single crystals shows that this cannot be the main reason.

**Kinetics of the martensitic phase transition**

The majority of martensitic transformations are characterised by

athermal kinetics. The degree of transformation in this case is determined only by temperature and is almost completely independent of time [6, 12–18].

The athermal kinetics is evidently determined by the expression which does not include the time *t*:

$$\xi = A \cdot \exp\left(-\Delta\Gamma_A / RT\right),\tag{8.1}$$

Here $\xi$ is the degree of transformation, *A* is the pre-exponential multiplier, $\Delta G_A$ is activation energy (for the case of a non-ideal interphase boundary).

These kinetic special features of the martensitic transformation are valid for the ideal crystal. In the real conditions, the transition is accompanied by plastic deformation or failure: martensite crystals are stress concentrators and areas of plastic failure. Some differences in the description of the experimental kinetics of the martensitic transformation are associated with the difficulties of fulfilling the isothermal conditions in the examination of the transition and with the effect of the inhomogeneous distribution of components in the crystals.

As a result of the martensitic phase transformation, the material is hardened. During the phase transition, the stored energy (elastic, surface, energy of defects) increases and the effect of dissipative forces, associated with the irreversible scattering of energy during the movement of the interphase boundary and dislocations in a medium with defects, becomes stronger. To overcome this 'friction' and for further development of the transition, it is necessary to increase constantly the thermodynamic driving force. This results in hardening of the material.

There are two qualitatively different types of kinetics of phase transformations in single-component crystalline solids. Depending on the external conditions, the same phase transition may take place at a high rate (of the order the speed of sound) which depends on temperature only slightly (for the majority of martensitic transformations) or exponentially. In the latter case, the transformation is limited by the diffusion kinetics of 'settling' of the vacancies at the interphase boundaries and by their reversed dissolution. The diffusion kinetics is observed in cases in which the crystal initially contains a large amount of the martensitic phase. The self-diffusion kinetics of the transformation does not exclude the crystallographic and morphological relationship of the initial and

new phases, in particular, a transformation may be accompanied by macrodeformation and the formation of a relief.

Attention should be given to the resultant contradiction between the diffusionless nature of the martensitic transformation and the presence of the two-phase region on the *T–x* diagram, where the composition of the phases should change in accordance with the lever rule. This is associated with the fact that the phase diagram is plotted without considering elastic stresses. A metastable (from the viewpoint of equilibrium thermodynamics) phase is actually stable. This may be accompanied by the formation of intermediate phases which are not reflected on the *T–x* diagram. This fact is confirmed by the existence of a large number of contradicting data on the phase composition of the ceramics and single crystalline materials based on zirconia and its dependence on the synthesis conditions. For example, the existence in single crystals of a 'frozen' tetragonal phase at concentrations of ~(1–2) mol% $Y_2O_3$ was explained by the fact that the rearrangement of the structure in the single crystal is more difficult in comparison with that in fine-dispersion powder in which the chain of the atoms, undergoing the transformation, breaks up on the surface of the particle. Therefore, the stresses do not reach high values, and the volume of the individual grains increases as a result of a decrease of their porosity. In contrast to the powders, the single crystals split up during transformation because the simultaneous breaking of a large number of atomic bonds may take place only at high energy losses $\Delta G_{t \rightarrow m}$. For example, the latter phenomenon takes place in the case of strong supercooling of a substance in relation to the phase transition temperature. As the crystal becomes more perfect and larger, the strength of its chemical bonds increases and the phase transition requires very high supercooling up to the complete freezing of the structure.

The data on the kinetics and thermodynamics of the phase transitions in PSZ crystals, grown from the melt, are very scarce. The kinetics of the $m \rightarrow t$ transition has a significant effect on the degree of stabilisation of the tetragonal phase because the possibility of quenching of this phase depends on the synthesis conditions. The authors of [19] investigated the $m \rightarrow t$ phase transitions in the crystals of PSZ in relation to the concentration of the stabilising oxide. The curves of differential-scanning calorimetry (DSC) for direct and reverse transitions of pure zirconia are shown in Fig. 8.1 [19] and were used to calculate the enthalpy of phase

**Table 8.1.** Thermal effects of the $m \rightarrow t$-phase transition and the content of the monoclinic phase in crystals*

| $x$ | $\Delta H$, J/g | Content of the monoclinic phase, wt.% | |
|---|---|---|---|
| | | DSC | XPA |
| 0.000 | 39.16 | 100 | 100 |
| 0.0086 | - | 59 | 100 |
| 0.0178 | 7.28 | 18.6 | 36 |
| 0.020 | 4.74 | 11.5 | 28 |
| 0.0234 | 3.03 | 7.5 | 21 |

*Evaluation on the basis of the results of DSC and XPA analysis

transitions (Table 8.1). In the case of zirconia crystals, the calorific effect of the direct and reverse transitions differs only slightly ($\Delta H_{m \rightarrow t}$ = 4.92 kJ/mol), being in the range of the experimental error and in good agreement with the literature data: 4.75 and 5.95 kJ/mol [20].

The experimental DSCdata on the calorific effects of transitions were used for the quantitative evaluation of the phase composition of specimens with different contents of the stabilising agent.

The amount of the monoclinic phase in the specimen of the given composition is determined by the $C_M = \Delta H / \Delta H_{ZrO2}$ relationship, where $\Delta H_{ZrO2}$ is the enthalpy of transition in pure zirconia (100% of the monoclinic phase), $\Delta H$ is the enthalpy of transition in the given specimen. The calculated concentrations are presented in Table 8.1. [19] This Table also gives the results of the quantitative evaluation of the phase composition of the specimens obtained by x-ray diffraction analysis of powders of refined crystals. Incomplete agreement in the data on the phase composition of the specimens evidently indicates that the refining of the crystals increases the content of the monoclinic phase in the specimen.

The characteristic feature of partially stabilised zirconia crystals produced from the melt is the formation of the cubic crystallographic system during crystallisation. Subsequent phase transitions take place in the solid phase. The initial composition, the rate of growth and cooling of the crystal and the annealing conditions determine the mechanisms of formation, the quantitative ratio of these phases and the degree of deviation from the thermodynamically equilibrium

state, corresponding to the phase diagram.

With an increase in the content of $Y_2O_3$ in the crystals, the temperatures of the $m \rightarrow t$ phase transitions decrease but do not coincide with the temperature range of the two-phase region ($m + t$) of the corresponding composition on the equilibrium diagram. This may be associated both with changes of the specimen composition and with the metastable state of the specimens: in transition through the two-phase range ($t + c$) in the process of synthesis (cooling) of the crystal, diffusion processes are incomplete and strongly depend on the cooling rate. This results in a change in the content of $Y_2O_3$ in the tetragonal phase (a decrease in comparison with the initial value) and the temperature of the phase transitions becomes higher than the temperatures corresponding to the initial composition on the equilibrium diagram.

On the basis of kinetic data, one can propose the following model of the process taking into account analysis of the phase transformations. The process may be regarded as a two-state process, consisting of the nucleation of a new phase and movement of the interphase boundaries. The limiting stage of the direct transition in pure zirconia is the nucleation stage. The initial parts of the kinetic curves are flat. During the formation of nuclei of the tetragonal phase, the interphase boundaries start to move at a high speed. This rapid movement is possible only within the limits of a specific zone of the crystal where the conjugation of the phases is coherent. A new act of nucleation is required in areas with a mismatch dislocation or a microcrack. This pattern is usually observed on a crystal with a low content of $Y_2O_3$ ($x = 0.005$) where the relief associated with the phase transition forms in different parts of the crystal and rapidly propagates within the limits of these areas. The rate of phase transition in the crystal is higher in comparison with the powder. This is associated with the fact that the crystal requires a smaller number of nuclei in comparison with that in the powder because in the powder one nucleus may cause a transition only within one grain.

It is evident that after completion of the $m \rightarrow t$ transition, the specimens consist of 100% of the tetragonal phase and in the reverse transition the nucleation process is always homogeneous and slow. In addition, mismatch dislocations and microcracks appear. The movement of the interphase boundary during the reversed transition is of the dissipative nature. Therefore, the reversed transition is slow in all specimens.

With an increase in the content of the stabilising oxide $x$ (mol) the concentration of vacancies increases and the rate of transition drops. The effect of oxygen vacancies on the kinetics of direct and reverse transitions is confirmed by the data on the kinetics of phase transitions in the specimens in which vacuum annealing results in the formation of additional vacancies. The slowdown of the direct transition is very marked, whereas in the case of the reversed transition it is less pronounced. As a result of annealing the hysteresis range becomes smaller and the same takes place with an increase in the content of the stabilising agent.

According to the theory of martensitic transformations, the main dissipative process during the displacement of the boundaries is the diffusion of vacancies. Transformation is limited by the 'settling' of vacancies (dissolved in the crystal) on the interphase boundaries and by the 'dissolution of the deposit' reversed process. If the crystal contains a large number of dislocations, acting as sources and sinks of the vacancies, there is no significant deceleration in the process and equilibrium is established very rapidly. However, if prior to the start of the phase transition the crystal contains a large amount of the new phase (for example, in specimens with $x = 0.02$ or $x = 0.0234$), the role of the dislocations in the establishment of equilibrium becomes less and less important, and the kinetics is controlled by self-diffusion interaction between the particles of the new tetragonal phase through the monoclinic phase. The self-diffusion process is far slower in comparison with the conservative movement of the boundary, limited by the removal of heat. Of all the examined specimens, only the specimen with $x = 0.0234$ could be quenched because with an increase in the content of the yttrium oxide the number of vacancies increases and the rate of the $t \rightarrow m$ transition greatly decreases.

The results of examination of the phase transitions in the $ZrO_2$–$Y_2O_3$ crystals show that:

1. The increase in the concentration of the stabilising oxide decreases the temperatures of the $m \rightarrow t$ and $t \rightarrow m$ transitions and the magnitude of the temperature hysteresis;

2. The kinetics of the $m \rightarrow t$ phase transformations in the crystals of partially stabilised zirconia depend on the concentration of the stabilising oxide and may be limited by both the stage of nucleation (for the pure zirconia crystal) and by the stage of movement of the interphase boundary (at $x > 0.02$); the maximum rate of transformation is recorded for the crystals with the composition $x = 0.0086$;

3. The $t \to m$ transition is characterised by homogeneous nucleation which also determines the rate of the transition;

4. At $x > 0.0234$, the crystals of partially stabilised zirconia did not contain any monoclinic phase, as established by the differential–thermal analysis method.

Differential–thermal and dilatometric analysis methods we used for the determination of the temperature ranges of transformations in the $ZrO_2$–$R_2O_3$ crystals (where R is Eu, Gd, Yd), Table 8.2 [21].

## 8.2. THE PHASE COMPOSITION OF THE CRYSTALS OF PARTIALLY STABILISED ZIRCONIA

The results of phase analysis of the synthesised specimens of the crystals of partially stabilised zirconia by the methods of x-ray diffraction analysis, crystallo-optical method and the Raman scattering method were presented previously in Chapter 7. It should be mentioned that in grinding the specimens, the phase composition of the specimens changed and the monotonic phase appeared in the specimens with 3 mol% $R_2O_3$, indicating the metastability of these materials and the presence in them of a transformed tetragonal phase [22].

The x-ray diffraction examination of the phase composition of the crystals of partially stabilised zirconia shows that the monoclinic phase is present in the specimens with the concentration of the stabilising oxide to ~2–2.3 mol% $Y_2O_3$; the crystals containing 3–4 mol% $Y_2O_3$ contained mainly the tetragonal phase. The structural characteristics of the crystals of partially stabilised zirconia are presented in Table 8.3.

The monoclinic phase formed only in certain cases in the upper part of the crystals of this composition. Evidently, at concentrations of < 1.5 mol% $Y_2O_3$, the tetragonal phase, detected at room temperature, was represented by the $t'$-phase, formed from the cubic phase, and the M-phase, formed from the $t$-phase. At a concentration of ~3–4 mol% $Y_2O_3$ and higher, the breakdown of the cubic phase, accompanied by the diffusion of the cations did not lead to the formation in the crystals of the $t$-phase with a low concentration of $Y_2O_3$, where further cooling would have been accompanied by the $t \to m$ transition. Only in individual upper regions of the crystals, absorption of the yttrium oxide by the inclusions of the second phase resulted in a decrease of the local concentration of $Y_2O_3$ to the limit at which both transitions $c \to t'$ and $t \to m$ take place.

**Table 8.2.** Temperature ranges of phase transitions in $ZrO_2$–$R_2O_3$ crystals (R – Eu, Gd, Yb)

| Composition of crystal | Content of stabilizing oxide | Transition temperature | |
|---|---|---|---|
| | | heating | cooling |
| *Differential thermal analysis* | | | |
| $ZrO_2$–$Eu_2O_3$ | 1 | 800 | 730 |
| | 2 | 670 | 600 |
| | 3 | 640 | 460 |
| $ZrO_2$–$Gd_2O_3$ | 1 | 880 | 800 |
| | 2 | 650 | 520 |
| | 3 | 520 | 400 |
| $ZrO_2$–$Yb_2O_3$ | 1 | 900 | 780 |
| | 2 | 620 | 470 |

*Dilatometric analysis*

| | mol % | $m \to t$ | | | $m \to t$ | | |
|---|---|---|---|---|---|---|---|
| | | $t_s$, ºC | $t_f$, ºC | $\Delta t$ | $t_s$, ºC | $t_f$, ºC | $\Delta t$ |
| $ZrO_2$–$Eu_2O_3$ | 1 | 780 | 900 | 120 | 900 | 400 | 320 |
| | 2 | 640 | 740 | 120 | 620 | 300 | 320 |
| | 3 | 520 | 660 | 140 | 1460 | 200 | 200 |
| $ZrO_2$–$Gd_2O_3$ | 1 | 890 | 900 | – | 900 | 800 | – |
| | 2 | 550 | 650 | 100 | 520 | 250 | 270 |
| | 3 | 480 | 600 | 120 | 400 | 280 | 120 |
| $ZrO_2$–$Yb_2O_3$ | 1 | 820 | 900 | | 780 | 500 | 280 |
| | 2 | 480 | 620 | 140 | 470 | 300 | 240 |

When examining the phase formation in the $ZrO_2$–$Ln_2O_3$ systems (where Ln = Y, Eu, Gd, Yb), quenched from the melt and crystalline specimens in the range of concentration of the stabilising agents 0–8mol% by the Raman scattering method in [22], the authors

**Table 8.3.** Characteristics of crystals of partially stabilized zirconia (PSZ)

| Composition ZrO₂–3 mol %Y₂O₃–0.3 mol % CeO₂ | | Colour | Heat treatment after growth | | Growth direction [hkl] of phase T | Phase composition | | Parameters of phase T, Å | | Size of mosaic blocks, nm | |
|---|---|---|---|---|---|---|---|---|---|---|---|
| $Y_2O_3$ | $CeO_2$ | | $T$ °C | $\tau$, h | | T | M | $a$ | $c$ | T | M |
| 3 | 0.3 | Red | | | 111 | 57 | 43 | 5.091 | 5.167 | 200 | 115 |
| 3 | 0.3 | Crimson | | | 111 | 71 | 29 | 5.091 | 5.167 | 81 | 78 |
| 3 | 0.3 | Gray | 1600 | 2 | 111 | | | 5.105 | 1.152 | 260 | >500 |
| 3 | | White | | | 331 | 61 | 39 | 5.090 | 5.166 | 67 | 243 |
| 3 | | Black | 2200 | 2 | 111 | | | 5.108 | 5.157 | >500 | 263 |

proposed two mechanisms of phase formation, depending on the synthesis conditions:

1. The tetragonal T-phase forms in the volume of the initial cubic solid solution as a result of the high mobility of the ions in accordance with equilibrium diagram of the $ZrO_2$–$Ln_2O_3$ systems. In the nuclei of the T-phase, the concentration of the stabilising oxide should change rapidly in relation to the initial concentration and may greatly differ from it. The remaining volume is enriched with $Ln_2O_3$ which may stabilise the cubic structure of the solid solution up to room temperature. If the increase of the concentration of $Ln_2O_3$ cannot prevent the $c \rightarrow t$ phase transition, two tetragonal phases $t$ and $t'$ form in the specimens, and the impurity concentration in the $t'$-phase is higher than the initial concentration and is characterised by a low value of the tetragonal shift in comparison with the t phase. Thus, the t-phase forms in the initial stage, and the $t'$-phase forms with a further decrease in temperature. The probability of this mechanism of phase formation decreases when the temperature is reduced to 1000–1200°C, because a large decrease in the diffusion rate complicates the nucleation process of the T-phase.

2. The formation of phases at temperatures below 1200°C (i.e. below the temperature of the $c \rightarrow t$ phase transition for the concentration of the stabilising oxide of 0–10 mol%) results in the formation of domains of the tetragonal phase without participation of the diffusion processes. The concentration of the stabilising agent in this case is close to the initial concentration. The concentration of $Ln_2O_3$ and the dimensions of the domains may vary subsequently during annealing and depend on the temperature and duration of the process.

On the basis of the examined phase formation processes it may be concluded that both mechanisms operate in directional

solidification of the melt in different stages of synthesis. For example, the mechanism of type 2 is controlling in growth from small volumes of the melt at high cooling rates of the crystals of ~400°C/min in the $ZnO_2$–$Ln_2O_3$ system. For the $ZrO_2$–(7–9)mol% $Gd_2O_3$ ($Eu_2O_3$) compositions, this mechanism results in the synthesis of transparent single crystals. The crystals contain *t*-domains, strictly oriented along the axis of the fourth order, with the concentration of the stabilising oxide of 2.5 mol% $Gd_2O_3$ ($Eu_2O_3$). These crystals are characterised by birefringence. This effect is not detected in the crystals of $ZrO_2$–$Ln_2O_3$ (Ln – Y, Yb, Lu) with the same concentration of $Ln_2O_3$, in which the T-phase disappears at the concentration of the stabilising oxide of ~6 mol%. This difference may be associated with different temperature ranges of existence of the phases in the crystals with different stabilising agents.

## 8.3. PRODUCTION OF CRYSTALS OF PARTIALLY STABILISED ZIRCONIA

The crystals were grown in equipment of series Kristall from large cold crucibles. The rate of growth of the single crystals was varied in the range (1–50) mm/h, the cooling rates, depending on the size of the crystal, were 4–250 °C/h [19].

For applications in practice, it is necessary to prepare large homogeneous single blocks of material without cracks. For this purpose, investigations were carried out into the effect of the initial composition and growth conditions on the physicomechanical properties and the size of the crystals. The range of the concentrations of the stabilising oxide (yttrium) characterised by the minimum number of cracks, formed after completion of crystal growth, was determined.

For example, at $Y_2O_3$ concentrations of ~0.5–2 mol%, the crystals were mat, oblique, with a large number of microcracks resulting from the tetragonal–monoclinic transition during cooling of the crystal after growth. Examination also showed the presence of a large number of macrocracks, formed as a result of thermal shocks during rapid stoppage of heating of the melt.

When the concentration of $Y_2O_3$ was increased from 2.5 to 5 mol%, the crystals were of the white milky colour, with the shiny or slightly mat surface; cracks formed mainly as a result of thermal shocks and growth residual stresses.

The increase of the yttrium oxide content above 5 mol% supported the formation of semi—transparent crystals with strong opalescence and a large number of growth cracks. Evidently, this is associated with an increase of the content of the cubic phase which does not have high strength characteristics. Inclusions of the resultant tetragonal phase caused high stresses in the cubic lattice.

At $Y_2O_3$ concentrations of (7.5–8) mol%, the number of cracks again decreased to the value typical of this method, the crystals were slightly opalescent, and examination in crossed polarisers showed the conoscopic pattern characteristic of strong stresses in the crystal (Chapter 6). Evidently, this is associated with a small content of the 2nd (tetragonal–pseudocubic) phase and the fact that the parameters of this phase were similar to those of the cubic lattice. The number of cracks was also affected by additional dopin with third impurities (Ce, Nd, Tb, Co, etc.).

The technological conditions of production of large crystals of partially stabilised zirconia were selected taking into account the dependence of the size of the crystals on the initial composition of the melt (Chapter 4). In the growth of crystals with low concentrations of the stabilising oxide, a decrease in the rate of crystallisation has almost no effect on the size of the crystals. To obtain large crystals, it is necessary to increase the distance between the solidification front and the front of the phase transformation. This was achieved by using a lower thermal screen which decreases the vertical temperature gradient in the growing crystal (Chapter 4). A second variant of technology is also possible in which the phase transformations take place only after completion of the growth process.

Large crystals of partially stabilised zirconia were grown using a seed crystal in the central part of the ingot. They showed no cracking during cooling. This technology was used to produce large single crystal blocks with a size of up to 40 mm in the cross-section and up to 120 mm long. The crystals of partially stabilised zirconia are presented in the insert.

## Distribution of the stabilising oxide in the crystals of partially stabilised the zirconia

Many mechanical and physical properties of partially stabilised zirconia depend on the chemical composition of the material. The heterogeneity of the distribution of the components of the solid

solution may result in the heterogeneity of the properties in the volume of the crystal. Therefore, the determination of the chemical composition and the distribution of the main and stabilising oxides along the length of the crystal are important characteristics of the material.

The composition was determined by x-ray spectrometric microanalysis. Figure 8.2 [19] shows the curves of distribution of yttrium oxide in the crystals of $ZrO_2$–(1.5–4)mol%$Y_2O_3$ along the growth axis.

There are several special features in the distribution of stabilising oxide:

–the characteristic decrease in the concentration of yttrium oxide towards the end of growth by 25–40%;

–the presence, on the distribution curves, of 'concentration waves' associated with the instability of the process of crystallisation, caused by concentration supercooling; the amplitude of these oscillations reaches 4–5% of the mean concentration in the crystal;

–the local (in areas ~100 μm in size) oscillations of the composition of the crystals with a low concentration of yttrium; at a concentration of 1.5 mol% $Y_2O_3$ in the initial charge, local deviations from the mean values may amount to ~25% and they are concentrated in the upper part of the crystal, corresponding to the final stage of growth (Fig. 8.2). Such deviation may be related to the phase transformations taking place during cooling of the crystals in the process of growth. At high temperatures of phase transformations (~2000°C) diffusion processes of the redistribution of yttrium between the cubic and tetragonal phases can occur in
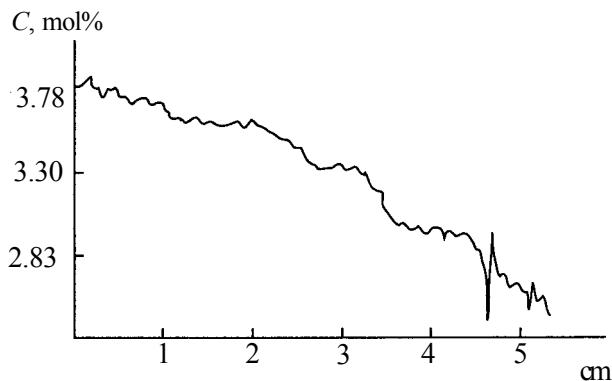


**Fig. 8.2.** Distribution of yttrium oxide in $ZrO_2$–3 mol.% $Y_2O_3$ crystals.

the solid phase. At low yttrium concentrations, the distribution coefficient is higher than unity and, consequently, the upper part of the crystal is depleted in this component and this increases the temperature of phase transformations. A decrease in the yttrium concentration is also supported by the presence in the melt of several impurities with a high chemical affinity for the yttrium oxide, such as: $SiO_2$, $Al_2O_3$, $TiO_2$, etc.

## 8.4. THE DOMAIN STRUCTURE OF CRYSTALS OF PARTIALLY STABILISED ZIRCONIA

The transition of the cubic to the tetragonal phase is accompanied by the formation of the domain structure in the crystal [23, 24]. The structure of the resultant domains are determined by the symmetry of the interacting phases, the initial cubic and ferroelastic tetragonal phases ($t'$). The domains in the crystals with 3 mol% $M_2O_3$ are distributed along the <001> direction in the {001} habit plane and their minimum size is 50 nm [23].

A detailed examination of the domain structure of the tetragonal phase was carried out in [25]. The results show that the individual domains form colonies distributed in the irregular structures in the form of 'fir trees' [26]. The spatial distribution of the colonies of the domains in tetragonal zirconia differ from the distribution in the partially stabilised zirconia where they are implanted in the uniform cubic matrix [27]. In the $t'$-phase of zirconia, the domains fill the entire volume and the spatial distribution of the domains should be highly symmetric for the minimisation of the energy of coherent strains. In order to confirm the mechanism of the formation of the $t'$ phase, the crystals were reheated to the temperatures of the stability of the cubic phase at 2150°C for 10 min and then quenched [25].

In tetragonal zirconia, there are three variants of the domains with the axes parallel to the axes of the cube of the initial phase [28]. The c axis is parallel to the axes $a_1$, $a_2$, $a_3$ of the cubic matrix. They are denoted by $t_1$, $t_2$, $t_3$ in accordance with the c axes of the cubic matrix, parallel to [100], [010], [001]. These domains form ordered colonies consisting of two alternative variants of the domains, separated by the habit planes {110}, which are at the same time the twinning planes of both variants. Each colony consists of the pairs $t_1/t_2$, $t_1/t_3$ or $t_2/t_3$. The appropriate designation of these colonies is $c_1$, $c_2$, $c_3$. For each pair (for example $t_1/t_2$) there are
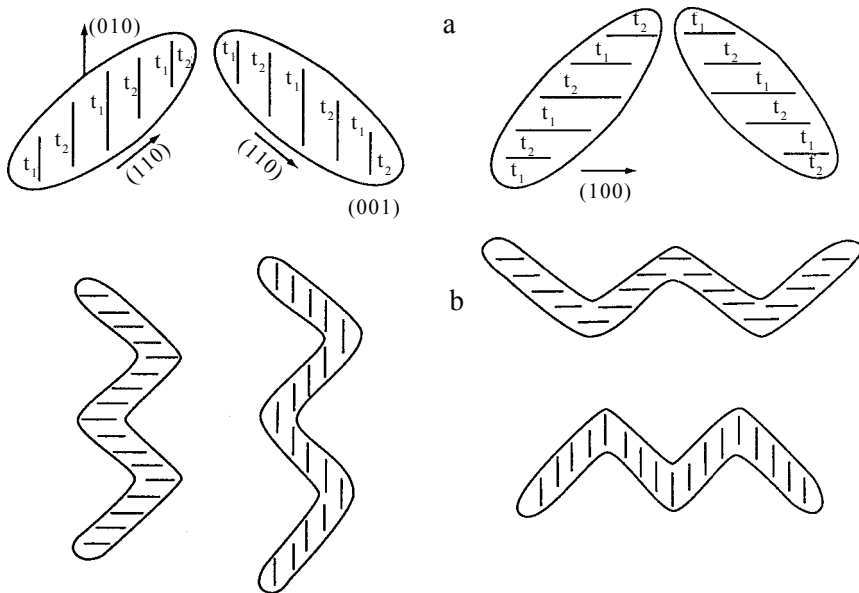
**Fig. 8.3.** Scheme of four variants of colonies in the (001) plane formed by domains $t_1$ and $t_2$ (a) and variants of 'fibres' of inclusions formed by four variants of colonies (b) [28].

four possible variants of colonies, including two twinning planes {110}, as shown in Fig. 8.3a.

Each pair of the domains in combination with two types of the twinning planes may form four types of colonies. Six twinning planes with three variants of the domains form 12 types of colonies.

In the $t'$-material, the colonies occupy the entire volume, are close to each other and form a regular structure. All colonies are arranged in the same manner, namely, they border with each other only by the {110} planes and are elongated along the <111> directions which are lines of intersection between the boundaries of the colonies. Three external planes of the colonies are situated under an angle of 60°. In all cases, one type of the domains of the colony at the boundary borders with approximately the same type of colony (for example, $t_1$), whereas other two types of domains (for example, $t_2$, $t_3$) border on the {110} plane which is the twinning plane (Fig. 8.4).

Different types of the structure of the colonies in the cross sections are produced by the single microstructure. The colonies may be connected along the <111> edge, completely filling the volume of the crystal. This geometry is shown in Fig. 8.5 (1). For the single variant of the domain structure to extend to the adjacent colony, and to ensure that in the following layer the domains border
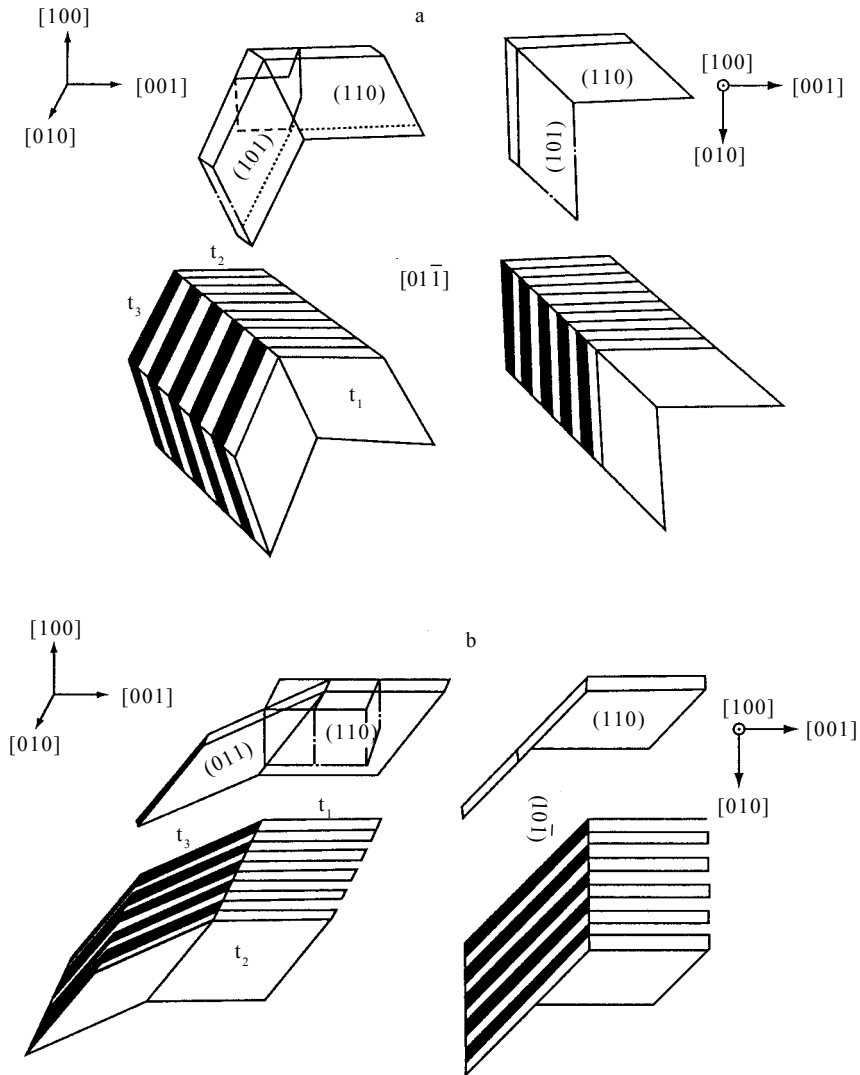
**Fig. 8.4.** Morphology of three variants of plate-shaped domains inclined in relation to the longitudinal axis of the colonies [28].

with the twinning planes and form the three-dimensional structure, the colonies should be linked in a unique manner. Analysis of the structure shows that three colonies are not in accurate contact along the <111> direction, and, as shown in Fig. 8.5 (2) *c, d*, the colonies $c_1$ and $c_3$ are shifted in relation to $c_2$ in the central region. This shift is caused by the shift of the domain $t_3$ of colony $c_3$, in the upward direction. If this shift is equal to the domain distance in the direction [111], the domain $t_3$ in $c_3$ of the lower level, Fig.

www.iran–mavad.com

مرجع دانشجویان و مهندسین مواد
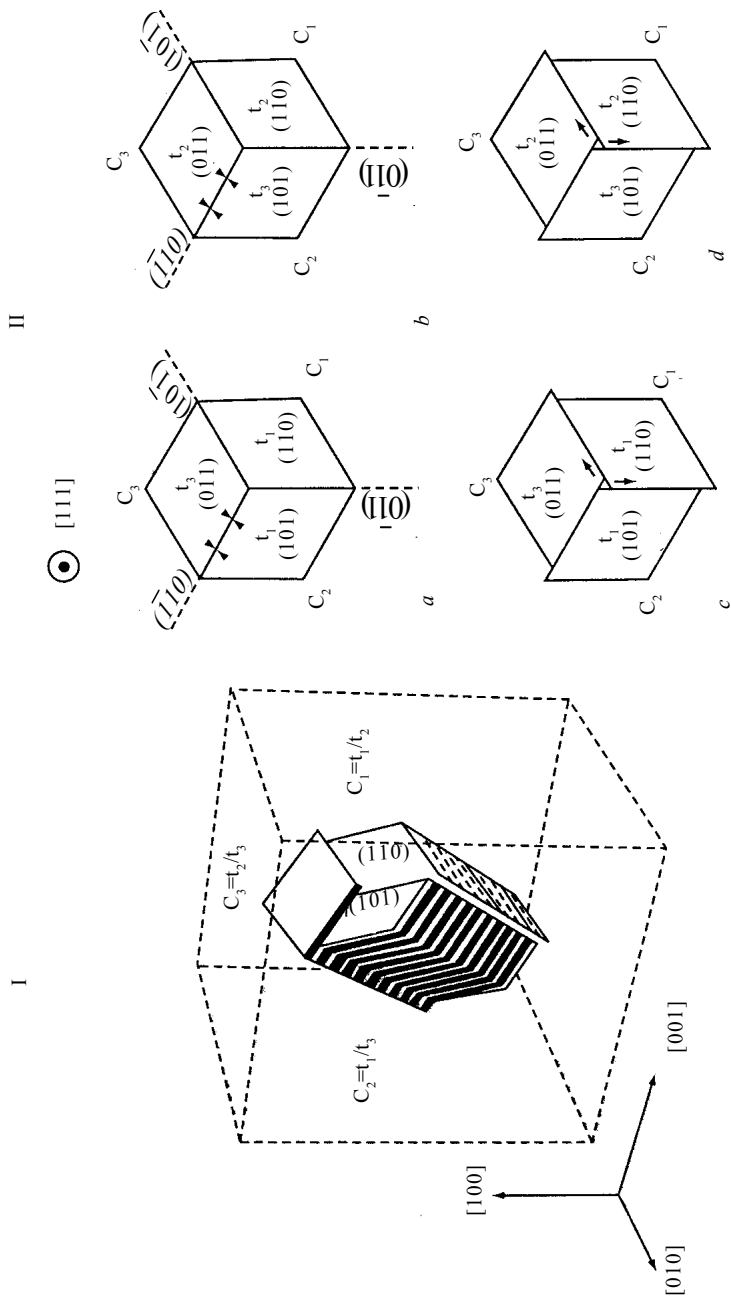
**Fig. 8.5.** Filling of the volume of a tetragonal crystal with domains [29].

8.5 (2)$c$, meets $t_3$ from $c_2$ of the upper level, Fig. 8.5 (2)$c$, and forms a helical structure around the longitudinal axis [111]. In subsequent rotation, $t_2$ from $c_3$ meets $t_1$ from $c_3$. In this case, the boundary of the colonies coincides with the twinning plane (110). The helical structural formations are shown schematically in Fig. 8.5 (1). Low stresses remain at the boundaries of the colonies. In accordance with the proposed model, all the boundary planes, namely the boundaries of the domains and colonies are twinning planes.

The examination of thin anti-phase boundaries between the domains shows that they form arbitrarily from different minimum domains, generating the structure similar to colonies but on a different scale because a structure of the Russian doll 'matryshka' [29].

The formation of colonies and their substructure provides for optimum accommodation of spontaneous stresses, caused by the transition of the cubic phase to the tetragonal phase. In the process of the cubic to tetragonal phase transition, the $c$ axis of the elementary cell is slightly elongated. In the $t'$-phase of $ZrO_2$ with 3 mol% $Y_2O_3$, the degree of elongation is not lower than 1%. This elongation, referred to as the tetragonality parameter, determines the mutual orientation of the $c$-axes of the domains, linked by twinning. The experimental results show that in the internal parts the domains are separated coherently by low-energy twinning planes {110}. Correspondingly, their $c$-axes are not orthogonal in relation to each other and form an angle of 89.4° for 1% of tetragonality.

This specific morphology represents a highly ordered structure, which effectively decreases the stresses formed as a result of the ferroelastic $c \rightarrow t$ phase transition. It should be mentioned that, in many cases, the colonies are distributed more or less without order in space. For example, the colonies are distributed in different directions <111> and are linked with each other. However, in structures that are less regular than the structures of the threefold symmetry, the domains and colonies are always connected by the {110} planes, which are in fact twinning planes, for both the adjacent domains and for the colonies as a whole.

This mutual distribution of the twins and extensive relaxation of the ferroelastic deformation of the alternating layers of different domains and colonies are the basis for the coherence of large macroscopic polydomain crystals.

As mentioned previously, if the concentration of the stabilising

oxide differs from 3 mol% then the crystals contain several phases. For example, it was shown in [30] that crystals with the composition 2.56–6.38 mol% $Y_2O_3$, grown by directional solidification of the melt, represent a matrix — a cubic solid solution with an inclusion of the tetragonal phase whose volume increases with a decrease in the content of yttrium oxide: 30 vol% at 4.2 mol% of $Y_2O_3$ and to 50 vol% at 2.56 mol% $Y_2O_3$.

The authors of [31] investigated specimens containing 4.5 mol% of $Y_2O_3$, produced by crystallisation in the cold crucible, which consisted of the $t'$-$ZrO_2$ (matrix) with a small number of disc-shaped inclusions of $t$-$ZrO_2$ (depleted in the yttrium oxide). These inclusions form during the period of cooling of the crystals after growth. In the course of additional annealing at 1600°C, the matrix continues diffusion separation. This is accompanied by the formation of the inclusions of $t$-$ZrO_2$ with a concentration of the order of 2 mol% $Y_2O_3$, whereas the c-$ZrO_2$ matrix is gradually enriched with the yttrium oxide to the equilibrium concentration of ~7 mol%. In subsequent cooling, the matrix transforms to $t'$-$ZrO_2$. The temperature of the $c \rightarrow t'$ transition differs for different authors [7, 32, 33], possibly as a result of complicated measurements. It is assumed that $T_{c-t} < 200°C$ for the composition $ZrO_2$–3 mol%$Y_2O_3$.

The development of the structure during annealing at 1600°C is determined by the minimum of the deformation energy in the formation of inclusions and by the energy of interaction between the inclusion and the matrix. The inclusions of $t'$–$ZrO_2$ form a structure of plate-shaped 'colonies', where each colony consists of two twinned $t$-$ZrO_2$ variants with the $c$-axis close to 90° and separated by coherent and low-energy habit planes {101}. This specific structure of the inclusions, which effectively minimises the energy of the stresses associated with the formation of inclusions, was investigated by high-resolution electron microscopy [13, 29, 34, 35]. During annealing, the dimensions of the colonies and the space occupied by the plates increased at a rate dependent on the diffusion kinetics. Examination of the annealing process showed that the kinetics of enlargement is controlled by the conventional diffusion-controlled ageing. In this case, the size of the plates increased as a function of $(t_{ann})^3$. The mean size of the plates after annealing at 1600°C for 2–150 hours changed from 15–20 nm to 60–70 nm.

The microstructure of the crystals with the composition $ZrO_2$– 4.5 mol%$Y_2O_3$ may be represented as a mutually penetrating grid of the fibres with a mean radius of 300–500 nm and with a length
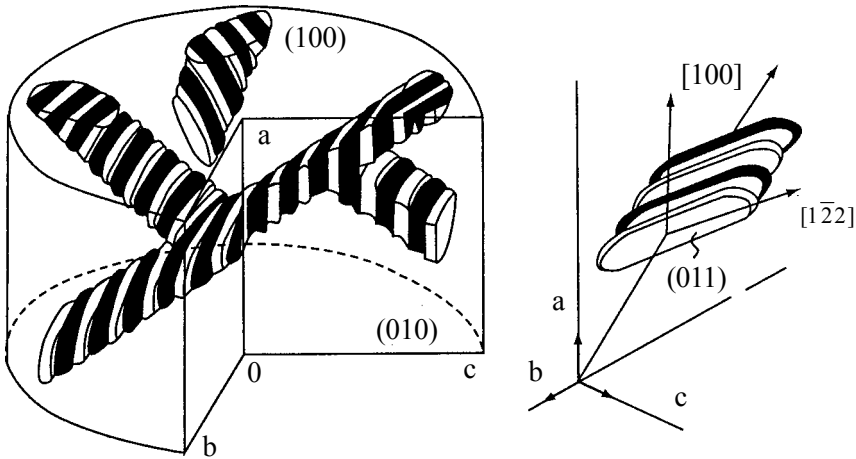
**Fig. 8.6.** Structural model of inclusions in a crystal of partially stabilised zirconia [36].

of several microns, elongated along the three directions <100>. Each fibre consists of continuously bending colonies in relation to the {110} planes.

A similar examination of the structure of the crystals with the composition $ZrO_2$–4.5 mol.% $Y_2O_3$, grown by the method of the floating zone was carried out in [36]. The crystals were grown on a sead crystal oriented in the [100] direction. After growth, the crystals were annealed at 1700°C. Analysis of the experimental results showed the three-dimensional structural model of the inclusions. The main structural unit of the inclusions is a thin sheet with a tetragonal symmetry and approximate dimensions of $3 \times 0.5 \times 0.07$ μm. The structural model is presented in Fig. 8.6.

The concentration of yttrium oxide in the inclusions and the matrix was 1.9 and 4.7 mol%, respectively. The volume of the fractions of the inclusions in the crystal was approximately 70%. This value is in agreement with the estimate obtained from the equilibrium diagram.

The crystals grown in the [100] direction by the floating zone method have a simpler microstructure. The method is characterised by high temperatures gradient along the axis of growth, and in the radial direction, the gradient has the axial symmetry in relation to the growth axis. All the *c*-axes of the tetragonal inclusions were distributed in the plane normal to the growth direction. There were no tetragonal inclusions with the *c* axis parallel to the axis of growth. The field of stresses, generated by these gradients, probably

decreases the number of variants of the microstructure.

The cubic–tetragonal phase transition affects the stress field in the crystal. The main axis of the tetragonal phase can rotate in relation to the axis of the cubic matrix in order to decrease the energy of elastic stresses, associated with the transition. The angle of rotation is 0.48° in relation to the tetragonal axis *a* which is parallel, with the limit of the experimental error, to the growth direction [34]. The direction of growth also corresponds to the axis *a* of the cubic prototype.

## 8.5. THE MICROSTRUCTURE OF PARTIALLY STABILISED ZIRCONIA CRYSTALS

It is well known that the properties of the crystals, including mechanical properties, are closely linked with the real structure of the crystals. The literature contains a large number of studies concerned with the examination of the microstructure of sintered polycrystalline and single crystals of partially stabilised zirconia. Like many other characteristics of this material, the microstructure depends strongly on the composition, synthesis conditions and subsequent treatment conditions. In this chapter, the microstructures of these materials have already been examined. The experimental results show that the material is characterised by a nanosized domain twinned structure. If the specimens consist only of the non-transformed tetragonal phase, the domains with the distribution close to orthogonal form a pseudo-cubic crystal. A matrix phase with inclusion forms in the case of the multiphase composition of the crystal, Because of the small size of the domains and the multilayer nature of the structure, the structure of this type is difficult to examine. Relatively detailed investigations can be carried out only on oriented crystals of partially oriented zirconia using high-resolution transmission electron microscopy. Information on the structure, in particular, on the size of the domains, is also provided by x-ray diffraction analysis.

**The morphology of the crystal surface**

It is well-known that the morphology of the crystal depends on the crystal structure of the given substance and reflects both the solidification conditions and the conditions of subsequent stages of formation of the actual structure of the crystal.

The authors of [19] investigated the morphology of crystals of partially stabilised zirconia by scanning and optical electron microscopy.

In the selection of the specimens for the investigations, special attention was given to the nature of temperature distribution in the diameter of the cold crucible, associated with the special features of the generation of heat in the melt, placed in the high frequency field. This distribution resulted in different conditions of growth of the crystals in the central zone, in the zone adjacent to the wall of the crucible and in the intermediate zone. The cooling conditions are different for dirrerent positions of the crystal in the volume of the melt, especially in the case of the crystals of partially stabilised zirconia from the viewpoint of the formation of its phase composition and microstructure as a result of phase transformations in the solid phase. The smaller the crucible diameter the stronger the conditions of formation of the actual structure of the crystal depend on its position inside the cold crucible. Since this material is of considerable interest for the practical application of the material, the crystals for investigations were grown in large diameter crucibles (> 200 mm). For comparison, investigations were also carried out on blocks taken from the central, intermediate and near-wall parts of a crystal boule.

The examination of the surface of the crystals after growth showed that the crystal morphology depends on the concentration of the stabilising oxide, the presence of third impurities and growth conditions. As an example, Fig. 8.7 shows the growth surface of crystals with different concentrations of the stabilising oxide.

The surface of the growth faces of the specimens of $ZrO_2$–0.5 mol%$Y_2O_3$ after the tetragonal–monoclinic transition shows the typical pattern of twinning of the monoclinic phase with a distinctive irregular network of microcracks at the boundaries of the regions (Fig. 8.7a). The growth of surfaces (Fig. 8.7 b,c) [19] of the $ZrO_2$–(1.0–2.5) mol%$Y_2O_3$ specimens shows clearly microcracks, and the structure contains elements of both the previous specimen and the resultant 'tweed' pattern (considerably finer), characteristic of high yttrium oxide concentrations. For the most relevant region of the yttrium oxide concentration of 2.5–4 mol%, examination showed two characteristic types (type 1 and 2) of the structure of the growth surface (Fig. 8.8) [19].

The surface of any of these types is characteristic either of all faces of the crystal block or of only several faces, or only of a part
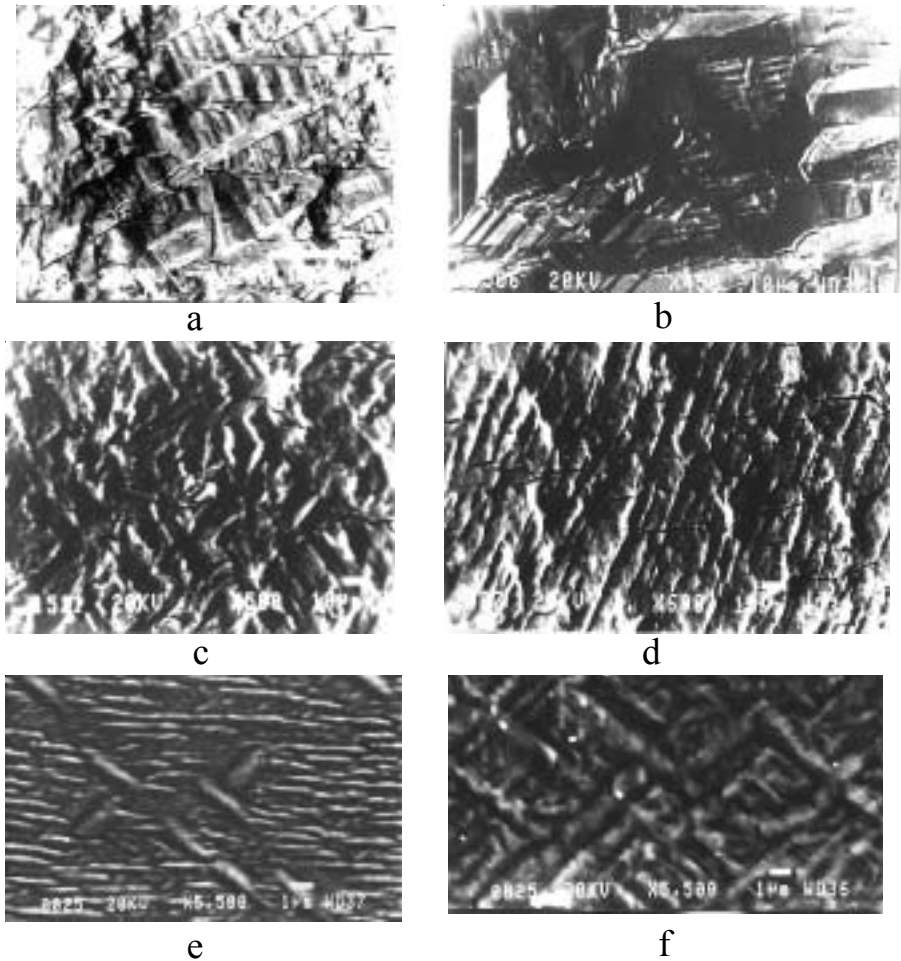
**Fig. 8.7.** Micrographs (a–c) and schemes (d) of three main types of deformation of the surface typical of crystals $(1-x)ZrO_2 \cdot x\ Y_2O_3$, $x = 0.0005$ (type I) (a); $x = 0.010$ (type II) (b); $x = 0.015$ (type III) (c). Magnification: a) 850; b) 500; c)1000.

of one of the faces. The surface of the first type (smooth) is shown in Fig. 8.8*a*, and represents a regular structure similar to the 'tweed' structure. The structure consists of fine (length 1–10 mm, width 0.5–3 μm ) parallel 'rods', distributed in groups. The groups themselves are oriented in relation to each other either under the right angle or under an angle close to 45°.

The structure of the surface of the second type (Fig. 8.8b) is characterised by a more pronounced relief and consists of larger convex 'rods', distributed in parallel (parallelepipeds), with elements
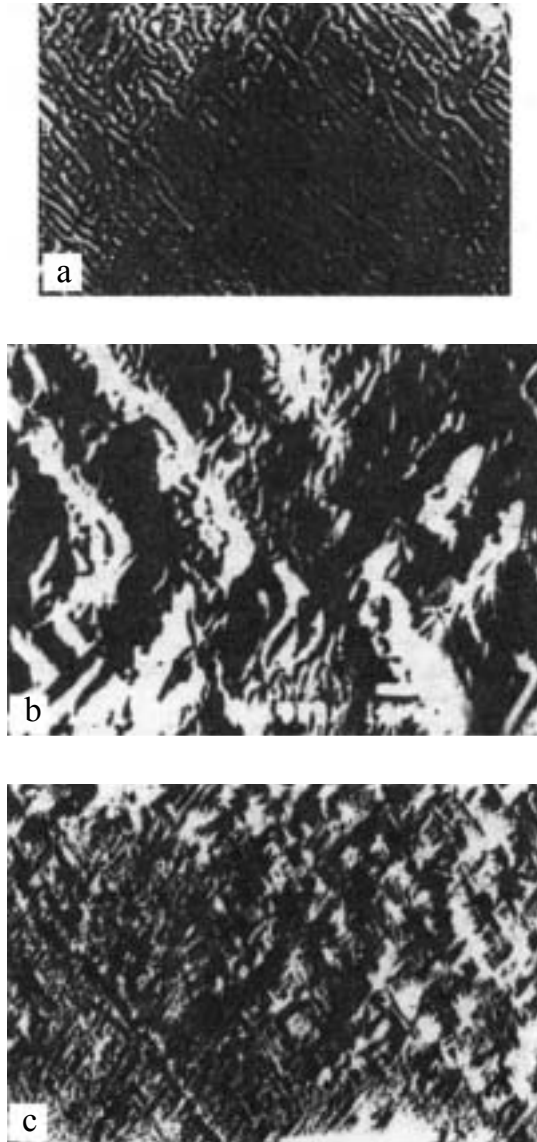
**Fig. 8.8.** Surace of growth faces of $ZrO_2$–2.5–4 mol% $Y_2O_3$ crystals [19]. a: type I – smooth faces; b: type 2 – matt faces; c: boundary of areas with smooth and matt faces.

of up to 50 μm long and more than 5 μm wide. The relief of the structure results in the mat appearance of the faces.

Similar surfaces are often found in the central and lower areas of the grown crystals, and the appearance of these surfaces is determined by the volume of the melt and the length of the crystals.

In this case, the single crystalline blocks often grow into each other and cannot be separated without breaking up the crystal themselves. The nature of the surface is also affected by thermal postgrowth annealing which determines the phase composition and formation of the microstructure.

It is important to note the effect of certain admixtures on the nature of the growth surface of the crystals. With the introduction of the admixtures Tb, Ce, Nb into the crystals of partially stabilised zirconia with an yttrium concentration of approximately 3 mol%, the characteristic appearance of the smooth faces is retained but the dimensions of the structural elements ('rods') greatly decrease. The nature of the structure of the mat faces varies greatly: the structure is characterised by intersections under an angle of 45° with the almost complete absence of perpendicular intersections. The surfaces are characterised by the presence of defects in the form of depressions resembling cracks. The relationship of the microstructure with the mechanical properties of these crystals will be discussed later.

The mat crystals grow when the initial melt contains a relatively large amount of admixtures, with the distribution coefficient considerably smaller than 1. However, in contrast to the pattern discussed previously, the surfaces of these crystals contain a characteristic deposit of the admixtures displaced by the crystal, which is clearly visible in the electron microscope, with the composition identified by the method of x-ray spectral analysis.

In most cases, the microstructure and the defects of partially stabilised zirconia are determined by the method of selective chemical etching [100, 101]. The rate of dissolution depends on the nature of the crystal, the crystallographic orientation of the surface, the presence of defects in the crystal, the composition of the etching agent and the etching conditions. These factors determine the shape of etch pits, the profile of the dissolved surface and also the rate of etching in the areas with defects. For water-insoluble crystals, such as the solid solutions of zirconia, suitable etching agents are acids and alkali.

Hot phosphoric acid is a contrast etching agent for partially stabilised zirconia so that it is possible to examine the microstructure of specimens in a scanning electron microscope.

Etching agents for the detection of the microstructure of the crystals of partially stabilised zirconia include solutions of HF, KOH, $H_3PO_4$. The results of action of these etching agents are

**Table 8.4.** Etching agents for PSZ crystals, etching time and temperature

| Composition of solid solution crystal | Etching agent | Etching temperature and time |
|---|---|---|
| PSZ | Concentrated HF | 20 °C, 5 min. |
| $ZrO_2$–9.4 mol% $Y_2O_3$ | KOH | 500–550 °C, 10–15 min |
| $ZrO_2$–2–14 mol% $Y_2O_3$ | $H_3PO_4$ | 100–300 °C |
| PSZ | HF | 20 °C, 4 min |

presented in Table 8.4 [19]. For selective etching, the best results have been obtained using phosphoric acid. It should be mentioned that after etching a deposit appears on the surface and it can be removed by the effect of HF acid during period of 40 s at room temperature.

The microstructure of the specimens was developed by etching crystals of partially stabilise zirconia in phosphoric acid at a temperature of 280°C for 10–30 min. Figure 8.9 shows the microstructure developed by chemical etching: in the volume of the crystal (a,b), in the cleavage plane (c) and on the growth surface (d). An increase in temperature to 310°C and an increase in etching time result in the formation of chemically polished areas on the surface of the specimens.

When discussing the hardening mechanisms, it was noted that significant factors affecting the strength characteristics of partially stabilised zirconia are the dimensions and morphology of the domains. It has also been noted that these characteristics of partially stabilised zirconia depend on the nature, composition of the solid solutiona and the synthesis and heat treatment conditions.

In order to determine the disorientation of the crystal block, the structure was examined in a two-crystal x-ray diffractometer by the 'tilting' method. The size of the region of coherent scattering was determined on the basis of the broadening of the diffraction maxima: (111), (221) for m- and (111), (222) for the t-phases. The results of the experiments are presented in Table 8.5 [22].

The presented results show that the crystals are characterised by a nanodomain crystalline structure. The dimensions and orientation of the domains depend on the composition, growth and heat treatment conditions.

Examination of the microstructure of the crystals by scanning
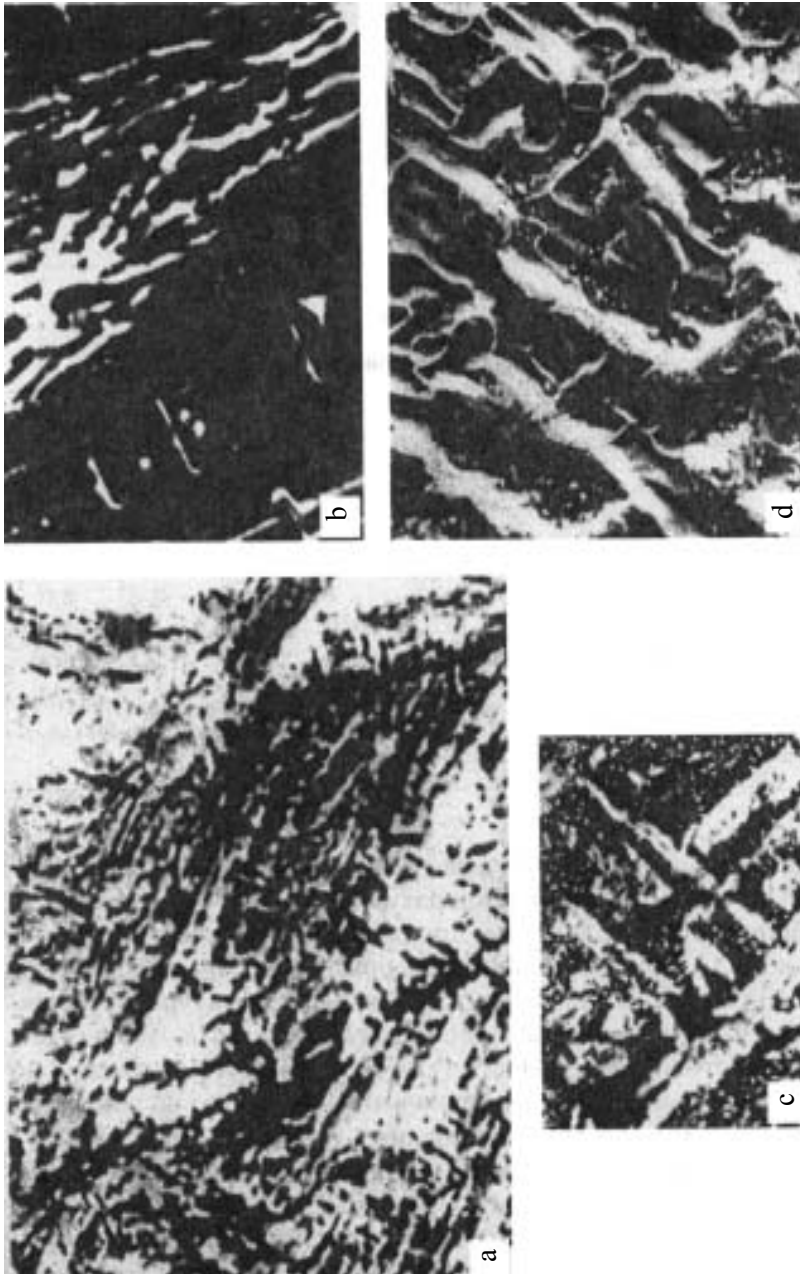
**Fig. 8.9.** Microstructure of crystals of partially stabilised zirconia in the temperature range 200–900°C

**Table 8.5.** Crystallographic characteristics of PSZ materials [22]

| Composition of PSZ crystal | $T$, °C | Growth direction | $\alpha$, deg | $D$, nm |
|---|---|---|---|---|
| $ZrO_2$–3 mol% $Y_2O_3$ | – | [331] | 1–2 | 6.7 |
| $ZrO_2$–2.5 mol% $Y_2O_3$–0.2 mol% $Ce_2O_3$ | | [111] | 2–8 | 20.0 |
| $ZrO_2$–3.5 mol% $Y_2O_3$–0.1 mol% $Ce_2O_3$ | | [111] | 2–8 | 8.1 |
| $ZrO_2$–3 mol% $Y_2O_3$ | 2100 | [111] | 1–2 | 50.0 |
| $ZrO_2$–3 mol% $Y_2O_3$–0.15 mol% $Ce_2O_3$ | 2100 | [111] | 1–2 | 26.0 |

Comment. T is the temperature of postgrowth vacuum treatment ($10^{-3}$–$10^{-4}$ mmHg for 2–10 h); $\alpha$ is the mean misorientation angle in relation to the growth direction; $D$ is the size of regions of coherent scattering.

electron microscopy, chemical etching, and optical microscopy shows that the colonies of the domains are ordered in regular structural formations with the size of several microns whose mutual distribution depends on many factors: the composition of the crystal, the growth conditions, the cooling conditions, thermal stresses, etc.

**The coefficient of thermal expansion of the crystals of partially stabilised zirconia**

The majority of the previously examined characteristics of partially stabilised zirconia were obtained on polycrystalline materials. However, the development of the technology of synthesis of single crystal materials from the melt has expanded the possibilities of examination of the structure, nature and properties of these materials.

Table 8.6 shows the coefficients of thermal expansion of crystal of partially stabilised zirconia.

## 8.6. THE MECHANICAL PROPERTIES OF CRYSTALS OF PARTIALLY STABILISED ZIRCONIA

As regards the properties of the crystals of partially stabilised zirconia, special interest has been attracted recently by the mechanical properties. This is associated with the high strength characteristics of these crystals, in particular, with high cracking resistance of the material (with high fracture toughness). Tables 8.6

**Table 8.6** Coefficients of thermal expansion of PSZ crystals in the temperature range 200–900°C

| Composition of crystal | | $l_0$, nm | $\alpha \cdot 10^6 \, deg^{-1}$ | | | | | | | |
|---|---|---|---|---|---|---|---|---|---|---|
| $R_2O_3$ | mol% | | 200° | 300° | 400° | 500° | 600° | 700° | 800° | 900° |
| $Eu_2O_3$ | 1 | 15.05 | 6.10 | 6.80 | 7.13 | 7.11 | 6.78 | 5.7 | −6.41 | −13.8 |
| | 2 | 47.00 | 7.38 | 8.05 | 8.44 | 7.63 | 5.72 | −27.4 | −28.3 | −23.8 |
| | 3 | 12.2 | 7.49 | 8.94 | 8.05 | 6.38 | -1.61 | −0.92 | 0.55 | 1.8 |
| | 5 | 17.4 | 8.32 | 8.94 | 9.23 | 9.51 | 9.69 | 9.81 | 9.84 | 10.04 |
| $Gd_2O_3$ | 1 | 19.00 | 7.78 | 8.23 | 8.59 | 8.68 | 8.66 | 8.64 | 8.63 | 8.28 |
| | 2 | 42.2 | 6.1 | 6.62 | 6.02 | 4.74 | 0.21 | −9.33 | −6.79 | −4.90 |
| | 3 | 21.9 | 9.16 | 9.66 | 9.89 | 9.92 | 6.92 | 8.74 | 7.85 | 8.28 |
| | 5 | 29.15 | 9.16 | 9.48 | 9.63 | 9.72 | 10.03 | 10.42 | 10.42 | 1.55 |
| | 8 | 32.8 | 8.6 | 9.12 | 9.23 | 9.40 | 9.68 | 9.96 | 10.04 | 0.20 |
| $Yb_2O_3$ | 1 | 18.8 | 9.4 | 9.85 | 10.0 | 9.7 | 9.7 | 9.6 | 8.65 | −21.5 |
| | 2 | 37.00 | 8.13 | 13.45 | 11.89 | 5.12 | −7.6 | −7.75 | −7.1 | −5.21 |
| | 3 | 21.1 | 9.44 | 10.01 | 10.02 | 9.61 | 8.82 | 8.61 | 9.08 | 9.36 |
| | 5 | 13.7 | 9.99 | 10.37 | 10.68 | 10.72 | 10.81 | 10.84 | 10.87 | 10.78 |

[19] and 8.7 *a,b* [30] show the coefficients of thermal expansion of the crystals of partiallt stabilised zirconia. Table 8.7 *a,b* gives several physical and mechanical properties of the crystals of partially stabilised zirconia (a) and of sintered ceramics of the same composition (b).

The hardness of different compositions decreases with an increase of the content of the tetragonal and monoclinic phases, and catastrophically decreases with an increase of the load on the indentor applied to the crystal. The decrease of hardness with increasing content suggests that the inclusions of the phase reduce the stresses in the vicinity of the indentor due to the phase transition and twinning [37]. The hardness of Mg-FSZ and Ca-FSZ is 14.4 and 17.2 GPa, respectively, and in the case of Y-FSZ it is 13.6 GPa. Fracture toughness was maximum at 2.56 mol% of $Y_2O_3$. Fracture toughness increases with increasing volume of the fraction of the tetragonal inclusions, i.e. with a decrease in the content of the stabilising oxide.

**Table 8.7.** Comparison on physical and mechanical properties of PSZ crystals and sintered ceramics of the same composition based on $ZrO_2$ [30]

(a)

| Crystal | Composition, wt% | Inclusions, vol% | Density, kg/m³ | Hardness, GPa | Young modulus, GPa | Bending strength, MPa | Fracture toughness, MPa·m^{1/2} |
|---|---|---|---|---|---|---|---|
| Mg-FSZ | 2.8 | 48 | 5790 | 14.4 | 200 | 685±48 | 4.82±0.56 |
| Ca-FSZ | 4.0 | 38 | 5850 | 17.1 | 210 | 661±33 | 3.97±0.46 |
| Ca-PSZ | 9 | 0 | 5680 | 17.2 | 210 | 241±28 | 2.54±0.13 |
| Y-FSZ | 5 | 52 | 6080 | 13.6 | 233 | 1384±80 | 6.92±0.14 |
| Y-PSZ | 20 | 0 | 5910 | 16.1 | 233 | 356±58 | 1.91±0.16 |

(b)

| Polycrystalline $ZrO_2$ | Young modulus, GPa | Bending strength, MPa | Fracture toughness, MPa·m^{1/2} |
|---|---|---|---|
| Mg-FSZ | 200 | 430–700 | 4.7–15 |
| Ca-FSZ | 200–217 | 400–650 | 5.0–9.6 |
| Y-FSZ | 210–238 | 696–980 | 5.8–9.0 |

Comment. Fully (FSZ) and partially (PSZ) stabilized zirconia

In heating the crystals of Y-FSZ and Y-PSZ, the strength and fracture toughness decrease with increasing temperature. However, the fracture toughness of Y-FSZ material is approximately twice that of Y-PSZ [38].

**The elastic properties**

The mechanical properties of the material, especially cracking resistance and fracture under loading, are determined to a large extent by the elastic properties of the material. Table 8.8 [39] shows the elastic constants of the single crystals of solid solutions based on zirconia and the Zener calculated ratio: $Z = Cu_{44}/(C_{11}-C_{12})$, which determines the degree of anisotropy of the elastic properties in the cubic crystals (for $Z = 1$ the material is isotropic). The value of this ratio also determines the direction of the extreme value of the Young modulus: for example, at $Z < 1$, the maximum value of the Young modulus is oriented in the direction <100>, at $Z > 1$ in the direction <111> [39].

Depending on the concentration of yttrium oxide in the entire range of composition, including the multiphase compositions, constant $C_{11}$ monotonically decreases, $C_{44}$ monotonically increases,

# Partially Stabilised Zirconia (PSZ) Crystals

**Table 8.8.** Elasticity constants of single crystals of solid solutions of PSZ

| $Y_2O_3$ mol% | Density, kg/m³ | $C_{11}$, GPa | $C_{12}$, GPa | $C_{44}$, GPa | Zener ratio $Z = C_{44}/(C_{11-}C_{12})$ |
|---|---|---|---|---|---|
| 20.00 | 5760 | 373.0 | 123.0 | 65.0 | 0.520 |
|  | 5760 | 372.0 | 117.0 | 68.0 | 0.533 |
| 17.90 | 5826 | 390.4 | 110.8 | 69.1 | 0.494 |
| 16.50 | 5810 | 381.0 | 80.0 | 63.0 | 0.419 |
|  | 5810 | 390.0 | 96.0 | 61.0 | 0.415 |
|  |  | 370.0 | 106.0 | 67.0 | 0.508 |
|  |  | 380.0 | 74.0 | 62.0 | 0.405 |
| 15.50 | 5868 | 397.6 | 108.6 | 65.8 | 0.455 |
| 12.10 | 5932 | 405.1 | 105.3 | 61.8 | 0.412 |
| 12.00 | 5890 | 403.0 | 100.0 | 57.0 | 0.376 |
|  |  | 385.0 | 108.0 | 59.0 | 0.426 |
|  |  | 391.0 | 71.0 | 60.0 | 0.375 |
|  |  | 388.0 | 70.0 | 56.0 | 0.352 |
|  | 5890 | 391.0 | 120.0 | 60.0 | 0.443 |
|  | 5910 | 403.0 | 100.0 | 46.0 | 0.304 |
|  | 5910 | 400.0 | 113.0 | 56.0 | 0.397 |
|  |  | 413.0 | 115.0 | 61.0 | 0.409 |
|  | 5908 | 404.0 |  | 62.0 |  |
|  |  | 413.0 | 112.0 | 61.0 | 0.405 |
| 11.10 | 5945 | 403.5 | 102.4 | 59.9 | 0.398 |
| 10.30 | 5910 | 403.0 | 83.0 | 58.0 | 0.363 |
| 10.00 | 5950 | 403.0 | 103.0 | 58.0 | 0.387 |
|  | 5950 | 395.0 | 117.0 | 61.0 | 0.439 |
| 9.00 | 5980 | 380.0 | 130.0 | 59.0 | 0.472 |

**Table 8.8.** continued

| $Y_2O_3$ mol% | Density, kg/m³ | $C_{11}$, GPa | $C_{12}$, GPa | $C_{44}$, GPa | Zener ratio $Z = C_{44}/(C_{11}-C_{12})$ |
|---|---|---|---|---|---|
| 20.00 | 5760 | 373.0 | 123.0 | 65.0 | 0.520 |
| | 5760 | 372.0 | 117.0 | 68.0 | 0.533 |
| 17.90 | 5826 | 390.4 | 110.8 | 69.1 | 0.494 |
| 16.50 | 5810 | 381.0 | 80.0 | 63.0 | 0.419 |
| | 5810 | 390.0 | 96.0 | 61.0 | 0.415 |
| | | 370.0 | 106.0 | 67.0 | 0.508 |
| | | 380.0 | 74.0 | 62.0 | 0.405 |
| 15.50 | 5868 | 397.6 | 108.6 | 65.8 | 0.455 |
| 12.10 | 5932 | 405.1 | 105.3 | 61.8 | 0.412 |
| 12.00 | 5890 | 403.0 | 100.0 | 57.0 | 0.376 |
| | | 385.0 | 108.0 | 59.0 | 0.426 |
| | | 391.0 | 71.0 | 60.0 | 0.375 |
| | | 388.0 | 70.0 | 56.0 | 0.352 |
| | 5890 | 391.0 | 120.0 | 60.0 | 0.443 |
| | 5910 | 403.0 | 100.0 | 46.0 | 0.304 |
| | 5910 | 400.0 | 113.0 | 56.0 | 0.397 |
| | | 413.0 | 115.0 | 61.0 | 0.409 |
| | 5908 | 404.0 | | 62.0 | |
| | | 413.0 | 112.0 | 61.0 | 0.405 |
| 11.10 | 5945 | 403.5 | 102.4 | 59.9 | 0.398 |
| 10.30 | 5910 | 403.0 | 83.0 | 58.0 | 0.363 |
| 10.00 | 5950 | 403.0 | 103.0 | 58.0 | 0.387 |
| | 5950 | 395.0 | 117.0 | 61.0 | 0.439 |
| 9.00 | 5980 | 380.0 | 130.0 | 59.0 | 0.472 |
| | | 475.0 | 144.0 | 61.0 | 0.369 |
| 8.50 | 5960 | 430.0 | 94.0 | 64.0 | 0.381 |
| 8.10 | 6011 | 401.8 | 95.2 | 55.0 | 0.359 |
| 8.00 | 5990 | 394.0 | 91.0 | 56.0 | 0.370 |
| | 6010 | 410.0 | 90.0 | 53.0 | 0.331 |
| | | 415.0 | 119.0 | 57.0 | 0.385 |
| 6.90 | 6008 | 405.0 | 110.0 | 58.0 | 0.393 |
| | | 410.0 | 103.0 | 58.0 | 0.378 |
| 3.90 | 6049 | 412.0 | | 60.0 | |
| | | 412.0 | 110.0 | 55.0 | 0.364 |
| 3.40 | 6075 | 406.0 | 105.0 | 55.0 | 0.365 |
| | | 407.0 | 101.0 | 55.0 | 0.359 |
| 2.80 | 6085 | 425.0 | | 56.0 | |
| | | 410.0 | 125.0 | 52.0 | 0.365 |
| | | 410.0 | | 52.0 | |
| | | 414.0 | | 56.0 | |
| 2.20 | 6044 | 390.5 | | 64.4 | |
| 1.7 | 5842 | 365.4 | | 73.6 | |

and $C_{12}$ remains constant. Direction [100] corresponds to the high value of the modulus $E \sim 360$ GPa, direction {111} to the minimum value of $E \sim 170$ GPa [36].

As already mentioned, the crystals of partially stabilised zirconia are characterised by high strength properties which, in combination with chemical inertia and high melting point, enable these materials to be used in different areas of science and technology. Many materials in the single crystal form and having the macroscopic dimensions have been obtained for the first time. The mechanical properties of partially stabilised zirconia depend greatly on the conditions of synthesis and subsequent heat treatment. Consequently,

it is necessary to estimate the effect on the mechanical properties of the technological factors, composition and nature of the stabilising oxide. Investigations were carried out into various characteristics of the materials, such as: microhardness, cracking resistance, compression strength, bending strength, the elastic properties of crystals, the temperature dependences of certain mechanical properties.

In most cases, the mechanical characteristics of low-formability materials, such as ceramics, are determined by the bend test with a relatively simple loading procedure which has been substantiated theoretically and tested in practice [40–53].

The method is based on recording the deformation diagram in loading of the specimen and determination, on the basis of these diagrams, of ultimate tensile strength, limiting deformation, the static modulus of elasticity and many other characteristics of the material. The deformation diagrams reflect the relationship between the stresses and strains, formed in the specimen during loading. Pure bending is preferred, but the method of bending the specimen with the application of a force concentrated in the centre of the specimen (three-point bending) is also used widely.

The measurements of specimens were taken in [45–53]. The specimens were in the form of prisms, with the dimensions $3.5 \times 5 \times 50$ mm. The dynamic modulus of elasticity ($E_d$) was determined from the values of the longitudinal speed of sound in specimens, the static modulus of elasticity ($E_s$) was determined on the basis of the dependences of the deflection of the load, applied to the specimen (0.5–0.15 of the limiting load. The ultimate strength was calculated in accordance with the classic Nadai equation [54], establishing the relationship between the stresses and strains in the process of loading of specimens.

The condition for the growth of brittle cracks is the violation of equilibrium between the released energy of elastic deformation and the increment of total surface energy. The brittle strength of the elements with a crack is inversely proportional to $l^{½}$, where $l$ is the half length of the crack.

The measure of brittleness $\chi$ is the energetic measure of the deviation from the linear stress–strain dependence and is calculated from the results of determination of the strength of single crystals in four-point bending. The stress intensity coefficients, characterising the crack resistance of the material, were determined in both the method of bending of prisms with a notch and by the

microindentation method. The *R*-curves were plotted in cyclic loading of specimens with a sharp crack [55].

Investigations were carried out on crystals of partially stabilised zirconia and, for comparison, on single-phase crystals with a cubic structure. Specimens were cut out in the direction parallel to the axis of growth, which was close to the direction <101> for the cubic single crystals, and to <111> for crystals of partially stabilised zirconia. The anisotropy of the mechanical properties was investigated on the specimens oriented along the specific crystallographic directions. The compression strength characteristics of the specimens were determined in an 1251 Instron machine (Great Britain). Tests were carried out on cylindrical specimens with a diameter of 10 + 0.5 mm and 10 mm long.

Microhardness was determined by a microhardness meter with a diamond Vickers pyramid as an indentor and was calculated using the equation

$$H = 1.854P/d^2 \tag{8.1}$$

where *P* is the load on the indentor, *d* is the diameter of the indentation.

The deformation and strength of crystals of partially stabilised zirconia were determined by the three-point method. Regardless of the difference in the dynamic moduli of elasticity and crystallographic orientation of the specimens, the values of the ultimate strength in three-bending were quite similar. The characteristics of the crystals are presented in Table 8.9 [56].

It should be mentioned that the moduli of elasticity of the specimens with the composition $ZrO_2$–3 mol%$Y_2O_3$ differ for different crystallographic directions. The static moduli of elasticity were slightly lower than the dynamic moduli of elasticity. This is characteristic of ceramic materials. In all experiments, examination showed a good agreement between the values of the dynamic and static moduli of elasticity. Figure 8.10 [50] shows the characteristic diagrams of deformation of the specimens with the composition $ZrO_2$–3 mol%$Y_{-2}O_3$ with the direction of the axis corresponding to <111>, the temperature range from −140 to 1100°C.

It should be mentioned that when the temperature is reduced − 140°C, the ultimate strength in bending rapidly increases (to 70%). With an increase of temperature, the deformation diagram for specimens with the composition $ZrO_2$–3 mol%$Y_2O_3$ (<111>) remains linear for up to 800°C, and for the composition $ZrO_2$–3mol%$Y_2O_3$ (<001>) up to 1000°C.

**Table 8.9.** Dependence of the mechanical properties of $ZrO_2$–$xY_2O_3$ crystals on the content of stabilizing oxide $x$ mol% (room temperature)

| Composition, mol% $Y_2O_3$ | 3 | 3 | 10 | 20 |
|---|---|---|---|---|
| Density, $10^3$ kg/m$^3$ | 6.04 | 6.03 | 5.85 | 5.75 |
| Direction of axis of specimen | <111> | <001> | <101> | <101> |
| Speed of ultrasound oscillations, m/s | 5357 | 7058 | 5965 | 6107 |
| Dynamic modulus of elasticity, $E_d$, GN/m$^2$ | 173 | 301 | 210 | 215 |
| Static modulus of elasticity, $E_{st}$, GN/m$^2$ | 149 | 397 | 180 | 185 |
| Ultimate strength in three-point bending, MN/m$^2$ | 862 | 738 | 224 | 158 |
| Ultimate strength in four-point bending, MN/m$^2$ | 642 | 506 | 135 | 139 |
| Critical stress intensity factor, N/mm$^{3/2}$ | 19 | 13.4 | 2.01 | 1.41 |
| Limiting strain $\varepsilon$, $10^{-4}$ m/m | 41.4 | | 7.5 | 6.6 |
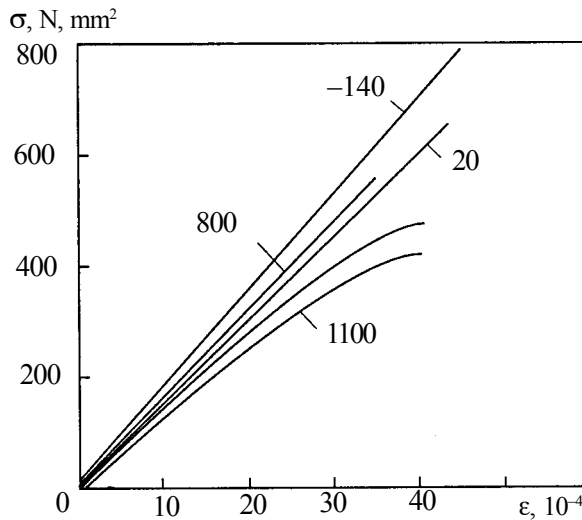


**Fig. 8.10.** Characteristic diagrams of deformation of specimens with the composition $ZrO_2$–3 mol% $Y_2O_3$ in the temperature range −140 to 1100°C. Direction of the growth axis of the crystals <111>.

Room-temperature tests show the linear–elastic nature of deformation of crystals up to breakdown, i.e. they belong to the group of brittle materials. The characteristics of these materials are sensitive to the rate of deformation at temperatures of inelastic

deformation [50]. The interest in these materials is determined by the possibility of using them as structural materials useable at high temperatures and in oxidation media and, therefore, investigations were carried out at different loading rates at a temperature of 1400°C, which is half as high as the melting point ($T_{test} \approx 0.5\ T_m$).

For comparison, single crystals of completely stabilised cubic solid solutions based on zirconia were investigated under the same conditions. These investigations are interesting because of the fact that their behaviour may reflect quite accurately the special features of deformation typical of the cubic matrix in partially stabilised zirconia.

The comparison of strength values at temperatures of up to 1400°C shows that the crystalline materials of partially stabilised zirconia are superior to sintered ceramics based on zirconia with identical composition and also to other similar materials [50]. The mean values of the mechanical characteristics of the cubic and tetragonal crystals annealed at a temperature of 1400°C are presented in Table 8.10 [50].

Analysing the behaviour of the mechanical properties of the materials, it should be noted that a temperature of 1400°C is characterised by the formation of high residual strains in the single crystals of cubic solid solutions, and also that the mechanical characteristics are highly sensitive to the strain rate. These factors may be explained by the result which shows that a decrease in the strain rate may lead to the activation of diffusion processes and formation in the specimens of an additional slip systems [56, 57] attributed to the appearance of the upper and lower yield limit, i.e. the characteristic peak of loading on the loading diagram (Fig. 8.11) [50]. The deformation diagrams of the single crystals of the cubic solid solutions, presented in [53,58,59] for compression of miniature cylindrical specimens are in almost complete quantitative and qualitative agreement with the deformation diagrams of crystalline specimens.

With an increase of the concentration of the stabilising oxide in the cubic solutions from 10 to 20 mol% $Y_2O_3$, the deformation diagrams show an increase in the difference ($\Delta P$) of the load corresponding to the upper and lower yield limits (Fig. 8.11) ($\Delta P_{20}/\Delta P_{10}$) $\approx 2.8$ at 1400°C and $V_{crack} = 0.005$ mm/min. Evidently, this is associated with a higher degree of ordering of the cubic solid solution with the composition $ZrO_2$–20 mol%$Y_2O_3$ in comparison with the composition $ZrO_2$–10 mol%$Y_2O_3$.
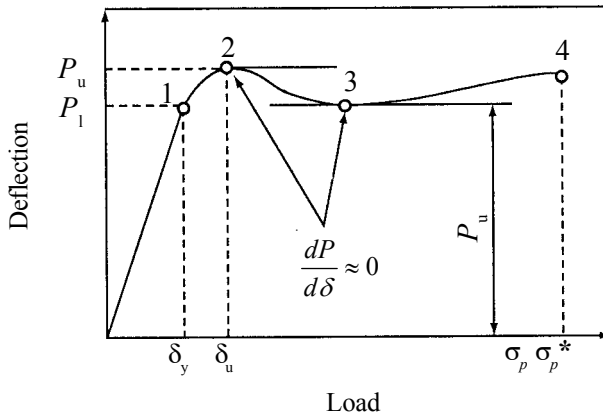
**Fig. 8.11.** Characteristic points of the deformation diagram. 1 – force **P**$_y$ and deflection $\delta_y$ corresponding to the upper yield limit; 3 – force $P_l$ corresponds to the lower yield limit; 4 – deflection $\delta_p$ at the moment of fracture of the specimen, $\delta_p$* – at the moment of unloading the specimen.

**Table 8.10.** Effect of chemical composition and annealing on mechanical characteristics of single crystals of cubic solid solutions based on zirconia ($V_{crack} = 0.5$ mm/min, $T_{test} = 20°C$)

| Material | $ZrO_2$–10 mol% $Y_2O_3$ | | $ZrO_2$–20 mol% $Y_2O_3$ | |
|---|---|---|---|---|
| | prior to annealing | after annealing* | prior to annealing | after annealing* |
| Ultimate strength, MN/m$^2$ | 134 | 172 | 144 | 216 |
| Limiting strain, $10^{-4}$ m/m | 7.4 | 10.2 | 7.7 | 11.7 |
| Statistical elasticity modulus $E_{st}$, GN/m$^2$ | 180 | 169 | 187 | 185 |

The crystals of partially stabilised zirconia are characterised by distinctive blocking of the slip systems in the crystals, presumably as a result of the presence of the domain structure with the size expressed in nanometres and the possible presence of inclusions of a second phase.

As regards the character of failure during deformation, the crystals of partially stabilised zirconia occupy an intermediate position between sintered ceramics and cubic crystals [50]. At all loading rates, the crystals break up into a smaller number of fragments in comparison with the specimens of the cubic crystals and their surface contains fine cracks near the main crack. The residual strain in the specimens was almost insignificant in

comparison with cubic crystals which indicates a low creep rate.

An increase in the strength of the single crystals with the cubic structure at 1400°C at all $V_{crack}$ rates in comparison with the strength at room temperature evidently is evidently caused by the a decrease of the degree of damage of the crystals during annealing as a result of mechanical treatment. This has been confirmed by testing specimens at room temperature after additional annealing at a temperature of ~1400°C for 15 min.

## 8.7. THE STRENGTH CHARACTERISTICS OF CRYSTALS OF PARTIALLY STABILISED ZIRCONIA

The results of examination of the compression strength characteristics are presented in Table 8.11 [19]. The Table shows that the maximum compression strength is shown by the materials with an yttrium oxide content of ~(2.5–3) mol%. The addition of other admixtures in small quantities has a strong effect on the mechanical characteristics of these crystals. The effect of the nature and concentration of a specific admixture on the properties of single crystals is specific and requires special investigations.

**The microhardness of crystals of partially stabilised zirconia**

The microhardness usually depends on the load at low loading and is independent at high loads. In [60–68] it is reported that in the case of ion crystals, the formation of an indentation is associated with the mobility and multiplication of dislocations in the field of concentrated loading.

The deviation of the shape of the indentation from the ideal shape in anisotropic materials results in a situation in which the diagonals of the same indentation differ. The values of microhardness, calculated on the basis of the length of the diagonals, may also differ. Thus, the microhardness may be anisotropic. To determine the anisotropy, the indentor is often represented by a Knoop pyramid in which the long diagonal is seven times longer than the short diagonal, with minimum cracking of the specimen. Microhardness is calculated from the following equation:

$$H_K = P / 0.07028d^2, \tag{8.2}$$

where $d$ is the length of the long diagonal.

**Table 8.11.** Strength characteristics of PSZ crystals

| Composition of crystals | | | Loading rate, mm/min | Compression strength $\sigma_B$, MPa | Strain $\Psi$ | Elasticity modulus $E$, GPa |
|---|---|---|---|---|---|---|
| $ZrO_2$, mol% | $Y_2O_3$ mol% | Additional admixture (0.1–0.3 wt.%) | | | | |
| 99.5 | 0.5 | – | 2 | 793.1 | 0.062 | 125 |
| 88.5 | 1.5 | – | 0.2 | 1510 | 0.0072 | 222.5 |
| 88.0 | 2.0 | – | 0.2 | 1556 | 0.00213 | 369.2 |
| 87.5 | 2.5 | – | 0.2 | 2133 | 0.0028 | 360.0 |
| 87.0 | 3.0 | – | 0.2 | 1729 | 0.0065 | 264 |
| 86 | 4 | – | 0.2 | 1552 | 0.00808 | 196 |
| 85.3 | 4.7 | – | 0.2 | 1305 | 0.0064 | 196 |
| 87.5 | 2.5 | Er | 2 | 1811.0 | 0.087 | 188 |
| 87.5 | 2.5 | Co | 2 | 2741 | 0.11 | 214 |
| 87.5 | 2.5 | Cr | 0.2 | 1323 | 0.081 | 151 |
| 87.5 | 2.5 | Tb | 0.2 | 1832.0 | 0.086 | 205 |

According to Griffith's fracture theory, the stress ($\sigma_f$), required for brittle fracture of material containing a crack is [60, 61]:

$$\sigma_f = (1/Y)\sqrt{2E'\Gamma/a}, \tag{8.3}$$

Here $\Gamma$ is the surface energy of fracture, $a$ is the length of the crack, $Y$ is a dimensionless parameter which depends on the shape of the crack; $E'$ is a coefficient which depends on Young's modulus (E) and Poisson's coefficient ($\nu$). At plane stress

$$E' = E, \tag{8.4}$$

and plane strain

$$E' = E/(1-v^2). \tag{8.5}$$

The methods of deformation of the material using an indentor have

been used for investigation of measurement of some mechanical properties of materials (hardness, microhardness, toughness, brittleness, etc). The anisotropy of microhardness is determined mainly by the structure of the lattice and primary slip systems, acting during indentation. The anisotropy of the elastic properties of the crystals of $ZrO_2$–$Y_2O_3$ with an yttrium oxide content of 1.7–20.0 mol% has been investigated in [39] on the basis of the speed of propagation of ultrasound. The experimental results show that cubic modification single crystals are characterised by the highest anisotropy. The presence of the tetragonal phase in the crystals decreases the anisotropy of the elastic properties.

The anisotropy of the microhardness of cubic zirconia crystals has been studied in greater detail using Knoop's indentor. No cracks were found in the vicinity of the indentations on the (100) plane in the load range of 0.5–2.0 N. The microhardness of the specimens changed depending on the orientation of the long diagonal of the indentor being maximum along the direction <100> and minimum along <110> crosses at an angle of 45° [63, 64]. The maximum and minimum values of microhardness were: 19.0 and 14.5 GPa for a load of 0.5 N; 15.7 and 13.7 GPa for a load of 1 N; 13.8 and 12.6 GPa for a load of 2 N.

The hardness anisotropy coefficient $H_{max}/H_{min}$ decreased from 1.3 to 1.11 with the load increasing from 0.5 to 2.0 N. The similar character of the effect of the load on the coefficient of microhardness was observed for the hardness of semiconductors and is explained by a strict restriction of the slip systems for small loads and by the activation of other slip systems at higher loads [65].

For monoclinic zirconia, the anisotropy of Knoop's hardness at a load higher than 1 N increases and the ratio $H_{max}/H_{min}$ is 1.62 at the absolute values of 9.4 GPa for the orientation <101>{010} and 5.8 GPa for <010>{100} [66]. No anisotropy of Vickers hardness was detected on the (100) plane of cubic crystals. With temperature increasing from 25 to 1300°C, microhardness decreased for the planes {100} and {111} from 14 to 2 GPa, for {110} from 16 to 2 GPa. Owing to the fact that no cracks formed during indentation at temperatures above 800 °C, this temperature is the temperature of the brittle–ductile transition [67].

The plastic deformation of cubic zirconia, stabilised with yttrium oxide, in indentation in the temperature range 200–800°C takes place as a result of dislocation slip and crack formation. Dislocation slip

takes place through the primary slip systems {001} <110> and
{111} $\langle 1\bar{1}0 \rangle$. The resultant geometry of the zone of plasticity is
characterised by strong anisotropy. At a temperature of > 400°C,
the mobility of edge dislocations is higher than that of screw
dislocations.

In single crystals of cubic zirconia, stabilised with 9.4 mol% of
yttrium oxide, special attention was given to the dislocation structure
around indentations of the indentor on the planes {111}, {011} at
temperatures of 200–800°C. Investigations were carried out in an
electron microscope with selective etching [67]. Indentation on the
(001) plane results in the formation of radial cracks propagating
along the <110> direction. The results show that the formation and
propagation of these cracks is a function of temperature and load.
Examination of a number of sections under an indentor shows that
cracks propagated along the {110} planes. This is in agreement with
the results obtained for indentation at room temperature [68]. No
lateral cracks were found in the examined temperature and load
ranges.

The indentation of partially stabilised materials based on zirconia
is characterised by a stress-initiated martensitic transition of
metastable tetragonal zirconia to the stable monoclinic phase [67,
69]. The compressive stresses, formed around the indentation,
improve the mechanical properties of tetragonal zirconia in
comparison with the completely stabilised zirconia (cubic) (CSZ).
The expansion, associated with phase transformation, also results
in the swelling of the surface around indentation, which was
detected in examination under an optical microscope by the phase
contrast method [68]. A second possible mechanism of increasing
the toughness of tetragonal zirconia may be the stress-induced
reorientation of ferroelastic domains [23, 70]. The majority of
investigations of these materials were carried out on ceramics and
polycrystals. The mechanical properties of single crystals of
tetragonal zirconia have been studied less extensively.

The anisotropy of failure in the crystals of partially stabilised
zirconia is clearly manifested in the orientation of the diagonal of
the indentor along <110> at which only radial cracks form, and
radial and lateral cracks appear at the orientation along <100> [71,
72]. The indentation on the (111) surface results in the formation
of radial cracks along the directions $\langle 2\bar{1}\bar{1} \rangle, \langle \bar{1}2\bar{1} \rangle$ and $\langle \bar{1}\bar{1}2 \rangle$. At higher
loads or low temperatures, fine cracks formed along the direction
[$\bar{2}11$]. A series of sections also confirms that these cracks

propagated along the {110} planes. Lateral cracks developed at higher loads or low temperatures.

The microhardness of the specimens with the composition $ZrO_2$–3 mol% $Y_2O_3$ at a load of (50–100) N is 14–15 GPa and is independent of the orientation of the indented polished surface, i.e. at higher loads the anisotropy of microhardness disappears.

## Crack resistance of the crystals of partially stabilised zirconia

The stress intensity factors, characterising the cracking resistance of the material, were determined by both the methods of bending crystalline parallelepipeds and by the microindentation method. The *R*-curves were plotted in cyclic loading of specimens with a sharp crack.

The stress field in the vicinity of the tip of the crack is characterised by a stress intensity factor. Catastrophic failure takes place when the intensity of the stress field at the tip of the crack reaches a limiting value. Deformation in this region can be divided into three types: I – tensile loading and opening of the crack; II – slip inside the crack surface; III – slip outside the crack surface. The deformation of the first type is most significant. The stress intensity factor for this deformation is determined by the equation:

$$K_{\mathrm{I}} = \sigma Y \sqrt{a}. \tag{8.6}$$

When the value of $K_{\mathrm{I}}$ reaches the critical value $K_{I} = K_{IC}$, fracture starts to take place (uncontrolled crack growth) and equation (8.6) takes the following form:

$$K_{1C} = \sigma_f Y \sqrt{a}. \tag{8.7}$$

This equation, 'criterion-1' of brittle fracture has been established from the conditions of the stress state at of the crack tip and is in fact identical to the Griffith criterion derived from the law of conservation of energy in this process:

$$\sigma_f = (1/Y)\sqrt{2}E'\Gamma/a = K_{1C}/Y\sqrt{a}. \tag{8.8}$$

The limiting value $K_{1C}$ is a parameter of the material referred to as the stress intensity factor which characterises the brittle fracture

resistance of material. The method of measuring $K_{1C}$ for brittle materials is the subject of discussion in many studies [73–75].

The crack formation resistance of the crystals of partially stabilised zirconia is determined by the method of three-point bending of notched specimens and by indentation of polished surfaces.

Examination of the cracking resistance of crystals with the composition $ZrO_2$–3 mol%$Y_2O_3$ shows that this material, characterised by a high elasticity modulus in the direction <001>, has a higher resistance to tensile loading of the cracks in this direction in comparison with the <111> direction (see Table 8.12). The maximum value of the stress intensity factor $K_{1C}$ for the specimens is 16 MPa m$^{1/2}$. The results obtained in the examination of the *R*-curves, i.e., the dependence of the stress intensity factor on the length of the sharp crack, are presented in Fig. 8.12 [44].

The cracking resistance (stress intensity factor) depends on the load and orientation of the surface of the specimen (Table 8.12).
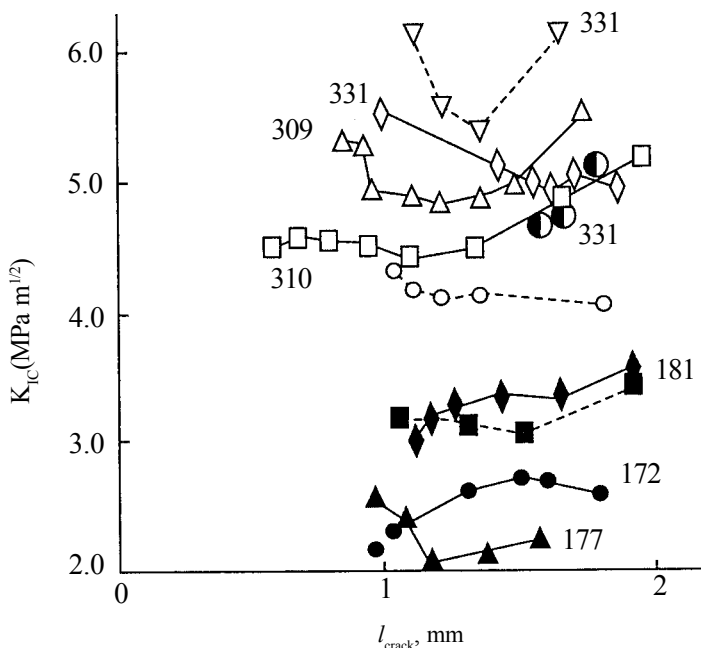


**Fig. 8.12.** Dependence of the stress intensity factor $K_{1C}$ of $ZrO_2$–3 mol%$Y_2O_3$ crystals on the length of a sharp crack $l_{crack}$ (numbers at the curves are the dynamic moduli of elasticity $E_d$, GPa).

**Table 8.12.** Critical coefficients of stress intensity of $ZrO_2$–3 mol% $Y_2O_3$ crystals ($10^3$ N/mm$^{3/2}$) [50]

| Load, N | Surface orientation | |
|---------|---------|---------|
|         | (111)   | (001)   |
| 50      | 8.7     | 10.2    |
| 100     | 5.3/3.9 | 7.7/5.7 |
| 300     | 4.2/2.3 | 6.8/4.6 |

## The effect of admixtures on the mechanical properties of crystals of partially stabilised zirconia

It is well-known that the addition of a small amount (<0.5 mol%) of rare-earth and transition elements to the composition of solid solutions based on zirconia with a stabilising admixture within a specific range of concentrations (away from the concentration boundaries of the phase fields) does not change the phase composition of the crystals but results in changes of certain characteristics. In order to examine these phenomena, in [19] the authors grew crystals of partially stabilised zirconia with different third admixtures, Ce, Nd, Pr, Sm, Tb, Er, Ho, Cu, Fe, Co, Mn (Table 8.11) and investigated several characteristics of these crystals in comparison with the crystals of partially stabilised zirconia without additional admixtures. As an example, the mechanical properties of crystals of partially stabilised zirconia with an addition of terbium oxide will now be discussed.

The crystals with the composition $ZrO_2$–3.3 mol%$Y_2O_3$–0.3 mol% $Tb_2O_3$ were grown in a cold crucible with a diameter of 400 mm. The mechanical characteristics of crystals from different parts of the ingot (the central path with a size of ~0.25 $D_c$ ($D_c$ is the crucible diameter), peripheral, adjacent to the walls of the crucible ~0.1–0.15 $D_c$, and intermediate) were investigated on specimens cut out along the axis of growth without any preliminary crystallographic orientation. The mechanical characteristics of the investigated crystals are presented in Table 8.13.

The experimental results show that the values of the dynamic elasticity moduli of this material are slightly lower in comparison with the crystals of partially stabilised zirconia without additional admixtures, and are independent of the position of the crystal block in the ingot. The values of the moduli did not exceed 220–230 kN/

**Table 8.13.** Physical–mechanical characteristics of $ZrO_2$–3.3 mol% $Y_2O_3$–0.3 mol% $Tb_2O_3$ crystals

| Composition, mol% $Y_2O_3$ | $ZrO_2$–3.3 mol% $Y_2O_3$–0.3 mol% $Tb_2O_3$ | | | | |
|---|---|---|---|---|---|
| | 1 (centre) | | | 2 | 3 |
| Crystal growth zone | After growth | Annealing (vacuum $10^{-3}$, 1400 °C, 2 h) | | Intermediate region | Periphery |
| | | prior to | after | | |
| Density, $10^3$ kg/mm$^3$ | | | 6.06 | | |
| Dynamic elasticity modulus, $E_d$, kN/mm$^2$ | 213 | 180 | 196 | 195 | 176 |
| Static elasticity modulus, $E_{st}$, kN/mm$^2$ | 163 | 141 | 155 | 155 | 136 |
| Ultimate strength in four-point bending, $\sigma_y$, N/mm$^2$ | 354 | 369 | 448 | 416 | 398 |
| Critical stress intensity factor, $K_{IC}$, N/mm$^{3/2}$ | 10.7 | 10.5 | 6.0 | 6.8 | 7.0 |

**Table 8.14.** Mechanical characteristics of oriented crystals of PSZ, activated with Ce and Tb

| Crystal (sample oriented in [100]) | Density, g/cm$^3$ | Speed of propagation of UW, m/s | Dynamic elasticity modulus, GPa | Bending strength, MPa | | $K_{IC}$, MPa·m$^{0.5}$ |
|---|---|---|---|---|---|---|
| | | | | Three-point | Four-point | |
| Y-Ce-PSZ | 6.07 | 7769 | 366 | 1378 | 1250 | 11.43 |
| Y-Tb-PSZ | 6.06 | 7730 | 352 | 1611 | - | 9.96 |

mm$^2$, and the elasticity moduli for other crystals of partially stabilised zirconia were in certain cases higher than 300 and even 350 kN/mm$^2$. Previously, it was reported that the elastic properties of the crystals of partially stabilised zirconia are anisotropic and the [100] direction is the 'high-modulus' direction with $E$ ~360 GPa, and {111} is the low-modulus direction with $E$ ~170 GPa. Therefore, specimens of crystals whose surfaces coincided with the {100} plane of the pseudocubic crystal system were prepared. The bend tests yielded the ultimate strength and critical stress intensity factors of the specimens of $ZrO_2$–3.3 mol%$Y_2O_3$–0.3 mol%$Tb_2O_3$ presented in Table 8.14.

Comparison of Tables 8.13 and 8.14 shows clear differences in the values obtained on the oriented and non-oriented specimens.

Vacuum annealing is characterised by a change of the valency state of terbium ion: $Tb^{4+} \rightarrow Tb^{3+}$. Recovery annealing increases the ultimate strength and decreases the cracking resistance of the material.

Tests carried out at a low temperature (–150°C) showed that the strength of the material increased by approximately 30% in comparison with the strength at room temperature. Microhardness depends only slightly on the load on the indentor and the crystallographic orientation of the plane on which the tests were carried out. For example, the hardness of crystals at a load of 10 N was 12.8–13.8 GPa and at a load of 200 N it was 12.2–13.0 GPa.

Thus, small variations of the concentration of admixtures within 1 mol% result in a large scatter of the mechanical characteristics of the crystals of partially stabilised zirconia. The experimental results show that in the synthesis of high-strength and crack-resistant crystals of partially stabilising zirconia by the method of directional crystallisation of the melt it is important to take into account many factors: the effective coefficient of distribution of the admixtures, the technological conditions of incorporation of admixtures (the rate of crystallisation, temperature gradient, etc), the effect of the type and concentration of the stabilising oxide and the third admixture, the thermal conditions of annealing and cooling of the crystals, containing ions of variable valency.

Thus, the following conclusions may be drawn: with increasing concentration of the stabilising oxide the coefficients of thermal expansion (CTE) of the material increases (Tables 8.1, 8.2 and 8.6), the phase transition temperature decreases, the magnitude of changes of the volume of the specimen during phase transitions becomes smaller and the hysteresis loop disappears. In stabilisation with the europium and gadolinium oxides, this transformations take place at a content higher than 3 mol%, and in the case of the ytterbium oxide the hysteresis loop disappears almost completely at 3 mol%. The shape and size of the loop are greatly affected by the synthesis conditions. In directional solidification of the melt, the specimens have zero porosity and are characterised by the nonuniform distribution of the phases along the length of the crystal. It is possible that this is the reason why the shape of the hysteresis loop is smooth and the inflection point on the curve corresponds to the temperature at which the rate of phase transformation is higher than expansion or compression of the

tetragonal phase present in the specimen. Therefore, the range of transformation becomes blurred and wide. A short measurement time and low temperatures resulted in the situation in which the metastable tetragonal phase (T'), present in the specimen, does not change its composition and does not undergo transformations, and changes take place only in the monoclinic phase, formed during crystal growth.

## 8.8. CURRENT VIEWS REGARDING THE MECHANISM OF HARDENING OF CRYSTALS OF PARTIALLY STABILISED ZIRCONIA

In order to explain the anomalously high mechanical properties of the crystals of partially stabilised zirconia, investigators have proposed several hardening mechanisms. The following mechanisms have been developed most extensively: 1) 'transformation'; 2) 'dispersion'; 3) ferroelastic.

The high strength and toughness of partially stabilised zirconia in the initial stage of development of theory were explained exclusively by transformation hardening in which the propagating microcrack results in the martensitic $t \leftrightarrow m$ transition which absorbs the energy of stresses, transforms this energy into thermal energy, and also constrains and arrests the propagating microcrack [76].

Subsequently, attention was given to the fact that the high strength characteristics of the single crystals of partially stabilised zirconia are also retained in the high-temperature range (higher than 1000°C) at which there is no $t \leftrightarrow m$ phase transition. In addition to this, in fracturing a crystal with the composition $ZrO_2$–4.5 mol%$Y_2O_3$ produced by directional crystallisation, there were no traces of the monoclinic phase on the fracture surface [28]. Regardless of this, the specimen were characterised by high strength and toughness. Examination of the microstructure and plastic deformation of these materials has resulted in a proposal for a new mechanism of hardening, i.e. dispersion hardening.

The experimental results show that the crystals contain inclusions of the disc-shaped tetragonal phase (*T*). In annealing of crystals (1400–1600°C), the inclusions gradually acquire the equilibrium shape and dimensions, determined by the minimum sum of the volume and surface energy. The annealing temperature and time have a significant effect of the mechanical properties of crystals.

For example, the yield limit rapidly increases with increasing annealing time because the density of the inclusions of the tetragonal phase is determined by the diffusion kinetics. An increase of the yield limit in annealing is directly proportional to the width of the inclusions and the distance between the colonies in which they are grouped.

Loading results in the formation of dislocations in the cubic matrix. According to the authors of [28], the dispersion hardening mechanism is associated with inhibition of the movement of matrix dislocations through a network of the inclusions of the second phase. For example, there were dislocations with the Burgers vector $b$ =1/2[110], which travelled along the (001) plane.

As shown previously, 12 variants of tetragonal inclusions may form in the cubic matrix. It may be shown that only for one of the 12 variants, the [110] vector represents the natural translation vector of the tetragonal lattice. When a sliding dislocation meets any of the remaining 11 variants of the inclusions, the dislocation is inhibited in its movement because it cannot enter the tetragonal inclusions without energy losses associated with the rotation of the Burgers vector. For a dislocation to enter the tetragonal inclusions, the dislocation reaction of the type $1/2[102] \leftrightarrow [101]+1/2[\bar{1}01]$ is required, i.e. the initial dislocation generates a dislocation pair. One dislocation enters the ([101]) tetragonal inclusions, the other one remains at the interphase boundary forming an Orowan's kink. This 'sessile' dislocation (identical with the well–known Lomer–Cottrell dislocation) is a barrier to the movement of the next dislocation inside the inclusions. A cluster of dislocations forms around the interphase boundaries. Each subsequent dislocation is arrested at larger and larger distances from the interface.

It is well-known that the dislocations, like a new phase, may nucleate homogeneously or heterogeneously (on dislocation clusters during closure of a vacancy disc, on the Frank–Read sources). The Lomer–Cottrell barriers around the interface suppress the generation of dislocations by means of the Frank–Read source. Homogeneous nucleation of dislocations requires high stresses increasing the yield and tensile strength, i.e. increasing the mechanical characteristics. This is the principle of the proposed hardening mechanism.

A number of authors [23, 25, 27, 29] explain the mechanism of hardening of the crystals of partially stabilised zirconia by a ferroelastic transformation associated with the transition of the

cubic phase into a tetragonal phase. It is well-known that the ferroelastic properties are shown by substances having two or more stable orientation states and capable of transferring from one state to another under mechanical loading. The ferroelastic transition differs from the martensitic transition induced by mechanical stresses by the fact that the process takes place by means of the reorientation of ferroelastic domains without any change of the crystal structure. The ferroelastic properties of the tetragonal zirconia form as a result of the *t'*-phase transition which decreases the symmetry of the initial cubic phase to the tetragonal phase. This results in the formation of three orientation states nonequivalent from the energy viewpoint which are referred to as variants of twins or domains. With the mutual distribution similar to orthogonal, these domains form pseudocubic crystals. During loading, the domains may reorient their axes in order to accommodate the stresses. The details of this effect were investigated by the authors of [70, 76–80]. They depend on the direction and the type of loading and also the orientation of the crystal and domain switching in the ferroelastic materials. X-ray diffraction and ultrasound examination of the crystals of partially stabilised zirconia under loading show that when loading with 1.5 GPa, the tetragonal axis *c* changes its direction by 90°, i.e. the tetragonal axis becomes the *a* axis. When the load is removed, a reversed transition takes place [78–81].

By analogy with the ferromagnetic transition, the ferroelastic transition has a hysteresis at loads below the ultimate strength. In ultrasonic examination, the hysteresis loop in the speed of sound–stress coordinate was clearly visible. At low loads of ~0.4 GPa, there was also a jump in the speed of ultrasound explained by the tetragonal–monoclinic transition. However, this jump is irreversible because at low temperatures the monoclinic phase cannot transfer to tetragonal. The hardening and high toughness of the ferroelastic material are explained by the absorption of the energy of the load in transition.

Thus, it may be assumed that there are at least three different mechanisms of hardening of partially stabilised zirconia. Evidently, one of the mechanisms may be dominant in the materials of partially stabilised zirconia of different composition and in different loading conditions, or several mechanisms may operate simultaneously. For example, the main contribution in the tetragonal partially stabilised zirconia should come from the ferroelasticity mechanism. If the material contains several phases, several mechanisms may act

simultaneously, depending on composition. In this case, the dispersion hardening mechanism will be controlling. For specimens containing the transformed *t*-phase, the controlling contribution is provided by the mechanism of transformation hardening, and for partially stabilised zirconia consisting of a mixture of cubic and nontransformed tetragonal *t'*-phases, the main role will be played by the mechanism of dispersion and ferroelastic hardening.

Since the composition, synthesis conditions and heat treatment parameters have the controlling effect on the degree of stabilisation of partially stabilised zirconia, its phase composition and microstructure, the mechanical properties of these materials also greatly depend on the above factors.

## 8.9 MOST PROMISING AREAS OF APPLICATION OF CRYSTALS OF PARTIALLY STABILISED ZIRCONIA

Recently, intensive research has been carried out into the application of ceramics of zirconia in many technical applications. The practical application of these materials is determined by a number of various characteristics such as: high melting point (~2800°C), the high-strength and cracking resistance ($\sigma$ = 600–1200 MPa; $K_{Ic}$ = 6–16 MPa m$^{1/2}$); high hardness (8.5 according to Moose, 1200–1500 kg/mm$^2$); low friction coefficient (0.04 on steel, 0.08 on tungsten–cobalt alloys); high resistance to abrasive wear; high coefficient of thermal expansion close to steel (10–11·10$^{-6}$ deg$^{-1}$); chemical resistance to corrosive media (acids, alkali, melts of metals, oxidation atmosphere at high temperatures); good heat resistance (280°C ); at low temperatures, partially stabilised zirconia has good electrical properties (at 20°C 2.2·10$^{10}$ ohm·cm). Other typical features of partially stabilised zirconia are bioinertia; retention of high mechanical properties in a wide temperature range (–140 to 1400°C).

The practical application of the materials of partially stabilised zirconia is being developed in the following directions:

1. Structural ceramics utilising high strength, wear resistance and low friction coefficient, and also heat insulating properties and corrosion resistance. These ceramics are promising for fabrication of:

–coatings on the components of internal combustion engines [82], increasing the efficiency of operation, the reliability and durability of the engine, decreasing the fuel consumption, etc;

–the components of pumps for chemical production (crystals, sleeves of cylinders, sleeves of valves, valves, based on links, etc) [83];

–bearings and various friction couples.

2. High hardness, cracking resistance and heat resistance make this material promising for fabrication of various cutting and processing tools. For example, dies made of ceramics based on partially stabilised zirconia in the drawing of copper wire showed durability values twice those of wires of any hard alloy [82].

3. Because of chemical and biological inertness, strength and high cracking resistance, this material is regarded as one of the promising materials for use in medicine for implants (bone replacement, joints, teeth) [48, 85, 86].

Single crystals of partially stabilised zirconia have a large number of valuable properties by which they differ from both metallic and, in particular, high-strength dielectric materials (including ceramics produced from partially stabilised zirconia). Because of the absence of the grain boundaries, the partially stabilised zirconia crystals have high strength (comparable with the strength of metals), fracture toughness and hardness. They are characterised by increased resistance to acids, alcohol, water vapours, high resistance to abrasive wear and are also distinguished by a low friction coefficient. The degradation of the mechanical properties at high temperatures (at up to 1400°C) in the oxidation media in single crystals of partially stabilised zirconia is considerably smaller in comparison with metals where the majority are subjected to high-intensity oxidation and structural ceramics undergoing recrystallisation processes. In addition to this, when the temperature is reduced to –140°C, the mechanical properties of the crystals decrease by 70%.

The crystals of partially stabilised zirconia may be used for the fabrication of components of mechanisms operating in extreme conditions of high mechanical loading, chemically corrosive media, increased temperatures, in the absence of lubrication. Because of the existence of the nanodomain structure in the crystals of partially stabilised zirconia and because of their high mechanical strength, it is possible to produce from them cutting tools with extremely sharp cutting edges, for both high-precision machining of different materials (metals, wood, glass, crystals, etc.) and for high quality medical tools.

The biological inertness [85, 86] of this material makes it

promising for application in medicine for implants. In recent years, mechanical and medical–biological comparative tests were carried out on partially stabilised crystals of zirconia, single crystals of cubic zirconia, tetragonal polycrystalline partially stabilised ceramics and also single crystals of aluminium oxide [48]. The single crystals of partially stabilised zirconia show highrt strength and failure resistance (toughness) in comparison with other materials. The experimental results show that the investigated implants of partially stabilised zirconia do not cause any inflammatory reactions in the living tissue and do not lead to pathological changes in the internal organs of animals. On the basis of the experimental results, the crystals of partially stabilised zirconia may be recommended as new materials for preparation of various implants.

Thus, the most promising areas of application of the crystals of partially stabilised zirconia are:

1. Wear resistant structural components for application in the conditions with increased temperatures, load and corrosive media: components of pumps for chemical production (pistons, the cylinder lining, valves sleeves, valves, piston rings, etc); components for mills (ball, roller), crushers, etc; filament guides for textile production; bearings (thrust, sliding), and different friction couples; prisms for precision devices; solid electrolytes, fuel elements, heaters; sensors of the oxygen content of exhaust gases, in water vapour and in molten metal; heat shielding screens, corrosion-resisting components, wear-resistant components for drilling equipment.
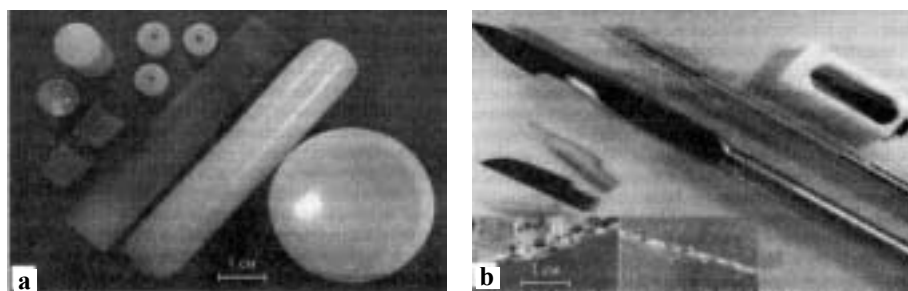


**Fig. 8.13.** Components made of PSZ crystals; a) medical scalpels, b) cutting edge of PSZ crystals.

2. Cutting and processing tools for machining the surface of components to the mirror-like state with a high degree of accuracy; in drawing wire; rolling rolls for the thinnest strips and foil

(platinum, gold, copper, aluminium), cutting tools for high precision machining of different materials (metal, wood, glass, crystals, etc); guide devices weaving machines; attachments for the formation of jets of high-pressure liquids; extruders and dies for the production of optical fibres for light guides; dies for the production of glass and basalt fibres, replacing platinum.

3. High-quality medical tools: scalpels with a large sharp cutting edge (~0.1 µm) for heart surgery, neurosurgery, vessels surgery, cosmetology, and opthalmology.

4. Bioinert implants with high fatigue strength for dental and orthopaedic surgery.

5. Goods of mass application: scissors, knives, components of meat-processing (knives, grates), golf clubs, links, jewellery components. Figure 8.13 shows several components produced from crystals of partially stabilised zirconia.

## References

1.  Y. Sakka, Y. Oishi, K. Ando, *Bull.Chem. Soc. Jpn*., 55, 420–422, 1982.
2.  N. Yoshikawa, H. Sato, *J. Jap. Inst. Metals*, v.50, 108–113, 1986.
3.  R.A. Miller, J. L. Smilek, R. G. Garlich, Phase Stability in Plasma-sprayed Partially Stabilized Zirconia-Yttriya, Adv. in Cer. V.3., Ed. By A.H. Heuer et. al, Columbus The American Ceramic Society, 1082113, 1981.
4.  G.V. Kurdyumov, Imperfections of the Crystal Structre and Martensitic Transformations, Nauka, Moscow, 1972.
5.  A.G. Khachaturyan, Theory of Phase Transformations and Structure of Solid Solutions, Nauka, Moscow, 1974.
6.  T. Mitsuhashi, Journal of American Ceramic Society, 48, 493, 1973.
7.  C.A. Ànderson, J, Greggi and T.K. Gupta, Diffusionless Transformations in Zirconia Alloys, p.78-85, Advances in Ceramics Vol.12, Science and Technology of Zirconia II., The American Ceramic Society, Columbus, Ohio, 1983.
8.  H.-H. Mobius, *Z. Chemie,* 4,3, 81–94, 1964.
9.  A.G. Kachaturyan, Theory of Structural Transformation in Solids, Chapter 8, Wiley, New York 1983.
10. B.Ya. Sukharevskii, B.G. Alapin, A.M. Gavrish, *Dokl. Akad. Nauk SSSR,* 156, 3, 677–680, 1964.
11. Yu.K. Sirotin, M.P. Shaskol'skaya, Fundamentals of Crystallography, Nauka, Moscow, 1979.
12. H. Varlimont, Martensitic Transformations in Alloys based on Copper, Silver and Gold, Nauka, Moscow, 1974.
13. V. Lantery, T.E. Mitchell, and A.N. Heuer, *Journal of American Ceramic Society*, 69, 7, 564–569, 1986.
14. J. Lefevre, *Ann. Chem.*, 8, 1-2, 117-149, 1963.
15. B.Ya. Sukharevskii, A.M. Gavrish, *Dokl. Akad. Nauk SSSR*, 155, 2, 438-441, 1964.

16.  H.S. Maiti, K.V.G.K. Gokhale and E.C. Subbarao, Journal fo the American Ceramic Society, 55, 6, 317–322, 1972.
17.  I.T. Dailey, D. Levis, Z.M. Librantand, L.I. Porter, *Trans. J. Brit. Ceram. Soc.*, 71, 1, 25–30, 1972.
18.  V. Ali, S.G.H. Bukhari, K.F. Shoaib and F.H. Hashmi, *Phys. Stat. Sol.* (a), 35, 181–184, 1976.
19.  E.E. Lomonova, Technology, Properties and Application of Crystals based on Zirconia, Dissertation, General Physics Institute, Moscow, 2001.
20.  G.V. Samsonov(editor), Physicochemical Properties of Oxides, Metallurgiya Moscow, 1978.
21.  E.E. Lomonova, Growth and Examination of Single Crystals of Solid Solutions based on Zirconia and Hafnium, Dissertation, FIAN, Moscow, 1980.
22.  A.F. Shchurov, I.F. Perevozchikov, *Neorg. Mater.*, 33, 9, 1087–1092, 1997.
23.  D. Michel, L. Mazerolles, M. Perez y Jorba, J. Mater. Sci., 18, 2618–2628, 1983.
24.  Yu.K. Voron'ko, et al., *Optika i Spektroskopiya*, 51, 4, 569–571, 1981.
25.  D. Baither, B. Baufeld, U. Messerschmidt, F.H. Foitzik, M. Ruhle, *Journal of the American Ceramic Society*, 80, 1691–98, 1997.
26.  K.M. Prettyman, J.-F. Jue, A.V. Virkar, C.R. Hubbard, O.B. Cavin, and M.K. Ferber, *J. Mater. Sci.*, 27, 4167–74, 1992.
27.  D. Baither, B. Baufeld and U. Messerschmidt, *Phys. Status Solidi* (a) 137, 569-76, 1993.
28.  A.H. Heuer, V. Lanteri, A.Dominguez-Rodriguez, Journal of the American Ceramic Society, 69, 3, 285–287, 1986.
29.  B. Baufeld, D. Baither, U. Messerschmidt, and L. Bartsch, *Physica Status Solidi* (a), 150, 1297–306, 1995.
30.  R.H. Ingel, D. Lewis, B.A. Bender, R.W. Rice, in: Advances in Ceramics, V.12, Science and Technology of Zirconia II, Ed. by N. Claussen, M. Ruhle and A. H. Heuer, American Ceramic Society, Columbus, OH, p.408–414, 1984.
31.  A.N. Heuer, V. Lantery, A. Dominguez-Rodriguez, *Acta Metall.*, 37, 2, 559-567, 1989.
32.  Yu.K. Voron'ko, et al., *Neorg. Mater.*, 34, 4, 439–443, 1998.
33.  A.N. Heuer, R.Chaim, and V. Lantery, *Acta Metall.*, 35, 3, 661–666, 1987.
34.  N. Ishizava, A. Saiki, T. Yagi, N. Mizutani, and M. Kato, Twin-Related Tetragonal Variants in Yttria Partially Stabilized Zirconia, *J.Amer.Ceram.Soc.*, 69, C-18 – C-20, 1986.
35.  M. Stadtwald-Klenke, Elektronenmikroskopische Untersuchungen an Inneren Grenzflechen in Verschidenen mit $Y_2O_3$ Dotierten $ZrO_2$-Keramiken, PhD Dissertation, Stuttgart University, 1994.
36.  N. Ishizava, A. Saiki, and M. Kato in: Advances in Ceramics, Vol. 24: Sience and Technology of Zirconia, The American Ceramic Society, Inc. p.479-484, 1988.
30.  R.H. Ingel D. Lewis, B.A. Bender, R.W. Rice, in: Advances in Ceramics, V.12, Science and Technology of Zirconia II, Ed. by N. Claussen, M. Ruhle and A. H. Heuer, American Ceramic Society, Columbus, OH, p.408-414, 1984.
37.  R.H.J. Hannink, K.A. Johnston, R.T. Pascoe, and R.C. Garvie, in: Advances In Ceramics, v.3, Ed. By A.H Heuer and L.W. Hobbs, The American Ceramic Society, Columbus, OH, 1981.
38.  R.P. Ingel, D. Lewis, B.A. Bender, P.W. Rice, Comm. Amer. Ceram. Soc.,

65, 9, C150-C152, 1982.

39.    R.P. Ingel, D. Lewis, Journal of the American Ceramic Society, 71, 4, 265-71, 1988.

40.    R.G. Hoagland, C.W. Marshall, W.M. Duckworth, Journal of the American Ceramic Society, 59, 5/6, 189-192, 1976.

41.    F.J. Baretta, In: Methods for assessing the structural reliability of brittle materials, ed. S.Freimann and C.Hudson, ASTM STP 844, 194-222, 1984.

42.    G.D. Quinn, F.J. Baretta., J.H. Conway, Commentary of Army Standart Test Method for Flexural stregth of High Performance Ceramics at Ambient Temperature, US Army Materials and Mechanics Research Center, AMMRG TR 85-21, August 11, 1985.

43.    G.D. Quinn, F.J. Baretta, Flexure test: can it be used for ceramics part design? MTS System Corporation, 1986, (Reprinted from Adv. Mater. And Processes, December 1985).

44.    G.A. Gogotsi, et al., *Ogneupory*, 8, 14–17, 1991.

45.    G.A. Gogotsi, et al., *Ogneupory*, 3, 15–19, 1992.

46.    G.A. Gogotsi, et al., *Ogneupory*, 6, 2–8, 1993.

47.    G.A. Gogotsi, E.E. Lomonova, V.G. Pejchev, *J. Eur. Cer. Soc.*, 11, 123-132, 1993.

48.    G.A. Gogotsi, E.E. Lomonova, Yu. Furmanova, and I.M. Savitskaya, *Ceramics Internationale*, 20, 343–348, 1994.

49.    S.N. Dub, G.A. Gogotsi, E.E. Lomonova, *J. Mat. Sci. Lett.,* 1, 446–49, 1995.

50.    D.Yu. Ostrovoi, Deformation and strength of ceramics at different tem-erature-rate effects, Dissertation, Kiev, 1993.

51.    G.A. Gogotsi, *Vestnik Mashinostroeniya*, 27–33, 1989.

52.    G.A. Gogotsi, et al., *Problemy Prochnosti*, 1, 73–77, 1991.

53.    A.Domingues-Rodriguez, K.P.D. Lagerlof, A.H. Heuer, *Journal of the American Ceramic Society*, 69, 3, 281-284, 1986.

54.    G.D. Quinn, *British Ceram. Trans. J.*, 88–94, 1989.

55.    G.A. Gogotsi, Problemy Prochnosti, 1, 77–87, 1977.

56.    N.N. Malinin, Applied Theory of Plasticity and Creep, Mashinostroenie, Moscow, 1968.

57.    K.G. Phillips, Fracture, Vol. 7, ed. H. Liebowitz, Mir, Moscow, 19–26, 1976.

58.    E. Fries, F. Guiberteau, A. Dominguez-Rodriguez, *Philosofical Magazine A*, 60, 1, 107–121, 1989.

59.    J. Lankford, R.A. Page, L. Rabenberg, J. Mater. Sci., 23, 4144–4156, 1988.

60.    Yu.S. Boyarskaya and O.Z. Grabno, Physics of Microindentation Processes, Shtinda, Kishinev, 1–170, 1986.

61.    K. Miyata, *Ceramikuusu,* 20, 1, 3–11, 1985.

62.    Yu.A. Kontsevoi,  et al., Physics and Strength of Semiconductor Materials and Structures, Radio i Svyaz', Moscow, 1982.

63.    A.Saiki, N. Jshizawa, N. Mizutani, K. Masanori, *J. Ceram. Soc. Jap.,* Int. Edn., 89, 1, 41–46, 1989.

64.    A. Pajares, F. Guiberteau, A. Dominguez-Rodriguez, A. H. Heuer,  *Journal of the American Ceramic Society*, 71, 7, 332–333, 1988.

65.    V. I.  Karban' and Yu.I. Borzakov, Processing of Crystals in Microelectronics, Radio i Svyaz', Moscow, 1988.

66.    Z. Li, Y. Li, Y. Fang, M.V. Nevitt, Microhardness Anisotropy of m-$ZrO_2$ Single Crystal., 11th Int. Ceram. Sci. and Technol. Congr., Anaheim, Oct. 31, v.3, 45, 1989.

67. D. Holmes, A.H. Heuer and P. Pirouz, *Philosophical Magazine,* A, 67, 2, 325-342, 1993.
68. A. Pajares, F. Guiberteau, A. Dominduez-Rodriguez, A.H. Heuer, *Journal of the American Ceramic Society*, 74, 4, 859-862, 1991.
69. J. Martines-Fernandez, M. Jimenez-Melendo, A. Dominguez-Rodriguez and A.H. Heuer, *Journal of the American Ceramic Society*, 74, 5, 1071–1081, 1991.
70. C.J. Chan, F.F. Lange, M. Ruhle, J.F. Jue, A.V. Virkar, *Journal of the American Ceramic Society*, 74, 8, 807–813, 1991.
71. G.A. Gogotsi, et al., *Ogneupory*, 3, 2–12, 1996.
72. G.N. Mosrcher, P. Pirouz, A.H. Heuer, *Journal of the American Ceramic Society*, 74, 3, 491–500, 1991.
73. G.P. Cherepanov, Brittle Fracture Mechanics, Nauka, Moscow, 1974.
74. V.I. Trefilov, et al., *Izv. AN SSSR, Neorg. Mater.*, 20, 6, 958–966, 1984.
75. G.A. Gogotsi and A.V. Bashta, *Problemy Prochnosti*, 9, 49–55, 1990.
76. R.H.J. Hannink, P.V. Kelly, B.C. Muddle, *Journal of the American Ceramic Society,* 83, 461–487 (2000).
77. F. Sanchez-Bajo, et al., *Journal of the American Ceramic Society*, 80, 1, 232-36 (1997).
78. A.V. Virkar, et al., Ferroelasticity and Related Properties of Crystals, pp.3-103, in: Phase Transitions, vol.3, Gordon and Breach Science Publishers, New York, 1982.
79. J.F. Jue, A.V. Vikar, Fabrication, *Journal of the American Ceramic Society*, 73, 3650–57, 1990.
80. A.V. Virkar, *Engineering Materials*, 1998, v.153–154, p.183–210.
81. M.G. Gain, M.H. Lewis, *Mat.Lett.*, v.9, 9, 309–312, 1990.
82. J. Huber, J. Heinrich, Ceramics in internal combustion engines, in: 2$^{nd}$ Eur. Symp. Eng. Ceram., London, 23-24 Nov., Proc. London; New York, 1989, 203–228, 1987.
83. K. Wolf, Th-Holschujer, Zirconoxid ein neuer Werkstoff fur den Pumpenbau in der chemischer Industrie., Chem-Techn. (BDR), 17, 8, 24–25, 1988.
84. V.G. Peichev, S.Y. Pliner, Ogneupory, 2, 12–14, 1987.
85. T. Motoxupo,Ceramikuusu, Ser. Jap. 23, 6, 25-26, 1988.
86. P. Christel, A. Meunir, M. Heller, Y.P. Torre, C.N. Peille, *J. Biomed. Mater. Res.*, 23, 1, 45–61, 1989.

# C–OX crystals

## 9.1. PRODUCTION OF C–OX CRYSTALS

In previous chapters, special attention has been paid to the examination of the conditions of growth and the possibilities of producing large single-phase cubic crystals in the $ZrO_2$–$R_2O_3$ systems (R=Eu, Gd, Yb, Y), i.e. fianites. The ranges of the concentration of the stabilizing oxide have been determined: 10–20 mol% $R_2O_3$ for R = Gd, Eu, and 8–20 mol% $R_2O_3$ for R =Yb, Y at the optimum growth rates of 10–20 mm/h. An increase in the concentration of the stabilising oxide above these limits results in a large decrease in the crystal size.

The difficulties in the growth of large single-phase single crystals $ZrO_2$– $R_2O_3$, R = Ce, Nd, Pr (elements of the beginning of the lanthanum series) are associated with the existence of relatively narrow ranges of the cubic solid solutions and with phase transformations in these systems at temperatures quite close to the crystallisation temperature. This is reflected in their phase homogeneity. The crystals grow either small (1–3 mm) or are turbid with a large number of cracks. Figure 9.1 presents the phase diagrams of the $ZrO_2$–$CeO_2$ and $ZrO_2$–$Nd_2O_3$ systems.

As shown in Chapter 7, the introduction into cubic fianite crystals of large quantities of oxides of cerium, praseodymium and neodymium in the form of additional admixtures, results in considerable difficulties because the distribution coefficients of these elements are considerably smaller than unity.

It was shown in Chapter 4 that the increase of the concentration of the stabilizing oxide requires a decrease in the rate of growth,
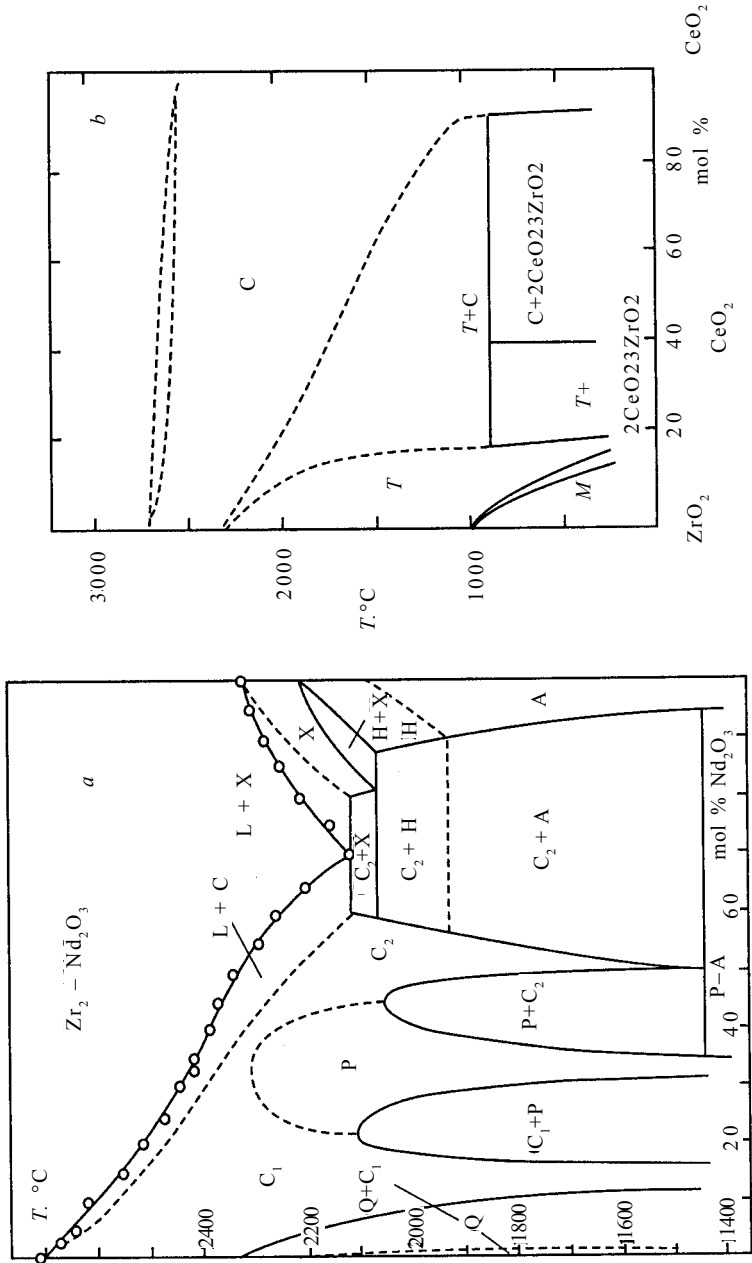
**Figure 9.1.** Equilibrium diagrams of the systems: $ZrO_2-Nd_2O_3$ (a) and $ZrO_2-CeO_2$ (b).

and the occurrence of the phase transformations, close to the crystallisation temperature, requires a decrease in the temperature gradient in the solid phase.

By taking into account the special features of crystallisation of solid solutions based on $ZrO_2$ in relation to the type and concentration of the stabilizing oxide, it has been possible to produce new large refractory oxide single crystals of cubic solid solutions based on zirconia and oxides of the rare-earth elements from the left half of the periodic table with a high content of stabilising oxides referred to as cubic oxides (C–OX).

Examination of the structure and optical properties of the C–OX crystals, activated by the ions of transition metals, as well as investigations of the effect of the heat treatment conditions on these crystals have shown large differences in the properties of C–OX crystals in comparison with the fianites which contain, as stabilizing oxides, rare-earth oxides of the right half of the series with the concentration not exceeding 20 mol%.

## The families of the $ZrO_2$–$R_2O_3$–$Pr_2O_3$ (R=Y, Yb, Lu) crystals

As shown in Chapter 4, the amount and dimensions of the crystals, produced by directional solidification in the cold crucible depend on many technological parameters: growth rate, the size of the crucible, thermal conditions, the purity of the initial reagents, the type and concentration of the stabilizing oxide, etc. Figure 9.2 shows the dependences of the mean size of $ZrO_2$–$R_2O_3$–$Pr_2O_3$ crystals on the concentration of the oxides of yttrium and praseodymium at a growth rate of 5 mm/h and a cold crucible diameter of 130 mm.

The presence of praseodymium oxide results in a decrease in the size of single crystals. This is most distinctive in the case of low concentrations of the praseodymium oxide. An addition of 5–8 mol% of $Pr_2O_3$ to crystals with 10 mol% $Y_2O_3$ results in the formation of an ingot consisting of small crystals. However, when the yttrium concentration is increased, the size of the crystals increases from 2–3 mm at 10 mol% to 10–15 mm at 20–30 mol% $Y_2O_3$. Thus, by combining the rare-earth elements from the left and the right hand parts of the rare-earth series, it is possible to produce cubic structure crystals containing high concentrations of 'light' rare-earth elements (Fig. 9.2).

It should be mentioned that in the $ZrO_2$–$R_2O_3$ systems, in the
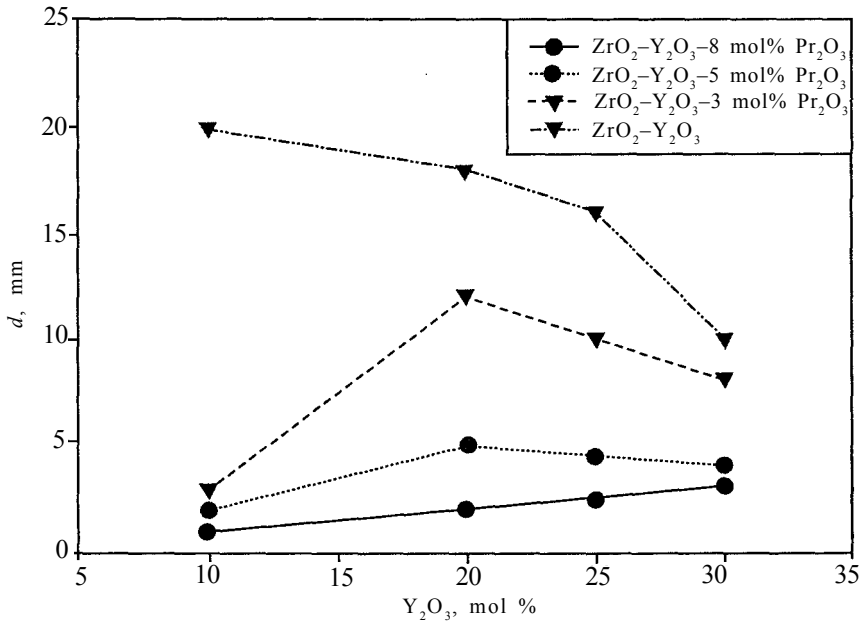
**Figure 9.2.** Dependence of the mean size of $ZrO_2$–$Y_2O_3$–$Pr_2O_3$ crystals on the concentration of yttrium and praseodymium oxides at a growth rate of 5 mm/h and the diameter of the cold crucible of 130 mm [1]

formation of substitution solid solutions, the dimensional factor of the rare-earth ions plays a significant role, for example, it affects the temperature of the eutectoid transformation and the width of the range of existence of the single-phase cubic solution with the fluorite structure (Table 9.1) [2, 3, 4–6]. It has also been established that the effect of two jointly present rare-earth ions on the phase composition and properties of solid solutions may be equivalent to the effect of the rare-earth ions with the mean radius equal to $r_m = x, r_1 + (1–x)\cdot r_2$. If the temperatures of the phase

**Table 9.1.** Effect of the concetration of stabilizing oxide on the eutectic of the phase diagrams of the $ZrO_2$–$R_2O_3$ systems [3]

| REE | $r_{R3+}$, Å | $C_{eut}$, mol% | $T_{eut}$, °C |
|------|------|------|------|
| La | 1.14 | 5 | 1850 |
| Ce | 1.07 | 10 | 1600 |
| Y | 0.92 | 25 | 300 |

transformations of the solid solutions are higher than 1600°C, the decomposition of the cubic solid solutions may take place in the growth process and it will affect the dimensions and phase composition of the crystals.

As indicated by Table 9.1, the addition of ions with a small radii together with the 'large' rare-earth ions may reduce the temperature of phase transformations and widen the range of existence of the compositions of the cubic solid solutions of the fluorite type. This circumstance also explains why it is possible to produce a large single phase crystals with the cubic structure containing a high concentration of the oxides of the rare-earth elements situated in the beginning of the series by simultaneous addition to the melt of large quantities of rare-earth element oxides with smaller ion radii.

The maximum concentration of $Pr_2O_3$ which could be introduced without breakdown of the cubic solid solution was 5 mol% for the $ZrO_2$–(20–30)mol% $Y_2O_3$ solid solution and 12 mol% for the $ZrO_2$–(14–20) mol% $Lu_2O_3$ solid solution. The x-ray diffraction patterns of the crystals with the $ZrO_2$–(20–30) mol% $Y_2O_3$–(3–5) mol% $Pr_2O_3$ and $ZrO_2$–(10–30) mol% $Yb_2O_3(Lu_2O_3)$–(3–12) mol% $Pr_2O_3$ composition showed the presence of only a fluorite-type cubic solution. In the crystals containing 15 mol% of $Pr_2O_3$, x-ray diffraction analysis showed the presence of the monoclinic phase.

The nature of distribution of the oxides of the rare-earth elements with large ion radii (cerium, neodymium) is identical with that described in Chapter 7. The effect of $Pr_2O_3$ on the growth of single crystals and the distribution of praseodymium in relation to its concentration is shown in Fig. 9.2. The boundaries of the crystals are characterised by an increased concentration of praseodymium and by a decrease in the content of yttrium. This indicates the displacement of praseodymium at the solidification front as a result of the low value of the effective distribution coefficient of $Pr^{3+}$.

In the growth of C-OX crystals, the authors of [1] used large diameter crucibles (400 mm, equipment Kristall-403) and low growth rates (up to 1–2 mm/h). A large diameter cold crucible supports the formation of favorable conditions for the growth of large crystals.

The dependence of several optical and mechanical properties of the C–OX crystals of the $ZrO_2$–$Y_2O_3$– $Pr_2O_3$ system on the chemical composition is presented in Table 9.2.

The comparison of these properties with the properties of fianite crystals shows that the C–OX single crystals are characterised by

**Table 9.2.** Dependence of the properties of C–OX crystals of the $ZrO_2$–$Y_2O_3$–$Pr_2O_3$ system [1]

| Composition, mol% | | | Refractive index ($\lambda = 582$ nm) | | Microhardness, kg/mm$^2$ | Density. kg/m$^3$ |
|---|---|---|---|---|---|---|
| $ZrO_2$ | $Y_2O_3$ | $Pr_2O_3$ | Prior to annealing* | After annealing | | |
| 78 | 19 | 3 | 2.04 | 2.07 | 1359±51 | 5626 |
| 78 | 20 | 2 | 2.12 | – | 1359±58 | – |
| 77 | 20 | 2 | 2.12 | 2.10 | 1272±73 | 5713 |
| 75 | 20 | 5 | 2.10 | – | 1231±49 | 5690 |
| 65 | 20 | 15 | – | – | 1123±45 | 5790 |
| 70 | 25 | 5 | 2.01 | – | 1325±56 | 5694 |
| 67 | 29 | 4 | 1.93 | – | 1499±45 | 5534 |
| 67 | 30 | 3 | 2.03 | – | 1364±38 | 5544 |
| 65 | 31 | 4 | 2.02 | 2.03 | 1155±57 | 5385 |
| 65 | 30 | 5 | 2.05 | 2.04 | 1235±49 | 5422 |
| 64 | 30 | 5 | 2.04 | 2.04 | 1287±53 | 5574 |

*Annealing: 1200–1400°C, vacuum $10^{-3}$ Pa, 2–5 h

lower density, microhardness and reflective index. This is associated with a high content of the stabilizing oxide. However, these differences are small. The content of oxides with high ion radii (cerium, neodymium) has a strong effect on the microhardness of crystals.

It should be mentioned that after growth a part of the praseodymium ions is situated in the crystals of cubic zirconia in the tetravalent state [7]. Vacuum annealing is followed by reduction to $Pr^{3+}$ and this is accompanied by a large change in the ion radius of praseodymium (from 0.96 A to 1.14 A). In the crystals containing even large quantities of the praseodymium oxide (up to 10–12 mol%), this transition takes place reversibly without destruction of the phase homogeneity and integrity of the specimens. The changes in the absorption spectra of the 80 mol% $ZrO_2$–14 mol% $Y_2O_3$–6 mol% $Pr_2O_3$ after annealing for two hours in a vacuum of $10^{-3}$ Pa at 1200°C are presented in Fig. 9.3.
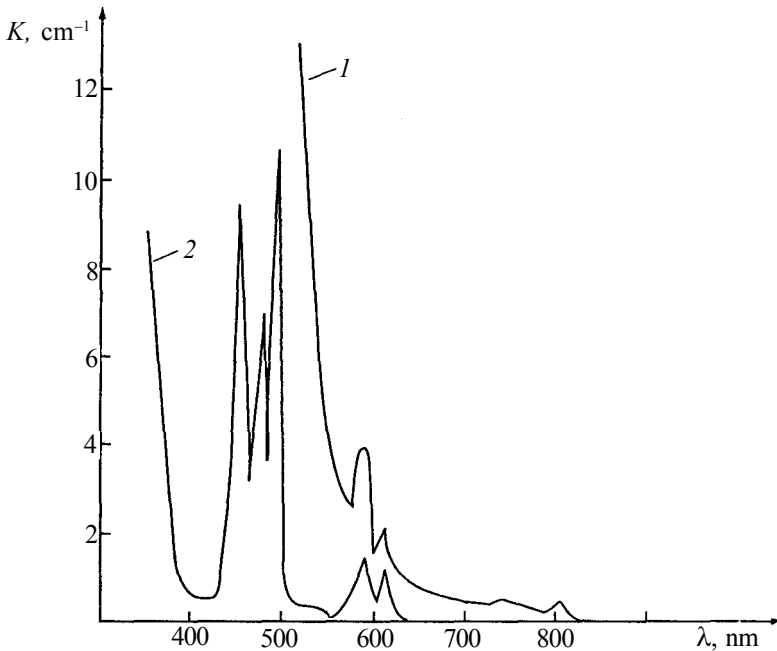
**Figure 9.3.** Transmission spectra of a 80 mol% $ZrO_2$–14 mol% $Y_2O_3$–6 mol% $Pr_2O_3$ crystal (1 – after growth, 2 – after vacuum annealing in a vacuum of $10^{-3}$ mm Hg, T = 1200 °C).

## 9.2. THE SPECTROSCOPIC PROPERTIES OF C–OX CRYSTALS

An increase in the concentration of the stabilising oxide has a strong effect on the optical properties of the crystals of cubic solid solutions based on zirconia. The absorption spectra of the transition elements are sensitive to the local structure of the nearest neighbourhood of the admixture ion. The authors of [1] investigated the effect of composition and heat treatment (in vacuum and in air) on the absorption spectra of 'pure' $Zr_{1-y}Y_yO_{2-y/2}$ crystals and similar crystals activated by transition metals (Co, Mn, V, Ni, Cr) in a wide yttrium concentration range $0.15 \leq y \leq 0.55$, {$ZrO_2$–(8–38) mol% $Y_2O_3$}. Investigations were carried out on the absorption spectra of the crystals in relation to the oxidation–reduction conditions of heat treatment. Admixtures were introduced into the melt in the form of oxides and their concentration was varied in the

range 0.01–1 wt%. A further increase in the concentration of the admixtures resulted in a large deterioration of the conditions of growth of single crystals and formation of growth defects in these crystals.

The effect of vacuum annealing on the absorption spectra of zirconia and solid solutions based on it depends on temperature, pressure, annealing time and cooling rate. 'Hard' annealing ($T >$ 1400°C and rapid cooling) results in darkening of the crystals caused by the presence of a high intensity wide absorption band with a maximum in the vicinity of 0.5 µm. In the investigations, the authors used 'soft' annealing ($T <$ 3000°C, cooling rate ~10°C/min). The crystals were annealed for 0.5–10 hours in a vacuum of $10^{-4}$–$10^{-5}$ Pa. Figure 9.4 shows the absorption spectra of non-activated crystals of $Zr_{1-y}Y_yO_{2-y/2}$, ($y$ = 0.21 and 0.5 prior to and after annealing at 1200°C), The figure indicates that the position and curvature of the edge of the absorption band in the ultraviolet region depends on the concentration of $Y_2O_3$ and on the heat treatment conditions. In the non-annealed crystals at $y$ = 0.55, the edge of the absorption band is relatively flat and extends into the visible range and, consequently, these crystals are characterised by yellow colour. In crystals with $y$ = 0.21, the edge is greatly displaced into the short wave range. Soft annealing in vacuum reduces the efficiency of absorption in the range $\lambda > 0.270$ µm and eliminates the difference in the spectra of the crystals with different concentrations of the yttrium oxide. The 0.5 µm band is not detected
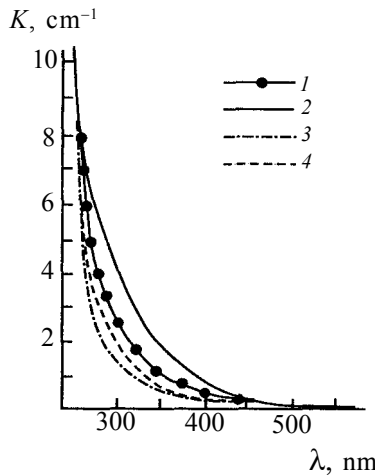


**Figure 9.4.** Absorption spectra of non-activated $Zr_{1-y}Y_yO_{2-y/2}$ crystals, $y$ = 0.21 (curves 1 and 2) and $y$ = 0.5 (curves 2 and 4) prior to (1, 2) and after vacuum annealing at 1200°C (3, 4).
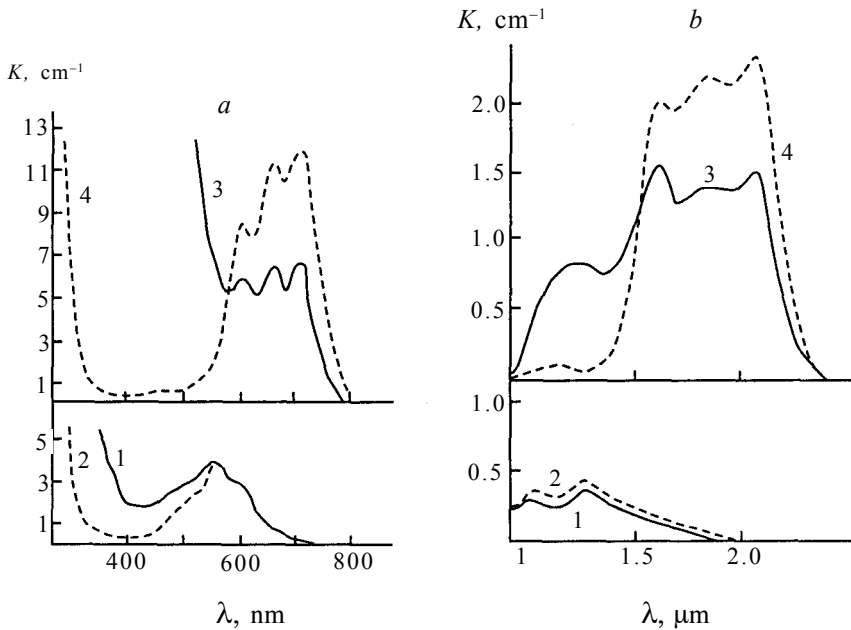
**Figure 9.5.** Spectra of $Zr_{1-y}Y_yO_{2-y/2}$–Co crystals, $y = 0.15$ (curves 1, 2) and $y = 0.55$ (curves 3, 4) in UV and visible (a) and IR ranges (b). Curves 1,3 – prior to, 3, 4 – after annealing of crystals.

in these conditions. The introduction of transition metals results in the formation of an absorption characteristic for these metals which also depends on the concentration of $Y_2O_3$ and on the heat treatment conditions (Fig. 9.5a, b, Fig. 9.6).

Prior to annealing, the spectra of the activated crystals contained two components: the relatively high intensity structureless absorption in the short-wavelength part of the spectrum detected to various degrees for all activating agents, and absorption bands, characteristic of the introduced activation agent which can be attributed to the *d–d* transitions of the metal ions [8]. An increase in the concentration of the yttrium oxide increases the intensity of absorption in the short-wavelength part of the spectrum and, in addition to this, results in changes in the *d–d* spectra in some cases. An especially strong effect of the concentration of the yttrium oxide on the absorption spectra is detected in the crystals with manganese, where the absorption coefficients for crystals with $y = 0.5$ in the entire visible range are 10–20 times higher than for crystals with $y = 0.15$ (Fig. 9.6b). Vacuum annealing in all cases greatly reduces the intensity of the short-wavelength structureless absorption and results in changes in the *d–d* spectra. The spectra of crystals with manganese
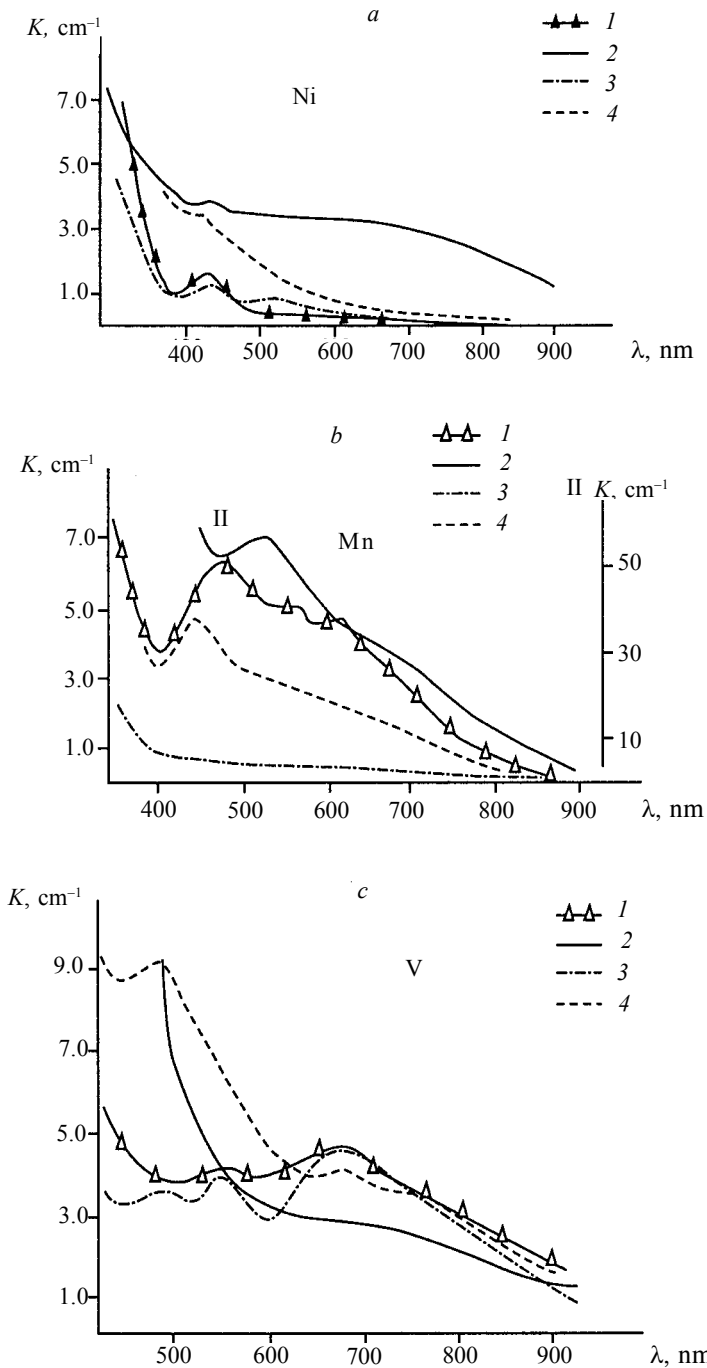
**Fig. 9.6.** Spectra of $Zr_{1-y}Y_yO_{2-y/2}$ crystals, $y = 0.15$ (curves 1, 3) and $y = 0.55$ (curves 2, 4) activated with oxides of Ni, Mn, V, Cr. Curves 1, 2 – prior to annealing, 3, 4 – after annealing.
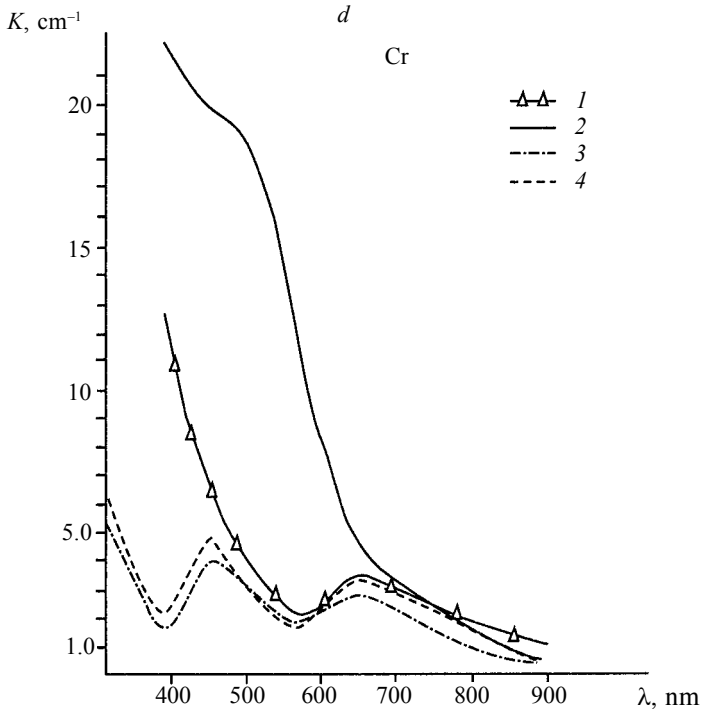
**Figure 9.6** (completion).

($y = 0.5$) show the largest changes in the *d–d* spectra.

The effect of the composition and heat treatment on the absorption spectra has been studied in detail on crystals with a cobalt admixture. Figure 9.5 shows that at a low $Y_2O_3$ concentration (curves *1, 2*), the cobalt spectra contain two complicated bands affected only slightly by annealing and causing only a small decrease in the efficiency of absorption in the short-wavelength part of the spectrum. High concentrations of $Y_2O_3$ (curves *3, 4*), result in the formation of new absorption bands and an increase in the intensity of short-wave structureless absorption in the non-annealed crystals. Vacuum annealing of crystals with a high concentration of $Y_2O_3$ not only causes 'bleaching' in the short-wavelength part of the spectrum but also results in a large increase of the intensity of the *d–d* bands (with the exception of a band with a maximum at 1.2 µm which weakens after annealing). Isochronous annealing (10 min) at different temperatures in a vacuum of $10^{-5}$ Pa shows that changes in the spectra take place mainly in the temperature range 600–700°C. Investigations of

crystals with different concentration of $Y_2O_3$ ($y = 0.15-0.5$) also shows significant changes in the profiles of the $d-d$ spectra of Co in $Zr_{1-y}Y_yO_{2-y/2}$ with an increase of the yttrium concentration. At $y = 0.28$ (16 mol%) the spectra are characteristic of a low concentration of $Y_2O_3$ (Fig. 9.5, curves *1*, *2*). With a further increase of the yttrium oxide concentration, new bands appear and the intensity of these bands increases with an increase of the $Y_2O_3$ concentration and at $y > 0.46$ (30 mol%) the new bands become controlling (Fig. 9.5, curves *3*, *4*). The short-wavelength absorption of the unannealed crystals is gradually enhanced with increasing content of yttrium oxide.

The determination of the composition of the crystals by the x-ray diffraction method shows that in most cases they include a small part of the cobalt present in the melt, i.e. the coefficient of distribution of cobalt in stabilised zirconium is smaller than unity. The limiting concentration of cobalt in the crystals did not exceed 0.10–0.15 wt% at a cobalt concentration in the initial mixture of up to 1.0 wt%. Excess cobalt precipitates in the form of inclusions of the second phase, and the distribution of this phase in the volume of the crystals depends on the initial concentration of cobalt. At a small concentration (up to 0.5 wt%) of the cobalt oxide, large inclusions (~10 µm) group at the beginning of the crystal, and the smaller ones form groups in the region of the cellular structure. With an increase of the cobalt concentration in the crystal $y > 0.4$, inclusions form throughout the entire volume, and no inclusions were detected at a concentration of $y < 0.4$.

The effect of heat treatment on the absorption spectra of the $Zr_{1-y}Y_yO_{2-y/2}$ crystals is associated with the changes of the charge state of the defects present in them. With a disruption of oxygen stoichiometry, every oxygen atom moving outside the limits of the crystal, leaves behind an anion vacancy and two electrons because of which the $ZrO_{2-\delta}$ crystal, where $\delta$ is the oxygen deficiency, contains $2\delta$ excess electrons distributed between defects depending on temperature, the concentration of defects and the binding energy of the electrons in the defects. The deviation from oxygen stoichiometry increases with increasing temperature and with a decrease in the partial pressure of oxygen in the atmosphere. Thus, vacuum annealing increases the concentration of excess electrons.

Oxygen vacancies form donor levels in the forbidden band of the crystal [9]. The stabilized crystals of zirconia contain large concentrations of the vacancies, comparable in the order of

magnitude with the concentration comparable with the concentration of the anion sites of the lattice. This may result in the formation of a 'band' of vacancies below the conduction band. It may be assumed that the probability of electronic transitions from the valence band to the levels of the oxygen vacancies is comparable with the probability of inter-band transitions and in this case, the short-wavelength edge of absorption of the non-activated crystals (Fig. 9.4) should be attributed to transitions to the levels of the vacancies, and not to the conduction band. Consequently, the position of the edge of absorption (approximately 5 eV) does not correspond to the width of the forbidden band but corresponds to the position of the levels of vacancies of oxygen in relation to the valence band of the crystal. The stabilizing oxide introduces, into the crystal lattice of zirconia, vacancies with the effective charge +2 ($V_O^{++}$) which may, in principle, trap one or two electrons with the formation of a singly ionised $V_O^+$ or neutral ($V^o$) vacancy [9]. Another type of trap is formed by admixtures of transition metals capable of changing valence quite easily, capturing an electron or a hole. The level of the admixture ion maybe regarded as empty or filled, depending on the valence state of the ion in the crystal. Therefore, the presence of, for example, $Co^{3+}$ in the crystal indicates the presence of empty levels of $Co^{2+}$ whose filling corresponds to the $Co^{3+} \rightarrow Co^{2+}$ transition.

In the crystals containing defects, inter-band electronic transitions are added to intra-centre transitions with charge transfer between the defects and the main ion. The charge state of the defect determines the nature of absorption spectra. In particular, transitions from the valence band are possible to the local empty level. In the crystals, grown in air, the deficit of oxygen is smaller, consequently, the levels in the forbidden band are mostly empty. The absorption spectra of these crystals should have the bands corresponding to the transitions from the valence band to the local levels. Vacuum annealing, accompanied by an increase in the oxygen deficit, results in filling of part of the local energy levels and transitions to these levels become impossible. This approach may be used to explain the weakening of absorption in the short-wavelength part of the spectrum after vacuum annealing. The transitions from the valence band to the levels of admixture ions correspond to the bands of charge transfer from a ligand to a metal ion, typical of transition metals in melts and solid solutions [8]. The levels, responsible for similar absorption in non-activated crystals (Fig. 9.4), which are

also removed by vacuum annealing, may be associated with non-controlled admixtures of the transition metals or vacancies. Evidently, the band in the vicinity of 0.5 $\mu$m, formed after 'hard' vacuum annealing, is determined by these transitions from the level of vacancies to the conduction band; possibly, vacancy levels are situated at a depth of 2.5 eV below the conduction band. The appearance of an electron on the local level changes the nature of intra-centre transitions. For an admixture centre, filling of the level by an electron indicates a decrease by unity of the charge of the ion and the appropriate change of the spectrum.

In the spectra of the $Zr_{1-y}Y_yO_{2-y/2}$–Co crystals (Fig. 9.5), the absorption in the range 0.270–0.500 μm, which disappeared after vacuum annealing, may be attributed to transitions with charge transfer. Cobalt in the crystal lattice of $ZrO_2$ may exist in the form of $Co^{2+}$ and $Co^{3+}$ ions The presence of the charge transfer band indicates the presence of $Co^{3+}$ ions in the unannealed crystals because only they are capable of accepting electrons from oxygen in the process of charge transfer $Co^{3+}+O^{2-} \rightarrow 5^{2+}.+O^-$. Since vacuum annealing changes $Co^{+3}$ to $Co^{+2}$, the spectra of annealed crystals in Fig. 9.5 should be attributed to bivalent cobalt. As indicated by the figure, $Co^{+2}$ is present in the crystals prior to annealing, therefore unannealed crystals contain simultaneously $Co^{+3}$ and $Co^{+2}$. Evidently, ions $Co^{+3}$ are related to the band $\lambda_{max} = 1.2$ μm which disappears after annealing. In the visible part of the spectra it is not possible to separate $Co^{+3}$ bands from $Co^{+2}$ bands. In $Co^{+2}$ spectra, attention should be given to special features, associated with the $Y_2O_3$ concentration: 1. existence of two types of $Co^{+2}$ spectra; 2. increase of the fraction of $Co^{+3}$ in the total concentration of cobalt prior to annealing with increasing concentration of yttrium oxide.

The existence of two different spectra of $Co^{+3}$ is naturally associated with the possibility of formation of centres with different coordinations of $Co^{+2}$. It is well known that an increase in the $Y_2O_3$ concentration increases the number of oxygen vacancies and, consequently, it may be assumed that the $Co^{+2}$ spectra in the crystals with the Co concentration $y = 0.55$ belong to centres with a lower coordination number than in the crystals with $y = 0.15$. Evidently, at $y = 0.15$ the coordination of $Co^{+2}$ is octahedral and at $y = 0.55$ it is basically tetrahedral. Consequently, for the sixfold coordination at $y = 0.15$ transitions in the optical range may be interpreted (Fig.9.7a) as the $^4T_1 \rightarrow {}^4T_2$ transitions (bands with max
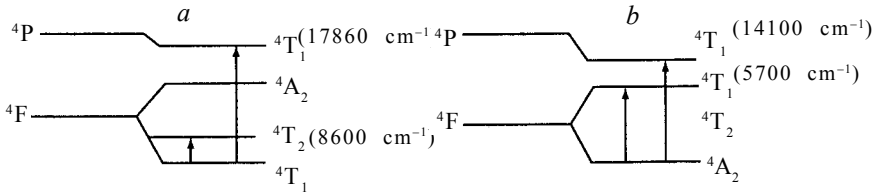
**Figure 9.7.** Scheme of transitions corresponds to absorption of the $Co^{2+}$ ions in nodes with coordination numbers 6 (a) and 4 (b) in $ZrO_2-Y_2O_3$ crystals

~1.15 µm) and ${}^4T_1(F) \rightarrow {}^4T_1(F) \rightarrow {}^4T_1(P)$ (bands with $\lambda_{max}$~ 0.56 µm). The ${}^4T_1(F) \rightarrow {}^4A_2(F)$ transitions are weak and almost completely merged with ${}^4T_1(F) \rightarrow {}^4T_1(P)$.

The spectrum of bivalent cobalt in quaternary coordination (Fig.9.7b) can be interpreted in the same manner. The band with maximum ~0.68 µm can be attributed to ${}^4A_2 \rightarrow {}^4T_1(P)$ transitions in the band with max~1.75 µm to ${}^4A_2 \rightarrow {}^4T_1(F)$ transitions. For $Co^{2+}$ in the tetrahedral environment the ${}^4A_2 \rightarrow {}^4T_2$ transition usually does not occur [8]. The splitting of the levels of the ion in the tetrahedral coordination is smaller in comparison with octahedral coordination and, correspondingly, the absorption spectra are displaced to longer wavelengths.

The fraction of $Co^{3+}$ in unannealed crystals may be estimated on the basis of the changes in the intensities of $Co^{2+}$ bands after annealing. Fig. 9.5 shows that after annealing the intensity of the 1.15 µm $Co^{2+}$ band in the crystal with $y = 0.15$ increases by 10%, and the intensity of the 1.85 µm band in the crystal with $y = 0.55$ increases by 50%. This means that prior to annealing the $Co^{3+}$ content in the crystals with $y = 0.15$ is less than 10%, and in the crystals with $y = 0.55$ the fraction of $Co^{3+}$ is 30% of the total cobalt concentration. An increase of the fraction of $Co^{3+}$ with increasing $Y_2O_3$ concentration is confirmed by an increase in the intensity of the charge transfer band in the crystals with $y = 0.55$. Consequently, it may be concluded that the oxygen non-stoichiometry in the crystals will also decrease with increasing $Y_2O_3$ concentration. Evidently, this conclusion also holds for non-activated crystals because in these crystals an increase of $Y_2O_3$ concentration is accompanied by intensification of absorption in the vicinity of the edge associated with the charge transfer from the valence band to the local level (Fig. 9.5).

The effect of $Y_2O_3$ concentration on the disruption of oxygen stoichiometry in $Zr_{1-y}Y_yO_{2-y/2}$ crystals is partially explained by the

"dilution" of the anion sublattice by the vacancies, i.e. by a decrease of the concentration of $O^{2-}$ in anion sites. However, dilution may result in a change not greater than 20% and not 300% as observed in the experiments. One of the possible explanations of the effect of the $Y_2O_3$ concentration on the disruption of oxygen stoichiometry is based on an assumption according to which the migration of oxygen from the crystal is affected by the vacancy concentration.

The process of oxygen exchange between the crystal and the atmosphere can be described as a result of three consecutive quasi-chemical reactions [10]:

$$O_O \leftrightarrow V_O + 1/2O_2, \ K_1 = [V_O]P_{O2}^{1/2}, \tag{9.1}$$

$$V_O \leftrightarrow V_O^+ + e', \ K_2 = [V_O^+][e']/[V_O], \tag{9.2}$$

$$V_O \leftrightarrow V_O^{++} + e', \tag{9.3}$$

where $O_o$ is the atom of oxygen in the anion site, $V_O$, $V_O^+$, $V_O^{++}$ are respectively the neutral (with two electrons), once ionised (with one electron) and twice ionised oxygen vacancy, e' is a free electron.

In a stabilized $Zr_{1-y}Y_yO_{2-y/2}$ crystal with slight disruption of stoichiometry (i.e. $\delta \ll y$) $[V_O^{++}] \approx y/2$, equations (9.1)–(9.3) show that:

$$[V_O] = K_1/P_{O2}^{1/2}, \tag{9.4}$$

$$[V_O^+] = (K_1/K_2/K_3)^{1/2}(y/2)^{1/2}P_{O2}^{-1/4}, \tag{9.5}$$

$$[e'] = (K_1/K_2/K_3)^{1/2}(y/2)^{-1/2}P_{O2}^{-1/4}, \tag{9.6}$$

The total concentration of excess electrons is $n = 2\delta = 2[V_O] + [V_O^+] + [e']$. Assuming that at the quenching temperature $[e'] \gg [V_O][e'] \gg [V_O^{++}]$, we have:

$$2\delta = [e'] \sim (y/2)^{-1/2} \tag{9.7}$$

In this case, an increase of $y$ from 0.15 to 0.55 halves electron density $[e']$. This is closer to the experimental results. Evidently, in addition to the investigated mechanisms, the stoichiometry is

affected by other factors: $Y^{3+}$ may affect the binding energy of $O^2$, and the mobility of vacancies also depends on the composition and quenching temperature, which can differ at the same cooling rate.

Thus, the investigations into the effect of vacuum annealing on the spectrum of absorption of pure and activated (by transition metals) crystals $Zr_{1-y}Y_yO_{2-y/2}$ with $y = 0.15–0.55$, carried out at [1] shows that:

a. Prior to annealing, the crystals have a small oxygen deficit, which decreases with increasing $Y_2O_3$ concentration. Vacuum annealing increases the oxygen deficit and, consequently, crystals contain excess electrons occupying the local levels in the forbidden band. This results in changes in the absorption spectra;

b. In the non-activated $Zr_{1-y}Y_yO_{2-y/2}$ crystals, the short-wavelength edge of the absorption band in the vicinity of 0.250 µm may be associated with the transition of electrons from the valence band to empty local levels of the oxygen vacancies. "Hard" vacuum annealing results in filling of these levels with electrons and in the appearance of a wide absorption band with a maximum near 0.5 µm;

c. The absorption spectra of activated crystals form as a result of the *d–d* intra-ion transitions and transitions between admixture local levels and the conduction band (transition with charge transfer). Vacuum annealing usually results in the reduction of admixture ions and, consequently, the bands of charge transfer from the oxygen to the admixture ion disappear;

d. Ions $Co^{2+}$ form two types of centres with different coordination in $Zr_{1-y}Y_yO_{2-y/2}$: at a low content of the stabilizing oxides, the coordination number is 6, at a higher content it is 4.

## 9.3 EFFECT OF ANNEALING ON THE VALENCE STATE OF COBALT IN THE $ZrO_2$–$Y_2O_3$ CRYSTALS

The processes of reversible exchange of oxygen between the crystal and the atmosphere, including diffusion in the single crystal and reactions in the volume and on the surface, as shown previously, may be investigated on the basis of changes in the absorption spectra accompanying these processes and associated with valence transitions of admixture elements.

The temperature dependences of equilibrium and rates of solid phase reactions $Co^{2+} \leftrightarrow Co^{3+}$ taking place during annealing of $ZrO_2$–30 mol%$Y_2O_3$ crystals with a cobalt admixture, were

investigated in [1]. The cobalt content in the crystals was $3 \cdot 10^{-2}$ wt.%. Plate-shaped specimens with a thickness of 0.5−0.6 mm were subjected to isothermal annealing in a vacuum of $3 \cdot 10^{-3}$ Pa and in air at 400 and 1400°C and then quenched. The absorption coefficients were measured at the maximum of the absorption band at 715 nm for $Co^{2+}$ and in the charge transfer band for $Co^{3+}$.

Valence transitions of cobalt in $ZrO_2$–$Y_2O_3$ crystals can be represented as a result of two consecutive quasi-chemical reactions [4]:

$$O_O \leftrightarrow V_O + 1/2O_2, \tag{9.8}$$

$$K_1 = K_{10} \exp(-\Delta H_1/kT) = [V_O]P_{O2}^{1/2} \tag{9.9}$$

$$V_O + 2Co^{3+} \leftrightarrow V_O^{++} + 2Co^{2+} \tag{9.10}$$

$$K_1 = K_{10} \exp(-\Delta H_1/kT) = [V_O]P_{O2}^{1/2} \tag{9.11}$$

where $O_O$ is the $O^{2-}$ ion in the anion site, $V_O$, $V_O^{++}$ are the neutral and twice-ionised oxygen vacancies, $[V_O]$, $[V_O^{++}]$ are the vacancy concentration, $c_2$ and $c_3$ are the concentrations of $Co^{3+}$ and $Co^{3+}$; $K_1$ and $K_2$ are equilibrium constants; $\Delta H_1$ and $\Delta H_2$ are the heats of reaction (9.9) and (9.11), $p$ is the partial pressure of oxygen above the crystal. The ratio of the equilibrium concentrations of $Co^{3+}$ and $Co^{2+}$ is determined by the equations:

$$c_3/c_2 = [V_O^{++}]^{1/2} K_0^{-1/2} \exp(-\Delta H/kT)P_{O2}^{1/4};$$
$$K_0 = K_{10}K_{20}; \quad \Delta H = (\Delta H_1 + \Delta H_2)/2$$

The variation of the enthalpy $\Delta H$ was determined by annealing the specimens to equilibrium conditions in air at different temperatures in the range 600–1000°C. After quenching, measurements were taken of absorption of $Co^{3+}$ at 500 nm ($k_3$) and $Co^{2+}$ at 715 nm ($k_2$). To establish the equilibrium state, the specimens were held in a furnace for a specific period of time. The dependence $k_3/k_2 = f(1/T)$ is sufficiently approximated by a straight line and by its slope, assuming that $[V_O^{++}] \approx$ const, the variation of enthalpy was calculated to be $\Delta H = 1.9 \cdot 10^4$ J/mol.

Using the correlation between $k_3$ and $k_2$, it is possible to determine the concentration of bivalent and trivalent cobalt in the
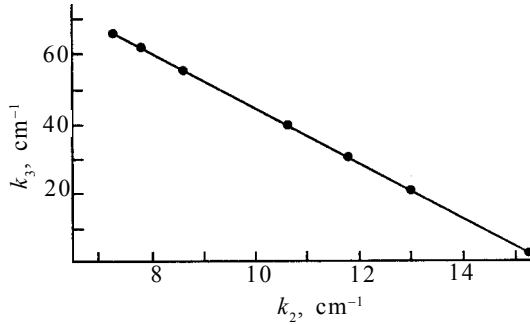
**Figure 9.8.** Correlation between the absorption coefficient of $Co^{3+}$ at $\lambda = 500$ nm ($k_3$) and $Co^{2+}$ at $\lambda = 715$ nm ($k_2$).
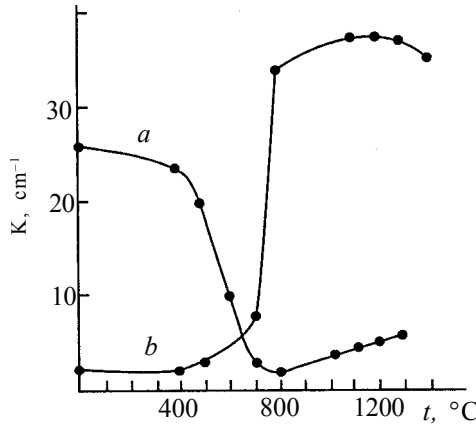


**Figure 9.9.** Dependence of the absorption coefficient of $Co^{3+}$ at $\lambda = 450$ nm on annealing temperature (10 min). a) in vacuum, b) in air after vacuum annealing.

crystals, $c_2$ and $c_3$. If the changes of $c_2$ and $c_3$ due to heat treatment are caused only by the transitions $Co^{2+} \leftrightarrow Co^{3+}$, then $c_2+c_3 = c_0=$const, and $k_3$ and $k_2$ are linked by a linear dependence $k_3 = c_0\varepsilon_3-(\varepsilon_3/\varepsilon_2){\cdot}k_2$, where $\varepsilon_3$ and $\varepsilon_2$ are molar coefficients of absorpt-ion. In the case of non-uniform distribution of $Co^{2+}$ and $Co^{3+}$ in the thickness of the crystal at intermediate stages of annealing, this dependence is fulfilled for mean absorption coefficients:

$$k = (\varepsilon/1)\int \sigma(x)dx \qquad (9.12)$$

Figure 9.8 shows a correlation between $k_3$ (500 nm) and $k_2$ (715 nm), obtained by measurements in different stages of transition from one equilibrium state (800°C in vacuum) to another (650°C in
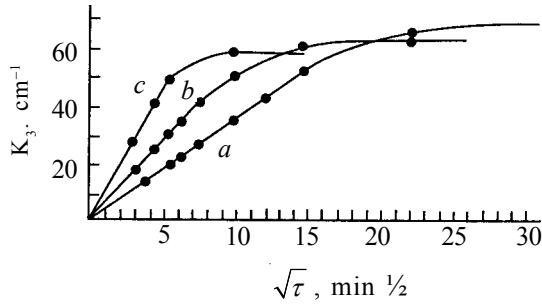
**Figure 9.10**. Dependence of the absorption coefficient of $Co^{3+}$ at wavelength $\lambda = 500$ nm on annealing time at temperatures, °C. a) 650, b) 700, c) 750 in coordinates: $k$ and $\sqrt{\tau}$ .

air), which gives $\varepsilon_3/\varepsilon_2 = 8.5$. The resultant ratio $\varepsilon_3/\varepsilon_2$ shows that in transition from the equilibrium state in vacuum at 800°C to equilibrium in air at 650°C, the fraction of $Co^{3+}$ in the total concentration of cobalt changes from 1 to 50% and the transition is accompanied by the absorption of $2 \cdot 10^{-5}$ g of oxygen by 1 g of the crystal with $c_0 = 3 \cdot 10^{-2}$ wt.%.

The curves of isochronous annealing (10 min) of crystal, in the non-equilibrium conditions, are presented in Fig.9.9.

Large changes start at $T > 400$°C, at relatively extensive diffusion of oxygen in the crystals. At $T > 1200$°C equilibrium is established throughout the entire thickness of the specimen after annealing for 10 min.

Figure 9.10 shows the kinetics of the $Co^{2+} \rightarrow Co^{3+}$ transition in annealing in air at 650–750°C. At the start of annealing, the thickness of the specimens has no significant effect, and a linear dependence of $k_3$ on annealing time $\sqrt{\tau}$ typical of diffusion kinetics, is observed.

The diffusion coefficients in initial sections are calculated for the total amount of the substance diffused into the specimens [10]. In the examined case, diffusion takes place through two surfaces and calculations are carried out using the equation:

$$(k - k_0)/(k - k_\infty) = (4/1\sqrt{\pi})\sqrt{D\tau} \qquad (13.13)$$

where $k_0$ is the initial value of the absorption coefficient, $k_\infty$ is the stationary value corresponding to diffusion through the entire thickness. The diffusion coefficients: $D = 0.64 \cdot 10^{-8}$, $2.24 \cdot 10^{-8}$, $21.5 \cdot 10^{-8}$ cm$^2$/s were determined at temperature lower

than 650, 700 and 750°C, respectively; activation energy was 1.8 eV. The numerical values of the diffusion coefficients do not characterise the free diffusion of neutral vacancies of oxygen (combined diffusion of ionised vacancies and electrons). Instead, they characterise "reaction" diffusion accompanied by binding of neutral vacancies by $Co^{3+}$ ions by reaction (9.2) and, according to [11], they represent effective coefficients which depend not only on the coefficients of diffusion of free defects but also on the parameters of the chemical reaction and concentration of the defects and admixtures. The activation energy is determined by the potential barrier of diffusion and by the energy of chemical bonding of defects by the reaction (9.2).

## 9.4 USING C–OX CRYSTALS IN JEWELLERY INDUSTRY

The large differences between C–OX crystals and fianites are associated with the possibility of introducing into them relatively high concentrations of oxides of Ce, Pr, Nd and with changing the optical characteristics by doping with ions of transition metals. A suitable example of this is the behaviour of $Co^{2+}$ ions in the $ZrO_2–Y_2O_3$ crystals. At a low content of yttrium oxides (fianites) the crystals after vacuum annealing are lilac-coloured and at a high content (>25mol%) they are cornflower-coloured. This is associated with the fact that at a low yttrium oxide content, the coordination of the $Co^{2+}$ ions is octahedral and there is a significant transmission in the red and yellow visible ranges of the spectrum, whereas at high yttrium oxide concentrations, the absorption spectrum of the $Co^{2+}$ ion in the tetrahedral coordination in these spectral regions is greatly increased (Fig. 9.10a,b).

When adding cobalt ions to crystals with a higher Pr (or Ce) oxide content it is possible to produce crystals with a wide range of colours and their shades from blue to green of various intensities [12,13]. Consequently, C–OX crystals may efficiently imitate different specimens of natural crystal sapphire and emerald which could not be achieved previously with fianite crystals. At present, C–OX crystals are used widely in jewellery industry.

## 10. CONCLUSION

The presented specific examples of synthesis and growth of crystals of different substances clearly demonstrate the individual and specific nature of the conditions dictated by the physicochemical properties of the synthesized compounds. However, it should be mentioned that heating of the melt, its maintenance and control of the temperature are common for the cold crucible technology. The main advantages of the cold crucible as the chemical reactor are an unlimited range of temperature variation, the possibility of using it for substances of different chemical nature in various atmospheres, the complete exclusion of the interaction of the melt with the crucible material, and the simple procedure of extracting the crystalline material from the crucible. All these special features and other potentialities place the cold crucible technology among promising methods of synthesis and growth of crystals of oxide compounds.

## References

1.  E.E. Lomonova, Technology, properties and application of zirconia-based crystals, Dissertation, General Physics Institute, Moscow, 2001.
2.  M. Perez-y-Jorba, *Ann. Chem.*, 7, 479-511, 1962.
3.  R. Collong, Nonstoichiometry, Mir, Moscow, 1974.
4.  Yoshimura Masahiro, Sata Toshiyuki, *Bull. Tokyo Inst.Technol.*, 108, 25-32, 1972.
5.  Alain Rovanet, Diagrammes de Solidification et Diagrammes de Phases Formes par la Zircone Avec les Sesquioxydes des Lanthanides, Colloques Internationaux du Centre National de la Recherche Scientifique, Paris-Grenoble, 1, 180, 221–235, 1970.
6.  Note de M.A.Rovanet, presentee par M.G.Chaudron, Etude a haute temperature du systeme Zircone-sesquioxide de neodime, CR. Sci. Paris, 270, C, 802–805, 1970.
7.  V.I. Aleksandrov, et al., *Izv. AN SSSR, Neorg. Mater.*, 11, 4, 664–667, 1975.
8.  D.T. Sviridov, et al., Optical spectra of ions of transition metals in crystals, Nauka, Moscow, 168–173, 179–180, 1976.
9.  F. Kröger, Chemistry of Imperfect Crystals, Mir, Moscow,
10. K. Hauffe, Reactions in Solids and on Their Surface, Vol. 1, IL, Moscow, 1962.
11. E.M. Akul'onok, et al., *J. Sol. St. Chem.*, 26, 1, 17–25, 1978.
12. V.I. Aleksandrov et al., A method of growth of coloured crystals of refractory oxides (its variants), Author's Cert. No. 1086833, 23.12.1983.
13. V.I. Aleksandrov et al., A method of growth of coloured crystals of refractory oxides (its variants), Author's Cert. No. 1112821, 09.02.1983.